UQAC

Université du Québec
à Chicoutimi

Stratégies d'alliage et de traitement thermomécanique pour des conducteurs en aluminium haute performance

par

Behrouz Abnar

Sous la direction du Prof. Mousa Javidani et la codirection du Dr. Paul Rometsch

Thèse présentée à l'Université du Québec à Chicoutimi en vue de l'obtention du grade de Philosophiae Doctor (Ph.D.) en Ingénierie

Défense présentée le 27 août 2026

Jury de Thèse:

Prof. Lukas Dion, Département des sciences appliquées, UQAC, Président du jury

Prof. Hatem Zurob, Faculté de génie, Université McMaster, Membre externe du jury

Prof. X.-Grant Chen, Département des sciences appliquées, UQAC, Membre interne du jury

Prof. Paul Rometsch, Rio Tinto Aluminium, Saguenay, Québec, Membre externe du jury

Prof. Mousa Javidani, Département des sciences appliquées, UQAC, Membre interne du jury

Québec, Canada

Résumé

La demande croissante de conducteurs en aluminium à haute performance pour les systèmes de distribution d'énergie exige des matériaux présentant simultanément une résistance mécanique élevée et une excellente conductivité électrique. Ce défi est particulièrement critique pour les applications de barres omnibus extrudées à chaud, où le renforcement par écrouissage après déformation n'est pas envisageable. Le présent projet répond à cette limitation par une étude approfondie des stratégies de conception d'alliages et des procédés thermomécaniques pour des alliages conducteurs d'aluminium des séries 6xxx et 1xxx, avec des ajouts de Cu, Sc et Zr pour des applications de barres omnibus. Un aspect clé de ce travail est l'adoption du vieillissement direct après extrusion à chaud (T5) de barres en forme de bandes, au lieu du traitement conventionnel T6 (mise en solution suivie de vieillissement). Le vieillissement direct offre des avantages importants, notamment une réduction du temps de traitement et de la consommation d'énergie, ainsi que la préservation des microstructures induites par la déformation, favorables au renforcement. Toutefois, en l'absence de mise en solution, les paramètres thermomécaniques, en particulier la température de préchauffage avant déformation, jouent un rôle déterminant dans la distribution des atomes de soluté sursaturés et, par conséquent, dans le comportement de précipitation lors du vieillissement. Ainsi, une conception rigoureuse du chemin de déformation, combinée à une optimisation du traitement de vieillissement, est essentielle pour obtenir un compromis efficace entre résistance et conductivité électrique.

La première phase du projet examine l'effet des ajouts de Cu (0,15–0,4 % massique) sur le comportement en déformation à chaud d'un alliage conducteur Al-Mg-Si, en mettant l'accent sur l'influence des paramètres de procédé sur la conductivité électrique et les propriétés mécaniques. Des essais de compression à chaud ont été réalisés à 450 °C et 550 °C, avec des vitesses de déformation comprises entre 0,1 et 10 s^{-1}. Les résultats montrent qu'à 450 °C, l'ajout de ≤0,3 % Cu augmente légèrement la contrainte d'écoulement (jusqu'à 8,2 %), tandis que 0,4 % Cu entraîne une augmentation significative (15–25,2 %). À 550 °C, l'effet du Cu diminue fortement (<3,5 %), notamment à faible vitesse de déformation. L'énergie d'activation augmente de 143,9 à 173,3 kJ/mol avec 0,15–0,4 % Cu, indiquant une résistance accrue à la déformation. Le Cu ralentit la restauration dynamique et réduit la taille des sous-grains ainsi que la désorientation moyenne des joints de grains. Globalement, les alliages déformés à 450 °C présentent une dureté inférieure de 8 à 20 %, mais une conductivité électrique plus élevée (1,0–2,5 % IACS) que ceux déformés à 550 °C après 8 h et 24 h de vieillissement, bien que cet écart diminue à 24 h. Ce comportement est attribué à la formation de précipités β-Mg_2Si grossiers à 450 °C, qui améliorent la conductivité mais réduisent la dureté. L'allongement du vieillissement de 8 h à 24 h augmente légèrement la conductivité (1–2,7 % IACS) avec une diminution minimale de la dureté (<4 HV). L'alliage contenant 0,3 % Cu présente le meilleur compromis, atteignant jusqu'à 75 HV (20–30 % de plus que l'alliage de base), avec une faible variation de la résistance à la déformation et une conductivité de 52,4–54,1 % IACS conforme aux normes.

La deuxième phase du projet étudie l'effet du préchauffage avant extrusion (420 °C contre 480 °C) et des stratégies de vieillissement direct (en une et deux étapes) sur la précipitation, la microstructure et les propriétés des alliages Al–0,1Sc–0,1Zr (% massique). Les résultats montrent qu'un préchauffage plus faible (420 °C) limite le grossissement précoce et favorise une forte densité de particules fines cohérentes $Al_3Sc/Al_3(Sc,Zr)$ de structure $L1_2$ après

vieillissement, améliorant ainsi la résistance. Le vieillissement en deux étapes (300 °C/24 h + 400 °C/8 h) appliqué à l'alliage extrudé à 420 °C produit la distribution de précipités la plus fine ($4{,}41\times10^{21}$ m^{-3}), grâce à la formation d'un cœur riche en Sc suivie d'une diffusion contrôlée du Zr, conduisant à une structure cœur–coquille très stable. Cet état optimisé favorise le renforcement par contournement d'Orowan et limite la croissance des sous-grains via une augmentation de la pression de traînée de Zener. Ainsi, la combinaison d'un faible préchauffage (420 °C) et d'un vieillissement en deux étapes permet d'atteindre le meilleur compromis, avec une résistance ultime de 172 MPa et une conductivité de 57,5 % IACS. À l'inverse, les alliages extrudés à 480 °C présentent un grossissement important des précipités, réduisant la résistance et la stabilité thermique.

La troisième phase analyse l'effet de la température de déformation à chaud sur l'évolution microstructurale de l'alliage Al–0,1 % Sc et son impact sur l'efficacité du vieillissement isotherme. Des essais de compression ont été réalisés entre 350 et 550 °C à une vitesse de déformation de 1 s^{-1} et une déformation vraie de 0,8, suivis d'un vieillissement à 300 °C pendant 24 h. Les résultats montrent qu'une déformation à 450 °C entraîne l'augmentation la plus élevée de la contrainte d'écoulement (39,7 %), tandis qu'à 550 °C, la contrainte est minimale et comparable à celle de l'aluminium pur. Après vieillissement, les conditions de déformation à 350 °C et 550 °C offrent le meilleur compromis entre conductivité (58,5–59 % IACS) et dureté (70–71 HV). En revanche, à 450 °C, la dureté est minimale (51 HV), soit une réduction d'environ 28 %. Les analyses MET révèlent que cette faible dureté est due à la formation de précipités Al_3Sc grossiers et hétérogènes lors du préchauffage, contrairement aux températures de 350 °C et 550 °C qui favorisent la formation uniforme de nanoparticules $L1_2$ lors du vieillissement.

Les résultats sont validés par des essais d'extrusion à l'échelle pilote, mettant en évidence l'influence du préchauffage des billettes, de la vitesse de refroidissement et des conditions de vieillissement sur la microstructure et les propriétés finales. Ce travail apporte également une compréhension fondamentale des mécanismes de précipitation dans les alliages conducteurs à base d'aluminium, appuyée par des approches de modélisation prédictive, et propose des lignes directrices pratiques pour la conception et la fabrication de conducteurs en aluminium à haute performance pour des applications industrielles.

Abstract

The increasing demand for high-performance aluminum conductors in power distribution systems requires materials that simultaneously exhibit high mechanical strength and excellent electrical conductivity. This challenge is particularly critical for hot extruded bus bar applications, where strengthening through post-deformation cold working is not feasible. The current project addresses this limitation through a comprehensive investigation of alloy design and thermomechanical processing strategies for both 6xxx and 1xxx aluminum conductor alloys, incorporating Cu, Sc, and Zr additions for electrical busbar applications. A key aspect of this work is the adoption of direct aging after hot extrusion (T5) of strip-shape bus bars instead of conventional T6 treatment (solutionizing followed by aging). Direct aging offers important advantages, including reduced processing time and energy consumption, as well as the preservation of deformation-induced microstructures that can enhance strengthening. However, in the absence of solution treatment, thermomechanical parameters, particularly the deformation preheating temperature, play a critical role in controlling the distribution of supersaturated solute atoms in the matrix and, consequently, the subsequent precipitation behavior during aging. Therefore, careful design of the deformation schedule, together with optimization of the aging treatment, is essential to achieve an effective trade-off between strength and electrical conductivity.

First phase of project examines the impact of Cu additions (0.15–0.4 wt.%) on the hot deformation behavior of an Al-Mg-Si conductor alloy with a focus on how process parameters influence electrical conductivity and mechanical properties. Hot compression tests were performed at 450°C and 550°C using strain rates ranging from 0.1 to 10 s^{-1} to achieve this objective. The results show that at 450°C, adding ≤0.3 wt.% Cu slightly raised flow stress (up to 8.2%), while 0.4 wt.% Cu caused a significant increase (15–25.2%). At 550°C, Cu's effect markedly decreased (<3.5%), especially at lower strain rates. Moreover, activation energy rose from 143.9 to 173.3 kJ/mol with 0.15–0.4 wt.% Cu, showing increased deformation resistance. Cu retarded the dynamic recovery and decreased the subgrain size and mean misorientation angle of the grain boundaries. Overall, alloys deformed at 450°C showed 8–20% lower hardness but higher electrical 1.0–2.5 %IACS than those deformed at 550°C after both 8 h and 24 h aging, though the difference narrowed at 24 h. This behavior is attributed to coarse β-Mg_2Si precipitates at 450°C, enhancing conductivity but reducing hardness. Extending aging from 8 h to 24 h slightly increased conductivity (1–2.7% IACS) with minimal hardness drop (<4 HV). The findings indicates that the 0.3% Cu alloy offered the best balance—achieving up to 75 HV (20–30% higher than base alloy), slight change in deformation resistance, and maintaining 52.4-54.1 %IACS conductivity within conductor standards.

Second phase of project explores how hot extrusion preheat (420 °C vs. 480 °C) and directly aging strategy (one- and two-step) affect precipitation, microstructure, and properties of Al–0.1Sc–0.1Zr (wt.%) alloys. Results indicate that lower preheat extrusion at 420 °C suppresses early coarsening and produces a higher density of fine, coherent $Al_3Sc/Al_3(Sc,Zr)$ particles with the $L1_2$ structure after aging, leading to enhanced strength. Aging conditions included one-step aging at 300, 350, and 400 °C, as well as a two-step schedule (300 °C/24 h + 400 °C/8 h). Two-step aging applied to the 420 °C-extruded alloy generated the finest precipitate distribution (4.41×10^{21} m^{-3}) by promoting Sc-rich core formation at 300 °C followed by controlled Zr diffusion at 400 °C, yielding a core–shell structure with superior coarsening

resistance. This optimized precipitation state delivered the highest strengthening contribution through Orowan bypass, along with controlled subgrain growth resulting from increased Zener drag pressure. Consequently, coupling a low extrusion preheat temperature (420 °C) with a tailored two-step aging treatment achieved the best property balance, delivering a UTS of 172 MPa and an electrical conductivity of 57.5% IACS—an effective pathway to producing high-strength, high-conductivity aluminum conductor alloys. In contrast, alloys extruded at 480 °C experienced significant precipitate coarsening across all aging treatments, resulting in lower strengthening and reduced thermal stability.

Third phase of project investigates the effect of hot deformation temperature on the microstructural evolution of Al–0.1 wt.% Sc alloy and assesses its impact on the effectiveness of subsequent isothermal aging. Uniaxial hot compression tests were conducted over a temperature range of 350–550 °C at a constant strain rate of 1 s^{-1} and a true strain of 0.8, followed by isothermal aging at 300 °C for 24 h. The stress–strain behavior of Al-Sc shows that deformation at 450 °C results in the greatest increase in flow stress (39.7%) compared to pure Al, whereas deformation at 550 °C yields the lowest flow stress, comparable to that of pure Al. The isothermally aged Al-Sc alloy at 300 °C shows that hot deformation at 350 °C and 550 °C provides a favorable balance between electrical conductivity and hardness, achieving 58.5–59 % IACS and 70–71 HV, respectively. In contrast, deformation at 450 °C results in a comparable EC (~59 % IACS) but yields the minimum hardness (51 HV), corresponding to a ~28 % reduction compared with the highest hardness value. TEM analysis reveals that the significantly lower hardness at 450 °C is attributed to the formation of coarse, chain-like Al_3Sc precipitates during preheating, which are heterogeneously distributed within the microstructure. In contrast, deformation at 350 °C and 550 °C suppresses such precipitates, favoring uniform nanoscale $L1_2$ Al_3Sc formation during aging.

The findings are validated through industrial-scale extrusion trials, examining how billet preheating, cooling rate, and aging conditions affect the final microstructure and properties. This work also provides fundamental insights into precipitation mechanisms in Al-based conductor alloys, using predictive modeling to clarify precipitate behavior and rationalize the success or failure of specific aging routes, offering practical guidelines for designing and manufacturing high-performance aluminum conductors for industrial applications.

Table des matières

Liste des tableaux

Liste des figures

Liste des abréviations

EC	Electrical Conductivity
IACS	International annealed copper standard
UTS	Ultimate tensile strength
Wt	Weight
TEM	Transmission electron microscope
MPa	Megapascale
ACSR	Aluminum conductor steel reinforced
AAAC	All-aluminum alloy conductor
AA	Aluminum Association
ASTM	American Society for Testing and Materials
DC	Direct Chill
GP	Guinier–Preston
DSC	Differential scanning calorimetry
OM	Optical microscope
DRX	Dynamic recrystallization
Eq	Equation
FCC	Faced centered cubic
CBED	Convergent beam electron diffraction
AQ	As-quenched
SEM	Scanning electron microscope
EDS	Energy Dispersive Spectroscopy
PIPs	Preheating-induced precipitateas
AIPs	Aging-induced precipitates
RMS	Root-mean-square

Liste des symboles

Al	Aluminium
Mg	Magnesium
Si	Silicon
Cu	Copper
β	Beta precipitate
β'	Beta prime precipitate
β''	Beta double prime precipitate
HV	Hardness (Vickers)
mm	Millimeter
°C	Centigrade degree
h	Hour
B	Boron
Ti	Titanium
Sc	Scandium
Zr	Zirconium
V	Vanadium
Mn	Manganese
Cr	Chromium
Fe	Iron
Ce	Cerium
α-Al8Fe2Si	Alpha intermetallics
β-Al5FeSi	Beta intermetallics
T5	Cooled after deformation, then artificially aged
T6	Solution heat treated, then artificially aged
d	Grain size
a	Lattice parameter
σ_{total}	Total strength
σ_{Al}	Strength of the aluminum matrix
σ_{prec}	Precipitate hardening
σ_{dis}	Strain hardening via dislocation forest

σ_{gb}	Grain boundary strengthening
σ_{SS}	Solute strengthening
M	Taylor factor
G	Shear modulus
b	Burger vector of the dislocations
N_d	Number density of precipitates
ρ_{total}	Total resistivity
ρ_{Al}	Resistivity of aluminum matrix
ρ_{pre}	Resistivity of precipitates
ρ_{dis}	Resistivity of dislocation
ρ_{gb}	Resistivity of grain boundaries
ρ_{ss}	Resistivity of solutes
μm	Micrometre
C_i	Concentration of the solute i
kHz	kilohertz
kV	Kilovolt
N	The number of precipitates
A	Area of the matrix containing the precipitates
t	TEM foil thickness
λ	Corrected average precipitate length
ρ	Dislocation number density
Q	Activation energy
R	Universal gas constant
T (K)	Absolute temperature

Dédicace

Je dédie cette thèse à mon épouse bien-aimée, Samaneh Gashtiazar, mère dévouée de notre fils; sans son soutien constant, sa patience et ses encouragements, ce travail n'aurait pas été possible.

Je dédie également ce travail à mes chers parents, Alireza Abnar et Fatemeh Nikseresht, qui ont toujours compté énormément pour moi et qui continuent d'être une source de force, de guidance et d'inspiration tout au long de ma vie.

Enfin, une dédicace toute particulière à mon cher fils, dont la présence remplit ma vie de joie et éclaire le chemin devant moi.

Remerciements

Avant tout, je tiens à exprimer ma sincère gratitude à mon directeur de thèse, le Prof. Mousa Javidani, pour son encadrement continu, son soutien et la confiance qu'il m'a accordée tout au long de mon doctorat. Son mentorat m'a offert de précieuses opportunités de développement en tant que chercheur et m'a permis d'acquérir des compétences essentielles.

Je remercie particulièrement mon codirecteur académique, le Dr. Paul Rometsch, pour ses discussions techniques approfondies, ses retours constructifs et son soutien constant à chaque étape de ce parcours, qui ont considérablement amélioré la qualité de mes recherches.

Je tiens également à remercier Rio Tinto, MindCore Technologies et CANMEC Group Inc. pour leur soutien et leur contribution à la réalisation de ce projet, ainsi que pour avoir fourni l'accès à des équipements et à des ressources essentiels.

J'exprime ma sincère reconnaissance au Professeur Emad Elgallad pour ses consultations précieuses, ses conseils éclairés et son accompagnement tout au long de mon doctorat. Je remercie aussi le Dr. Siamak Nikzad Khangholi pour ses discussions utiles et ses contributions importantes durant mon parcours de recherche.

Ma profonde gratitude s'adresse à M. Zhixing Chen pour son aide précieuse dans les techniques de caractérisation, notamment les essais de traction, la DSC, la MEB et la MET.

Je remercie chaleureusement mes collègues pour leur collaboration fructueuse, leurs discussions scientifiques enrichissantes et le partage de leurs expériences de recherche : Ahmed Algendy, Ali Elashery, Esmaeil Pourkhorshid, Mohammad Khoshghadam, Rasoul Khajeh, Hamed Kamali, Ramezanali Farajollahiseresty, Alyaa Bakr, Naser Valipour Motlagh, Musa Muhammed, Adolor David Aiyeki, Farnaz Yavari, Siavash Imanian Ghazanlou et Mojtaba Karamimoghadam.

Enfin, j'exprime ma plus profonde gratitude à mon épouse bien-aimée, Samaneh Gashtiazar, ainsi qu'à ma famille, pour leur amour inconditionnel et leur soutien indéfectible tout au long de ce parcours.

Chapitre 1. Introduction

1.1. Contexte

Au cours des dernières décennies, l'industrie électrique a connu une demande généralisée pour les alliages d'aluminium (Al). Les alliages d'Al ont été considérés comme un remplacement approprié des conducteurs en cuivre en raison de leurs propriétés uniques, notamment leur coût plus faible, leur haute résistance à la corrosion et un rapport résistance/poids plus élevé comparé aux conducteurs en Cu [1, 2]. Bien que les conducteurs fabriqués à partir d'alliages d'Al présentent une conductivité électrique (CE) plus faible, leur densité est trois fois inférieure à celle des conducteurs en Cu. Par conséquent, les conducteurs en alliages d'Al constituent le choix privilégié pour de nombreuses applications de conducteurs électriques. Ils sont largement utilisés dans divers domaines électriques, notamment le transport et la distribution d'énergie, tels que les lignes aériennes, les câbles électriques et les jeux de barres électriques [1, 3, 4].

La demande croissante d'alliages d'Al dans l'industrie électrique, motivée par leur rentabilité et leurs propriétés uniques, les positionne comme des conducteurs privilégiés, comme en témoigne la forte croissance prévue des marchés des conducteurs haute, moyenne et basse tension. En général, la basse tension (BT) couvre jusqu'à 1000 V et concerne des applications telles que le câblage résidentiel et les conducteurs automobiles. La moyenne tension (MT) s'étend de 1000 V à 45 kV et alimente principalement les réseaux de distribution. La haute tension (HT) fonctionne entre 45 kV et 230 kV et est essentielle pour un transport efficace de l'énergie électrique. Au-delà de 230 kV, la très haute tension (THT) devient critique, permettant le transport de l'électricité sur de longues distances avec des pertes minimales [5, 6]. Les différentes prévisions de marché indiquent une forte croissance des conducteurs haute, moyenne et basse tension, principalement fabriqués en Al, en raison de la demande mondiale croissante [7].

Les jeux de barres, fabriqués à partir d'alliages d'Al, servent de conducteurs électriques efficaces dans les systèmes de distribution d'énergie, en fournissant un chemin fiable pour le passage du courant. Les principaux alliages utilisés pour les jeux de barres électriques en Al comprennent AA6101 (ASTM B236M) et AA1350 (ASTM B317). AA1350 est un alliage

d'Al de haute pureté, offrant une excellente CE (minimum 61,8 % IACS). L'alliage AA1350 présente toutefois une résistance à la traction plus faible (minimum 85 MPa pour l'état H12) par rapport à d'autres alliages d'Al, ce qui le rend facile à plier et à mettre en forme en tant que jeu de barres. En revanche, l'alliage AA6101 (Al-Mg-Si), avec une résistance à la traction d'au moins 200 MPa pour l'état T6, est couramment utilisé dans les jeux de barres électriques en raison de sa CE acceptable d'au moins 55 % IACS [8, 9]. L'un des principaux défis liés à l'utilisation des conducteurs en alliages Al–Mg–Si est le compromis entre résistance mécanique et CE. Il est bien établi qu'il existe un compromis général entre la résistance et la conductivité électrique, de sorte que les facteurs qui améliorent la résistance des alliages d'Al sont intrinsèquement en conflit avec l'amélioration de la conductivité électrique [10, 11].

Dans ce projet en cours, la recherche porte à la fois sur les alliages d'aluminium des séries 6xxx et 1xxx pour des applications de jeux de barres électriques, en ajustant leur composition chimique et leurs paramètres de transformation thermomécanique. Dans un premier temps, les effets de l'ajout de Cu et des paramètres thermomécaniques sur le comportement en déformation à chaud et la CE des alliages conducteurs Al–Mg–Si(–Cu) ont été étudiés. Dans les phases suivantes du projet, les alliages 1xxx avec additions de Sc et Zr sont étudiés pour leur potentiel à améliorer significativement la résistance tout en minimisant les effets négatifs sur la CE, dans le but de développer des conducteurs thermiquement résistants pour les applications à haute tension. Compte tenu de l'augmentation des besoins énergétiques et de la faible résistance thermique des conducteurs 6xxx conventionnels, le Sc et le Zr ont également été explorés pour leur capacité à former des précipités stables contenant Sc et/ou Zr, améliorant la résistance mécanique et la stabilité thermique. Des essais de compression à chaud uniaxiale et des procédés d'extrusion à chaud ont été réalisés afin d'optimiser la conception des alliages et les procédés thermomécaniques pour obtenir un compromis supérieur entre résistance et conductivité. L'essai de compression à chaud fournit des données importantes pour la simulation des procédés de déformation à chaud tels que l'extrusion. Ensuite, sur la base des résultats optimaux des essais de compression à chaud, le procédé d'extrusion sera optimisé afin de produire des alliages d'Al extrudés présentant une CE élevée et une résistance suffisante. À cette fin, la température de préchauffage, les

paramètres d'extrusion, les conditions de refroidissement post-traitement et les conditions de vieillissement sont pris en compte.

1.2. Énoncé du problème

Le développement d'alliages d'aluminium extrudés pour conducteurs présentant une résistance mécanique élevée et une conductivité électrique (CE) élevée nécessite la mise en œuvre de certaines pratiques. L'exploration du rôle des éléments d'alliage dans le comportement thermomécanique, l'optimisation des paramètres de déformation à chaud, ainsi que l'identification de traitements thermiques post-déformation efficaces constituent des aspects essentiels à étudier [2, 12].

Comme illustré à la Figure 1-1, la voie conventionnelle de mise en forme thermomécanique des conducteurs en fil d'aluminium comprend l'homogénéisation de l'alliage brut de coulée, suivie d'une déformation à chaud, d'un traitement de mise en solution et d'un tréfilage pour les alliages traitables thermiquement tels que les 6xxx, avec une étape finale de vieillissement artificiel visant à favoriser la précipitation durcissante, correspondant à l'état métallurgique T8. En revanche, les barres omnibus électriques produites par les procédés conventionnels diffèrent des fils en ce sens que les barres extrudées de section rectangulaire ne subissent pas de tréfilage après la déformation à chaud, comme illustré à la Figure 1-1. Par conséquent, elles ne bénéficient pas du durcissement par densité de dislocations dans la même mesure que les fils tréfilés [3].

Dans le cadre du présent projet, une voie thermomécanique modifiée est développée pour les barres omnibus électriques en supprimant l'étape de mise en solution et en appliquant directement le vieillissement (état T5). Ce procédé simplifié permet de réduire les coûts, la consommation d'énergie et le temps de transformation, tout en améliorant la productivité et en minimisant les distorsions ainsi que les contraintes résiduelles. Pour cette voie basée sur l'état T5, les paramètres de déformation à chaud, en particulier la température de préchauffage, jouent un rôle critique afin d'obtenir un équilibre optimal entre la résistance mécanique et la conductivité électrique après le vieillissement final.

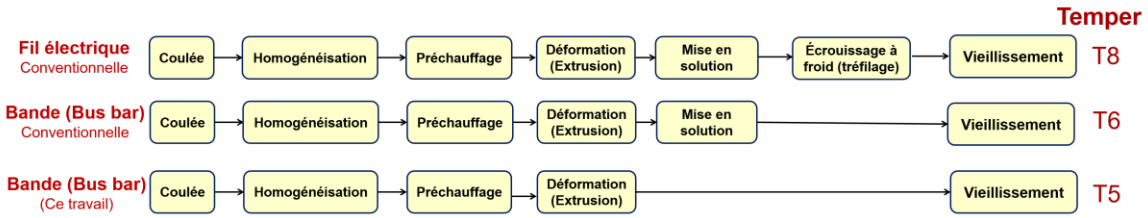

Figure 1-1. Voies de mise en forme des conducteurs en aluminium traitables thermiquement montrant les séquences d'états métallurgiques T5, T6 et T8.

La présente étude se concentre de manière unique sur l'investigation et l'optimisation des stratégies d'alliage ainsi que des paramètres de mise en forme thermo

[19, 20]."

mécanique à l'état T5 pour des barres omnibus en alliages 6xxx et 1xxx, afin d'atteindre un équilibre supérieur entre la CE et la résistance mécanique.

Pour les alliages conducteurs en aluminium 6xxx, le maintien du Mg et du Si en solution solide sursaturée après la déformation à chaud est essentiel pour un traitement de vieillissement direct efficace, car il permet la formation ultérieure de précipités fins responsables du durcissement [10]. Leur appauvrissement de la matrice diminue l'efficacité du vieillissement ultérieur en limitant la formation de précipités durcissants. Des paramètres de déformation inappropriés, en particulier des températures élevées, peuvent entraîner une consommation prématurée de ces éléments d'alliage par la formation de précipités β grossiers et non durcissants avant le vieillissement. L'ajout de Cu complique davantage ce comportement en raison des températures de solvus différentes des phases contenant du Cu par rapport aux précipités Mg–Si [13-16]. Par conséquent, un contrôle précis de la température de déformation est critique afin de préserver le Cu, le Mg et le Si en solution solide avant le vieillissement. Étant donné le rôle bénéfique du Cu dans l'amélioration des performances des conducteurs, son influence sur le comportement en déformation à chaud au cours du procédé mérite une étude systématique, d'autant plus qu'elle reste insuffisamment explorée dans les alliages d'aluminium électriques Al–Mg–Si(–Cu) pour barres omnibus.

Pour les alliages conducteurs d'aluminium 1xxx, les effets bénéfiques des additions de Sc et de Zr sur le durcissement et la stabilité thermique ont été largement rapportés, en particulier

pour les produits sous forme de fils utilisés dans les câbles, avec une diminution minimale de la CE [17, 18]. Dans la plupart des cas, un traitement de mise en solution après déformation à chaud est utilisé afin de garantir que le Sc et le Zr restent en solution solide, favorisant ainsi la précipitation à l'échelle nanométrique lors du vieillissement ultérieur [19, 20]. Toutefois, pour les alliages conducteurs 1xxx extrudés à chaud contenant du Sc et du Zr et soumis à un vieillissement direct sans traitement de mise en solution, cette approche ne s'est pas encore révélée efficace pour les applications de conducteurs. Dans de tels procédés, l'obtention d'une résistance élevée dépend fortement du contrôle de la température de déformation, laquelle joue un rôle critique pour éviter une consommation excessive du Sc et du Zr durant la déformation et pour maintenir leur disponibilité en vue de la précipitation lors du vieillissement.

Une autre considération importante pour les alliages d'aluminium 1xxx contenant à la fois du Sc et du Zr est l'établissement d'une température de vieillissement optimale. Étant donné que le Sc et le Zr présentent des diffusivités et des mobilités différentes, leurs températures d'activation pour la précipitation diffèrent également : les précipités riches en Sc nucléent typiquement entre 250–300 °C, tandis que les précipités riches en Zr nucléent entre 350–400 °C. Par conséquent, la plage de température favorable à la précipitation du Zr est défavorable à la précipitation du Sc, favorisant la coalescence et entraînant un sur-vieillissement. Ainsi, l'optimisation de la température de vieillissement pour les systèmes ternaires Al–Sc–Zr est essentielle afin de tirer pleinement parti des effets des deux éléments. Bien que des traitements de vieillissement en deux étapes aient été recommandés pour les alliages en fils [18, 21], leurs effets n'ont pas encore été étudiés de manière systématique dans les produits sous forme de barres omnibus et de bandes. De plus, les structures de précipités dans les systèmes Al–Sc–Zr sous différentes conditions de vieillissement restent insuffisamment étudiées, en particulier en ce qui concerne leur influence sur la taille des précipités, leur densité numérique et leur distribution.

Par ailleurs, il existe une lacune de recherche dans le fait que l'essai de compression à chaud n'a pas été utilisé pour étudier l'influence des paramètres de déformation (tels que la température et la vitesse de déformation) sur les performances (à la fois la CE et la résistance mécanique) des conducteurs en alliages d'aluminium contenant du Zr et du Sc. De plus, les

paramètres thermomécaniques développés à l'échelle de laboratoire à partir des essais de compression à chaud n'ont pas été transposés à l'échelle industrielle afin d'optimiser le procédé industriel pilote d'extrusion. En outre, il existe encore un manque d'investigation microstructurale dans les conducteurs en alliages d'aluminium ayant subi une déformation à chaud. Par conséquent, il serait pertinent d'étudier comment les paramètres de déformation à chaud influencent le développement de la résistance mécanique et de la CE dans les alliages conçus.

1.3. Objectifs de la recherche

Phase 1 : Cette phase vise à étudier l'influence des ajouts de Cu (0,15–0,4 % massique) sur le comportement à la déformation à chaud, l'évolution microstructurale et les performances des alliages conducteurs Al–Mg–Si. À travers des essais systématiques de compression à chaud uniaxiale réalisés à 450 °C et 550 °C sous des vitesses de déformation de 0,1 à 10 s^{-1}, l'étude cherche à comprendre comment le Cu et les paramètres de déformation influencent la restauration dynamique, la recristallisation, la contrainte d'écoulement, la microdureté et la conductivité électrique. L'objectif ultime est d'optimiser la composition de l'alliage ainsi que les conditions de traitement thermomécanique afin d'obtenir un équilibre supérieur entre la résistance mécanique et la conductivité électrique (CE), adapté aux conducteurs industriels en aluminium de type bus bar sous procédé de revenu T5, tout en apportant une compréhension fondamentale de la corrélation entre la teneur en soluté, les mécanismes de déformation et les performances électriques dans les alliages de série 6xxx modifiés au Cu.

Phase 2 : Cette deuxième phase vise à étudier l'effet du traitement thermomécanique, plus particulièrement le préchauffage des billettes et différents traitements de vieillissement, sur la microstructure, la résistance mécanique et la conductivité électrique d'un alliage conducteur Al–0,1Sc–0,1Zr (% massique). En étudiant systématiquement l'extrusion à chaud à 420 °C et 480 °C suivie de procédés de vieillissement artificiel en une étape et en deux étapes, la recherche cherche à comprendre le comportement de précipitation des phases $Al_3(Sc,Zr)$ et leur influence sur le renforcement et la conductivité. L'objectif est d'optimiser les paramètres de procédé afin d'obtenir un équilibre supérieur entre la résistance et la conductivité grâce à une évolution contrôlée des précipités, une stabilité thermique améliorée et une croissance minimisée des sous-grains, permettant ainsi de développer un alliage

conducteur d'aluminium haute performance adapté aux applications de bus bars dans les systèmes de distribution électrique.

Phase 3: Cette phase vise à déterminer les paramètres optimaux de déformation à chaud pour les alliages conducteurs d'aluminium de série 1xxx contenant du Sc, afin d'améliorer la résistance mécanique et la CE pour les applications de bus bars. À travers des essais systématiques de compression à chaud uniaxiale réalisés entre 350 et 550 °C, suivis d'un vieillissement isotherme, cette étude examine les effets des paramètres de déformation — notamment la température de déformation et la déformation appliquée — sur le comportement de la contrainte d'écoulement, l'évolution microstructurale et les caractéristiques de précipitation. L'objectif est de déterminer les conditions optimales de déformation à chaud permettant de supprimer le grossissement des précipités durant la déformation et de favoriser une précipitation uniforme à l'échelle nanométrique des phases Al_3Sc durant le vieillissement subséquent, afin d'obtenir un équilibre optimal entre la résistance mécanique et la CE pour des conducteurs en aluminium haute performance.

1.4. Originalité du projet

Les aspects novateurs de cette recherche sont présentés comme suit :

- L'impact de l'incorporation d'éléments d'alliage sur le comportement à la déformation à chaud des alliages d'aluminium pour diverses applications a été largement étudié. Cependant, il subsiste un manque notable concernant l'étude de l'influence des éléments d'alliage, tels que le Cu, le Sc et le Zr, sur le comportement à la déformation à chaud des « alliages conducteurs d'aluminium ». Cela inclut des paramètres tels que la contrainte d'écoulement, la contrainte maximale d'écoulement et la structure des grains. Des recherches supplémentaires dans ce domaine sont nécessaires afin de comprendre de manière approfondie les implications sur les performances des conducteurs en aluminium. Dans la présente étude, un essai de compression à chaud sera développé afin de générer des données pour de futures études prédictives dans ce domaine.
- Le rôle des paramètres de déformation à chaud (par exemple, la température de déformation et la vitesse de déformation) sur les performances des conducteurs en alliage d'aluminium sous revenu T5 est peu documenté. De plus, il existe un manque d'examens

microstructuraux des conducteurs en alliage d'aluminium ayant subi une déformation à chaud. Dans ce projet, l'impact des paramètres de déformation à chaud sur la résistance mécanique et la CE des nouvelles compositions chimiques conçues sera étudié de manière approfondie.

- La plupart des études précédentes se sont principalement concentrées sur l'amélioration de la résistance mécanique et de la CE des alliages conducteurs d'aluminium, tels que les alliages 6201 et 1350, par l'ajout d'éléments d'alliage et l'optimisation des procédés thermomécaniques pour les traitements T8 ou T6. Cependant, le traitement des alliages conducteurs d'aluminium pour les applications de barres omnibus électriques par vieillissement artificiel direct après déformation à chaud a rarement été étudié, en particulier pour les systèmes Al-Mg-Si(-Cu) et Al-Sc, Al-Sc-Zr, qui présentent des défis pour atteindre un équilibre optimal entre la résistance mécanique et la CE. La présente recherche étudie de manière approfondie les paramètres de traitement thermomécanique de ces alliages, en tenant compte spécifiquement des étapes de fabrication des barres omnibus.

Dans le présent travail, une zone d'intérêt pour le développement d'alliages avancés destinés aux barres omnibus est mise en évidence. Cette approche vise à explorer l'effet d'éléments d'alliage efficaces, tels que le Zr et le Sc, afin d'identifier des compositions et des conditions de traitement permettant d'obtenir des conducteurs en aluminium extrudé combinant une conductivité électrique élevée, proche de celle de l'alliage AA1350 (environ 61 % IACS), et une résistance mécanique élevée, comparable à celle de l'alliage AA6101 (environ 200 MPa à l'état T6).

1.5. Contenu de la thèse

Cette thèse de doctorat comprend sept chapitres. Après l'introduction, le Chapitre 2 présente une revue de littérature principalement axée sur l'effet du Cu dans les alliages conducteurs d'aluminium. Il met en évidence que, dans les alliages d'aluminium de série 6xxx, la résistance mécanique et la conductivité électrique sont gouvernées par la formation et l'évolution de précipités nanométriques durant les traitements thermiques. Les éléments d'alliage tels que Mg, Si et Cu influencent le type, la fraction et la stabilité de ces précipités, contrôlant ainsi le renforcement et les performances électriques globales. Les effets du Sc et du Zr sont également brièvement introduits dans ce chapitre.

Compte tenu de leur importance, le Chapitre 3 est consacré à une revue complète des alliages conducteurs d'aluminium contenant du Sc et du Zr, intitulée « Advanced thermal-resistant aluminum conductor alloys: A comprehensive review », publiée dans l'International Journal of Minerals, Metallurgy and Materials. Ce chapitre résume les avancées récentes dans la conception d'alliages conducteurs à base d'aluminium contenant du Sc et du Zr présentant une résistance mécanique, une stabilité thermique et une conductivité électrique améliorées. Il met l'accent sur le microalliage avec le Sc et le Zr, conduisant à la formation de précipités cohérents Al_3Sc et $Al_3(Sc,Zr)$, ainsi que sur le rôle des éléments de terres rares tels que l'Er et des stratégies optimisées de traitement thermomécanique. De plus, les avancées récentes dans les stratégies de traitement thermomécanique sont examinées, en mettant l'accent sur des approches évolutives visant à optimiser l'équilibre entre la résistance mécanique et la conductivité. Ces approches impliquent des traitements thermiques en plusieurs étapes et des séquences de fabrication soigneusement contrôlées, notamment la combinaison du tréfilage à froid et du traitement de vieillissement afin de favoriser une précipitation uniforme et efficace.

Le Chapitre 4 présente l'article publié intitulé «Effect of hot deformation parameters on the performance and thermomechanical behavior of Cu-modified Al–Mg–Si conductor alloys», publié dans le Journal of Materials Science. Ce travail étudie l'influence des ajouts de Cu (0,15–0,4 % massique) sur le comportement à la déformation à chaud des alliages conducteurs Al–Mg–Si, avec une attention particulière portée à la relation entre les paramètres de procédé, les propriétés mécaniques et la conductivité électrique. Cette étude se concentre de manière unique sur l'investigation et l'optimisation des stratégies d'alliage et des paramètres de traitement thermomécanique spécifiquement pour les applications de bus bars électriques, dans le but d'obtenir un équilibre supérieur entre la CE et la résistance mécanique.

Le Chapitre 5 comprend l'article intitulé «Influence of extrusion preheating temperature and aging strategy on precipitation and performance of Al–Sc–Zr conductor alloys», publié dans Materials Today Communications. Cette étude examine les effets de la température de préchauffage avant extrusion (420 °C contre 480 °C) et des stratégies de vieillissement (une étape et deux étapes) sur le comportement de précipitation, l'évolution microstructurale et

les propriétés résultantes d'un alliage Al–0,1Sc–0,1Zr (% massique). Ce chapitre discute de manière approfondie la modélisation de l'évolution de la composition des précipités, en intégrant une approche unidimensionnelle du déplacement quadratique moyen (RMS), ainsi que sa relation avec la résistance au grossissement. De plus, des relations quantitatives entre la microstructure et la résistance mécanique sont établies dans la dernière section de ce chapitre.

Le Chapitre 6 présente le manuscrit intitulé «The role of preheating-induced precipitates in tailoring the electrical and mechanical properties of deformed Al–0.1 wt.% Sc conductors», prêt à être soumis. Cette étude explore l'effet de la température de déformation à chaud (350–550 °C) sur l'évolution microstructurale durant différentes étapes du procédé thermomécanique, plus particulièrement le préchauffage avant la déformation, ainsi que son influence sur le comportement de vieillissement subséquent. Une attention particulière est accordée à la précipitation et à la structure des grains, analysées à l'aide du MET (TEM) et de l'EBSD, afin d'établir des liens entre les procédés, les mécanismes de renforcement à l'échelle nanométrique et les performances globales.

Enfin, le Chapitre 7 résume les principales conclusions de la thèse et fournit des recommandations pour les recherches futures.

1.6. Références

[1] Y. Wang, L. Zhu, G. Niu, and J. Mao, "Conductive Al alloys: the contradiction between strength and electrical conductivity," *Advanced Engineering Materials,* vol. 23, no. 5, p. 2001249, 2021.

[2] S. N. Khangholi, M. Javidani, A. Maltais, and X. G. Chen, "Review on recent progress in Al–Mg–Si 6xxx conductor alloys," *Journal of Materials Research,* vol. 37, no. 3, pp. 670–691, 2022.

[3] *ASTM B317/B317M: Standard Specification for Aluminum-Alloy Extruded Bar, Rod, Tube, Pipe, and Structural Profiles for Electrical Purposes (Bus Conductor)*, A. International, 2017.

[4] M. Yokota, "Aluminum alloy electric conductor wire," Patent Appl. Appl. 5/838,762, 1980.

[5] B. M. Weedy, B. J. Cory, N. Jenkins, J. B. Ekanayake, and G. Strbac, *Electric power systems*. John Wiley & Sons, 2012.

[6] A. A. Sallam and O. P. Malik, "Electric distribution systems," 2018.

[7] "Power Market Research Report " https://www.fortunebusinessinsights.com/power-industry (accessed.

[8] X. Li *et al.*, "Influence of Mg and Si content and heat treatment on electrical conductivity and hardness of AA6101 Al alloy," *Journal of Materials Science,* vol. 58, no. 20, pp. 8478–8488, 2023.

[9] W. Yuan and Z. Liang, "Effect of Zr addition on properties of Al–Mg–Si aluminum alloy used for all aluminum alloy conductor," *Materials & Design,* vol. 32, no. 8-9, pp. 4195–4200, 2011.
[10] Z. Chen *et al.*, "Microstructural characteristics and deformation behaviors of an Al–Mg–Si alloy with improved strength and conductivity processed by continuous casting and expansion extrusion," *Journal of Materials Research and Technology,* vol. 22, pp. 445–460, 2023.
[11] X. Meng, Y. Huang, J. Cao, J. Shen, and J. F. dos Santos, "Recent progress on control strategies for inherent issues in friction stir welding," *Progress in Materials Science,* vol. 115, p. 100706, 2021.
[12] H. Zhang, L. Li, D. Yuan, and D. Peng, "Hot deformation behavior of the new Al–Mg–Si–Cu aluminum alloy during compression at elevated temperatures," *Materials Characterization,* vol. 58, no. 2, pp. 168–173, 2007.
[13] D. Chakrabarti and D. E. Laughlin, "Phase relations and precipitation in Al–Mg–Si alloys with Cu additions," *Progress in Materials Science,* vol. 49, no. 3-4, pp. 389–410, 2004.
[14] J. Kim, C. D. Marioara, R. Holmestad, E. Kobayashi, and T. Sato, "Effects of Cu and Ag additions on age-hardening behavior during multi-step aging in Al□ Mg□ Si alloys," *Materials Science and Engineering: A,* vol. 560, pp. 154–162, 2013.
[15] S. Duan, K. Matsuda, Y. Zou, and T. Wang, "Influence of two-stage ageing process and Cu additions on conductive Al alloys based on AA 6063," *Materials Research Express,* vol. 6, no. 10, p. 106509, 2019.
[16] S. Gashtiazar, E. Elgallad, B. Abnar, M. Javidani, A. Maltais, and X.-G. Chen, "Effect of solution heat treatment on the microstructure of hot-rolled Al-Mg-Si 6xxx alloy microalloyed with Sc and Zr," *Materials Letters,* p. 138784, 2025.
[17] S. Fan *et al.*, "Achieving superior strength and conductivity for Al-Zr-Sc wires by coupling design of deformation and ageing," *Materials Research Letters,* vol. 12, no. 8, pp. 590–598, 2024.
[18] L. Liu, J.-T. Jiang, B. Zhang, W.-Z. Shao, and L. Zhen, "Enhancement of strength and electrical conductivity for a dilute Al-Sc-Zr alloy via heat treatments and cold drawing," *Journal of Materials Science & Technology,* vol. 35, no. 6, pp. 962–971, 2019.
[19] R. Guan, Y. Shen, Z. Zhao, and X. Wang, "A high-strength, ductile Al-0.35 Sc-0.2 Zr alloy with good electrical conductivity strengthened by coherent nanosized-precipitates," *Journal of Materials Science & Technology,* vol. 33, no. 3, pp. 215–223, 2017.
[20] Q. Shao, E. M. Elgallad, A. Maltais, and X.-G. Chen, "Development of thermal-resistant Al-Zr based conductor alloys via microalloying with Sc and manipulating thermomechanical processing," *Journal of Materials Research and Technology,* 2023.
[21] C. Booth-Morrison, D. C. Dunand, and D. N. Seidman, "Coarsening resistance at 400 C of precipitation-strengthened Al–Zr–Sc–Er alloys," *Acta Materialia,* vol. 59, no. 18, pp. 7029–7042, 2011.

Chapitre 2. Revue de la littérature

2.1. L'effet du Cu sur les alliages conducteurs d'Al

Le Mg et le Si sont reconnus comme les principaux éléments d'alliage dans les alliages de la série 6xxx, conduisant à la formation des phases renforçantes β″/β′ lors du traitement de vieillissement. L'augmentation de l'addition de Mg et de Si produit un double effet. Premièrement, tous les atomes de Mg et de Si ne participent pas à la formation des précipités Mg–Si ; une partie reste en solution solide dans la matrice d'Al, où ils introduisent des défauts de réseau. Ces défauts diffusent les électrons plus efficacement que les précipités de seconde phase, réduisant ainsi la conductivité électrique (EC). Deuxièmement, la combinaison du Mg et du Si conduit à la formation de précipités Mg–Si, ce qui améliore la résistance mécanique de l'alliage. Pour les alliages Al-Mg-Si, la séquence de précipitation est généralement considérée comme suit [1, 2]:

SSSS → Atomic clusters → GP zones → β″→ β′, U1, U2, B′→ β, Si

Ici, SSSS désigne une solution solide sursaturée, et les zones GP (Guinier–Preston) sont les premières phases distinctes à se former lors du vieillissement, croissant de manière cohérente avec des atomes de soluté arrangés sur les positions du réseau de l'Al. La phase β″ en forme d'aiguilles, semi-cohérente avec la matrice, est la plus efficace pour le renforcement de ces alliages et fournit la dureté maximale. Lors du sur-vieillissement, des phases post-β″ plus grossières — telles que β′, U1, U2 et B′ — se forment, entraînant une perte significative de résistance.

L'ajout de Cu dans les alliages Al de la série 6xxx est bien documenté pour sa capacité à améliorer la résistance mécanique. Le Cu peut augmenter significativement la cinétique de durcissement structural des alliages Al-Mg-Si en facilitant la formation des précipités renforçants [3]. Des études montrent que l'interaction plus forte entre les atomes de Cu et de Mg conduit à la formation précoce d'amas Mg–Cu lors du vieillissement, qui, avec les amas Mg–Si, agissent comme sites de nucléation pour la formation de nouveaux précipités [4, 5]. Les atomes de Cu s'intègrent dans les amas atomiques et dans la phase β″ et accélèrent les

vitesses de nucléation de ces précipités. La séquence de précipitation généralement acceptée des alliages Al-Mg-Si-Cu est rapportée comme suit [6, 7]:

SSSS →Atomic clusters → GP zones → β″, L/S/C, QP, QC → β′, Q′→ Q, Si

Toutes les phases de précipitation métastables dans le système Al–Mg–Si–Cu partagent un cadre structural commun caractérisé par un réseau continu de colonnes atomiques de Si le long de la longueur des précipités [8]. Les différents types de précipités se distinguent par les arrangements spécifiques des colonnes atomiques d'Al, de Mg et de Cu par rapport à ce réseau de Si [9]. Les vitesses de nucléation et la cinétique de croissance de ces précipités peuvent toutefois varier considérablement en fonction de la composition chimique de l'alliage, notamment de la teneur en Cu, Mg et Si. Selon les concentrations relatives de ces éléments, certaines phases contenant du Cu peuvent être favorisées, tandis que leur fraction volumique peut également diminuer jusqu'à devenir très faible, voire pratiquement négligeable. Ainsi, la séquence de précipitation présentée ci-dessus doit être considérée comme une séquence générale, dont les étapes et les phases effectivement observées dépendent de la composition de l'alliage et des conditions de traitement thermique.

L'ajout de Cu diminue la formation de β″ et favorise la formation d'autres précipités métastables contenant du Cu durant le vieillissement. La phase β″ ne représente que 20 % à 30 % de l'ensemble des précipités observés au pic de vieillissement [1]. Les phases S, L, C, QP, QC, Q′ et Q rapportées se forment dans les alliages Al-Mg-Si contenant du Cu [10]. La phase hexagonale QP, ainsi que la phase hexagonale QC, sont observées au pic de vieillissement. La phase Q′ hexagonale en forme de lattes, formée lors du sur-vieillissement, se transforme finalement en phase Q d'équilibre après un sur-vieillissement suffisant. Au pic de vieillissement, une phase L en forme de lattes se forme parallèlement à β″ et est considérée comme un précurseur de Q′ ayant un effet significatif sur le durcissement. D'autres précurseurs de Q′, tels que les phases S et C formées au pic de vieillissement, présentent des morphologies en lattes ou en plaquettes [6, 11]. La phase Q′ nucléé souvent le long des interfaces cohérentes avec la matrice α-Al dans les alliages Al-Mg-Si-Cu, tandis que la phase L présente un champ de déplacement interfacial plus faible, indiquant une meilleure cohérence et un désaccord de réseau réduit par rapport à Q′, ce qui améliore la stabilité

mécanique [12]. Les phases L restent stables lors d'une exposition thermique prolongée, résistant au grossissement en raison de leurs interfaces cohérentes et de leur faible énergie interfaciale [7]. En revanche, les phases Q′ tendent à perdre en densité sous l'effet de la chaleur, bien qu'elles présentent une stabilité supérieure à celle de la phase métastable β″. Dans la microstructure sur-vieillie des alliages Al–Mg–Si–Cu, les précipités Q′ et L coexistent et peuvent même croître de manière interconnectée. Les deux phases présentent un ordre des atomes de Si, bien que cela soit le seul ordre clairement observé dans L [9]. Il a été montré que la maille élémentaire de Q′ partage les mêmes paramètres de réseau que la phase Q d'équilibre, mais avec une composition différente [11]. Plus précisément, Q′ a été mesurée comme Al3.8Mg8.6Si7.0Cu1.0, contenant environ un atome de Cu en moins et un atome d'Al en plus par maille élémentaire par rapport à Q [11]. Au pic de vieillissement, une phase L en forme de lattes se forme parallèlement à β″ et est considérée comme un précurseur de Q′ ayant des effets de durcissement significatifs. Sa structure désordonnée rend sa composition et son arrangement distincts de ceux de Q′, évoluant finalement vers la phase Q. La phase L désordonnée ne possède pas de maille élémentaire définie et contient moins de Mg que Q′ [11]. D'autres précurseurs de Q′, tels que les phases S et C, se forment également au pic de vieillissement et présentent des morphologies en lattes ou en plaquettes. La phase C présente une forme en plaquette avec une section transversale rectangulaire, tandis que la phase L est proposée comme une variante désordonnée de C avec une morphologie en lattes, contribuant de manière notable au durcissement de l'alliage [6, 11].

La caractérisation révèle que la phase Q′ nucléé souvent le long des interfaces cohérentes avec la matrice α-Al dans les alliages Al-Mg-Si-Cu, tandis que la phase L présente un champ de déplacement plus faible à l'interface, indiquant une cohérence supérieure et un désaccord de réseau réduit par rapport à Q′, ce qui améliore la stabilité mécanique [12, 13]. Les phases L restent stables lors d'une exposition thermique prolongée, résistant au grossissement en raison de leurs interfaces cohérentes et de leur faible énergie interfaciale. Cela explique pourquoi les alliages enrichis en phases L présentent une meilleure conservation de la résistance et de la ductilité à haute température. En revanche, les phases Q′ tendent à perdre en densité sous l'effet de la chaleur, bien qu'elles offrent néanmoins une meilleure stabilité que la phase métastable β″ [7, 14].

Les caractéristiques des précipités métastables dans les alliages Al–Mg–Si–Cu sont fortement dépendantes de la composition, et le rapport Mg/Si contrôle de manière critique les types de précipités dominants au cours du vieillissement [15, 16]. Zhang et al. [7], ont rapporté que, dans les alliages riches en Si, les précipités dominants sont les phases β″ et Q′ dans les alliages Al–Mg–Si–Cu, tandis que les alliages riches en Mg forment principalement des phases L. Leurs résultats soulignent l'influence critique du rapport Mg/Si, en particulier pour l'optimisation de la stabilité thermique dans ces systèmes d'alliages. Liu et al. [17], ont démontré que les alliages Al-Mg-Si-Cu à teneurs élevées en Mg et Cu présentent une précipitation importante des phases QP et d'autres sous-phases mixtes. Cependant, lorsque le rapport Mg/Si est trop élevé, la formation de clusters et de précipités est fortement inhibée en raison d'un manque d'atomes de Si pour la formation initiale des clusters Mg–Si–Cu. Les clusters Mg–Si–Cu, lors de l'ajout de 0,2 à 0,5 % en masse de Cu, contiennent environ 30 à 80 atomes de soluté. Le Cu est initialement présent uniquement à l'état de traces (Cu/Mg ≈ 0,05), indiquant que son rôle principal ne réside pas dans la formation des premiers clusters, mais dans la stabilisation des précipités de plus grande taille [18, 19].

Malgré les nombreux travaux consacrés à l'effet du Cu sur la précipitation des alliages Al–Mg–Si, plusieurs questions demeurent ouvertes, notamment concernant le rôle exact du Cu dans la sélection et la stabilité des différentes phases métastables. L'influence combinée de la teneur en Cu et du rapport Mg/Si sur la compétition entre les phases β″, L et Q′ reste particulièrement complexe et n'est pas encore complètement établie. De plus, le mécanisme par lequel le Cu modifie la cinétique de précipitation et la stabilité thermique des précipités lors d'expositions prolongées demeure sujet à débat. Ces incertitudes sont particulièrement importantes pour les alliages conducteurs, où l'amélioration de la résistance mécanique par le Cu doit être conciliée avec la préservation d'une conductivité électrique élevée.

2.2. Effet du Sc et du Zr sur les alliages conducteurs d'Al

L'ajout de Sc et de Zr permet le développement de conducteurs en aluminium thermiquement stables, présentant une résistance mécanique améliorée et une conductivité électrique élevée [15,21]. Le Sc forme des précipités cohérents Al_3Sc de structure $L1_2$, offrant un fort durcissement par précipitation grâce à leur distribution fine et homogène. Cependant, le coût élevé du Sc limite son utilisation à grande échelle, ce qui rend le Zr une alternative

économique permettant de réduire les coûts globaux d'alliage [21]. Le Zr favorise la formation de précipités nanométriques $Al_3(Sc,Zr)$ lors du vieillissement, où il ségrège à l'interface précipité/matrice et forme une coque qui ralentit le grossissement et améliore la stabilité thermique [22,23]. Cette structure cœur–coquille se développe lorsque des précipités Al_3Sc riches en Sc nucléent en premier, en raison de la plus grande diffusivité du Sc, suivie d'un enrichissement progressif de la région externe en Zr [17,24]. Ces précipités renforcent la résistance en empêchant le mouvement des dislocations et augmentent significativement la résistance à la recristallisation grâce à un effet efficace de blocage de Zener [15,25].

Une revue plus détaillée et complète des alliages conducteurs d'Al contenant Sc et Zr est présentée au chapitre 3, qui est basée sur un article de revue publié sur ce sujet.

2.3. Références

[1] L. Ding *et al.*, "The structural and compositional evolution of precipitates in Al-Mg-Si-Cu alloy," *Acta Materialia,* vol. 145, pp. 437–450, 2018.

[2] M. Van Huis, J. Chen, M. Sluiter, and H. Zandbergen, "Phase stability and structural features of matrix-embedded hardening precipitates in Al–Mg–Si alloys in the early stages of evolution," *Acta Materialia,* vol. 55, no. 6, pp. 2183–2199, 2007.

[3] Y. Weng, Z. Jia, L. Ding, S. Muraishi, and Q. Liu, "Clustering behavior during natural aging and artificial aging in Al-Mg-Si alloys with different Ag and Cu addition," *Materials Science and Engineering: A,* vol. 732, pp. 273–283, 2018.

[4] S. N. Khangholi, M. Javidani, A. Maltais, and X.-G. Chen, "Effect of Ag and Cu addition on the strength and electrical conductivity of Al-Mg-Si alloys using conventional and modified thermomechanical treatments," *Journal of Alloys and Compounds,* vol. 914, p. 165242, 2022.

[5] H. Jin, D. Tie, and R. Guan, "Precipitation behavior during re-aging of Al-Mg-Si-Cu alloy," *Materials & Design,* vol. 220, p. 110883, 2022.

[6] C. Marioara *et al.*, "The effect of Cu on precipitation in Al–Mg–Si alloys," *Philosophical Magazine,* vol. 87, no. 23, pp. 3385–3413, 2007.

[7] S.-Y. Zhang, Y.-T. Mo, Z.-M. Hua, X. Liu, Z.-T. Liu, and H.-Y. Wang, "Improving long-term thermal stability in twin-roll cast Al-Mg-Si-Cu alloys by optimizing Mg/Si ratios," *Journal of Materials Science & Technology,* vol. 206, pp. 164–175, 2025.

[8] S. J. Andersen *et al.*, "Directionality and column arrangement principles of precipitates in Al-Mg-Si-(Cu) and Al-Mg-Cu linked to line defect in Al," in *Materials Science Forum*, 2017, vol. 877: Trans Tech Publ, pp. 461–470.

[9] J. K. Sunde, C. D. Marioara, and R. Holmestad, "The effect of low Cu additions on precipitate crystal structures in overaged Al-Mg-Si (-Cu) alloys," *Materials Characterization,* vol. 160, p. 110087, 2020.

[10] M. Zandbergen, Q. Xu, A. Cerezo, and G. Smith, "Study of precipitation in Al–Mg–Si alloys by Atom Probe Tomography I. Microstructural changes as a function of ageing temperature," *Acta Materialia,* vol. 101, pp. 136–148, 2015.

[11] M. Torsæter, W. Lefebvre, C. Marioara, S. Andersen, J. Walmsley, and R. Holmestad, "Study of intergrown L and Q′ precipitates in Al–Mg–Si–Cu alloys," *Scripta Materialia,* vol. 64, no. 9, pp. 817–820, 2011.

[12] X. Wu, X. Liu, X. Wang, P.-K. Ma, and Z.-P. Guan, "Effect of Cu and Sn additions on the thermal stability of Al–Mg–Si alloy," *Materials Science and Engineering: A,* vol. 894, p. 146158, 2024.
[13] Y. Chen *et al.*, "Deformation-mediated cyclic evolution of precipitates in Al-Mg-Si-Cu alloy by multi-pass ECAP and thermal treatments," *Journal of Materials Science & Technology,* vol. 213, pp. 42–54, 2025.
[14] S. Fan, M. Chen, K. Jiang, Y. Lan, and G. Rong, "The effects of Cu and Mg contents on the thermal stability of 6XXX-series aluminum alloy," *Advances in Mechanical Engineering,* vol. 15, no. 1, p. 16878132221148909, 2023.
[15] S. N. Khangholi, M. Javidani, A. Maltais, and X.-G. Chen, "Optimization of mechanical properties and electrical conductivity in Al–Mg–Si 6201 alloys with different Mg/Si ratios," *Journal of Materials Research,* vol. 35, no. 20, pp. 2765–2776, 2020.
[16] L. Ding, Z. Jia, Z. Zhang, R. E. Sanders, Q. Liu, and G. Yang, "The natural aging and precipitation hardening behaviour of Al-Mg-Si-Cu alloys with different Mg/Si ratios and Cu additions," *Materials Science and Engineering: A,* vol. 627, pp. 119–126, 2015.
[17] X. Liu, S.-Y. Zhang, Z.-T. Liu, and H.-Y. Wang, "Effect of Mg/Si ratio on synergistic improvement of formability and yield strength in Al-Mg-Si-Zn alloys," *Materials Characterization,* vol. 214, p. 114095, 2024.
[18] P. Aster *et al.*, "Effect of long-term aging and Cu addition on clustering, strength and strain hardening in Al-Mg-Zn-(Cu) crossover alloys," *Materials & Design,* p. 114341, 2025.
[19] L. Ding *et al.*, "Study of the Q′(Q)-phase precipitation in Al–Mg–Si–Cu alloys by quantification of atomic-resolution transmission electron microscopy images and atom probe tomography," *Journal of Materials Science,* vol. 54, no. 10, pp. 7943–7952, 2019.

Chapitre 3. Alliages avancés de conducteurs en aluminium résistants à la chaleur : une revue exhaustive (Article 1)

Cet article a été publié dans:

International Journal of Minerals, Metallurgy and Materials, volume 33, numéro 1, 22 décembre 2025, page 68.

Résumé

Cette revue fournit une vue d'ensemble complète des avancées récentes dans les alliages conducteurs à base d'aluminium, conçus pour atteindre une résistance mécanique supérieure et une stabilité thermique élevée sans compromettre la conductivité électrique. Une attention particulière est accordée au rôle des éléments de microalliage — en particulier le Sc et le Zr — dans la promotion de la formation de précipités nanométriques cohérents tels que Al_3Zr, Al_3Sc et les structures cœur–coquille $Al_3(Sc,Zr)$ présentant une structure cristalline métastable de type $L1_2$. Ces précipités contribuent de manière significative aux performances à haute température en assurant le durcissement par précipitation et en stabilisant les joints de grains. La revue examine également le rôle émergent d'autres éléments de terres rares (REE), tels que l'erbium (Er), dans l'accélération de la cinétique de précipitation et l'amélioration de la stabilité thermique par le ralentissement du grossissement des précipités. En outre, les avancées récentes dans les stratégies de procédés thermomécaniques sont analysées, avec un accent sur des approches applicables à grande échelle visant à optimiser le compromis résistance–conductivité. Ces approches impliquent des traitements thermiques en plusieurs étapes et des séquences de fabrication soigneusement contrôlées, en particulier la combinaison du tréfilage à froid et des traitements de vieillissement pour favoriser une précipitation uniforme et efficace. Cette revue fournit des informations précieuses pour orienter le développement d'alliages d'aluminium économiques, à haute résistance et résistants à la chaleur au-delà des applications de conducteurs, en particulier ceux renforcés par microalliage avec Sc et Zr.

Mots-clés: Conductivité électrique, Propriétés mécaniques, éléments de terres rares, stabilité thermique, alliages d'Al contenant Sc et Zr.

Advanced thermal-resistant aluminum conductor alloys: A comprehensive review

Behrouz Abnar [a], Samaneh Gashtiazar [a], Paul Rometsch[b], Mousa Javidani [a]

[a] University Research Centre on Aluminium (CURAL) and Aluminium Research Centre–REGAL, Department of Applied Science, University of Québec at Chicoutimi (UQAC), Saguenay, QC G7H 2B1, Canada.

[b] Arvida Research and Development Centre, Rio Tinto Aluminium, Saguenay, QC, G7S 4K8, Canada

This article has been published in:

International Journal of Minerals, Metallurgy and Materials, Volume 33, Number 1, 22 December 2025, Page 68

Abstract

This review provides a comprehensive overview of recent advancements in aluminum-based conductor alloys engineered to achieve superior mechanical strength and thermal stability without sacrificing electrical conductivity. Particular emphasis is placed on the role of microalloying elements—particularly Sc and Zr— in promoting the formation of coherent nanoscale precipitates such as Al_3Zr, Al_3Sc, and core-shell $Al_3(Sc,Zr)$ with metastable $L1_2$ crystal structures. These precipitates contribute significantly to high-temperature performance by enabling precipitation strengthening and stabilizing grain boundaries. The review also explores the emerging role of other rare earth elements (REEs), such as erbium (Er), in accelerating precipitation kinetics and improving thermal stability by retarding coarsening. Additionally, recent advancements in thermomechanical processing strategies are examined, with a focus on scalable approaches to optimize the strength–conductivity balance. These approaches involve multi-step heat treatments and carefully controlled manufacturing sequences, particularly the combination of cold drawing and aging treatment to promote uniform and effective precipitation. This review offers valuable insights to guide the development of cost-effective, high-strength, heat-resistant aluminum alloys beyond conductor applications, particularly those strengthened through microalloying with Sc and Zr.

Keywords: Electrical conductivity, Mechanical properties, rare earth elements, Thermal stability, Sc- and Zr-containing Al alloy

3.1. Introduction

With the advancement of technology and expanding economic activities, energy consumption is increasing significantly, leading to a rapid growth in the demand for efficient power transmission and distribution systems [1, 2]. As a result, there has been significant research in recent decades focused on developing conductors that combine superior strength with high electrical conductivity (EC). Copper conductors are widely valued for their exceptional EC and durability, making them the benchmark in power transmission and electronics. However, Al is increasingly replacing Cu due to its lower cost, lighter weight, higher strength/weight ratio and relative abundance, offering a more economical and sustainable alternative in various applications [3, 4].

Common types of Al alloy electric conductors include all-Al alloy conductors (AAAC), Al conductor steel reinforced (ACSR), and electrical bus bars which are made by hot deformation, e.g., rolling or extrusion [4-6]. The AAAC type is composed entirely of Al alloy strands twisted together to form a single conductor cable. These conductors are specifically chosen for their mechanical strength, EC, and resistance to environmental factors. The 6xxx Al-Mg-Si alloys are generally used to make AAAC, specifically alloys AA6201 and AA6101 [7-10]. The ACSR conductors consist of Al strands surrounding a central steel core. The steel core provides mechanical strength, while the aluminum strands offer good conductivity. Alloy AA1350 is commonly used in such conductors [11]. Additionally, Al electrical bus bars are commonly manufactured in a rectangular bar form using alloys like AA6101 or AA1350, to efficiently distribute electrical power [12, 13].

With rising energy consumption, the demand for conducting wires capable of carrying high currents has increased, inevitably raising the wire temperatures. Elevated temperatures severely degrade the mechanical properties of Al wires, compromising power network reliability. Conventional 6xxx series Al alloys, limited by poor thermal resistance, struggle to meet these requirements due to the coarsening or dissolution of strengthening precipitates, restricting their prolonged service temperature to 100°C and limiting current-carrying capacity [14-16]. Recent work has aimed at developing Al conductors with superior strength, high EC, and thermally stable precipitates, addressing the need for enhanced power transmission capabilities [2]. The addition of scandium (Sc) and zirconium (Zr) demonstrates

considerable potential for developing Al alloys with high strength and improved thermal stability [17]. During the aging of supersaturated solid solutions in Sc- and Zr-containing Al alloys, nanoscale precipitates such as Al_3Sc, Al_3Zr, or core-shell $Al_3(Sc_{1-x}Zr_x)$, with the metastable $L1_2$ structure, are formed [17, 18]. These coherent precipitates exhibit strong interactions with the α-Al matrix, significantly enhancing mechanical strength at both ambient and elevated temperatures [19-22]. The ambient-temperature strength is generally attributed to mechanisms such as precipitate shearing, dislocation looping (Orowan bowing), or a combination of both [23]. At elevated temperatures, Sc- and Zr-containing precipitates effectively pin grain boundaries through the Zener pinning effect, inhibiting grain boundary migration and recrystallization, thus enhancing resistance to grain structure changes [24-26].

The high cost of Sc in its various forms (master alloy, metal, or oxide) has driven the search for lower cost microalloying alternatives for Al alloys. Market data shows that erbium (Er), ytterbium (Yb), and yttrium (Y) are more affordable [27-32]. Providing an exact price is challenging due to significant variations among sources, largely influenced by purity levels. However, scandium in scandium oxide typically ranges from approximately 3,000 to 10,000 USD/kg, while erbium oxide is priced around 40 to 45 USD/kg [29-33]. Under controlled conditions, these rare earth elements (REEs) influence the precipitation behavior by forming a specific structure. Although they (like Zr) cannot fully substitute Sc in terms of performance improvement, partially replacing Sc with REEs (and/or Zr) can offer a cost-effective solution without compromising the performance of Al conductor alloys [34-36].

Selecting optimal temperatures for hot deformation and aging in 1xxx alloys containing Zr, Sc, and other REEs is challenging due to the varying precipitation temperatures of these alloying elements. For example, Sc precipitates at a lower temperature than Zr, and the optimal temperature for Zr precipitation is too high for Sc or most REEs. This disparity can result in precipitate coarsening, which negatively impacts strength at both room and elevated temperatures [2, 27, 37]. Additionally, for 6xxx alloys, the heat treatment is also complex due to the significant mismatch in aging temperatures required for the formation of Sc- and Zr-containing precipitates compared to Mg-Si precipitates, which affects optimal precipitation hardening. The aging temperature for Mg-Si precipitates (β″, β′) typically ranges between 170-200°C, whereas Sc precipitate formation requires temperatures of

≥300°C and Zr precipitates form at ≥400°C [7, 25, 38]. This difference complicates the task of balancing precipitation processes to optimize the performance of an alloy.

Although numerous studies have explored processing techniques for Al alloys containing Sc and Zr, and other REEs, some challenges specific to both 1xxx and 6xxx alloys remain unresolved. This review begins by outlining the fundamental principles of Sc- and Zr-containing conductor alloys, focusing on their strengthening mechanisms and the key factors influencing electrical conductivity (Section 2). Section 3 explores precipitate evolution in 1xxx and 6xxx Al alloys, linking nanoscale structures to strength and conductivity, and evaluates REE additions for enhanced performance and thermal stability. The processing strategies for 1xxx and 6xxx Al alloys microalloyed with Sc and Zr are explored in detail in Section 4, highlighting multi-step heat treatments to optimize strength, conductivity, and thermal stability. The discussion of property trade-offs—particularly between strength and electrical conductivity—is addressed throughout, but is especially emphasized in Sections 2.2, 3.1, 3.3, and 4.1, where alloying effects and processing routes are evaluated for optimal performance.

3.2. Influence of Sc and Zr on strengthening mechanisms and electrical properties

3.2.1. Overview of main mechanisms

The mechanical strength of pure Al is insufficient for most industrial applications, necessitating the development of effective strengthening techniques for Al-based alloys. Several mechanisms contribute to the enhancement of alloy strength, including grain boundary strengthening, dislocation strengthening, precipitation strengthening, and solid solution strengthening [39-42]. Grain refinement reduces the grain size, increasing the density of grain boundaries that act as barriers to dislocation movement, thereby enhancing material strength. This is explained by the Hall-Petch effect, where smaller grains lead to higher strength [43-45]. Additionally, dislocation strengthening involves increasing the density of dislocations, with their entanglement making movement more difficult and improving strain hardening [46, 47]. Precipitation strengthening occurs when precipitates form from a supersaturated solid solution, strengthening the material through the shearing and Orowan bypassing effects [48, 49]. Furthermore, solid solution strengthening results

from solute atoms causing lattice distortion, which generates internal stresses that hinder dislocation motion, improving mechanical properties [45, 50]. The overall contribution of potential hardening mechanisms can be estimated using the following general equation [48]:

$$\sigma_{\mathrm{y}} = \sigma_0 + \sigma_{\mathrm{gb}} + \sigma_{\mathrm{dis}} + \sigma_{\mathrm{prec}} + \sigma_{\mathrm{ss}} \quad (1)$$

where σ_0 is the Peierls-Nabarro stress, which corresponds to the strength of pure Al [51], σ_{GB} is grain boundary strengthening, σ_{Dis} is dislocation strengthening, σ_{Pt} represents precipitation strengthening, and σ_{ss} is solid solution strengthening [52].

In terms of conductive mechanisms, an electron is treated as a small particle with mass and electric charge. Electrons can move freely through the metal lattice, but their motion is influenced by scattering events [53]. The mean free path of an electron, which represents the average distance it travels between scattering events, is inversely proportional to the probability of scattering during each encounter. Interactions between electrons and the metal lattice, as well as defects in the lattice structure, increase scattering events [4, 53]. These interactions lead to higher electrical resistivity, as electron scattering impedes their flow through the metal [54]. The total electrical resistivity can be estimated by Matthiessen's rule, where the overall resistivity (ρ) of an Al alloy can be expressed in Eq. 2 [4], which could be converted to the EC (% IACS) using Eq. 3 [4].

$$\rho_{\mathrm{total}} = \rho_0 + \Delta\rho_{prec} + \Delta\rho_{dis} + \Delta\rho_{gb} + \Delta\rho_{ss} + \Delta\rho_{vac} \quad (2)$$

$$EC(\%\mathrm{IACS}) = \frac{172.4}{\rho_{total}(\mu\Omega\mathrm{cm})} \quad (3)$$

where the total resistivity (ρ_{total}) is equal to the sum of the resistivity from the Al matrix (ρ_{Al}), precipitates ($\Delta\rho_{\mathrm{prec}}$), the dislocations formed through the work hardening ($\Delta\rho_{dis}$), grain boundaries ($\Delta\rho_{gb}$), the solutes ($\Delta\rho_{sol}$), and the vacancies ($\Delta\rho_{vac}$) [4].

A comparison of strengthening and conductive mechanisms reveals that most strengthening factors induce lattice distortion, resulting in electron scattering and reduced EC. This mutual exclusivity between strength and conductivity in metals poses a significant challenge in overcoming the trade-off between these properties in Al conductors [54].

3.2.2. Impact of Sc and Zr on strengthening mechanisms and conductivity of Al alloys

The addition of Sc and Zr to Al alloys significantly influences several strengthening mechanisms, including precipitation strengthening, solid solution strengthening, and grain boundary strengthening [19, 55].

Sc leads to the formation of fine Al_3Sc precipitates that hinder dislocation movement, significantly enhancing strength. In addition, Zr promotes the formation of Al_3Zr precipitates, which further enhance the strength through similar mechanisms [55-59]. Under appropriate thermomechanical processing, when Sc is combined with Zr, it can lead to the formation of fine, coherent $Al_3(Sc_{1-x}Zr_x)$ precipitates with a core-shell or double-shell structure [60, 61]. These precipitates have a Sc-rich core surrounded by a Zr-rich shell, which results in a more stable phase and improves the resistance to softening at high temperatures by inhibiting grain boundary sliding and restricting dislocation motion, thereby effectively inhibiting recovery and recrystallization to higher temperatures [62-65]. As dislocations become pinned by precipitates, a higher stress is required for the dislocations to escape the blockage of the precipitates [14, 66].

Furthermore, both Sc and Zr atoms can dissolve in the Al matrix, creating a solid solution that impedes dislocation motion, increasing the yield strength. However, the contribution of Zr to solid solution strengthening is typically smaller than that of Sc, due to its lower solubility in Al [65], and these effects are relatively small compared to the precipitation strengthening potential of Sc. Moreover, Sc and Zr play a role in refining the grain structure, leading to grain boundary strengthening. The primary Al_3Zr or $Al_3(Sc_{1-x}Zr_x)$ phases formed during solidification act as heterogeneous nucleation sites for α-Al grains, eventually resulting in a finer microstructure that contributes to higher strength [67, 68]. However, for Sc this grain refinement effect only happens above the eutectic concentration, which is at about 0.6 wt% Sc for a binary Al-Sc alloy [69]. All strengthening mechanisms associated with Sc and Zr disrupt the free flow of conduction electrons by introducing scattering centers, such as solute atoms and precipitate-matrix interfaces, which result in increased electrical resistivity [53, 70].

It is worth noting that solid solution strengthening is the most detrimental mechanism for EC compared to grain boundary strengthening and precipitation strengthening [71]. For instance,

in the study by Mohammadi et al. [48], the Al-Zr alloy was investigated using high-pressure torsion (HPT). The findings revealed that even after ultra-SPD processing and aging, the main contribution to electrical resistivity originated from Zr solute atoms (4.1 μΩ.cm). Grain boundaries were identified as the second major factor influencing resistivity with 0.5 μΩ.cm, while the impact of other microstructural features on electrical resistivity was found to be relatively negligible (<0.1 μΩ.cm).

This presents an opportunity for Sc, where the precipitation strengthening increment due to Al_3Sc precipitates can be of the order of 50 MPa per 0.1 wt% Sc addition and the negative effect on EC is relatively small (less than 0.5% IACS per 0.1 wt% of Sc) [25, 36, 72, 73]. Furthermore, it has been demonstrated recently that the yield strength of an extruded 1xxx alloy aged for 1h at 350°C could be increased by 91 MPa per 0.1 wt% Sc addition, or by up to 96 MPa per 0.1 wt% Sc with the addition of both 0.1 wt% Sc and 0.1 wt% Zr [74]. This significant increase in strength was caused by a combination of precipitation strengthening and substructural strengthening from the mostly non-recrystallized grain structure, which decreased the EC by 0.5% IACS per 0.1 wt% Sc compared to the fully recrystallized base alloy without Sc or Zr [36, 74].

3.3. Precipitate evolution and its impact on the performance of Sc- and Zr-containing Al conductor alloys in various systems

3.3.1. 1xxx systems

3.3.1.1. Precipitate structures

The binary Al-Zr and Al-Sc phase diagrams, calculated using Thermo-Calc™ software with the TCAL7 database and shown in Figure 3-1, illustrate the solubility limits and phase transitions of Zr and Sc in Al. These diagrams describe the phases present across various compositions and temperatures. The maximum solubilities of Zr and Sc in Al are comparably low at approximately 0.27 wt.% and 0.33 wt.% at ~660°C, respectively. The primary phases identified are α-Al, Al_3Zr, and Al_3Sc. The formation of these phases is influenced by the Zr and Sc contents as well as the thermal treatment applied to the alloy.

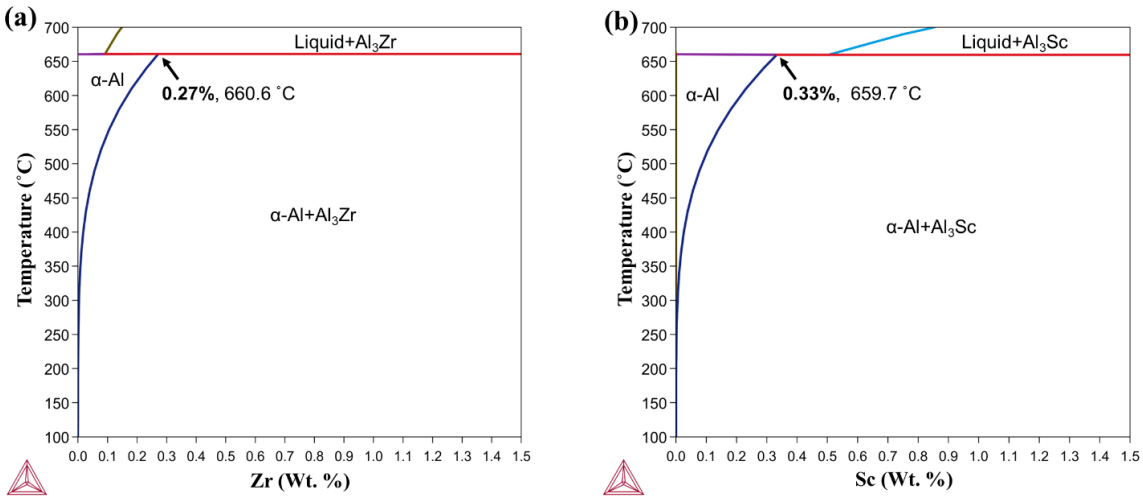

Figure 3-1. Al-rich corner of the phase diagrams for (a) Al-Zr and (b) Al-Sc systems.

In terms of solidification behavior for Al-Sc and Al-Zr alloys, Knipling et al. [75] used electron probe microanalysis (EPMA) to demonstrate that in an as-cast Al–0.06Sc (at.%) alloy, dendritic cells show a slight depletion of Sc concentration compared to the interdendritic regions (Figure 3-2). In contrast, the as-cast Al–0.06Zr (at.%) alloy exhibited significant variation in Zr concentration around the mean value, with dendritic cells being Zr-rich and interdendritic regions Zr-poor, a pattern that persists even after solidification [23, 75]. Therefore, in the as-cast alloys, Sc concentrates at the dendrite peripheries, while Zr segregates at the dendrite cores. This behavior arises because Sc solidifies via a eutectic reaction, whereas Zr undergoes a peritectic reaction during solidification.

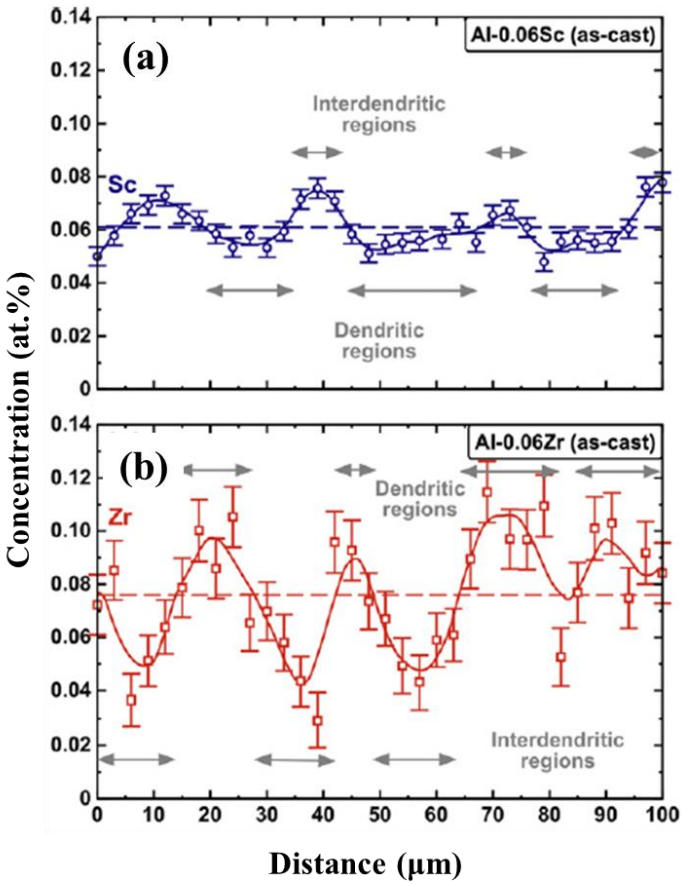

Figure 3-2. Concentration profiles of Sc and Zr, measured by EPMA, (a) as-cast Al–0.06Sc (at.%) ; (b) as-cast Al-0.06Zr [75]. With permission from Elsevier.

It is well documented that Zr enhances the thermal resistance of Al alloys, primarily due to the precipitation of $L1_2$-Al_3Zr nanoparticles which remain stable at elevated temperatures due to the low diffusivity of Zr within the Al matrix [76-79]. The coherent metastable face centered cubic (FCC) $L1_2$-structured $A1_3Zr$ phase forms under non-equilibrium conditions, such as in rapidly solidified Al-Zr systems [80]. These $L1_2$ precipitates often exhibit a spherical morphology, maintaining full coherency with the α-Al matrix and showing a high resistance to coarsening up to 400 °C [81, 82]. The high-temperature stability of the metastable $L1_2$ phase is primarily due to the slow diffusion kinetics of Zr in α-Al and the minimal lattice parameter mismatch between Al_3Zr ($L1_2$) and α-Al [83]. However, prolonged thermal exposure at elevated temperatures promotes coarsening and the phase transformation into the equilibrium $D0_{23}$-structured Al_3Zr phase, which typically cannot nucleate directly within α-Al solid solutions [75, 82, 84]. Knipling et al. [81] reported that the structural transformation from $L1_2$ to DO_{23} occurs at approximately 500 °C, which corresponds to the

onset of significant over-aging, as evidenced by microhardness measurements. Figure *3-3* illustrates examples of FCC $L1_2$-Al_3Zr and tetragonal $D0_{23}$ structures within the Al matrix of Al-Zr-based Al alloys. The lattice parameter of the $L1_2$ structure is a= 0.408 nm (compared to a=0.405 nm for FCC Al), while the $D0_{23}$ unit cell is characterized by lattice parameters a= 0.4014 nm and c= 1.732 nm, reflecting its tetragonal symmetry [64, 81, 85]. This $L1_2 \rightarrow D0_{23}$ transformation involves the formation of antiphase boundaries (APBs) parallel to the (001)-plane and exhibits preferential growth along the ⟨100⟩ directions, resulting in elongated ellipsoidal morphologies [81, 86]. The DO_{23} equilibrium structure exhibits a disk-shaped particle morphology, characterized by denser atomic packing and smaller lattice parameters compared to the $L1_2$ structure [81-83]. Figure 3-4 presents bright-field and dark-field TEM micrographs illustrating the transformation of the spheroidal metastable $L1_2$ phase into the disk-shaped equilibrium $D0_{23}$ tetragonal phase at elevated treatment temperatures [86, 87]. In terms of mechanical properties, cubic $L1_2$ nanoscale precipitates enhance hardness and deformation resistance via precipitation hardening, while tetragonal $D0_{23}$ exist as larger, less coherent particles, offering lower hardening contributions due to reduced interaction with dislocations in the aluminum matrix [64, 88].

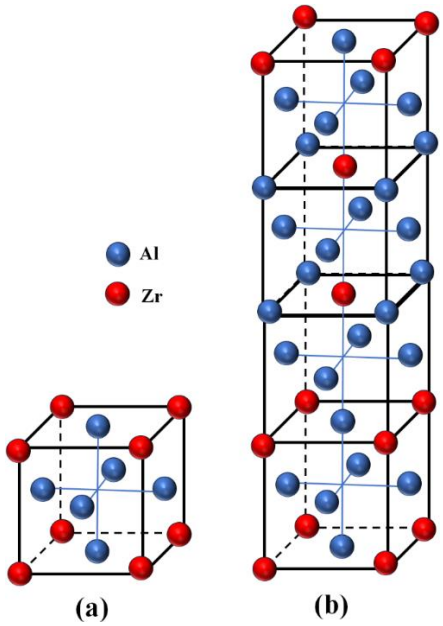

Figure 3-3. Schematic representation of the Al_3Zr crystal lattice: (a) cubic $L1_2$ structure, (b) tetragonal $D0_{23}$ structure.

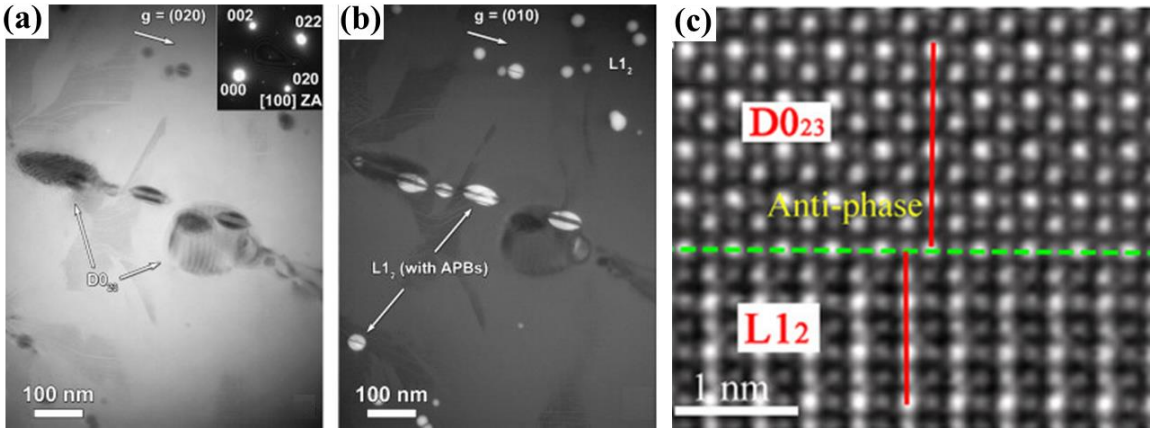

Figure 3-4. (a) Bright-field and (b) Dark-field TEM micrographs showing the transformation of Al_3Zr ($L1_2$) precipitates into their equilibrium $D0_{23}$ structures, highlighting the presence of antiphase boundaries (APBs) [86]. (c) Enlarged HAADF-STEM images of the $L1_2/D0_{23}$ interface with APBs [87]. With permission from Elsevier.

Sc is known to substantially improve the strength of Al alloys by the formation of nanoscale coherent Al_3Sc precipitates [89, 90]. In the Al-Sc alloy system, the Al_3Sc phase forms a face-centered cubic (FCC) lattice with an $L1_2$ structure and a lattice parameter of a=0.410 nm at room temperature [91, 92]. The atomic arrangement of the Al_3Sc phase is identical to that shown in Figure 3-3 (a), with Sc atoms occupying the positions of Zr atoms [83]. On the other hand, in a binary Al-Sc system, the coherent $L1_2$ Al_3Sc hardening precipitates initially exhibit a spherical morphology. However, these precipitates transform to incoherent, non-hardening structures with non-spherical morphologies when they reach a critical size, e.g. above 40 nm after 24 hours at 350 °C [93]. Figure 3-5 shows the morphological evolution of Al_3Sc precipitates in an Al–0.1 wt.% Sc alloy aged at 350 °C for 24, 72, and 250 hours. Initially, the precipitates exhibit a spherical morphology; however, over time, they develop irregular shapes, indicating unstable growth characteristics. Furthermore, Marquis and Seidman [93] have demonstrated that Sc content significantly influences both the nucleation and morphology of Al_3Sc precipitates during prolonged aging time at 350 °C. In Al–0.3wt% Sc alloys, precipitates tend to adopt spherical equilibrium shapes, whereas in Al–0.1wt% Sc alloys, non-spherical, non-equilibrium morphologies are observed (Figure 3-5).

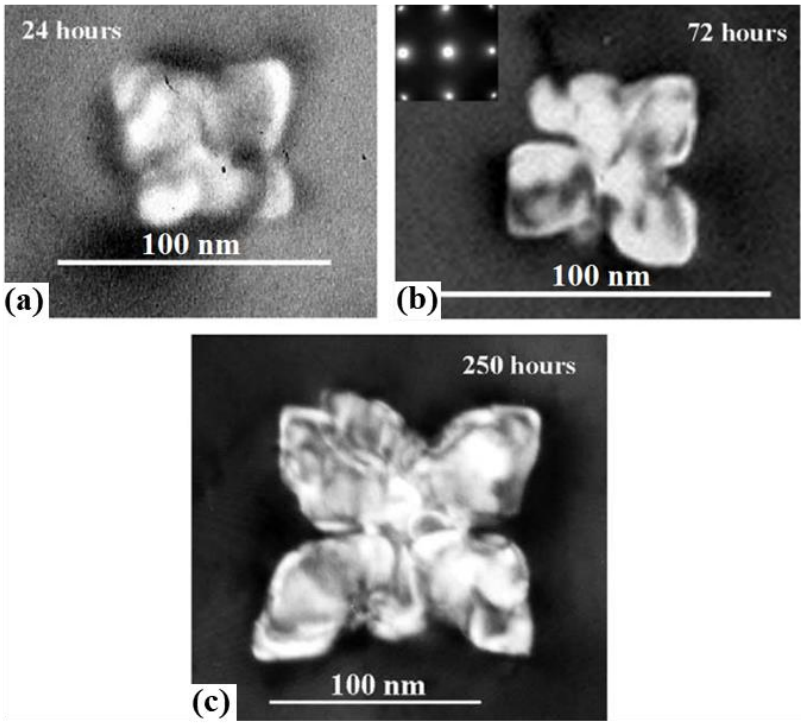

Figure 3-5. Dark-field TEM micrographs showing Al_3Sc precipitates in an Al–0.1wt% Sc alloy aged at 350°C for (a) 24, (b) 72, and (c) 250 hours. All images were captured along the [1 0 0] zone axis, with scale bars representing 100 nm [93]. With permission from Elsevier.

Although Al-Zr alloys exhibit high thermal stability, their low strength typically restricts their use as electrical overhead line conductors. The combined addition of Sc and Zr leads to improved mechanical properties compared to adding either Sc or Zr individually [21, 94, 95]. When Sc and Zr are used together in Al, complex core-shell precipitates with an $L1_2$ structure are likely to form within the Al-Sc-Zr system [60, 96]. High resolution transmission electron microscopy (HRTEM) and atom probe tomography (APT) have been employed in several studies to characterize the complex nanostructures and morphologies of $Al_3(Sc,Zr)$ precipitates [97-99]. Figure 3-6 (a) illustrates a schematic representation of core-shell precipitates in the Al-Sc-Zr system, showing the core enriched in Sc, the shell enriched in Zr, and the transition zone between them. Figure 3-6 (b) illustrates the atomic arrangement within the precipitates, showing the ordered distribution of Al, Sc, and Zr atoms. It highlights how Zr atoms gradually replace Sc atoms in Al_3Sc particles from the core to the shell. The formation of core-shell $Al_3(Sc,Zr)$ precipitates with an $L1_2$ structure can be attributed to the distinct diffusivities of Sc and Zr in Al, as well as their interactions during heat treatment

[61, 100-102]. The temperature-dependent diffusion coefficients (D) of Sc and Zr in Al were calculated using the Arrhenius equation given by:

$$D = D_0 \exp(\frac{Q}{RT}) \qquad (4)$$

where D_0 (m^2/s) is the pre-exponential factor, Q (J/mol) is the activation energy for diffusion, R (8.314 J/(mol·K)) is the universal gas constant, T (K) is the absolute temperature. The activation energy (Q) is 173 kJ/mol for Sc, and 242 kJ/mol for Zr. The corresponding pre-exponential factors (D_0) are 5.31×10^{-4} m^2/s for Sc and 7.28×10^{-2} m^2/s for Zr [23, 102, 103]. The results are presented in the diagram in Figure 3-7. Here Sc shows a significantly higher diffusivity in Al compared to Zr, implying that Sc is more mobile in the Al matrix under the same conditions. Accordingly, during the initial stages of aging, Sc atoms precipitate first to form more finely distributed coherent Al_3Sc precipitates with an $L1_2$ structure. As aging progresses, Zr atoms, characterized by a much lower diffusivity, migrate and precipitate onto the existing Al_3Sc particles. This transition occurs through the intermediate $Al_3(Sc_{1-x}Zr_x)$ phase, ultimately forming a Zr-rich Al_3Zr shell (see Figure 3-6). This core-shell solute distribution becomes more apparent with increasing aging temperature, and the gradient reflects the substitution of Sc by Zr as the precipitate grows [64, 83, 104]. The interaction between Sc and Zr, along with the core-shell structure of the precipitates, delays the transformation of the metastable $L1_2$ structure into the equilibrium $D0_{23}$ structure. This stabilization enhances the thermal resistance of the precipitates, making the alloy more resistant to precipitate coarsening at elevated temperatures [17, 18, 105]. It is worth mentioning that $Al_3(Sc_{1-x}Zr_x)$ specifies the exact substitutional solid solution relationship between Sc and Zr with defined proportions, whereas $Al_3(Sc,Zr)$ provides a general indication of both elements being part of the phase without detailing their ratio or arrangement.

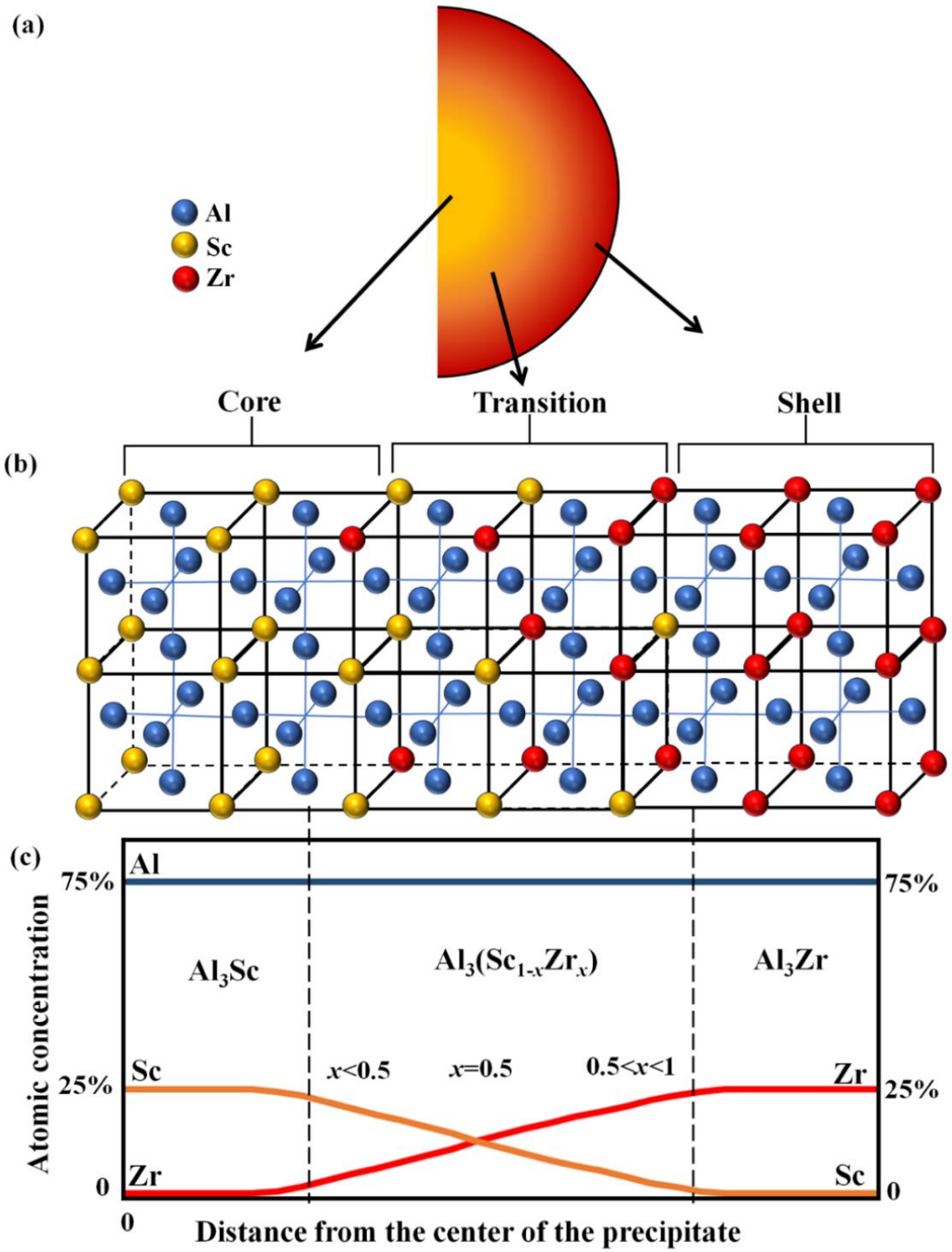

Figure 3-6. (a) Schematic representation of the core-transition-shell structure of $Al_3(Sc,Zr)$ precipitates in Al alloys. (b) The chemical composition gradient in the crystal lattice from core to shell. (c) The atomic concentration profiles of Sc, Zr, and Al as a function of distance from the center of the precipitate.

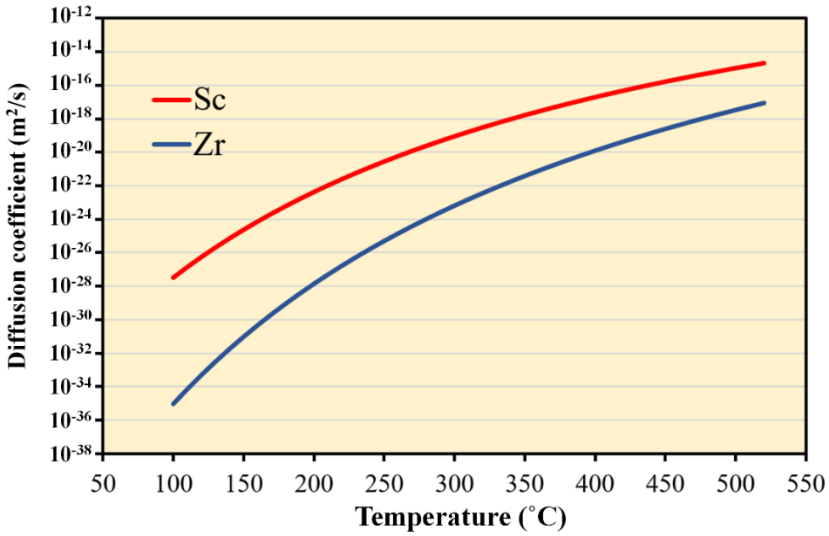

Figure 3-7. Diffusion coefficients of Sc and Zr in Al at different temperatures.

3.3.1.2. Correlation between precipitate evolution and mechanical and electrical properties

The evolution of precipitates in Al alloys containing Sc and Zr significantly influences their mechanical and electrical properties. Knipling et al. [23, 75, 86] conducted isochronal aging (with 3 hours at each successive 25°C temperature increment) on Al-Sc, Al-Zr, and Al-Sc-Zr alloys to investigate the effects of aging at various temperatures on phase transformations, precipitate formation, and their subsequent impact on strength, hardness, conductivity, and thermal stability. A summary of their findings is presented in Figure 3-8, which illustrates the variation in microhardness and EC. Unless otherwise specified, EC values reported in the reviewed studies were primarily measured using an eddy current apparatus at ambient temperature. These results offer valuable insights into the peak hardness achieved with individual Zr (blue) and Sc (green) additions in Al, as well as the combined effects of both elements (red). Furthermore, Figure 3-9 presents a schematic illustration of the precipitate evolution in the microstructure of Al-Sc, Al-Zr, and Al-Sc-Zr alloy systems as the aging temperature increases. At the same atomic percent of Sc and Zr, Al_3Sc precipitation in the Al-Sc system starts at ~250°C and peaks at 300-325°C, while Al_3Zr precipitation in the Al-Zr system starts at ~375°C and peaks at 425-475°C.

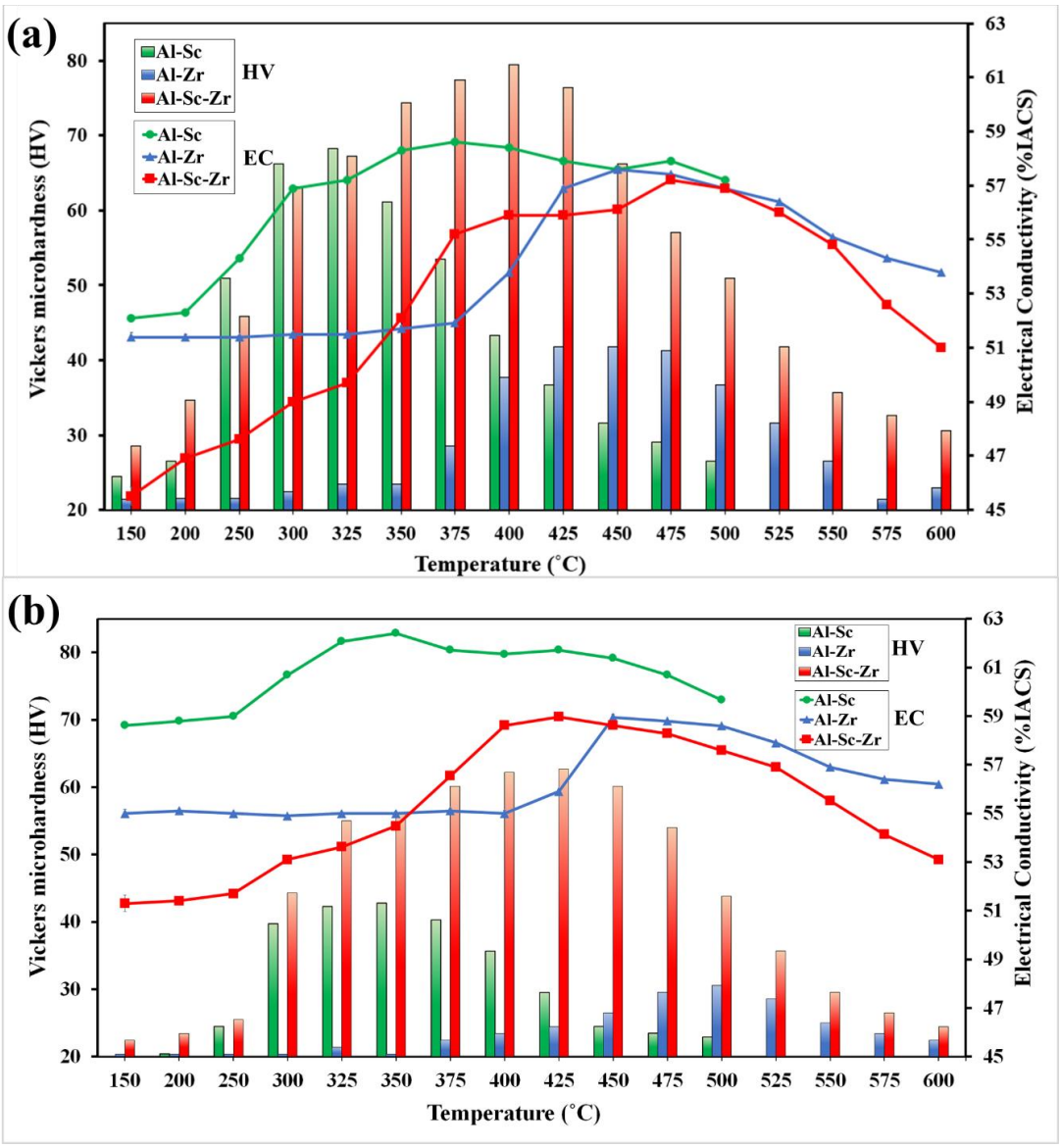

Figure 3-8. The evolution of Vickers microhardness and EC during multi-step isochronal aging (with 3 hours at each successive 25°C temperature increment) for (a) Al–0.1Sc, Al–0.1Zr, and Al–0.1Sc–0.1Zr (**at.**%) (or Al–0.17Sc, Al–0.34Zr, and Al–0.17Sc–0.34Zr (**wt.**%)) alloys and (b) Al–0.06Sc, Al–0.06Zr, and Al–0.06Sc–0.06Zr (at.%) (or Al–0.1Sc, Al–0.2Zr, and Al–0.1Sc–0.2Zr (wt.%)) alloys [23, 75].

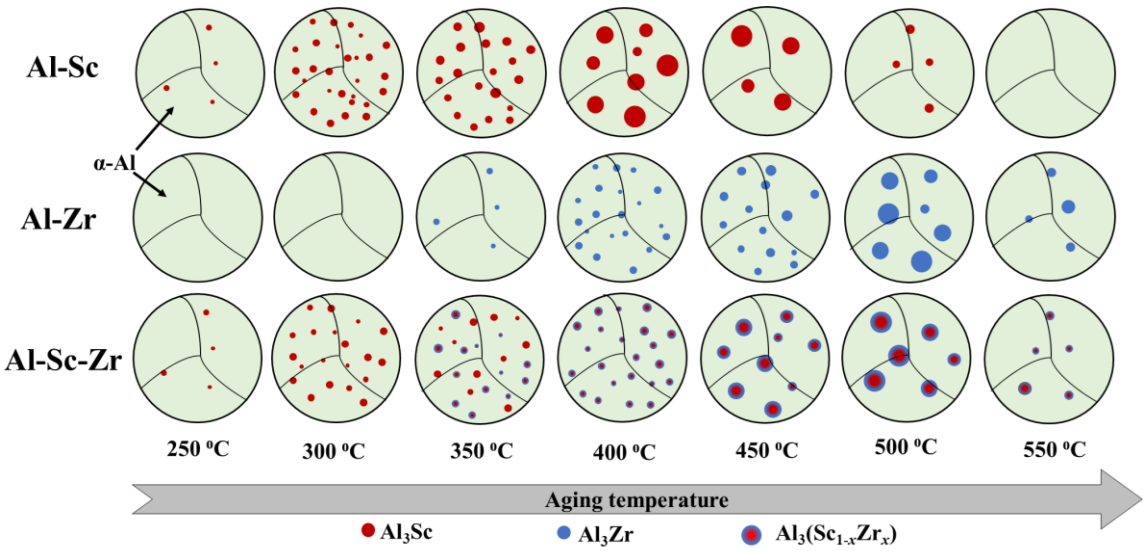

Figure 3-9. Schematic for precipitate evolution in Al-Sc, Al-Zr, and Al-Sc-Zr alloys, with reference to Figure 3-7 and Figure 3-8.

As mentioned above, Sc diffuses more rapidly than Zr in α-Al. This results in faster nucleation and growth of Al_3Sc precipitates compared to Al_3Zr precipitates. Sc promotes the formation of a high number density of fine precipitates at lower temperatures, leading to earlier strengthening of the alloy, as shown in Figure 3-8 (green vs. blue). The ternary Al-Sc-Zr system (red) exhibits a higher microhardness compared to the Al-Zr and Al-Sc systems. The peak microhardness of the Al-Sc-Zr system occurs at a temperature between the peak microhardness temperatures of the Al-Sc and Al-Zr alloys. It can be concluded that Zr does not contribute to the precipitation strengthening of Al-Sc-Zr alloys at temperatures up to ~325°C. As isochronal aging progresses to higher temperatures, coarsening of precipitates (over-aging) occurs in all alloys, although at different temperature thresholds. The slower diffusivity of Zr leads to slower coarsening of Al_3Zr precipitates compared to Al_3Sc, as shown in Figure 3-9. In Figure 8, the over-aging effect, characterized by a decrease in hardness, begins at ~325°C for Al_3Sc, whereas for Al_3Zr, it occurs above ~475°C. It is worth mentioning that the onset temperature of over-aging may vary slightly depending on the aging process, such as whether isothermal or isochronal treatment is used. The faster coarsening of Al_3Sc results in a lower temperature threshold for hardness degradation in Al-Sc alloys compared to Al-Zr and Al-Sc-Zr systems. Overall, under isochronal aging across various temperatures, the ternary Al–0.1Sc–0.1Zr (at.%) alloy achieves the highest peak microhardness of 79.5 HV at ~400 °C, accompanied by an EC of 55.9% IACS. In contrast,

Al–0.1Sc exhibits the highest EC of 58.4% IACS with a lower hardness of 43.3 HV at the same temperature. As shown in Figure 3-9, at 400 °C, the Sc precipitates in the Al–Sc system become too coarse, resulting in inadequate hardness despite its promising EC. In contrast, in the Al–Sc–Zr system, Al_3Sc precipitates initially formed at lower temperatures are restricted from further coarsening at higher temperatures due to the presence of a surrounding Zr-rich shell. This layer maintains an optimal number and distribution of precipitates at higher temperatures, ensuring that the effectiveness of Al_3Sc precipitates is not diminished as the temperature increases.

The variation in EC for Al-Sc and Al-Zr follows a similar trend to microhardness. As the aging temperature increases and solute (Sc and Zr) is removed from the matrix, the EC begins to rise. This occurs at lower temperatures for Sc compared to Zr. The Al-Zr system consistently exhibits lower electrical conductivity across all aging temperatures, indicating a more pronounced detrimental effect of Zr—at the same atomic percentage as Sc—due to greater atomic lattice distortion and increased electron scattering. For the ternary Al-Sc-Zr system, the EC at 350°C and below is the lowest compared to the Al-Zr and Al-Sc systems. However, above 350°C, the EC of this alloy first exceeds and then becomes similar to that of the Al-Zr alloy. As aging progresses to higher temperatures, the EC decreases, indicating the start of dissolution. As illustrated in Figure 3-9, the dissolution temperatures vary between the different systems. According to Figure 3-1, the solvus temperature of binary Al-Sc is about 25°C lower than that of binary Al-Zr. For instance, with 0.1 wt.% Sc or 0.1 wt.% Zr, the solvus temperatures are ~520°C and ~545°C for binary Al-Sc and Al-Zr alloys, respectively. Given this, Sc precipitates begin to dissolve at a lower temperature, as observed in Figure 3-8. The dissolution of these precipitates release Sc and Zr into solid solution, thereby decreasing the EC.

During the aging of Al-Sc-Zr alloys, the precipitate structure significantly influences the EC as well. Above 325°C, Al_3Sc remains stable without coarsening due to the formation of Al_3Zr around it, which delays precipitate dissolution with increasing temperature. As a result, the EC of Al-Sc-Zr alloys continues to increase up to ~450°C due to the retention of Al_3Sc and the precipitation of Zr.

Figure 3-10 summarizes the peak aged hardness and EC of 1xxx series Al alloys containing Sc and/or Zr across various processing conditions. It can be concluded that the strength of Al-Sc alloys is generally higher than that of Al-Zr alloys under similar thermomechanical treatments at peak aging temperatures [105, 106]. However, by selecting the optimal aging temperature, the Al-Sc-Zr system can achieve superior mechanical properties compared to the individual use of Zr or Sc. In the Al-Sc-Zr alloy system, Sc facilitates faster and more uniform precipitation. Meanwhile, Zr combines with Sc to form coherent core-shell $L1_2$ $Al_3(Sc_{1-x}Zr_x)$ precipitates, which significantly reduce the coarsening rate of Al_3Sc at high temperatures [107]. This enhances the thermal stability and mechanical properties of the alloy without compromising its EC [107, 108].

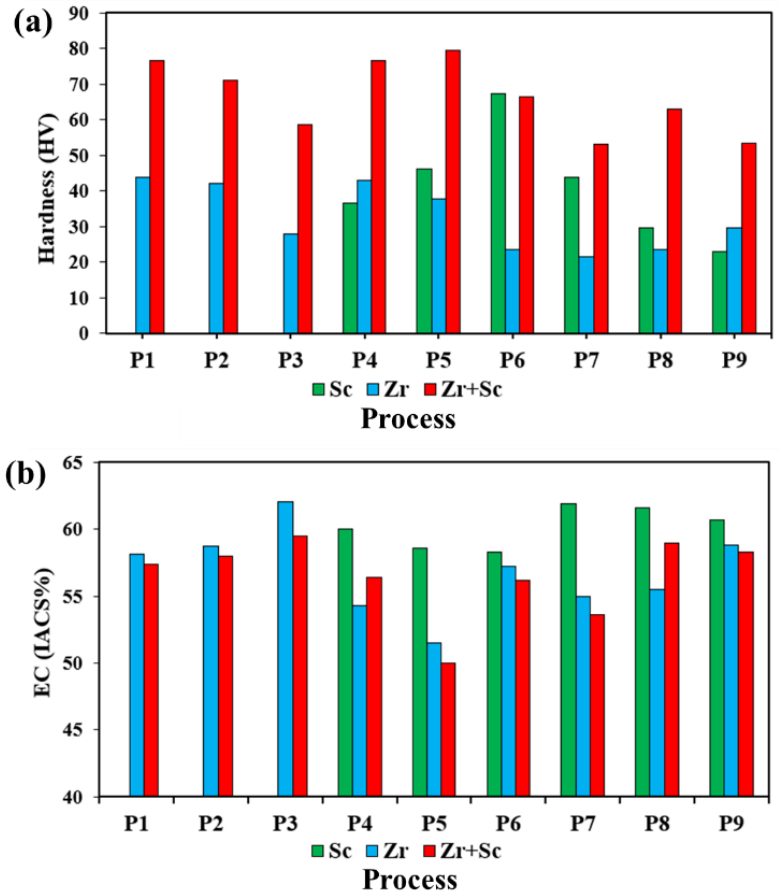

Figure 3-10. (a) Hardness and (b) EC variations of 1xxx Al conductor alloys with changes in chemical composition, including the addition of Sc (blue), Zr (green) or both (red), under various thermomechanical treatments. Each process corresponds to a distinct set of thermomechanical sequence, **as detailed in Table** 3-1.

Table 3-1. Summary of processing conditions and alloy compositions for each treatment route represented in Figure 3-10.

Process designation	Nominal alloy composition	Summary of process steps	Ref.
P1	Al-0.1Zr and Al-0.1Sc-0.1Zr (wt. %)	HR (550 °C)-ST (600 °C, 8h)-AG (400 °C, 48h)-CD-O (350 °C,5h)	[15]
P2	Al-0.2Zr and Al-0.2Zr-0.1Sc (wt. %)	HR (550 °C)-ST (600 °C, 8h)-CD-AG (400 °C, 48h)	[15]
P3	Al-0.1Zr and Al-0.1Sc-0.1Zr (wt. %)	Homo (620 °C, 48h)-HE (550 °C) (9.5 mm)-CD (5.7 mm)-O (400 °C, 36h)	[109]
P4	Al-0.1Sc, Al-0.1Zr and Al-0.1Sc-0.1Zr (at. %)	Isochronal aging at 200-425 °C	[23]
P5	Al-0.1Sc, Al-0.1Zr and Al-0.1Sc-0.1Zr (at. %)	Isochronal aging at 200-400 °C	[23]
P6	Al-0.1Sc, Al-0.1Zr and Al-0.1Sc-0.1Zr (at. %)	Isochronal aging at 200-325 °C	[23]
P7	Al-0.06Sc, Al-0.06Zr and Al-0.06Sc-0.06Zr (at. %)	Isochronal aging at 200-325 °C	[75]
P8	Al-0.06Sc, Al-0.06Zr and Al-0.06Sc-0.06Zr (at. %)	Isochronal aging at 200-425 °C	[75]
P9	Al-0.06Sc, Al-0.06Zr and Al-0.06Sc-0.06Zr (at. %)	Isochronal aging at 200-475 °C	[75]
HR: Hot rolling, ST: Solution heat treatment, AG: aging, CD: cold wire drawing, O: Annealing, Homo: Homogenization, HE: hot extrusion			

For instance, Shao et al. [15] demonstrated the superiority of the Al-Sc-Zr system over the binary Al-Zr system in terms of mechanical properties and thermal stability. As shown in Figure 3-11, the number density of precipitates increased from 0.03×10^{22} m^{-3} for Al-Zr to 1.19×10^{22} m^{-3} for Al-Sc-Zr, while the average particle diameter decreased from 8.8 nm to 5.6 nm, respectively. This difference in precipitate characteristics explains the significant variation in mechanical properties between the samples with and without Sc addition. Additionally, Tolley et al. [110] showed the significant role of Zr in preventing precipitate coarsening at higher temperatures, as illustrated in Figure 3-12. After 69 hours of aging at 450 °C, the average precipitate diameter in the binary Al-Sc alloy (74 nm) was larger than in the ternary Al-Sc-Zr alloy (54 nm) [110].

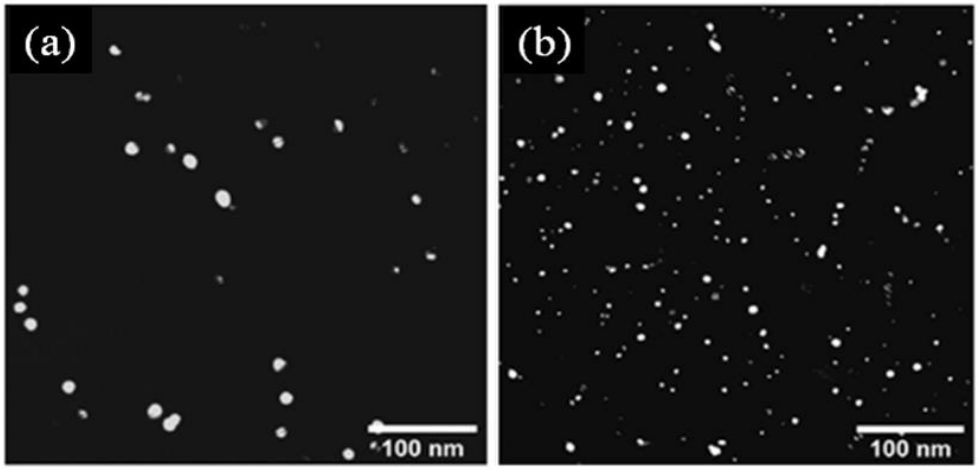

Figure 3-11. Dark-field TEM images showing precipitates in (a) Sc-free Al-0.1Zr (wt. %) alloy after 48h at 400˚C, (b) 0.1Sc-containing Al-0.1Zr (wt. %) alloy after 48 h at 350 °C [15]. With permission from Elsevier.

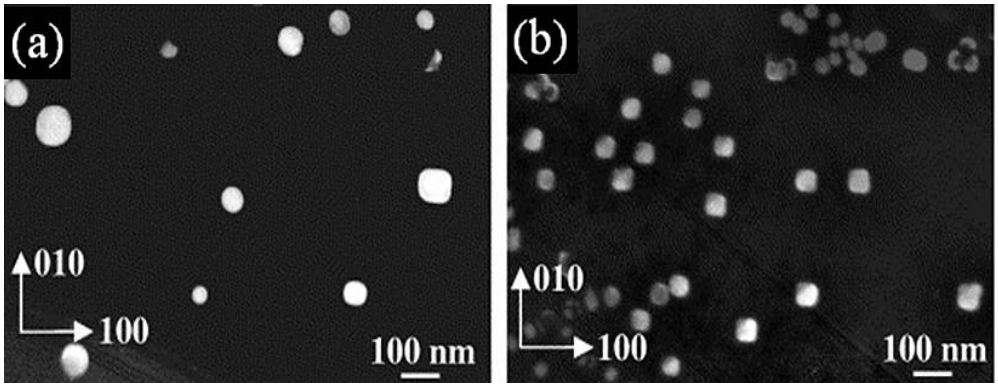

Figure 3-12. Dark-field TEM images showing precipitates after 69 h at 450 °C in (a) binary Al–0.61Sc (wt.%) and (b) ternary Al–0.61Sc–0.40Zr (wt.%) [110]. With permission from Elsevier.

In Al-Zr-Sc alloys, the presence of additional elements can influence the evolution of precipitation. For instance, the addition of Si to Al-Zr-Sc alloys accelerated the precipitation kinetics and increased the heterogeneous precipitation of $Al_3(Sc,Zr)$ nanoparticles [111]. The mechanism underlying this phenomenon involves the unique interaction between Si atoms and the vacancy structure within the Al matrix. Due to the differences in atomic size and bonding characteristics, Si atoms in the Al matrix can distort the surrounding lattice, potentially increasing the vacancy concentration around these solute atoms. These distortions, combined with the natural attraction between Si atoms and vacancies, make them prone to forming Si-vacancy clusters. The formation energies of these clusters suggest that

they can act as inhomogeneous nucleation sites for nano-precipitate formation during aging [111-113].

The presence of Si in Al–Sc alloys significantly influences the precipitation kinetics of Al_3(Sc,Zr) phases. The faster diffusion rate of Si compared to Sc and Zr plays a key role in accelerating the nucleation of Al–Si–Sc clusters and the subsequent precipitation of Al_3(Sc,Zr) during aging. This acceleration is mainly attributed to strong Si–Sc clustering in the Al matrix, driven by attractive Si–Sc binding energies at the first and second nearest-neighbor distances. Si modifies the transition state energy during Sc diffusion, leading to a substantial reduction in migration energy, further facilitating the precipitation process [111, 114, 115]. Studies, such as those by Booth-Morrison et al. [114], have demonstrated that adding 0.06 atomic percent Si to an Al–0.06Sc–0.06Zr (at.%) alloy accelerates Al_3(Sc,Zr) precipitation kinetics during the early stages of aging at 275 °C and 300°C. Si preferentially partitions to the Al sublattice sites of the $L1_2$-ordered phase in $(Al,Si)_3Sc$ precipitates, promoting the rapid formation and growth of these strengthening phases.

Additionally, microalloying with slow-diffusing transition metals like vanadium (V) and tungsten (W) can form stable or metastable tri-aluminide phases in Al-Sc or Al-Sc-Zr alloys, potentially enhancing the creep resistance and/or reducing coarsening [108, 111, 112, 116]. Farkoosh et al. [108] showed that a W-modified Al-0.11Zr-0.005Er (at.%) alloy with a 0.1 at.% Si addition enhances the coarsening resistance of precipitates, which can improve the thermal stability of the alloys. Moreover, Vafaeenezhad et al. [112, 115] investigated the effects of 0, 0.05, and 0.1 at.% V on the aging response, the coarsening of the nano-precipitates, as well as the resulting EC and hardness, during both isochronal and isothermal aging of Al-Sc-Zr alloys. As shown in Figure 3-13 (a), during the isochronal aging, the microhardness of Al-Sc-Zr alloys with 0, 0.05, 0.1 at.% V and 0.18 at.% Si reached peaks at 425 °C, with values of 540 MPa (55.0 HV), 570 MPa (58.1 HV), and 603 MPa (61.5 HV), respectively. At 425 °C, the alloys V0, V0.05, and V0.10 exhibited maximum EC values of 33.5 MS/m (57.8% IACS), 29.4 MS/m (50.69% IACS), and 27.7 MS/m (47.7% IACS), respectively. The peak EC observed during isochronal aging at this temperature suggests that the matrix has been depleted of alloying elements, and nanoprecipitates have formed at their highest density. The main role of V in Al-Zr-Sc alloys is to inhibit coarsening at elevated

temperatures, thereby enhancing the strength of alloy. The slower coarsening kinetics in alloys V0.05 and V0.10 can be attributed to the higher concentration of V at the interfaces, as V diffuses more slowly compared to other elements in the precipitates [83]. The nanoprecipitates exhibited a core-shell structure, consisting of a Sc-enriched core, a Zr-enriched shell, and an additional V-enriched outer layer. Vanadium partitioning at the precipitate shells occurred because of the increasing influence of silicon, which accelerated the diffusion rates of both Zr and V. This is driven by thermodynamic conditions that favor the diffusion of Zr and V, resulting in the stabilization of these nanoprecipitates and contributing to an improved mechanical performance at elevated temperatures [83]. However, it should be noted that V decreases the EC quite significantly.

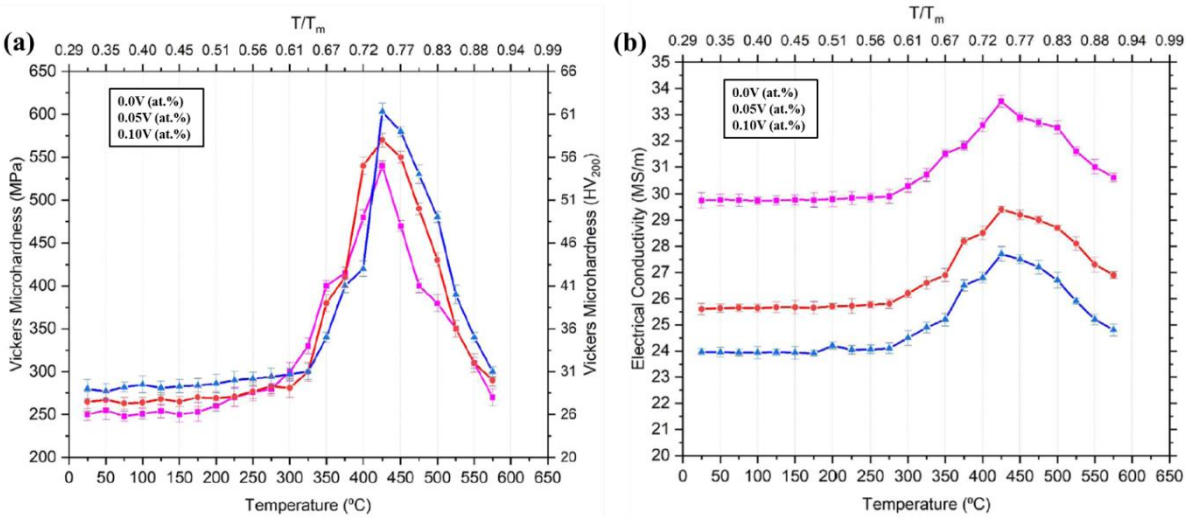

Figure 3-13. Effects of multi-step isochronal aging (with 1 hour at each successive temperature) on: (a) Vickers microhardness and (b) EC in Al-0.06Zr-0.06Sc-0.18Si (at.%) alloys containing 0, 0.05, and 0.10 at.% V. [115]. With permission from Elsevier.

3.3.2. 6xxx systems

Al-Mg-Si 6xxx series alloys, such as 6201 and 6101, are heat-treatable Al alloys primarily used for high-strength overhead conductors [4, 117]. The addition of Sc and Zr to these alloys introduces complex precipitation behaviors, influencing their mechanical properties and EC [25]. In Al-Mg-Si alloys, precipitation strengthening occurs mainly through the formation of Mg-Si clusters, coherent Guinier-Preston (GP) zones and β" precipitates. The aging process typically begins with a supersaturated solid solution, followed by the formation of atomic clusters and spherical GP zones enriched with Mg and Si atoms. These zones elongate into

needle-shaped coherent β″ phases, which then grow into semi-coherent rods (β′ phase) and ultimately develop into non-coherent platelets (β stable phase) [118-120]. The incorporation of Sc and Zr into Al-Mg-Si alloys results in the formation of Al_3Sc and Al_3Zr precipitates, which significantly affect the precipitation sequence and aging response. These precipitates form at higher temperatures (approximately 300–500°C) compared to the (Mg, Si)-based precipitates, which form below 200°C. Therefore, Sc and Zr precipitates should be formed first at higher temperatures, followed by the precipitation of the (Mg, Si)-based phases. Promoting Sc- and Zr-containing precipitates after forming Al-Mg-Si hardening precipitates, such as the β″ and β′ phases, can diminish their strengthening effect due to over-aging [38, 56].

Achieving optimal performance in Al-Mg-Si alloys containing Sc and Zr requires carefully tailored heat treatments to manage the interactions between Sc, Zr, Mg, and Si precipitates. This involves complex heat treatments, including multi-step homogenization and pre- or post-solutionizing treatments. If these treatments are not precisely tailored to the specific alloy composition, the potential benefits of Sc and Zr additions may be minimal in the Al-Mg-Si system [121, 122]. Recent advances in the thermomechanical processing of Sc- and Zr-containing Al-Mg-Si conductor alloys are discussed in Section 4.2.

The presence of Si in $Al_3(Sc,Zr)$ phases is expected, as Si has been shown to substitute for Al in the Al_3Sc lattice structure in alloys containing both Si and Sc [123]. Figure 3-14 shows a schematic diagram of the Sc and Zr precipitation phenomena in Al-Mg-Si-Zr-Sc alloys. The initial aging step at 300 °C facilitates the precipitation of the $(Al,Si)_3Sc$ core while subsequent aging at 450 °C results in the precipitation of the Al_3Zr shell directly on the surface of the $(Al,Si)_3Sc$ precipitates. Furthermore, if any Sc remains in solution after the 300 °C heating stage, it will likely lead to the formation of $Al_3(Sc_{1-x}Zr_x)$ precipitates with a more homogeneous core structure [121].

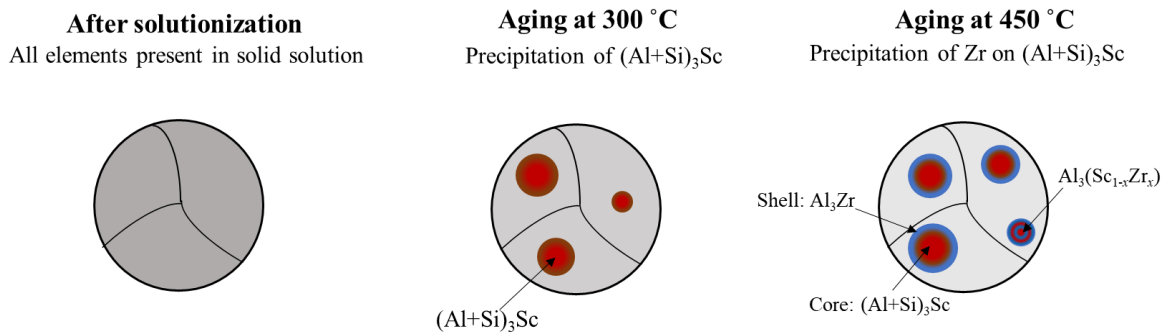

Figure 3-14. Schematic diagram of the Sc and Zr precipitation phenomena during multi-stage trial heat treatments of Sc- and Zr-containing Al-Mg-Si alloys [121].

In the Al-Mg-Si-Sc-Zr system, the formation of Sc- and Zr-containing precipitates can be followed by heating to 500-540 °C for a few minutes to redissolve the Mg and Si containing phases. Normal aging at 170-200 °C then forms Mg-Si strengthening precipitates [25, 124]. The presence of $Al_3(Sc,Zr)$ precipitates affects Mg and Si precipitate formation. The consumption of Si in $(Al,Si)_3(Sc,Zr)$ precipitates reduces the amount of Si available for Mg-Si precipitate formation, effectively making the alloy leaner and increasing the diffusion distances between Mg-Si precipitates [125]. This can slow down the precipitation kinetics and delay the over-aging of Mg- and Si-containing precipitates [38, 121]. Additionally, the Mg and Si containing precipitates (specifically β') have been observed to nucleate on Al_3Sc phases in the interdendritic regions of as-cast Al-Mg-Si-Cu-Sc-Zr alloys [126]. Conversely, recent studies suggest that Al_3Sc/Al_3Zr phases can nucleate on pre-existing β phases, highlighting a mutual relationship between these precipitates that influences the overall microstructure and properties [38, 126].

The influence of Zr and Sc on the hot deformation behavior of 6xxx alloys should be considered to fully understand their effects. It has been reported that adding 0.2 wt.% Zr to an Al-0.8Mg-1.0Si (wt.%) alloy, combined with homogenization at 450 °C, increases the high-temperature flow stress by 20% compared to the Zr-free base alloy [127]. Additionally, Babaniaris et al. [66] found that an Al–Mg–Si-Sc-Zr alloy has a higher activation energy for hot deformation (202.4 kJ/mol) than an Al–Mg–Si–Mn–Cr alloy (177.2 kJ/mol), due to strengthening by $Al_3(Sc,Zr)$ particles. The former alloy had lower misorientation angles and smaller subgrain sizes, indicating less dynamic recovery and inhibited recrystallization. This

was attributed to limited dislocation movement due to dislocation pinning by $Al_3(Sc,Zr)$ precipitates [66].

Adding Sc to Si-containing Al alloys can present challenges due to the strong interaction between Sc and Si, leading to the formation of coarse primary particles. These particles consume Sc, reducing its availability for subsequent precipitation hardening and potentially diminishing the mechanical properties of the alloy. However, employing sufficiently rapid solidification rates during casting can mitigate this issue by refining the microstructure and promoting a more uniform distribution of alloying elements [128-130].

3.3.3. Effects of REE on the performance of Sc- and Zr-containing Al conductor alloys

Sc and Zr-containing Al alloys can become more economical by reducing the Sc content or substituting it with more cost-effective alternatives. Recently, the focus has shifted to Zr-based alloys with trace rare earth element (REE) additions, particularly Er, which are strengthened by metastable L12-ordered $Al_3(Zr, REE)$ nanoprecipitates [108, 131, 132]. In $Al_3(Zr, REE)$ nanoprecipitates, Al atoms occupy the face-centered positions, while Zr and REEs occupy the body-centered positions within the unit cell [132]. The combined presence of Sc and Zr, along with other REEs, can lead to synergistic effects that further enhance the strength and electrical performance of Al conductor alloys containing Sc and Zr [36, 133]. Elements such as Zr, Sc, and Er can refine α-Al grains and secondary phases, reduce the adverse effects of impurities, and promote the formation of thermally stable Al_3M (M = Zr, Sc, and rare earth elements) precipitates with an $L1_2$ structure. Consequently, these modifications enhance the material's strength while preserving its excellent conductivity [37, 131].

Figure 3-15 summarizes the REE impact on the mechanical and electrical properties of Al alloys containing Sc and/or Zr. For Al-Zr based alloys, Sc remains more effective at increasing the hardness compared to REEs. At lower aging temperatures, some REEs like Er can form Al_3M (L12) structures more quickly than Sc or Zr, leading to a higher hardness compared to Sc-containing Al-Zr alloys (e.g., P5 in Figure 3-15). However, at higher aging temperatures (above 350°C), the strength of Al-Zr alloys with Sc surpasses that of those containing REEs [28, 109].

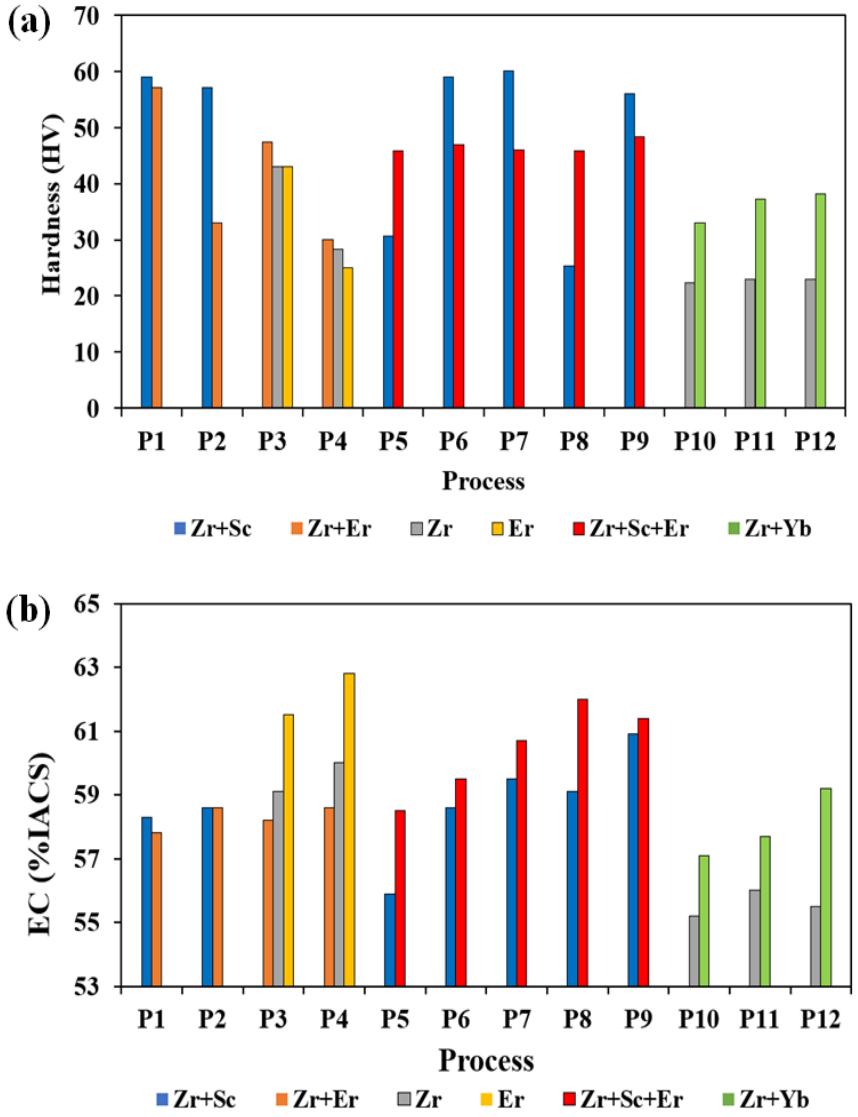

Figure 3-15. (a) Hardness and (b) EC variations for Zr- and Sc-containing 1xxx Al conductor alloys with the addition of rare earth elements (REEs), subjected to different thermomechanical treatments. Each process corresponds to a distinct set of thermomechanical sequence, **as detailed in Table** 3-2.

Table 3-2. Summary of processing conditions and alloy compositions for each treatment route represented in **Figure** 3-15**.**

Process designation	Nominal alloy composition	Summary of process steps	Ref.
P1	0.2Zr, 0.1Sc, 0.1Er wt.%	Homo (620 °C/48 h), HE, CD, Isothermal aging 400 °C/8 h	[109]
P2	0.2Zr, 0.1Sc, 0.1Er wt.%	Homo (620 °C/48 h), HE, CD, Isothermal aging 400 °C/36 h	[109]
P3	0.2Zr, 0.2Er wt.%	Homo (600 °C/20 h), HR, CD, Isothermal aging at 300 °C/1h	[131]
P4	0.2Zr, 0.2Er wt.%	Homo (600 °C/20 h), HR, CD, Isothermal aging at 350 °C/1h	[131]
P5	0.20Zr, 0.08Sc, 0.06Er wt.%	Homo (640 °C/72 h), Isochronal aging at 25-300 °C	[28]
P6	0.20Zr, 0.08Sc, 0.06Er wt.%	Homo (640 °C/72 h), Isochronal aging at 25-350 °C	[28]
P7	0.20Zr, 0.08Sc, 0.06Er wt.%	Homo (640 °C/72 h), Isochronal aging at 25-450 °C	[28]
P8	0.20Zr, 0.08Sc, 0.06Er wt.%	Homo (640 °C/72 h), Isothermal aging at 450 °C/24 h	[28]
P9	0.20Zr, 0.08Sc, 0.06Er wt.%	Homo (640 °C/72 h), Isothermal two step aging 300 °C/24 h and 400 °C/24 h	[28]
P10	0.27Zr, 0.10Y wt.%	Homo (620 °C/ 50 h), Isochronal aging at 50-225 °C	[27]
P11	0.27Zr, 0.10Y wt.%	Homo (620 °C/50 h), Isochronal aging at 50-325 °C	[27]
P12	0.27Zr, 0.10Y wt.%	Homo (620 °C/50 h), Isochronal aging at 50-475 °C	[27]
HR: Hot rolling, ST: Solution heat treatment, AG: aging, CD: cold wire drawing, O: Annealing, Homo: Homogenization, HE: hot extrusion			

Zhang et al. [109] conducted a comparative analysis of the effects of Sc and Er additions on the microstructure and performance of Al-0.2Zr-based cables fabricated through extrusion and cold drawing. In the Al-0.2Zr (wt%) alloy, Al_3Zr precipitates were unevenly distributed. In contrast, Al_3(Zr,Sc) and Al_3(Zr,Er) precipitates in the Al-0.2Zr-0.1Sc and Al-0.2Zr-0.1Er (wt.%) alloys were uniformly distributed, effectively inhibiting dislocation movement through the Zener pinning effect and significantly enhancing mechanical strength [134]. The effectiveness of the precipitates in their pinning effect and ability to impede recrystallization follows the order: Al_3(Zr, Sc) > Al_3(Zr, Er) > Al_3Zr [109, 135]. Additionally, Al-0.2Zr-0.1Sc exhibited better EC than Al-0.2Zr-0.1Er (wt.%) at long annealing times due to the ability of Sc to inhibit recrystallization, resulting in fewer grain boundaries and reduced electron scattering, as shown in Figure 3-16 [109]. Similar results for a lower peak hardness of a

quaternary Al-0.06Zr-0.05Sc-0.01Er (at.%) alloy compared with a ternary Al-0.06Zr-0.06Sc (at.%) alloy following isochronal aging were reported by Booth-Morrison et al. [28]. The decrease in strength when partially substituting Er for Sc is attributed to the solute consumption by Al_3Er primary precipitates during solidification and homogenization, which reduces the available solute for strengthening the matrix [136].

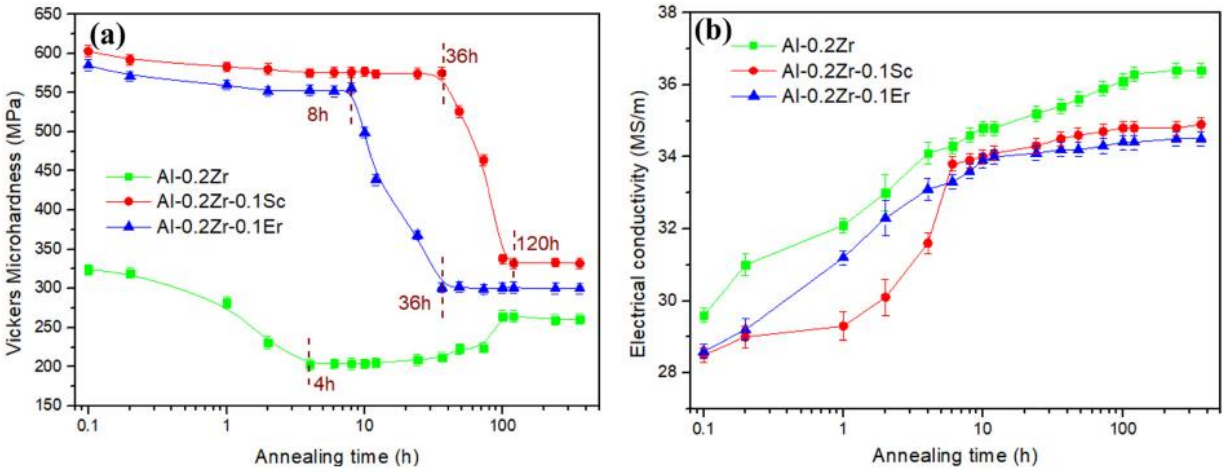

Figure 3-16. Variation in (a) Vickers microhardness (MPa) and (b) electrical conductivity of Al-0.2Zr, Al-0.2Zr-0.1Sc, and Al-0.2Zr-0.1Er (wt.%) cables with annealing time at a constant temperature of 400 °C [109]. With permission from Elsevier.

As shown in Figure 3-17, replacing 0.01 and 0.02 at.% Er with 0.01 and 0.02 at.% Sc in the Al-0.06Zr-Sc-Er (at.%) system leads to a 10-15% increase in hardness. However, the Er enhances the early-stage aging kinetics and lowers the onset temperature for precipitation during aging, shifting it from 300°C to 200°C [28]. The addition of Er to Al-0.06Zr-0.06Sc (at%) alloys alters the kinetic pathways governing phase precipitation, accelerating the nanoscale precipitation process [137]. The higher diffusivity of Er compared to Sc results in a lower nucleation free energy and higher interfacial energy, leading to shorter nucleation times and precipitation at lower temperatures [118, 136]. As shown in Figure 3-18 (a), the concentration profiles across the matrix/precipitate interface reveal that in the Al–0.06Zr–0.06Sc (at%) alloy, the precipitates have a Sc-enriched core surrounded by a Zr-enriched shell. In contrast, in the Al–0.06Zr–0.04Sc–0.02Er (at%) alloy, the $L1_2$-structure precipitates exhibit an Er-enriched core, a Sc-enriched inner shell, and a Zr-enriched outer shell, as shown in Figure 3-18 (b). This core/double-shell structure forms during aging as the solute elements precipitate sequentially according to their diffusivities ($D_{Er} > D_{Sc} > D_{Zr}$) [28]. The layered structure helps prevent particle coarsening, ensuring stable precipitates even under prolonged

thermal exposure [138]. The stability of the core/double-shell structure is determined by thermodynamics, specifically the total interfacial energy between the core, shells and matrix. Mao et al. [35] have shown that the total interfacial energy of the Al–Zr–Sc–Er system is minimized by the formation of the core/double shell structure. The interfacial energies of α-Al/Al_3Zr ($L1_2$), α-Al/Al_3Sc ($L1_2$), and α-Al/Al_3Er ($L1_2$) are 128 mJ/m^2, 171 mJ/m^2, and 312 mJ/m^2, respectively. Consequently, the outer shell is enriched in Zr. The inner shell is enriched in Sc because Al_3Zr ($L1_2$)/Al_3Sc ($L1_2$) has a lower interfacial energy of 115 mJ/m^2 compared to 234 mJ/m^2 for Al_3Zr ($L1_2$)/Al_3Er ($L1_2$) [35].

Based on the microhardness results in Figure 3-17, the three alloys exhibit a double-peak age-hardening behavior during isochronal aging at 300–350°C and 450°C. Al_3Sc/Al_3(Sc,Er) precipitates first at lower temperatures (between 325-350°C), contributing to the initial hardness peak. Subsequently, at higher temperatures (above 400°C), the precipitation of Al_3Zr or Al_3(Sc,Zr) occurs, resulting in a second hardness increase [131, 139]. The maximum EC for each alloy is achieved at a temperature near the second microhardness peak, where Zr atoms come out of the matrix, leading to an increase in EC.

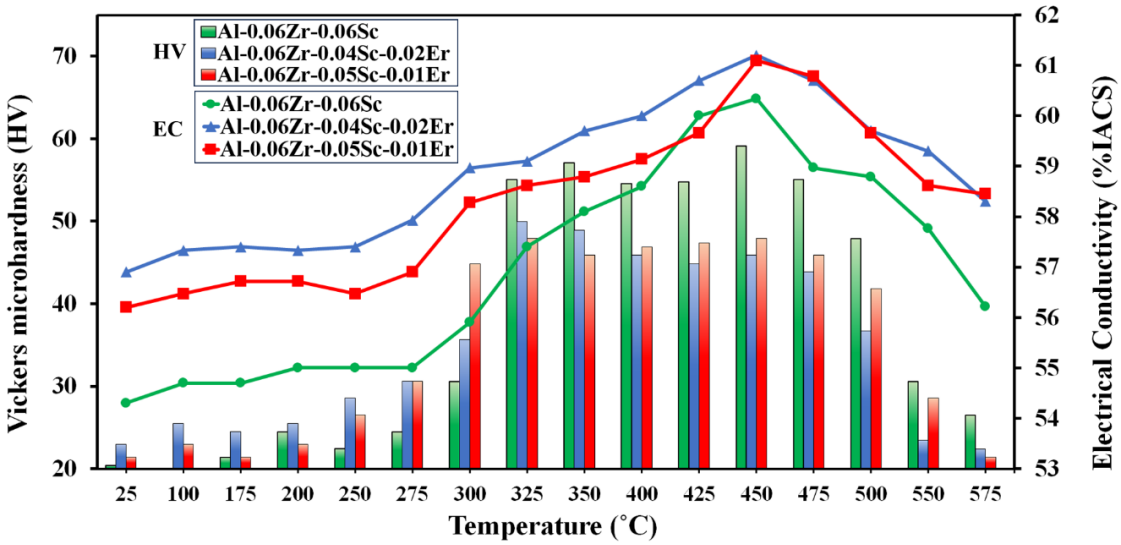

Figure 3-17. Evolution of Vickers microhardness and EC during isochronal aging with 3-hour steps at each successive 25°C temperature increment, for Al-0.06Zr (at.%) alloys with various Sc and Er contents [28].

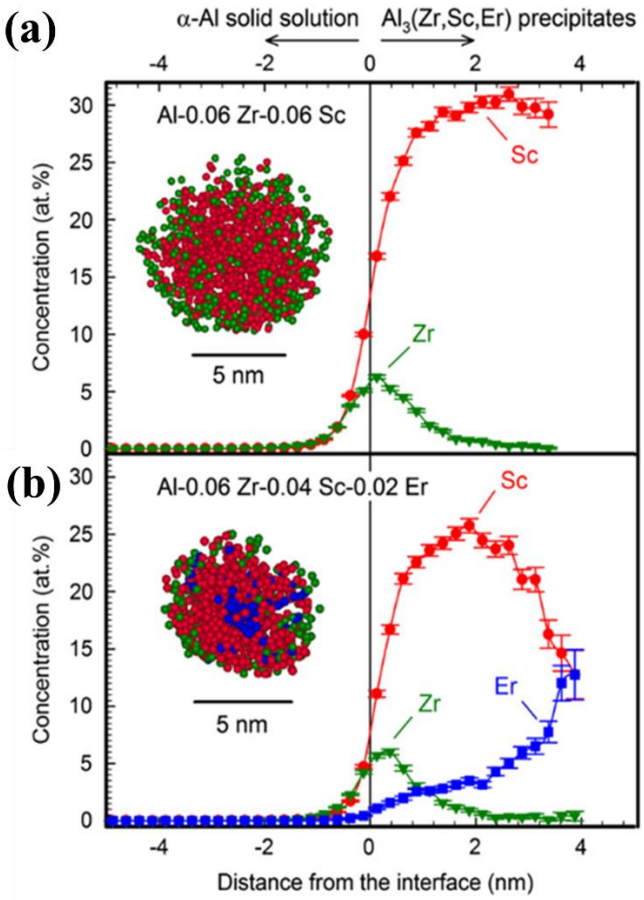

Figure 3-18. Atomic concentration profiles across the matrix/precipitate interface following isochronal aging up to 450 °C for (a) Al–0.06Zr–0.06Sc (at%), and (b) Al–0.06Zr–0.04Sc–0.02Er (at%) [28]. With permission from Elsevier.

In the context of the role of Er on the thermal stability of 1xxx conductor alloys, Kong et al. [131] demonstrated that the use of Zr (alloy A2) is more effective than Er (alloy A3) in restraining softening, as shown in Figure 3-19 (a). However, the combined addition of Zr and Er (alloy A4) provides a more pronounced effect on thermal stability compared to their individual additions. Furthermore, as illustrated in Figure 3-19 (b), the effect of Er on EC is slight, whereas Zr has a more detrimental impact, reducing EC by 2.5–4% IACS compared to Zr-free alloys. This gap is attributed to the differing maximum solid solubilities of Zr (0.27 wt.%) and Er (near zero) in α-Al [23, 131]. Consequently, more Zr than Er will remain in solid solution, causing lattice distortion and increased electron scattering, which lowers the EC [131]. Similarly, Zhang et al. [27] found that Yb, as a REE, enhances the synergistic effect of the Al–Zr system in improving the hardness. Their study revealed significant precipitation strengthening in the Al–Zr–Yb alloy system compared to the Al–Yb and Al–Zr

systems during isochronal aging between 100 °C and 550 °C [27]. Overall, it can be concluded that while REEs alone may not significantly strengthen Al alloys, their combination with Zr and/or Sc can be highly effective for strengthening. REEs contribute to a higher number density of precipitates at lower temperatures, while Zr helps prevent precipitate coarsening and enhances thermal stability.

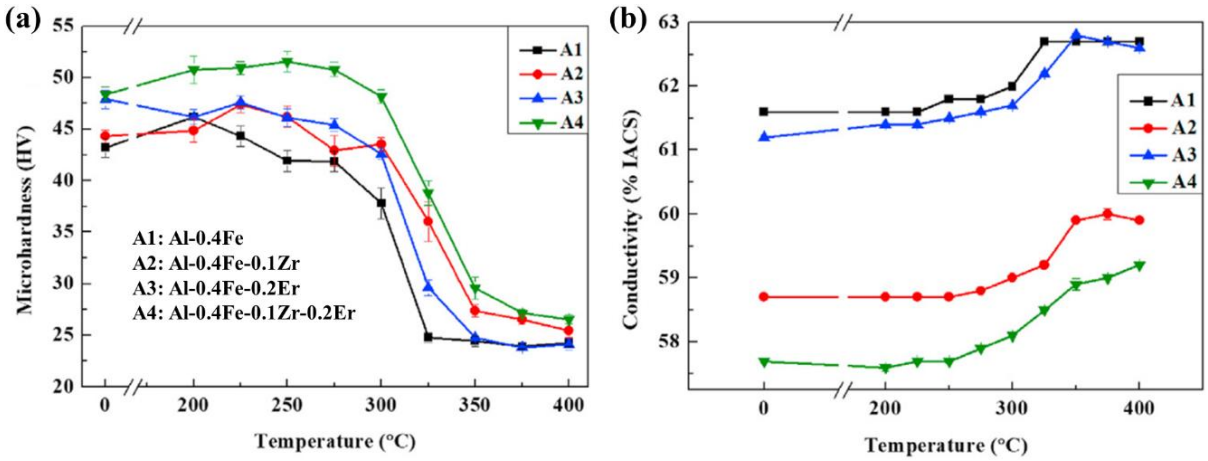

Figure 3-19. The microhardness (a) and EC (b) variations of cold-rolled alloys after annealing for 1 h, with compositions shown in wt% [131]. With permission from Elsevier. With permission from Elsevier.

Other REEs, including yttrium (Y), cerium (Ce), and lanthanum (La), have been widely studied for their effects on Zr- and Sc-containing Al conductor alloys [36, 131, 140-143]. Ce and Y can effectively improve the EC of Sc- and Zr-containing Al conductor alloys by decreasing Fe and Si impurities in the matrix. During solidification, these elements promote the precipitation of Fe, Si, and other impurities as micron-scale secondary phases [142] such as AlFeCe(Y) intermetallics. At the nanoscale, the main second phases are $Al_{11}Ce_3$ and Al_3Y, with lattice mismatches of 4.43% and 0.85%, respectively, relative to α-Al. These nanoscale precipitates are more likely to form within the α-Al matrix during solid-state aging, contributing to precipitation hardening. The precipitation of these second phases significantly reduces the negative impact of solute atoms on EC. Additionally, the good lattice compatibility of $Al_{11}Ce_3$ and Al_3Y with α-Al further enhances the EC of the alloy [142, 144].

For 6xxx conductor alloys, Yuan [145] reported that while the addition of La to Al–Mg–Si–Zr alloys based on AA6201 does not improve the tensile strength, it enhances the thermal

resistance and EC of the alloy. The addition of 0.22 wt.% La has been validated as a beneficial approach for manufacturing thermally-resistant aluminum alloy conductors [145]. The addition of La to Al–Mg–Si alloys may lead to hardness loss due to the formation of La-Si compounds, which reduces the precipitation of Si particles and Mg-Si hardening precipitates. However, La also promotes the formation of the thermally stable AlLaSi compound, which helps to resist further hardness loss. Research indicates that La can also lead to the formation of a new nonstoichiometric intermetallic phase, $La(Al,Si)_2$, which consumes Si and reduces the Si/Fe ratio in the remaining melt, thereby favoring the formation of α-AlFeSi. Despite a 15 MPa decrease in tensile strength (from 280 MPa to 265 MPa) with the 0.22 wt% La addition, it is nevertheless beneficial for improving the thermal-resistance [145-147].

To address the trade-off between strength and EC in Al alloy conductors, Wang et al. [36] explored Al-Ce-Sc, Al-Ce-Zr, and Al-Ce-Sc-Y alloys produced through die casting, hot extrusion, and cold drawing. The Al-0.2Ce-0.2Sc-0.1Y (wt.%) alloy demonstrated the best overall performance, as shown in Table *3-3*. The Al-Ce-Sc alloy exhibited a higher hardness and ultimate tensile strength compared to the Al-Ce-Zr alloy due to the greater number density of Al_3Sc precipitates relative to Al_3Zr precipitates. Furthermore, it was shown that for the Al-0.2Ce-0.2Sc-0.1Y alloy, the Fe containing intermetallic particles (specifically $Al_{13}Fe_3Ce$) remove more Fe and Si atoms from the Al matrix [143]. Compared to the other alloys, the addition of Y to the Al-0.2Ce-0.2Sc alloy further enhances the EC by minimizing cold drawing defects such as dislocations, stacking faults, and subgrain boundaries. In this alloy system, Y atoms surround the Al_3Sc precipitates, contributing to these improvements [36].

Table 3-3. Mechanical properties and EC values of the alloys after cold drawing and annealing [36].

Alloy (wt.%)	Hardness (HV)	UTS (MPa)	EC (% IACS)
Al-0.2Ce-0.12Zr	42.5 ± 0.5	157 ± 2	58.51 ± 0.11
Al-0.2Ce-0.2Sc	58.6 ± 0.8	188 ± 2	60.71 ± 0.16
Al-0.2Ce-0.2Sc-0.1Y	58.3 ± 0.6	198 ± 2	61.77 ± 0.11

3.4. Recent progress in thermomechanical processing of Sc and Zr containing Al conductor alloys

3.4.1. Strengthening approaches for 1xxx alloys

Based on previous studies on various 1xxx Al conductor alloy systems containing Zr, Sc, and REEs, either individually or in combination, the temperature ranges for achieving optimum hardness and EC have been provided in Figure 3-20. Isochronal studies, which monitored microhardness and EC during precipitation in Al-Zr, Al-Sc, Al-Sc-Zr, Al-Zr-Yb, and Al-Sc-Zr-Er systems, were used to identify these temperature ranges. As shown in Figure 3-20 (a), the maximum hardness for Al-Zr alloys occurs in the 425-475 °C range, while the nucleation and growth of precipitates in Al-Sc alloys occur at significantly lower temperatures (300-350 °C). In ternary Al-Sc-Zr systems, the peak hardness temperature typically falls between 375 and 425 °C, aligning between the ranges of the individual Al-Zr and Al-Sc systems. For quaternary Al-Sc-Zr-Er systems, the peak hardness temperature is closer to that of the Al-Sc system, occurring within the 325-375 °C range. In contrast, for the Al-Zr-Yb system, the maximum hardness is observed at a higher temperature range, between 450 and 500 °C, making it the highest temperature range for peak hardness among these systems. It is worthwhile to note that the aging temperature also depends on the Zr and Sc solute atom concentrations and the presence of other alloying elements besides the Zr and Sc. In general, nucleation kinetics are accelerated in the more concentrated alloys because the larger supersaturation decreases the effective diffusion distances and increases the thermodynamic chemical driving force [23, 75, 109].

By comparing the temperature ranges for achieving maximum hardness and EC in Figure 3-20, it is clear that the temperatures required for peak EC in a given alloy system are typically higher than those for peak hardness. This suggests that, as the temperature increases, precipitate coarsening leads to a reduction in strength while solute atoms continue to be removed from the matrix. To achieve a promising balance between hardness and EC, an optimum temperature must therefore be chosen to prevent excessive coarsening, which lowers the hardness, while also avoiding temperatures that are too low. Low temperatures are not effective in sufficiently precipitating solute atoms (such as Zr, Sc, and REEs), which leads to lower EC due to their presence in solid solution. As shown in Figure 3-20 (b), the peak EC range for Al-Zr and Al-Zr-Er systems is broader and shifted to higher temperatures

compared to their peak hardness. The Al-Zr-Yb system achieves its maximum EC between 475°C and 525°C, while the Al-Sc system has the lowest range, between 375°C and 425°C.

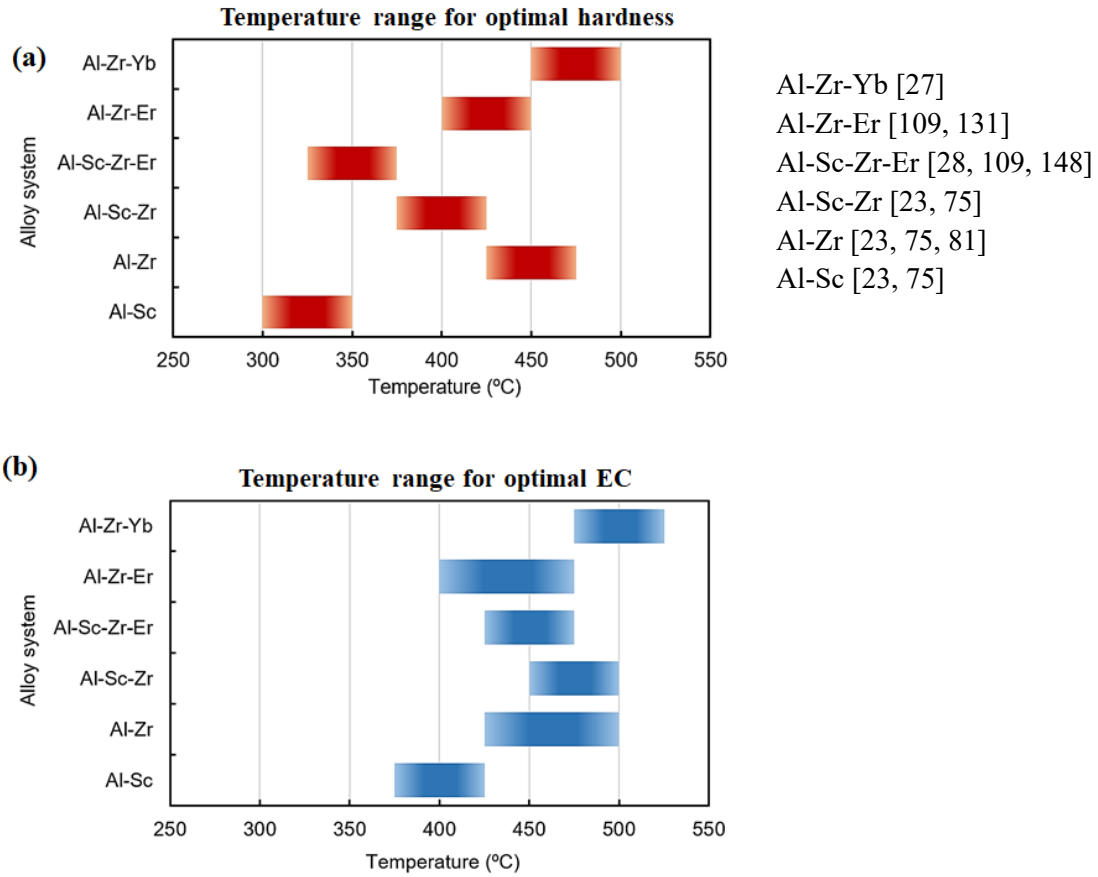

Figure 3-20. The temperature ranges for achieving optimum (a) hardness and (b) EC in 1xxx Al conductor alloys containing Sc and Zr.

The thermomechanical processing sequence for 1xxx conductor alloys containing Sc and Zr, including aging and cold wire drawing, could influence both mechanical and electrical properties. Shao et al. [15] performed thermomechanical processing on Al-Sc-Zr conductor alloys, which included hot rolling, solution heat treatment, aging, and cold wire drawing. As shown in Figure 3-21, in route 1, the aging treatment preceded the wire drawing, whereas in route 2, the aging process was conducted after the cold wire drawing. In route 1, the increase in hardness from the aging process, which occurred via precipitation hardening from the $Al_3(Sc,Zr)$ precipitates, was significantly higher than that from the strain hardening of the cold wire drawing. In route 2, a lower microhardness was observed compared to that achieved after aging in route 1 [15]. Furthermore, in terms of EC, route 2 shows an increase of ~1% IACS compared to route 1. Similar results have been reported by Liu et al. [2] when

evaluating the effective strengthening mechanisms for Al-0.06Sc-0.3Zr (wt.%). As depicted in Figure 3-22, after solution treatment, the samples were exposed to the following conditions: (1) cold drawing + two-stage ageing (CD-A); (2) two-stage ageing + cold drawing (A-CD). Although the tensile strength of A-CD is slightly higher than that of CD-A, the EC is about 3.5% IACS lower [2].

Aging temperatures for Sc and Zr are high (300-400°C), so when aging follows cold drawing, most dislocations introduced during cold drawing are recovered, making dislocation strengthening negligible. The high strength of these alloys is then mainly due to enhanced precipitation strengthening from fine Al_3(Sc,Zr) precipitates. On the other hand, for alloys aged before cold drawing, both precipitation strengthening and dislocation strengthening from post-deformation contribute significantly to the overall strength. The lower EC of alloys cold-worked after aging is due to the high density of dislocations and vacancies introduced during cold drawing, which significantly reduce the EC by increasing electron scattering. Al_3(Sc,Zr) precipitates are coherent with the matrix and have a negligible effect on resistivity [14, 94]. When aging is the final step, the precipitation of Sc and Zr atoms alleviates lattice distortion, reducing the resistivity caused by solute atoms. Additionally, most dislocations are recovered, and fine recrystallized grains form during aging, mitigating the impact of dislocations on EC. For example, route 1 in Figure 3-21 (cold drawing after aging) results in 6% recrystallization, whereas route 2 (aging after cold drawing) leads to 12% recrystallization. Accordingly, the wire materials in route 1 exhibited a higher fraction of deformed structure with high induced dislocations compared to route 2 [15].

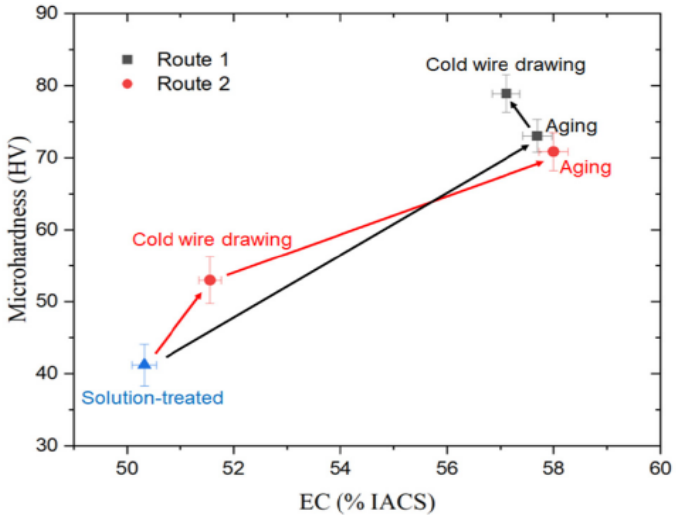

Figure 3-21. Evolution of the microhardness and EC of an Al-0.1Sc-0.1Zr (wt.%) alloy during thermomechanical processing in Route1 and Route 2 [15]. With permission from Elsevier.

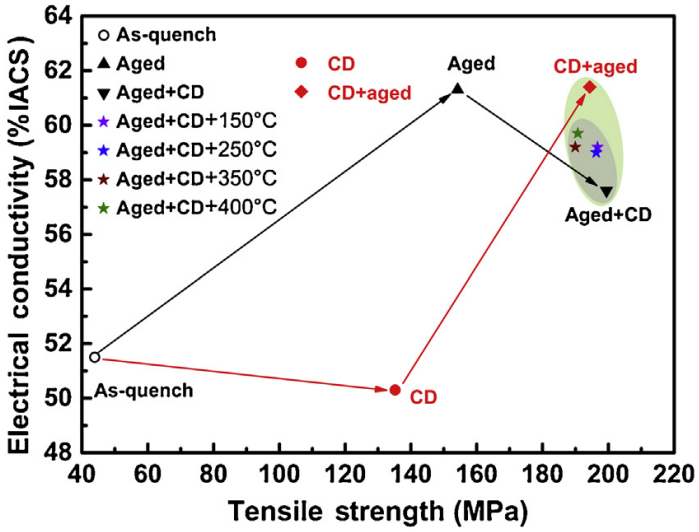

Figure 3-22. Electrical conductivity of Al-0.06Sc-0.23Zr (wt.%) under various processes plotted vs. their corresponding ultimate tensile strengths [2]. With permission from Elsevier.

One of the effective techniques introduced for enhancing the strength and thermal stability of Al-Sc-Zr systems is two-stage aging [149]. During the first stage, Sc-rich precipitates (Al_3Sc) form, contributing to initial strengthening at around 300°C, while Zr remains in solution within the α-Al matrix due to its reduced mobility. In the second stage at a higher temperature, Zr-rich precipitates form around the Sc-rich core, creating a core-shell structure, as presented in Figure 3-6 [28, 150, 151]. This Zr-rich shell, with its reduced lattice parameter mismatch to the Al matrix, improves the thermal stability by acting as a diffusion barrier, preventing the coarsening of the precipitates, which maintains the strength of alloy at higher

temperatures [17, 152]. Figure 3-23 illustrates the hardness and EC of ternary Al-Sc-Zr and quaternary Al-Sc-Zr-Er alloys after both one-stage and two-stage aging. The results indicate that two-stage aging offers a promising compromise between hardness and EC compared to one-stage aging. During the first stage of aging, elements with higher diffusivity, such as Sc and Er, form nanoscale precipitates that act as heterogeneous nucleation sites for the less mobile Zr atoms. The second stage, typically around 400°C, results in spheroidal core/shell precipitates with Zr-enriched outer shells [2, 121, 153]. The two-stage ageing therefore tends to result not only in higher strength, but also in higher EC.

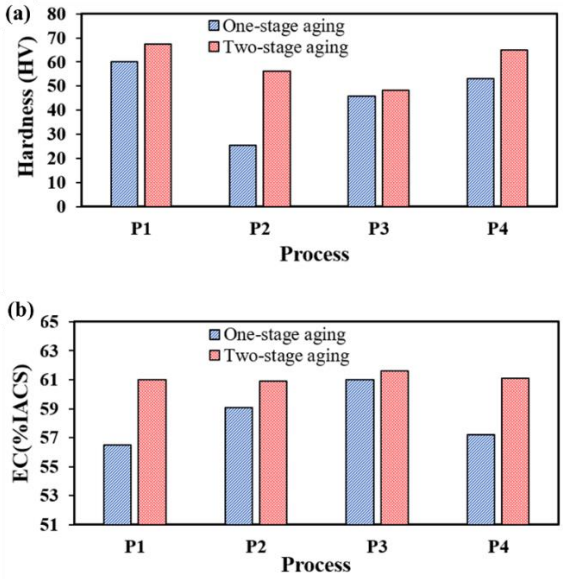

P1 [2]

Al-0.06Sc-0.23 Zr (wt.%)
One stage aging: 300 °C/50 h
Two stage aging: 300 °C/25h, 400 °C/50 h

P2 [28]

Al-0.2Zr-0.1Sc (wt.%)
One stage aging: 400 °C/24 h
Two step aging: 300 °C/24h, 400 °C/24h

P3 [28]

Al-0.2Zr-0.1Sc-0.06Er (wt.%)
One stage aging: 400 °C/24 h
Two step aging: 300 °C/24h, 400 °C/24h

P4 [154]

Al-0.2Zr-0.06Sc (wt.%)
One stage aging: 250 °C/24 h
Two stage aging: 250 °C/24h, 400 °C/48 h

SHT: Solution heat treatment,
Homo: Homogenization

Figure 3-23. Comparison of (a) hardness and (b) EC in Sc- and Zr-containing 1xxx aluminum conductor alloys subjected to one-stage and two-stage aging treatments.

As shown in Figure 3-24 (a), after one-stage aging at 300°C for 25 hours, Sc atoms segregate from the Al matrix into precipitates, forming Al_3Sc. Figure 3-24 (b) indicates that the Zr concentration in the precipitates remains nearly zero during this stage, while the Al and Sc concentrations in the precipitates are about 75 and 25 at%, respectively, as expected from the Al_3Sc stoichiometry. After the second aging step at 400°C for 50 hours, Sc and Zr segregation

becomes evident, as depicted in Figure 3-24 (c). The Sc concentrates in the precipitate cores, while the Zr forms a Zr-rich shell around them, as confirmed by the 3DAP analysis in Figure 3-24 (d) [2]. Similarly, Yang et al. [153] reported comparable structures following a two-stage heat treatment, showing atomic concentration variations between the matrix and precipitates. EDS mapping and line scan analysis, as illustrated in Figure 3-25, further validated this phenomenon [153].

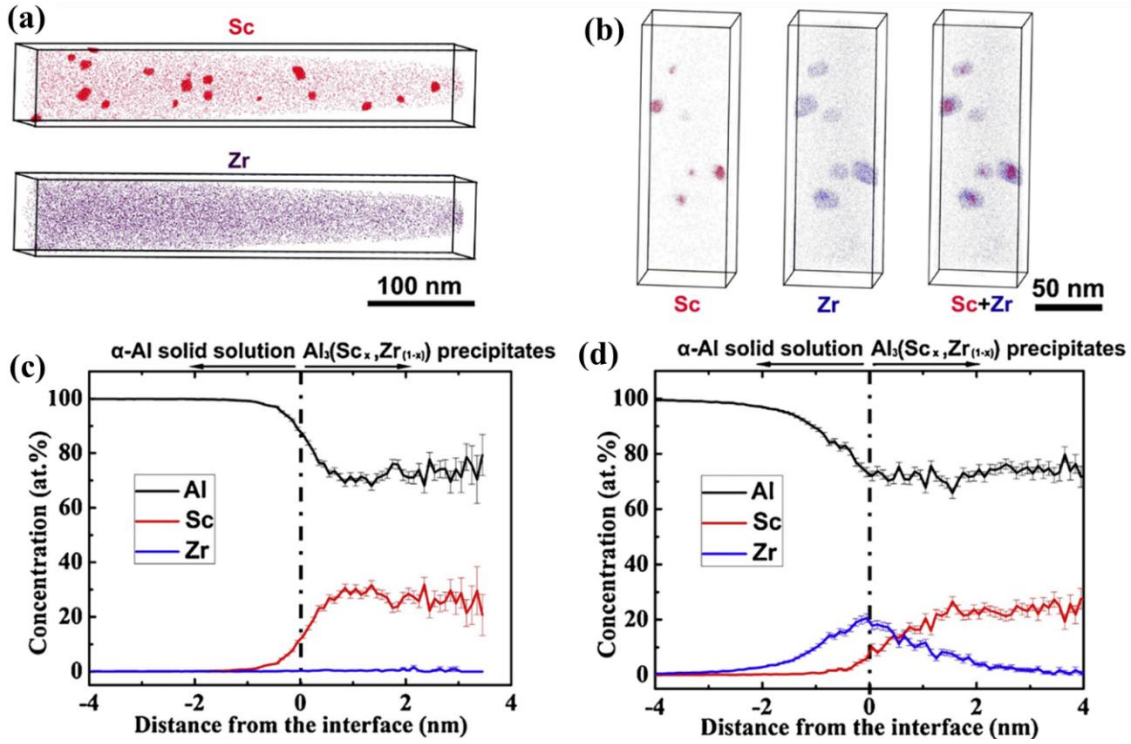

Figure 3-24. Three-dimensional atom probe reconstructions of Al-0.06Sc-0.23Zr (wt.%) and proxigrams showing the concentration profiles of Al, Sc, and Zr in $Al_3(Sc,Zr)$ precipitates (a) and (b) after ageing at 300°C for 25 h, and (c) and (d) after two-stage ageing (300°C/25 h + 400°C/50 h) [2]. With permission from Elsevier.

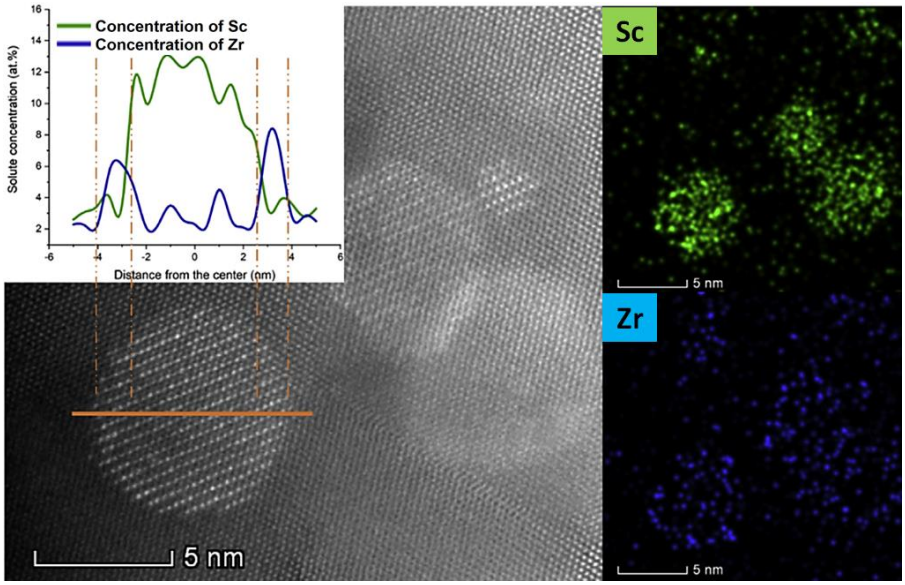

Figure 3-25. HAADF-STEM image of precipitates and EDS maps showing the distribution of Sc and Zr after aging at 350 °C for 5 hours followed by 400 °C for 5 hours [153]. With permission from Elsevier.

3.4.2. Multi-step heat treatment strategies for strengthening of 6xxx alloys containing Zr and Sc

Conflicting reports exist in the literature regarding the ability of Sc and Zr to enhance strength through the formation of Sc and Zr precipitates in Al–Mg–Si alloys. This is because in Al-Mg-Si-Zr-Sc alloy systems, managing the solution and aging temperature and time to obtain the benefits of both Zr/Sc and Mg-Si precipitates (β″ and β′) is complicated [155, 156]. Several thermomechanical processes have been proposed in the literature to optimize the strength of Al-Mg-Si alloys containing Sc and/or Zr, as summarized in Table 3-4. The formation of strengthening precipitates occurs at two distinct temperature stages. The Sc and/or Zr strengthening precipitates form at higher temperatures (300°C-400°C), whereas the Mg-Si strengthening precipitates emerge at around 170°C-200°C. Therefore, the aging temperature range for Sc/Zr precipitates causes over-aging for the Mg-Si precipitates [38, 121, 145].

In general, a heat treatment stage should be applied either before or after the hot rolling or extrusion process to promote the precipitation of Sc and Zr [38]. The timing of this stage, whether before or after hot deformation, depends on the deformation temperature and on the alloy composition. If the deformation temperature is too high relative to the solvus, Sc and Zr precipitates may coarsen or dissolve, reducing their strengthening effect. In this case, the

heat treatment for forming Sc and Zr precipitates should be applied after deformation. The process design should account for the coarsening onset temperature of Sc and Zr, which is typically above 350°C, depending on the composition. However, for Al-Mg-Si-Zr systems, this temperature can exceed 450°C due to the higher thermal stability of Zr precipitates. It is worth noting that in some studies, the promotion of Zr and/or Sc precipitates is considered during the hot deformation step, without a separate heat treatment specifically for their formation [157, 158]. This approach requires precise control of the deformation temperature due to the short time available for precipitate formation.

Table 3-4. Summary of prior studies on Sc- and Zr-containing 6xxx alloys, including their proposed thermomechanical processing treatments

Alloy system (wt.%)	**Process Sequence**	**Ref.**
Al-1.4Mg-0.5Si-0.2Sc	Homogenization: 500°C for 10 h, Hot Rolling, Cold Drawing, Solution Treatment: 565°C for 0.5 h, Aging: 180°C for 100 h	[158]
Al-0.5Mg-0.5Si-0.05Sc-0.1Zr	Homogenization: 575°C for 5 h, Aging: 300°C for 3 h - 450°C for 3 h, 500°C for 0.5 h, Hot Extrusion, Aging: 175°C for 8 h	[121]
Al-0.5Mg-0.5Si-0.05Sc-0.1Zr	Aging: 300°C for 3 h - 450°C for 3 h, Hot Extrusion, Aging: 175°C for 8 h	[121]
Al-0.85Mg-0.6Si-0.3Sc-0.14Zr	Homogenization: 540°C for 24 h, Hot Rolling, Aging: 400°C, Cold Drawing, Solution Treatment: 535°C for 1 h, Aging: 190°C	[159]
Al-0.6Mg-0.5Si-0.2Zr	Homogenization: 530°C for 14 h, Hot Extrusion: 460°C, Cold Drawing, Aging: 200°C	[157]
Al-0.67Mg-0.67Si-0.5Cu-0.08Sc-0.08Zr	Homogenization: 350°C for 48 h, Hot Rolling at 300–375 ◦C, Solution Treatment: 500°C & 530°C for 15 min, Aging: 180°C for 8 h	[155]

Next, the focus shifts to the formation of Mg-Si strengthening precipitates (β″ and β′). This requires a brief solutionizing step at 475 °C to 550 °C to dissolve as much of the Mg_2Si phases as possible, thereby achieving a properly supersaturated solid solution (SSSS) [25, 38, 158]. The wider range observed here is due to the dependence of the solvus temperature of Mg_2Si on the Mg and Si content. For instance, Figure 3-26 illustrates the phase diagram of the Al-Mg-Si alloy system, calculated using Thermo-Calc^{TM} with the TCAL7 database, for a fixed Si content of 0.65 wt.% while varying the Mg content. As shown, decreasing the Mg content results in a decrease in the solvus temperature, meaning that a lower temperature is required for solutioning. For example, when the Mg content is 0.6 wt.%, the solvus

temperature is ~510°C, while at 0.3 wt.%, the solvus temperature drops to around 450°C. The time and temperature of the solutionizing step are critical, as prolonged solutionizing can adversely affect the strengthening effect of pre-existing Zr and Sc precipitates by coarsening. Therefore, extended solutionizing should be avoided (unless the intention is to use a higher temperature to also place the Sc and Zr in solution). The final step involves low-temperature aging to form Mg-Si strengthening precipitates. Figure *3-27* illustrates the proper temperature ranges for each step in the thermomechanical process along with recommended processing sequence to achieve a well-balanced compromise between EC and strength in Al-Mg-Si alloys containing Sc and Zr. This is a general practical guide and does not include wire drawing steps. For wire conductors, the wire drawing process is added either before or after the final low-temperature aging. Homogenization is not recommended in some studies for Zr-containing alloys as it can prematurely nucleate coarse Al_3Zr precipitates, diminishing the effectiveness of precipitation hardening during subsequent aging [23, 75, 81]. This will of course depend on the homogenization temperature with respect to the Al_3Zr solvus. However, in general, homogenization treatments are beneficial as they also reduce segregation of Sc and other elements [23].

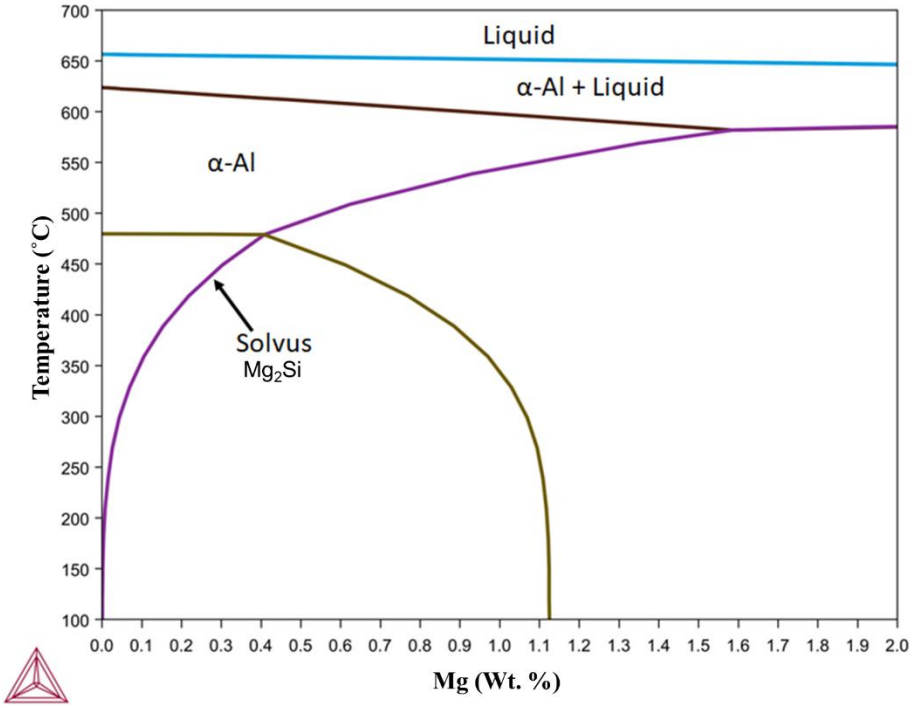

Figure 3-26. Phase diagram of an Al-Mg-Si alloy system with 0.65 wt.% Si and varying Mg content.

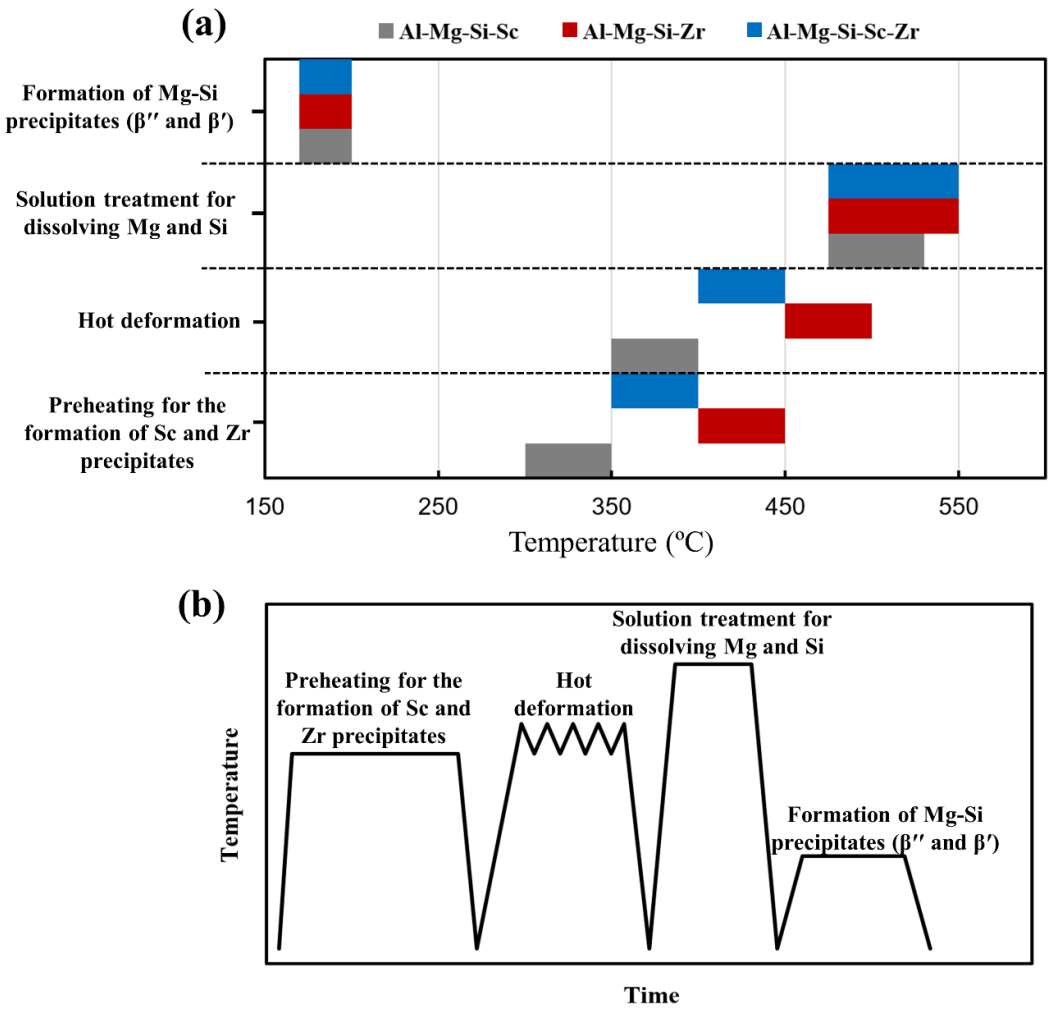

Figure 3-27. Key steps in the thermomechanical processing along with (a) optimal temperature ranges (b) recommended processing sequence to achieve a good compromise between EC and strength in Al-Mg-Si alloys containing Sc and/or Zr.

3.5. Future Perspectives for Aluminum Conductor Alloys

As the global energy demand continues to rise and sustainability becomes a primary concern, future advances in Al conductor alloys will focus on optimizing material performance while addressing cost and processing challenges. Power transmission networks require materials capable of withstanding higher currents and temperatures without significant degradation. The demand for conductors that operate at elevated temperatures (>150°C) without substantial loss of strength or EC is driving the development of next-generation thermally stable Al-Sc-Zr-based alloys. These alloys offer enhanced strength, EC, and thermal stability, making their development a significant advance in Al conductor technology.

One of the primary challenges in Al conductor alloys is balancing strength, EC, and cost. The high cost of Sc has pushed some research towards REE alternatives, which can partially replace Sc while maintaining comparable performance. Future studies will explore the effects of these elements on precipitation behavior, grain refinement, and thermal stability. Additionally, the further development of core-shell $Al_3(Sc,Zr)$ precipitates and their evolution in multi-element alloys (e.g., in the presence of other alloying elements like Cu) will be crucial. Advanced computational modeling and atomic-scale characterization techniques, such as atom probe tomography (APT) and high-resolution transmission electron microscopy (HRTEM), will play an instrumental role in understanding and optimizing these precipitate structures to maximize strength and stability.

The interaction between thermomechanical treatments and precipitation kinetics remains a critical research area. Current multi-step aging and deformation sequences have shown promise in improving the mechanical properties and EC. However, precise optimization of processing parameters is required to fully exploit the potential of alloying elements like Sc and Zr for given applications. Future work will focus on refining two-stage aging techniques to control precipitate distributions and minimize coarsening. Additionally, investigating new processing strategies such as severe plastic deformation (SPD) could enhance grain refinement and precipitation kinetics [160].

Another promising direction is the development of advanced composite materials that integrate Al-Sc-Zr-based alloys with high-performance reinforcements such as graphene, carbon nanotubes, or ceramics. These hybrid materials have the potential to significantly enhance the EC, mechanical strength, and thermal stability, making them ideal for next-generation conductor applications. Graphene and carbon nanotubes provide exceptional electrical and thermal conductivity, while ceramic reinforcements improve wear resistance and high-temperature performance. By optimizing processing techniques and interfacial bonding, researchers can unlock new possibilities for lightweight, high-performance conductors that meet the increasing demands of modern power transmission and electronic applications [161, 162].

The rapid advance of computational materials science and machine learning (ML) presents a promising direction for accelerating conductor alloy development. Future research will

leverage density functional theory (DFT) calculations and phase-field modeling to predict phase stability and precipitation kinetics [163]. Additionally, ML algorithms will be employed to analyze vast experimental datasets and optimize alloy compositions and processing conditions [164]. Integrated Computational Materials Engineering (ICME) approaches will streamline alloy design and manufacturing, providing deeper insights into structure-property relationships, mechanical responses, and multi-phase material behavior across different length scales [165]. ICME studies will be particularly useful for investigating the EC and thermodynamic stability in precipitation-strengthened ternary systems like Al-Sc-Zr.

One of the most powerful tools in this domain is computational thermodynamics (e.g. with tools such as Thermo-Calc™), which enables the prediction of composition- and temperature-dependent material properties. By employing thermodynamic and kinetic models, Thermo-Calc™ provides valuable insights into phase stability, phase transformations, and diffusion-controlled processes, significantly reducing the time and cost associated with traditional trial-and-error experimentation [166, 167].

Furthermore, optimizing hot deformation parameters, particularly deformation temperature and strain rate, is essential for Al alloys, including binary and ternary systems like Al-Sc and Al-Sc-Zr. This optimization helps prevent the formation of coarse precipitates during hot deformation. For this purpose, Gleeble™ thermal-mechanical simulation systems can be used for hot compression tests. These tests provide critical data for simulating hot deformation processes such as rolling and extrusion. Based on the results of hot compression tests, extrusion and rolling processes can be optimized to develop Al alloys with high EC and sufficient strength [6, 127, 168].

Briefly, the future of Al conductor alloys depends on refining compositions, processing, and integration into advanced power systems. Using materials science, computational modeling, and sustainable methods, researchers can develop high-performance, cost-effective, and eco-friendly alloys, enhancing energy efficiency and ensuring reliable modern electrical grids.

3.6. Summary

This review explores the effects of Sc and Zr microalloying on the mechanical properties, thermal stability, and electrical conductivity (EC) of Al conductor alloys, focusing on precipitation behavior across various alloy systems and thermomechanical processing routes.

Individual additions of Sc and Zr can result in $L1_2$-structured Al_3Sc and Al_3Zr precipitates in Al-Sc and Al-Zr alloys, respectively. In Al-Sc-Zr alloys, these elements can combine to form core-shell $Al_3(Sc_{1-x}Zr_x)$ precipitates, characterized by Sc-rich cores surrounded by Zr-enriched outer shells. This structure delays the metastable coherent $L1_2$ to equilibrium $D0_{23}$ phase transformation, enhances the resistance to coarsening, and increases the precipitate number density, thereby improving the strength at both ambient and elevated temperatures.

Al-Sc alloys exhibit higher peak strength compared to Al-Zr alloys at equivalent concentrations of these alloying elements. Al_3Sc precipitates optimally around 325 °C, while Al_3Zr forms near 450 °C, due to the higher diffusivity of Sc in Al. Ternary Al-Sc-Zr alloys have better performance compared to the binary systems, with peak strength achieved after aging at approximately 400 °C. The highest EC in the three alloy systems (Al-Sc, Al-Zr, and Al-Sc-Zr) is achieved at temperatures 50–100°C higher than the temperatures corresponding to peak strength.

While Sc is the most effective element for enhancing hardness, rare earth elements (REEs) like Er can provide a more cost-effective alternative by partially substituting Sc in Sc-containing Al conductor alloys. With the addition of REEs, the precipitation kinetics are accelerated, leading to the formation of coherent, spheroidal, $L1_2$-ordered precipitates with a distinct core-shell or double-shell structure. The core is enriched with Er, while a Sc-enriched inner shell and a Zr-enriched outer shell surround it.

Two-stage aging improves the strength and thermal stability of Al-Sc-Zr alloys. First, Sc-rich Al_3Sc precipitates form at ~300 °C with a high number density. Second, Zr-rich shells form at ~400 °C around the Al_3Sc precipitates, creating fine core-shell structures. These shells act as diffusion barriers, resisting coarsening and enhancing high-temperature performance.

6xxx conductor alloys containing Sc and Zr exhibit a complex precipitation sequence because $Al_3(Sc,Zr)$ precipitates form at 300°C-400°C, while Mg-Si precipitates (β″ and β′) form at 170°C-200°C. One possible processing route involves a heat treatment at 300°C-400°C for forming $Al_3(Sc,Zr)$ precipitates, followed by a short solution treatment at 520°C-550°C to dissolve Mg_2Si and then a low-temperature aging treatment at 175°C-200°C to promote the formation of Mg-Si strengthening precipitates. Another option is to keep as much solute in solution as possible before and during hot deformation, followed by appropriate quenching and aging.

3.7. References

[1] X. Li *et al.*, "Study on the improvement and mechanism of AA6101 electrical conductivity by trace TM (Zr, V, Ti) elements-assisted boron treatment," *Journal of Alloys and Compounds,* vol. 939, p. 168728, 2023.

[2] L. Liu, J.-T. Jiang, B. Zhang, W.-Z. Shao, and L. Zhen, "Enhancement of strength and electrical conductivity for a dilute Al-Sc-Zr alloy via heat treatments and cold drawing," *Journal of Materials Science & Technology,* vol. 35, no. 6, pp. 962–971, 2019.

[3] S. N. Khangholi, M. Javidani, A. Maltais, and X.-G. Chen, "Effects of natural aging and pre-aging on the strength and electrical conductivity in Al-Mg-Si AA6201 conductor alloys," *Materials Science and Engineering: A,* vol. 820, p. 141538, 2021.

[4] S. N. Khangholi, M. Javidani, A. Maltais, and X. G. Chen, "Review on recent progress in Al–Mg–Si 6xxx conductor alloys," *Journal of Materials Research,* vol. 37, no. 3, pp. 670–691, 2022.

[5] M. Yokota, "Aluminum alloy electric conductor wire," Patent Appl. Appl. 5/838,762, 1980.

[6] B. Abnar, S. N. Khangholi, P. Rometsch, and M. Javidani, "Effects of Cu Addition and Temperature on Hot Deformation Behavior of Al–Mg–Si 6201 Conductor Alloys," in *Conference of Metallurgists*, 2024: Springer, pp. 1649–1651.

[7] W. Yuan and Z. Liang, "Effect of Zr addition on properties of Al–Mg–Si aluminum alloy used for all aluminum alloy conductor," *Materials & Design,* vol. 32, no. 8-9, pp. 4195–4200, 2011.

[8] J. R. Davis, *Aluminum and aluminum alloys*. ASM international, 1993.

[9] H. McQueen, X. Xia, Y. Cui, B. Li, and Q. Meng, "Solution and precipitation effects on hot workability of 6201 alloy," *Materials Science and Engineering: A,* vol. 319, pp. 420–424, 2001.

[10] M. Khoshghadam-Pireyousefan, M. Javidani, A. Maltais, J. Lévesque, and X.-G. Chen, "Breaking the strength-conductivity paradigm in hypoeutectic Al–Si alloy via annealing-induced Si nanoprecipitation," *Materials Science and Engineering: A,* vol. 911, p. 146924, 2024.

[11] P. Rocha, S. Langlois, S. Lalonde, J. Araújo, and F. Castro, "Influence of 1350 and 6201 aluminum alloys on the fatigue life of overhead conductors—A finite element analysis," *Tribology International,* p. 108661, 2023.

[12] *ASTM B317/B317M: Standard Specification for Aluminum-Alloy Extruded Bar, Rod, Tube, Pipe, and Structural Profiles for Electrical Purposes (Bus Conductor)*, A. International, 2017.

[13] *ASTM B236: Standard Specification for Aluminum Bars for Electrical Purposes (Bus Bars)*, A. International, 2015.

[14] R. Guan, Y. Shen, Z. Zhao, and X. Wang, "A high-strength, ductile Al-0.35 Sc-0.2 Zr alloy with good electrical conductivity strengthened by coherent nanosized-precipitates," *Journal of Materials Science & Technology,* vol. 33, no. 3, pp. 215–223, 2017.
[15] Q. Shao, E. M. Elgallad, A. Maltais, and X.-G. Chen, "Development of thermal-resistant Al–Zr based conductor alloys via microalloying with Sc and manipulating thermomechanical processing," *Journal of Materials Research and Technology,* vol. 25, pp. 7528–7545, 2023.
[16] E. Elgallad, S. Khangholi, M. Javidani, A. Maltais, and X.-G. Chen, "Development of ultra-high-strength Al-Mg-Si conductor alloys with copper addition via scalable thermomechanical processes," *Scripta Materialia,* vol. 257, p. 116462, 2025.
[17] T. Dorin, S. Babaniaris, L. Jiang, A. Cassel, A. Eggeman, and J. Robson, "Precipitation sequence in Al-Sc-Zr alloys revisited," *Materialia,* vol. 26, p. 101608, 2022.
[18] K. Deane, S. Kampe, D. Swenson, and P. Sanders, "Precipitate evolution and strengthening in supersaturated rapidly solidified Al-Sc-Zr alloys," *Metallurgical and Materials Transactions A,* vol. 48, pp. 2030–2039, 2017.
[19] R.-Z. Chao *et al.*, "Effect of Zr and Sc on mechanical properties and electrical conductivities of Al wires," *Transactions of Nonferrous Metals Society of China,* vol. 24, no. 10, pp. 3164–3169, 2014.
[20] E. A. Marquis, D. N. Seidman, and D. C. Dunand, "Effect of Mg addition on the creep and yield behavior of an Al–Sc alloy," *Acta Materialia,* vol. 51, no. 16, pp. 4751–4760, 2003.
[21] C. B. Fuller, D. N. Seidman, and D. C. Dunand, "Mechanical properties of Al (Sc, Zr) alloys at ambient and elevated temperatures," *Acta materialia,* vol. 51, no. 16, pp. 4803–4814, 2003.
[22] O. Senkov, M. Shagiev, S. Senkova, and D. Miracle, "Precipitation of Al3 (Sc, Zr) particles in an Al–Zn–Mg–Cu–Sc–Zr alloy during conventional solution heat treatment and its effect on tensile properties," *Acta materialia,* vol. 56, no. 15, pp. 3723–3738, 2008.
[23] K. E. Knipling, R. A. Karnesky, C. P. Lee, D. C. Dunand, and D. N. Seidman, "Precipitation evolution in Al–0.1 Sc, Al–0.1 Zr and Al–0.1 Sc–0.1 Zr (at.%) alloys during isochronal aging," *Acta Materialia,* vol. 58, no. 15, pp. 5184–5195, 2010.
[24] F. Czerwinski, "Critical Assessment 36: Assessing differences between the use of cerium and scandium in aluminium alloying," *Materials Science and Technology,* vol. 36, no. 3, pp. 255–263, 2020.
[25] S. Babaniaris, M. Ramajayam, L. Jiang, T. Langan, and T. Dorin, "Developing an optimized homogenization process for Sc and Zr containing Al-Mg-Si alloys," in *Light Metals 2019*, 2019: Springer, pp. 1445–1453.
[26] Y.-C. Tzeng, C.-Y. Chung, and H.-C. Chien, "Effects of trace amounts of Zr and Sc on the recrystallization behavior and mechanical properties of Al-4.5 Zn-1.6 Mg alloys," *Materials Letters,* vol. 228, pp. 270–272, 2018.
[27] Y. Zhang *et al.*, "Precipitation evolution of Al–Zr–Yb alloys during isochronal aging," *Scripta Materialia,* vol. 69, no. 6, pp. 477–480, 2013.
[28] C. Booth-Morrison, D. C. Dunand, and D. N. Seidman, "Coarsening resistance at 400 C of precipitation-strengthened Al–Zr–Sc–Er alloys," *Acta Materialia,* vol. 59, no. 18, pp. 7029–7042, 2011.
[29] "Rare Earths Statistics and Information " The United States Geological Survey. https://www.usgs.gov/centers/national-minerals-information-center/rare-earths-statistics-and-information (accessed.
[30] "Rare earths." The Institute of Rare Earths and Metals https://en.institut-seltene-erden.de/rare-earths-and-metals/rare-earth/ (accessed.
[31] "Rare Earth Prices." Scrap Monster. https://www.scrapmonster.com/metal-prices/rare-earth (accessed.
[32] "Rare Earth Metals Price." SMM, The leading Metals information Provider. https://www.metal.com/Rare-Earth-Metals (accessed.

[33] H. U. Sverdrup and A. E. Sverdrup, "On the supply dynamics of scandium, global resources, production, oxide and metal price, a prospective modelling study using WORLD7," *Biophysical Economics and Sustainability,* vol. 9, no. 2, p. 2, 2024.
[34] A. Mochugovskiy and A. Mikhaylovskaya, "Comparison of precipitation kinetics and mechanical properties in Zr and Sc-bearing aluminum-based alloys," *Materials Letters,* vol. 275, p. 128096, 2020.
[35] Z. Mao, D. N. Seidman, and C. Wolverton, "First-principles phase stability, magnetic properties and solubility in aluminum–rare-earth (Al–RE) alloys and compounds," *Acta Materialia,* vol. 59, no. 9, pp. 3659–3666, 2011/05/01/ 2011, doi: https://doi.org/10.1016/j.actamat.2011.02.040.
[36] W. Wang *et al.*, "Microstructure and properties of novel Al-Ce-Sc, Al-Ce-Y, Al-Ce-Zr and Al-Ce-Sc-Y alloy conductors processed by die casting, hot extrusion and cold drawing," *Journal of Materials Science & Technology,* vol. 58, pp. 155–170, 2020.
[37] A. E. Medvedev, M. Y. Murashkin, N. A. Enikeev, R. Z. Valiev, P. D. Hodgson, and R. Lapovok, "Enhancement of mechanical and electrical properties of Al-RE alloys by optimizing rare-earth concentration and thermo-mechanical treatment," *Journal of Alloys and Compounds,* vol. 745, pp. 696–704, 2018.
[38] T. Dorin, M. Ramajayam, S. Babaniaris, L. Jiang, and T. Langan, "Precipitation sequence in Al–Mg–Si–Sc–Zr alloys during isochronal aging," *Materialia,* vol. 8, p. 100437, 2019.
[39] K. Ma *et al.*, "Mechanical behavior and strengthening mechanisms in ultrafine grain precipitation-strengthened aluminum alloy," *Acta Materialia,* vol. 62, pp. 141–155, 2014.
[40] Y. Wang, L. Zhu, G. Niu, and J. Mao, "Conductive Al alloys: the contradiction between strength and electrical conductivity," *Advanced Engineering Materials,* vol. 23, no. 5, p. 2001249, 2021.
[41] E. Huskins, B. Cao, and K. Ramesh, "Strengthening mechanisms in an Al–Mg alloy," *Materials Science and Engineering: A,* vol. 527, no. 6, pp. 1292–1298, 2010.
[42] Z.-Z. Jin *et al.*, "Exploring the Hall-Petch relation and strengthening mechanism of bimodal-grained Mg–Al–Zn alloys," *Journal of Alloys and Compounds,* vol. 833, p. 155004, 2020.
[43] N. Hansen, "Hall–Petch relation and boundary strengthening," *Scripta materialia,* vol. 51, no. 8, pp. 801–806, 2004.
[44] J. Embury, D. Lloyd, and T. Ramachandran, "Strengthening mechanisms in aluminum alloys," in *Treatise on materials science & technology*, vol. 31: Elsevier, 1989, pp. 579–601.
[45] W. D. Callister Jr and D. G. Rethwisch, *Fundamentals of materials science and engineering: an integrated approach*. John Wiley & Sons, 2020.
[46] E. Totten George, *ASM Handbook Volume 4E-Heat Treating of Nonferrous Alloys*. ASM International., 2016.
[47] A. Azarniya, A. K. Taheri, and K. K. Taheri, "Recent advances in ageing of 7xxx series aluminum alloys: A physical metallurgy perspective," *Journal of Alloys and Compounds,* vol. 781, pp. 945–983, 2019.
[48] A. Mohammadi, N. A. Enikeev, M. Y. Murashkin, M. Arita, and K. Edalati, "Developing age-hardenable Al-Zr alloy by ultra-severe plastic deformation: Significance of supersaturation, segregation and precipitation on hardening and electrical conductivity," *Acta Materialia,* vol. 203, p. 116503, 2021.
[49] Z. Zhang and D. Chen, "Contribution of Orowan strengthening effect in particulate-reinforced metal matrix nanocomposites," *Materials Science and Engineering: A,* vol. 483, pp. 148–152, 2008.
[50] K. Yang *et al.*, "Recent development of advanced precipitation-strengthened Cu alloys with high strength and conductivity: A review," *Progress in Materials Science,* p. 101141, 2023.
[51] S. Jiang and R. Wang, "Grain size-dependent Mg/Si ratio effect on the microstructure and mechanical/electrical properties of Al-Mg-Si-Sc alloys," *Journal of Materials Science & Technology,* vol. 35, no. 7, pp. 1354–1363, 2019.

[52] Y. Li *et al.*, "Al alloys and casting processes for induction motor applications in battery-powered electric vehicles: A review," *Metals,* vol. 12, no. 2, p. 216, 2022.
[53] P. Andrews, M. West, and C. Robeson, "The effect of grain boundaries on the electrical resistivity of polycrystalline copper and aluminium," *Philosophical Magazine,* vol. 19, no. 161, pp. 887–898, 1969.
[54] J. Hou *et al.*, "Breaking the trade-off relation of strength and electrical conductivity in pure Al wire by controlling texture and grain boundary," *Journal of Alloys and Compounds,* vol. 769, pp. 96–109, 2018.
[55] J. Li *et al.*, "Effects of Sc and Zr addition on microstructure and mechanical properties of AA5182," *Materials,* vol. 14, no. 16, p. 4753, 2021.
[56] R. Wang, S. Jiang, and Z. Zhu, "Size effect in the Al3Sc dispersoid-mediated precipitation and mechanical/electrical properties of Al-Mg-Si-Sc alloys," *Journal of Materials Science & Technology,* vol. 57, pp. 78–84, 2020.
[57] E. A. Marquis, D. N. Seidman, and D. C. Dunand, "Precipitation strengthening at ambient and elevated temperatures of heat-treatable Al (Sc) alloys [Acta Materialia 50 (16), pp. 4021-4035]," *Acta Materialia,* vol. 51, no. 1, pp. 285–287, 2003.
[58] E. A. Marquis and D. N. Seidman, "Coarsening kinetics of nanoscale Al3Sc precipitates in an Al–Mg–Sc alloy," *Acta Materialia,* vol. 53, no. 15, pp. 4259–4268, 2005/09/01/ 2005, doi: https://doi.org/10.1016/j.actamat.2005.05.025.
[59] Y. Deng, Z. Yin, K. Zhao, J. Duan, and Z. He, "Effects of Sc and Zr microalloying additions on the microstructure and mechanical properties of new Al–Zn–Mg alloys," *Journal of Alloys and Compounds,* vol. 530, pp. 71–80, 2012.
[60] J. Zhang, T. Hu, D. Yi, H. Wang, and B. Wang, "Double-shell structure of Al3 (Zr, Sc) precipitate induced by thermomechanical treatment of Al–Zr–Sc alloy cable," *Journal of Rare Earths,* vol. 37, no. 6, pp. 668–672, 2019.
[61] T. Dorin *et al.*, "Stability and stoichiometry of L12 Al3 (Sc, Zr) dispersoids in Al-(Si)-Sc-Zr alloys," *Acta Materialia,* vol. 216, p. 117117, 2021.
[62] M. Zhang *et al.*, "Microstructure evolution and strengthening mechanisms of an additive friction stir deposited multi-layer Al-Mg-Sc-Zr alloy," *Journal of Alloys and Compounds,* vol. 1004, p. 175783, 2024.
[63] X. Huang, Q. Pan, B. Li, Z. Liu, Z. Huang, and Z. Yin, "Effect of minor Sc on microstructure and mechanical properties of Al–Zn–Mg–Zr alloy metal–inert gas welds," *Journal of Alloys and compounds,* vol. 629, pp. 197–207, 2015.
[64] S. Tian, J. Li, J. Zhang, Z. Wulabieke, and D. Lv, "Effect of Zr and Sc on microstructure and properties of 7136 aluminum alloy," *Journal of Materials Research and Technology,* vol. 8, no. 5, pp. 4130–4140, 2019.
[65] K. Kendig and D. Miracle, "Strengthening mechanisms of an Al-Mg-Sc-Zr alloy," *Acta Materialia,* vol. 50, no. 16, pp. 4165–4175, 2002.
[66] S. Babaniaris, M. Ramajayam, L. Jiang, R. Varma, T. Langan, and T. Dorin, "Effect of Al3 (Sc, Zr) dispersoids on the hot deformation behaviour of 6xxx-series alloys: A physically based constitutive model," *Materials Science and Engineering: A,* vol. 793, p. 139873, 2020.
[67] K. Dai, J. Ye, Z. Wang, M. Gao, J. Chen, and R. Guan, "Effects of Sc and Zr addition on the solidification and mechanical properties of Al–Fe alloys," *Journal of Materials Research and Technology,* vol. 18, pp. 112–121, 2022.
[68] Z. Lei, S. Wen, H. Huang, W. Wei, and Z. Nie, "Grain refinement of aluminum and aluminum alloys by Sc and Zr," *Metals,* vol. 13, no. 4, p. 751, 2023.
[69] J. Røyset and N. Ryum, "Scandium in aluminium alloys," *International Materials Reviews,* vol. 50, no. 1, pp. 19–44, 2005.
[70] S. Kasap and P. Capper, *Springer Handbook of Electronic and Photonic Materials*. Springer International Publishing, 2017.

[71] S. N. Khangholi, M. Javidani, A. Maltais, and X.-G. Chen, "Optimization of mechanical properties and electrical conductivity in Al–Mg–Si 6201 alloys with different Mg/Si ratios," *Journal of Materials Research,* vol. 35, no. 20, pp. 2765–2776, 2020.
[72] T. Dorin, M. Ramajayam, A. Vahid, and T. Langan, "Aluminium scandium alloys," in *Fundamentals of aluminium metallurgy*: Elsevier, 2018, pp. 439–494.
[73] D. G. Eskin, "Sc applications in aluminum alloys: Overview of Russian research in the 20th century," *Light Metals 2018,* pp. 1565–1572, 2018.
[74] P. Rometsch and J. Fourmann, "Potential for Using Scandium in Extrusion Alloys," presented at the Thirteenth International Aluminum Extrusion Technology Seminar & Exposition, Orlando, Florida, USA, 2024.
[75] K. E. Knipling, D. N. Seidman, and D. C. Dunand, "Ambient-and high-temperature mechanical properties of isochronally aged Al–0.06 Sc, Al–0.06 Zr and Al–0.06 Sc–0.06 Zr (at.%) alloys," *Acta Materialia,* vol. 59, no. 3, pp. 943–954, 2011.
[76] A. Elasheri, N. Parson, and X.-G. Chen, "Microstructure, tensile and bending properties of extruded Al–Mg–Si 6xxx alloys with individual and combined additions of Zr and Mn," *Materials Science and Engineering: A,* vol. 894, p. 146156, 2024.
[77] F. Czerwinski, "Thermal stability of aluminum alloys," *Materials,* vol. 13, no. 15, p. 3441, 2020.
[78] V. S. Muthaiah and S. Mula, "Effect of zirconium on thermal stability of nanocrystalline aluminium alloy prepared by mechanical alloying," *Journal of Alloys and Compounds,* vol. 688, pp. 571–580, 2016.
[79] J. Robson and P. Prangnell, "Dispersoid precipitation and process modelling in zirconium containing commercial aluminium alloys," *Acta Materialia,* vol. 49, no. 4, pp. 599–613, 2001.
[80] J. Murray, A. Peruzzi, and J. Abriata, "The Al-Zr (aluminum-zirconium) system," *Journal of phase equilibria,* vol. 13, no. 3, pp. 277–291, 1992.
[81] K. E. Knipling, D. C. Dunand, and D. N. Seidman, "Precipitation evolution in Al–Zr and Al–Zr–Ti alloys during isothermal aging at 375–425 C," *Acta Materialia,* vol. 56, no. 1, pp. 114–127, 2008.
[82] S. Pan, C. Li, F. Qian, L. Hao, and Y. Li, "Diffusion controlled early-stage L12-D023 transitions within Al3Zr," *Scripta Materialia,* vol. 231, p. 115460, 2023.
[83] K. E. Knipling, D. C. Dunand, and D. N. Seidman, "Criteria for developing castable, creep-resistant aluminum-based alloys–A review," *International Journal of Materials Research,* vol. 97, no. 3, pp. 246–265, 2022.
[84] K. E. Knipling, D. C. Dunand, and D. N. Seidman, "Nucleation and precipitation strengthening in dilute Al-Ti and Al-Zr alloys," *Metallurgical and Materials Transactions A,* vol. 38, pp. 2552–2563, 2007.
[85] E. Nes, "Precipitation of the metastable cubic Al3Zr-phase in subperitectic Al-Zr alloys," *Acta Metallurgica,* vol. 20, no. 4, pp. 499–506, 1972.
[86] K. E. Knipling, D. C. Dunand, and D. N. Seidman, "Precipitation evolution in Al–Zr and Al–Zr–Ti alloys during aging at 450–600 C," *Acta Materialia,* vol. 56, no. 6, pp. 1182–1195, 2008.
[87] L. Ding *et al.*, "On the formation of anti-phase boundaries and interphase boundaries in Al3Zr precipitates of Al-Cu-Zr alloy studied at atomic scale," *Journal of Alloys and Compounds,* vol. 887, p. 161442, 2021.
[88] E. Clouet, J.-M. Sanchez, and C. Sigli, "First-principles study of the solubility of Zr in Al," *Physical Review B,* vol. 65, no. 9, p. 094105, 2002.
[89] J.-Y. Zhang *et al.*, "Microalloying Al alloys with Sc: a review," *Rare Metals,* vol. 39, pp. 636–650, 2020.
[90] Y. Wang *et al.*, "Effects of Sc and Zr on microstructure and properties of 1420 aluminum alloy," *Materials Characterization,* vol. 154, pp. 241–247, 2019.

[91] Y. Harada and D. Dunand, "Microstructure of Al3Sc with ternary transition-metal additions," *Materials Science and Engineering: A,* vol. 329, pp. 686–695, 2002.
[92] K. Fukunaga, T. Shouji, and Y. Miura, "Temperature dependence of dislocation structure of L12–Al3Sc," *Materials Science and Engineering: A,* vol. 239, pp. 202–205, 1997.
[93] E. Marquis and D. N. Seidman, "Nanoscale structural evolution of Al3Sc precipitates in Al (Sc) alloys," *Acta materialia,* vol. 49, no. 11, pp. 1909–1919, 2001.
[94] C. B. Fuller, J. L. Murray, and D. N. Seidman, "Temporal evolution of the nanostructure of Al (Sc, Zr) alloys: Part I–Chemical compositions of Al3 (Sc1− xZrx) precipitates," *Acta materialia,* vol. 53, no. 20, pp. 5401–5413, 2005.
[95] Q. Shao, E. M. Elgallad, A. Maltais, and X.-G. Chen, "Thermal stability of Al–Zr-Sc conductor alloys during long-term elevated-temperature exposures," *Journal of Materials Research and Technology,* vol. 35, pp. 164–175, 2025.
[96] L. Toropova, D. G. Eskin, M. Kharakterova, and T. Dobatkina, *Advanced aluminum alloys containing scandium: structure and properties*. Routledge, 2017.
[97] E. Clouet, L. Laé, T. Épicier, W. Lefebvre, M. Nastar, and A. Deschamps, "Complex precipitation pathways in multicomponent alloys," *Nature materials,* vol. 5, no. 6, pp. 482–488, 2006.
[98] J. Zhang, H. Zhao, J. Zhu, B. Wang, and D. Yi, "Relationship between electrical resistivity and Al3 (Zr, Sc) core–shell dispersoids of Al–Zr–Sc electrical transmission cable: Modeling and experimental results," *Electric Power Systems Research,* vol. 168, pp. 1–7, 2019.
[99] B. Forbord, W. Lefebvre, F. Danoix, H. Hallem, and K. Marthinsen, "Three dimensional atom probe investigation on the formation of Al3 (Sc, Zr)-dispersoids in aluminium alloys," *Scripta materialia,* vol. 51, no. 4, pp. 333–337, 2004.
[100] Y. Wang *et al.*, "Ambient-temperature mechanical properties of isochronally aged 1420-Sc-Zr aluminum alloy," *Materials Science and Engineering: A,* vol. 745, pp. 411–419, 2019.
[101] Y. Wang *et al.*, "Coarsening kinetics and strengthening mechanisms of core-shell nanoscale precipitates in Al-Li-Yb-Er-Sc-Zr alloy," *Journal of Materials Science & Technology,* vol. 61, pp. 197–203, 2021.
[102] Y. Qi *et al.*, "Achieving superior high-temperature mechanical properties in Al-Cu-Li-Sc-Zr alloy with nano-scale microstructure via laser additive manufacturing," *Materials Research Letters,* vol. 12, no. 1, pp. 17–25, 2024.
[103] T. Marumo, S. Fujikawa, and K.-i. Hirano, "Diffusion du zirconium dans l'aluminium," 1973.
[104] Y. Deng, Z. Yin, Q. Pan, G. Xu, Y. Duan, and Y. Wang, "Nano-structure evolution of secondary Al3 (Sc1− xZrx) particles during superplastic deformation and their effects on deformation mechanism in Al-Zn-Mg alloys," *Journal of Alloys and Compounds,* vol. 695, pp. 142–153, 2017.
[105] Y. Sun *et al.*, "The effects of scandium heterogeneous distribution on the precipitation behavior of Al3 (Sc, Zr) in aluminum alloys," *Materials Characterization,* vol. 174, p. 110971, 2021.
[106] D. N. Seidman, E. A. Marquis, and D. C. Dunand, "Precipitation strengthening at ambient and elevated temperatures of heat-treatable Al(Sc) alloys," *Acta Materialia,* vol. 50, no. 16, pp. 4021–4035, 2002/09/20/ 2002, doi: https://doi.org/10.1016/S1359-6454(02)00201-X.
[107] X. Na, L. Wenqing, Z. Liu, and T. Muthuramalingam, "Effect of scandium in Al–Sc and Al–Sc–Zr alloys under precipitation strengthening mechanism at 350 C aging," *Metals and Materials International,* vol. 27, pp. 5145–5153, 2021.
[108] A. R. Farkoosh, D. C. Dunand, and D. N. Seidman, "Effects of W and Si microadditions on microstructure and the strength of dilute precipitation-strengthened Al–Zr–Er alloys," *Materials Science and Engineering: A,* vol. 798, p. 140159, 2020.
[109] J. Zhang, H. Wang, D. Yi, B. Wang, and H. Wang, "Comparative study of Sc and Er addition on microstructure, mechanical properties, and electrical conductivity of Al-0.2 Zr-based alloy cables," *Materials Characterization,* vol. 145, pp. 126–134, 2018.

[110] A. Tolley, V. Radmilovic, and U. Dahmen, "Segregation in Al3 (Sc, Zr) precipitates in Al–Sc–Zr alloys," *Scripta materialia,* vol. 52, no. 7, pp. 621–625, 2005.
[111] S. Wu *et al.*, "Effect of Si addition on the precipitation and mechanical/electrical properties of dilute Al–Zr-Sc alloys," *Materials Science and Engineering: A,* vol. 812, p. 141150, 2021.
[112] H. Vafaeenezhad and H. R. Shahverdi, "Impact of Vanadium Presence on the Mechanical and Microstructural Characteristics of a Dilute Al–Sc–Zr–Si Alloy During Isothermal Aging," *Journal of Materials Research and Technology,* vol. 30, pp. 2406–2419, 2024.
[113] X. Xu, Z. Yang, Y. Ye, G. Wang, and X. He, "Effects of various Mg/Si ratios on microstructure and performance property of Al-Mg-Si alloy cables," *Materials Characterization,* vol. 119, pp. 114–119, 2016.
[114] C. Booth-Morrison, Z. Mao, M. Diaz, D. Dunand, C. Wolverton, and D. Seidman, "Role of silicon in accelerating the nucleation of Al3 (Sc, Zr) precipitates in dilute Al–Sc–Zr alloys," *Acta Materialia,* vol. 60, no. 12, pp. 4740–4752, 2012.
[115] H. Vafaeenezhad and H. R. Shahverdi, "Synergic effects of Si and V micro-additions on microstructural and mechanical properties of a dilute Al–Sc–Zr alloy containing L12 Al3 (Sc, Zr, V) nanoprecipitates," *Journal of Alloys and Compounds,* vol. 967, p. 171747, 2023.
[116] D. Erdeniz *et al.*, "Effect of vanadium micro-alloying on the microstructural evolution and creep behavior of Al-Er-Sc-Zr-Si alloys," *Acta Materialia,* vol. 124, pp. 501–512, 2017.
[117] J. Zhang and J. Peng, "A review on aluminum alloy conductors influenced by alloying elements and thermomechanical treatments: Microstructure and properties," *Journal of Materials Research,* vol. 38, no. 6, pp. 1488–1509, 2023.
[118] N. Vo, D. Dunand, and D. Seidman, "Improving aging and creep resistance in a dilute Al–Sc alloy by microalloying with Si, Zr and Er," *Acta Materialia,* vol. 63, pp. 73–85, 2014.
[119] G. Edwards, K. Stiller, G. Dunlop, and M. Couper, "The precipitation sequence in Al–Mg–Si alloys," *Acta materialia,* vol. 46, no. 11, pp. 3893–3904, 1998.
[120] X. Yuan *et al.*, "Microstructures and mechanical properties of cast Al–Mg–Si alloy with combined addition of Sc and Zr," *Journal of Materials Research and Technology,* vol. 35, pp. 5097–5106, 2025.
[121] S. Babaniaris, M. Ramajayam, L. Jiang, T. Langan, and T. Dorin, "Tailored precipitation route for the effective utilisation of Sc and Zr in an Al-Mg-Si alloy," *Materialia,* vol. 10, p. 100656, 2020.
[122] T. Dorin, L. Jiang, and T. Langan, "Formation of Al3Sc Dispersoids and Associated Strengthening," in *TMS Annual Meeting & Exhibition*, 2023: Springer, pp. 1207–1212.
[123] E. Aryshenskii, M. Lapshov, D. Y. Rasposienko, S. Konovalov, A. Drits, and V. Makarov, "Studying the effect of small additives of Sc and Zr on the microstructure of Al–Mg–Si alloy with excess silicon during multi-step heat treatment," *Physics of Metals and Metallography,* vol. 125, no. 2, pp. 142–155, 2024.
[124] P. A. Rometsch, Z. Xu, H. Zhong, H. Yang, L. Ju, and X. H. Wu, "Strength and electrical conductivity relationships in Al-Mg-Si and Al-Sc alloys," in *Materials Science Forum*, 2014, vol. 794: Trans Tech Publ, pp. 827–832.
[125] M. Yu, B. Zhu, N. Li, H. Zheng, Y. Lu, and X. Yu, "Study on microstructure, tensile performance and creep resistance of Al–Mg–Si-Sc-Zr alloy strengthened by Al3 (Sc, Zr) nanoprecipitates," *Materials Science and Engineering: A,* vol. 897, p. 146362, 2024.
[126] T. Dorin, M. Ramajayam, S. Babaniaris, and T. Langan, "Micro-segregation and precipitates in as-solidified Al-Sc-Zr-(Mg)-(Si)-(Cu) alloys," *Materials Characterization,* vol. 154, pp. 353–362, 2019.
[127] A. Elasheri, E. Elgallad, N. Parson, and X.-G. Chen, "Evolution of Zr-bearing dispersoids during homogenization and their effects on hot deformation and recrystallization resistance in Al-0.8% Mg-1.0% Si alloy," *Journal of Materials Engineering and Performance,* vol. 30, pp. 7851–7862, 2021.

[128] E. Aryshenskii, M. Lapshov, S. Konovalov, J. Hirsch, V. Aryshenskii, and S. Sbitneva, "The casting rate impact on the microstructure in Al–Mg–Si alloy with silicon excess and small Zr, Sc additives," *Metals,* vol. 11, no. 12, p. 2056, 2021.
[129] E. Aryshenskii *et al.*, "Influence of the small sc and zr additions on the as-cast microstructure of al–mg–si alloys with excess silicon," *Metals,* vol. 11, no. 11, p. 1797, 2021.
[130] A. De Luca, D. C. Dunand, and D. N. Seidman, "Microstructure and mechanical properties of a precipitation-strengthened Al-Zr-Sc-Er-Si alloy with a very small Sc content," *Acta Materialia,* vol. 144, pp. 80–91, 2018.
[131] Y. Kong, Z. Jia, Z. Liu, M. Liu, H. J. Roven, and Q. Liu, "Effect of Zr and Er on the microstructure, mechanical and electrical properties of Al-0.4 Fe alloy," *Journal of Alloys and Compounds,* vol. 857, p. 157611, 2021.
[132] C. Zhang, D. Yin, Y. Jiang, and Y. Wang, "Precipitation of L12-phase nano-particles in dilute Al-Er-Zr alloys from the first-principles," *Computational Materials Science,* vol. 162, pp. 171–177, 2019.
[133] F. Czerwinski, "Aluminum alloys for electrical engineering: a review," *Journal of Materials Science,* pp. 1–46, 2024.
[134] Y. Sun *et al.*, "Evolutions of diffusion activation energy and Zener–Hollomon parameter of ultra-high strength Al-Zn-Mg-Cu-Zr alloy during hot compression," *Progress in Natural Science: Materials International,* vol. 28, no. 5, pp. 635–646, 2018.
[135] T.-A. Pan, Y.-C. Tzeng, H.-Y. Bor, K.-H. Liu, and S.-L. Lee, "Effects of the coherency of Al3Zr on the microstructures and quench sensitivity of Al–Zn–Mg–Cu alloys," *Materials Today Communications,* vol. 28, p. 102611, 2021.
[136] C. Booth-Morrison, D. N. Seidman, and D. C. Dunand, "Effect of Er additions on ambient and high-temperature strength of precipitation-strengthened Al–Zr–Sc–Si alloys," *Acta Materialia,* vol. 60, no. 8, pp. 3643–3654, 2012.
[137] Y. Guo *et al.*, "Effect of Er and Zr additions and aging treatment on grain refinement of aluminum alloy fabricated by laser powder bed fusion," *Journal of Alloys and Compounds,* vol. 912, p. 165237, 2022.
[138] W. Nasim *et al.*, "Structure and growth of core–shell nanoprecipitates in Al–Er–Sc–Zr–V–Si high-temperature alloys," *Journal of materials science,* vol. 54, pp. 1857–1871, 2019.
[139] S. Wen, K. Gao, Y. Li, H. Huang, and Z. Nie, "Synergetic effect of Er and Zr on the precipitation hardening of Al–Er–Zr alloy," *Scripta materialia,* vol. 65, no. 7, pp. 592–595, 2011.
[140] Y. Kong *et al.*, "Microstructure and property evolution of Al-0.4 Fe-0.15 Zr-0.25 Er alloy processed by high pressure torsion," *Journal of Alloys and Compounds,* vol. 824, p. 153949, 2020.
[141] F. Czerwinski, "Cerium in aluminum alloys," *Journal of materials science,* vol. 55, no. 1, pp. 24–72, 2020.
[142] G. Lin *et al.*, "Influence of cerium and yttrium addition on strength and electrical conductivity of pure aluminum alloys," *Journal of Rare Earths,* vol. 42, no. 3, pp. 600–611, 2024.
[143] A. Pozdniakov, A. Aitmagambetov, S. Makhov, and V. Napalkov, "Effect of impurities of Fe and Si on the structure and strengthening upon annealing of the Al–0.2% Zr–0.1% Sc alloys with and without Y additive," *Physics of Metals and Metallography,* vol. 118, pp. 479–484, 2017.
[144] F. Czerwinski and B. Shalchi Amirkhiz, "On the Al–Al11Ce3 eutectic transformation in aluminum–cerium binary alloys," *Materials,* vol. 13, no. 20, p. 4549, 2020.
[145] W. Yuan, Z. Liang, C. Zhang, and L. Wei, "Effects of La addition on the mechanical properties and thermal-resistant properties of Al–Mg–Si–Zr alloys based on AA 6201," *Materials & Design,* vol. 34, pp. 788–792, 2012.
[146] T. Moons, P. Ratchev, B. Verlinden, P. Van Houtte, and P. De Smet, "A comparative study of two Al-Mg-Si alloys for automotive applications," *Scripta Materialia,* vol. 35, no. 8, 1996.

[147] M. Hosseinifar and D. V. Malakhov, "The sequence of intermetallics formation during the solidification of an Al-Mg-Si alloy containing La," *Metallurgical and Materials Transactions A,* vol. 42, pp. 825–833, 2011.
[148] W. Kang, H. Li, S. Zhao, Y. Han, C. Yang, and G. Ma, "Effects of homogenization treatments on the microstructure evolution, microhardness and electrical conductivity of dilute Al-Sc-Zr-Er alloys," *Journal of Alloys and Compounds,* vol. 704, pp. 683–692, 2017.
[149] S. Fan *et al.*, "Achieving superior strength and conductivity for Al-Zr-Sc wires by coupling design of deformation and ageing," *Materials Research Letters,* vol. 12, no. 8, pp. 590–598, 2024.
[150] M. Wang *et al.*, "Optimizing the Heat Treatment Method to Improve the Aging Response of Al-Fe-Ni-Sc-Zr Alloys," *Materials,* vol. 17, no. 8, p. 1772, 2024.
[151] A. Y. Algendy, K. Liu, P. Rometsch, N. Parson, and X.-G. Chen, "Effects of AlMn dispersoids and Al3 (Sc, Zr) precipitates on the microstructure and ambient/elevated-temperature mechanical properties of hot-rolled AA5083 alloys," *Materials Science and Engineering: A,* vol. 855, p. 143950, 2022.
[152] J.-G. Jung, A. R. Farkoosh, and D. N. Seidman, "Microstructural and mechanical properties of precipitation-strengthened Al-Mg-Zr-Sc-Er-Y-Si alloys," *Acta Materialia,* vol. 257, p. 119167, 2023/09/15/ 2023, doi: https://doi.org/10.1016/j.actamat.2023.119167.
[153] Y. Yang, J. J. Licavoli, and P. G. Sanders, "Improved strengthening in supersaturated Al-Sc-Zr alloy via melt-spinning and extrusion," *Journal of Alloys and Compounds,* vol. 826, p. 154185, 2020.
[154] S. Fan *et al.*, "Effects of processing paths on the microstructure, mechanical properties and electrical conductivity of dilute Al-Zr-Sc alloy conductive wires," *Journal of Materials Science & Technology,* vol. 188, pp. 202–215, 2024.
[155] S. Gashtiazar, E. Elgallad, B. Abnar, M. Javidani, A. Maltais, and X.-G. Chen, "Effect of solution heat treatment on the microstructure of hot-rolled Al-Mg-Si 6xxx alloy microalloyed with Sc and Zr," *Materials Letters,* p. 138784, 2025.
[156] M. Yu, B. Zhu, N. Li, H. Zheng, Y. Lu, and X. Yu, "Research on microstructure and mechanical properties at elevated temperature of Al-Mg-Si-Sc-Zr alloy strengthened by Al3 (Sc, Zr) nanoprecipitates," *Journal of Alloys and Compounds,* vol. 985, p. 174050, 2024.
[157] J. Fu, Z. Yang, Y. Deng, Y. Wu, and J. Lu, "Influence of Zr addition on precipitation evolution and performance of Al-Mg-Si alloy conductor," *Materials Characterization,* vol. 159, p. 110021, 2020.
[158] Y. Liu, Y. Lai, Z. Chen, S. Chen, P. Gao, and J. Chen, "Formation of β"-related composite precipitates in relation to enhanced thermal stability of Sc-alloyed Al-Mg-Si alloys," *Journal of Alloys and Compounds,* vol. 885, p. 160942, 2021.
[159] E. P. Kwon, K. D. Woo, S. H. Kim, D. S. Kang, K. J. Lee, and J. Y. Jeon, "The effect of an addition of Sc and Zr on the precipitation behavior of AA6061 alloy," *Metals and Materials International,* vol. 16, no. 5, pp. 701–707, 2010/10/01 2010, doi: 10.1007/s12540-010-1002-y.
[160] E. Avtokratova, O. Sitdikov, M. Markushev, M. Linderov, D. Merson, and A. Vinogradov, "The processing route towards outstanding performance of the severely deformed Al–Mg–Mn-Sc-Zr alloy," *Materials Science and Engineering: A,* vol. 806, p. 140818, 2021.
[161] J. Lai, Z. Zhang, and X.-G. Chen, "The thermal stability of mechanical properties of Al–B4C composites alloyed with Sc and Zr at elevated temperatures," *Materials Science and Engineering: A,* vol. 532, pp. 462–470, 2012.
[162] G. Huang *et al.*, "A novel two-step method to prepare fine-grained SiC/Al-Mg-Sc-Zr nanocomposite: Processing, microstructure and mechanical properties," *Materials Science and Engineering: A,* vol. 823, p. 141764, 2021.

[163] Y. Liu, C.-C. Zhang, X.-Y. Zhang, and Y.-C. Huang, "Understanding grain refinement of Sc addition in a Zr containing Al-Zn-Mg-Cu aluminum alloy from experiments and first-principles," *Intermetallics,* vol. 123, p. 106823, 2020.
[164] B. Li *et al.*, "Manipulation of mechanical properties of 7xxx aluminum alloy via a hybrid approach of machine learning and key experiments," *Journal of Materials Research and Technology,* vol. 19, pp. 2483–2496, 2022.
[165] W. Yi, G. Liu, J. Gao, and L. Zhang, "Boosting for concept design of casting aluminum alloys driven by combining computational thermodynamics and machine learning techniques," *Journal of Materials Informatics,* vol. 1, no. 2, pp. N/A–N/A, 2021.
[166] A. Korkmaz, T. Yağcı, and O. Çulha, "Optimization of T6 Heat Treatments for AlSi5Mgx Alloys via Computational Materials Engineering and Experimental Validation for Automotive Applications," *Journal of Materials Engineering and Performance,* pp. 1–10, 2024.
[167] E. V. Aryshenskii, S. Konovalov, V. Bazhenov, and J. Hirsch, "Features of the Microstructural Composition of Low-Alloyed Aluminum Alloys of the 6XXX Series with Small Additions of Zr and Sc," *Key Engineering Materials,* vol. 910, pp. 994–1001, 2022.
[168] A. Ghosh, A. Elasheri, N. Parson, and X.-G. Chen, "Microstructure and texture evolution during high-temperature compression of Al-Mg-Si-Zr-Mn alloy," *Materials Characterization,* vol. 205, p. 113312, 2023.

Chapitre 4. Effet des paramètres de déformation à chaud sur les performances et le comportement thermomécanique des alliages conducteurs Al-Mg-Si modifiés au Cu

Cet article a été publié dans:
Journal of Materials Science, Volume 60, 06 octobre 2025, pages 19912–19941

Résumé

Cette étude examine l'impact des additions de Cu (0,15–0,4 % en masse) sur le comportement de déformation à chaud d'un alliage conducteur Al-Mg-Si, en mettant l'accent sur l'influence des paramètres de procédé sur la conductivité électrique et les propriétés mécaniques. Des essais de compression à chaud ont été réalisés à 450 °C et 550 °C avec des vitesses de déformation comprises entre 0,1 et 10 s^{-1} afin d'atteindre cet objectif. Les résultats montrent qu'à 450 °C, l'ajout de ≤0,3 % Cu augmente légèrement la contrainte d'écoulement (jusqu'à 8,2 %), tandis que 0,4 % Cu entraîne une augmentation significative (15–25,2 %). À 550 °C, l'effet du Cu diminue fortement (<3,5 %), en particulier à faibles vitesses de déformation. Par ailleurs, énergie d'activation de la déformation à chaud augmente de 143,9 à 173,3 kJ/mol avec 0,15–0,4 % Cu, indiquant une résistance accrue à la déformation. Le Cu retarde la restauration dynamique et réduit la taille des sous-grains ainsi que l'angle moyen de mésorientation des joints de grains. Globalement, les alliages déformés à 450 °C présentent une dureté inférieure de 8–20 %, mais une conductivité électrique supérieure de 1,0–2,5 % IACS par rapport à ceux déformés à 550 °C après 8 h et 24 h de vieillissement, bien que cet écart diminue après 24 h. Ce comportement est attribué à la formation de précipités grossiers β-Mg_2Si à 450 °C, améliorant la conductivité mais réduisant la dureté. L'allongement du vieillissement de 8 h à 24 h augmente légèrement la conductivité (1–2,7 % IACS) avec une diminution négligeable de la dureté (<4 HV). Les résultats indiquent que l'alliage contenant 0,3 % Cu offre le meilleur compromis, atteignant jusqu'à 75 HV (20–30 % supérieur à l'alliage de base), une légère variation de la résistance à la déformation, et maintenant une conductivité de 52,4–54,1 % IACS conforme aux normes des conducteurs.

Mots-clés: conducteurs Al-Mg-Si, comportement de déformation à chaud, conductivité électrique, microdureté, contrainte d'écoulement

Effect of hot deformation parameters on the performance and thermomechanical behavior of Cu-modified Al-Mg-Si conductor alloys

Behrouz Abnar [a], Siamak Nikzad Khangholi [a], Paul Rometsch[b], Mousa Javidani [a]

[a] University Research Centre on Aluminium (CURAL) and Aluminium Research Centre–REGAL, Department of Applied Science, University of Québec at Chicoutimi, Saguenay, QC, G7H 2B1, Canada
[b] Arvida Research and Development Center, Rio Tinto Aluminum, Saguenay, QC, G7S 4K8, Canada

This article has been published in:
Journal of Materials Science, Volume 60, 06 October 2025, pages 19912–19941

Abstract

This study investigates the impact of Cu additions (0.15–0.4 wt.%) on the hot deformation behavior of an Al-Mg-Si conductor alloy with a focus on how process parameters influence electrical conductivity and mechanical properties. Hot compression tests were performed at 450°C and 550°C using strain rates ranging from 0.1 to 10 s^{-1} to achieve this objective. The results show that at 450°C, adding ≤0.3 wt.% Cu slightly raised flow stress (up to 8.2%), while 0.4 wt.% Cu caused a significant increase (15–25.2%). At 550°C, Cu's effect markedly decreased (<3.5%), especially at lower strain rates. Moreover, hot deformation activation energy rose from 143.9 to 173.3 kJ/mol with 0.15–0.4 wt.% Cu, showing increased deformation resistance. Cu retarded the dynamic recovery and decreased the subgrain size and mean misorientation angle of the grain boundaries. Overall, alloys deformed at 450°C showed 8–20% lower hardness but higher electrical 1.0–2.5 %IACS than those deformed at 550°C after both 8 h and 24 h aging, though the difference narrowed at 24 h. This behavior is attributed to coarse β-Mg_2Si precipitates at 450°C, enhancing conductivity but reducing hardness. Extending aging from 8 h to 24 h slightly increased conductivity (1–2.7% IACS) with minimal hardness drop (<4 HV). The findings indicates that the 0.3% Cu alloy offered the best balance—achieving up to 75 HV (20–30% higher than base alloy), slight change in deformation resistance, and maintaining 52.4-54.1 %IACS conductivity within conductor standards.

Keywords: Al-Mg-Si conductors, Hot deformation behavior, Electrical conductivity, Microhardness, Flow stress

4.1. Introduction

In recent decades, advancing technology and growing electrification demand innovative, cost-effective, high-performance aluminum alloys for efficient power transmission and power distribution, supporting global decarbonization goals [1]. These alloys have been seen as a promising replacement for copper (Cu) conductors due to their unique properties, including lower cost (2-4 times less per kilogram than Cu), high corrosion resistance, and a higher strength-to-weight ratio compared to Cu conductors [2-4]. Although conductors made of Al alloys present lower electrical conductivity (EC), their density is one-third that of Cu conductors. Therefore, Al alloy conductors are the preferred choice for numerous electrical conductor applications. They are utilized across various electrical applications, including power transmission, and distribution systems, such as electrical cables and bus bars [5, 6].

Bus bars, made from Al alloys, serve as efficient electrical conductors in power distribution systems, providing a reliable pathway for high-current power over short distances. They efficiently distribute electrical power from the main source to various devices and are designed in a multitude of shapes and forms to suit specific applications [7, 8]. Bus bars are widely used in various industries, including automotive (EVs), switchgear, renewable energy systems, railway, aerospace, power electronics, UPS, and data centers [9-13]. Electrical bus bars are typically manufactured in a rectangular bar shape, with hot extrusion being the most common manufacturing method for this shape [6, 14].

Common Al alloys used in Al conductors include AA1350, AA6201, and AA6101, each offering specific advantages based on conductivity, strength, and corrosion resistance [15, 16]. AA6201 alloys possess higher Mg and Si, so these alloys achieve greater strength after age hardening compared to AA6101. However, the EC of AA6201 is lower than that of AA6101 due to the higher Mg and Si amounts [16]. The addition of Cu in 6xxx series Al alloys is well documented for its ability to enhance strength [17-20]. Cu promotes the age-hardening response in Al-Mg-Si alloys by facilitating the formation of L and Q′ precipitates, which coexist with β" phases in the peak-aged condition [21, 22]. This results in a higher number density of precipitates, leading to improved mechanical properties of the alloys [23-26]. Studies show that the stronger interaction between Cu and Mg atoms leads to the early

formation of Mg-Cu clusters during aging, which, alongside Mg-Si clusters, act as nucleation sites for further precipitates [23, 27].

According to the Aluminum Association's Teal Sheets and the ASTM B398 and B317 standards, the maximum allowable Cu content in AA6201 and AA6101 conductor alloys is restricted to 0.10 wt% [6, 28]. Beyond these standard specified values, although Cu can improve the strength, the alloys generally exhibit lower EC under conventional thermomechanical processing. Therefore, further development of thermomechanical processing is required to achieve a more favorable balance between conductivity and strength. S. N. Khangholi et al. [23] reported that the addition of 0.3% Cu enhances the strength of an Al-Mg-Si conductor wire from 317 MPa to 348 MPa using a modified thermomechanical treatment (MTMT), which involves pre-aging for 6 hours at 180°C before wire drawing and post-aging at 180°C for 0–24 hours, while maintaining EC above the minimum required level of 52.5% IACS.

Since Cu positively affects the performance of Al 6xxx conductors, investigating its effect on hot deformation behavior during the manufacturing process is essential. Solid solution atoms tend to segregate at (sub)grain boundaries, significantly impeding grain boundary mobility [29]. This segregation lowers the grain boundary energy, reducing the thermodynamic impetus for grain growth [30]. This phenomenon hinders dynamic softening processes, such as dynamic recovery (DRV) and dynamic recrystallization (DRX) by restricting dislocation motion, which ultimately leads to a reduction in the ductility of alloy [31-33]. Both the size mismatch and differences in shear modulus between solute atoms and the solvent matrix play crucial roles in the strengthening effects of solute elements [34, 35]. Shakiba et al. [31] demonstrated that the addition of 0.3 wt.% Cu significantly increased the flow stress of an Al-Fe-Si alloy by 19% during hot deformation at 400 ˚C at a strain rate of 0.01 s^{-1}. The effect of Cu content on the hot deformation behavior of 6xxx series alloys has been rarely studied, particularly for conductor alloys, where EC must also be considered in the investigation.

Unlike wire, extruded rectangular electrical bus bars do not undergo cold drawing after hot deformation, which means they do not benefit from dislocation strengthening in the same manner [6]. This fundamental difference has received limited attention in the literature and

highlights a critical knowledge gap. Therefore, this study uniquely focuses on investigating and optimizing alloying strategies and thermomechanical processing parameters specifically for bus bars, aiming to achieve a superior balance between EC and mechanical strength. We followed standard 6xxx electrical bus bars manufacturing process but replaced hot extrusion with uniaxial hot-compression tests to assess deformation behavior across Cu levels. Hot compression testing enables systematic evaluation of deformation behavior under controlled conditions, reducing cost and material needs, while providing reliable data to guide industrial extrusion or rolling process optimization [36, 37]. We examined how temperature and other thermomechanical parameters affect microhardness and EC of Al–Mg–Si(–Cu) alloys under industrially relevant conditions.

4.2. Experimental procedure

Table 4-1 shows the chemical compositions of the alloys analyzed using optical emission spectroscopy (OES). Mg, Si, and Fe levels were maintained nearly constant, while Cu concentrations were varied. The alloy designation is based on the Cu levels. Commercial pure Al (99.85%) and pure Mg (99.8%), and Al-50%Si and Al-50%Cu master alloys (in wt. %) were used for casting. The molten metal, prepared in an electrical resistance furnace, was poured into a permanent steel mold measuring 30 mm × 40 mm × 80 mm. Figure *4-1* displays the schematic diagram of the experimental process in the present research. The as-cast alloys were homogenized at 550°C for 6 hours, and machined into cylindrical samples with a diameter of 10 mm and a length of 15 mm.

Table 4-1. Chemical compositions of studied alloys (wt%).

Alloys	Mg	Si	Cu	Fe	Ti	B	Al
Base	0.67	0.41	Trace	0.11	0.011	0.002	Bal.
Cu1	0.67	0.38	0.15	0.11	0.012	0.002	Bal.
Cu3	0.63	0.37	0.28	0.10	0.012	0.003	Bal.
Cu4	0.69	0.53	0.42	0.09	0.014	0.002	Bal.

Compression tests were performed on cylindrical samples using a Gleeble^{TM} 3800 thermomechanical simulator at temperatures of 450°C and 550°C, with strain rates of 0.1, 1, and 10 s^{-1}, up to a true strain of 0.8. These parameters were selected based on industrial practices for 6xxx Al conductors and prior studies [36, 37]. Compression tests were performed at 450°C (below Mg_2Si solvus, equilibrium Mg_2Si remains) and 550°C (above solvus, Mg_2Si fully dissolves) [38]. Tests at 500°C were additionally performed to support a

more accurate activation energy calculation but were excluded from mechanical/microstructural analysis due to their proximity to the solvus, where Mg_2Si dissolution is uncertain and beyond our scope. The specimens were heated at a rate of 2 ℃/s and held for 3 min at the target temperature to establish a uniform temperature distribution before compression. After deformation, the samples were rapidly cooled with water spray to preserve the deformed microstructure. Graphite foils were placed between the cylindrical samples and the anvils to minimize friction during deformation. For each deformation condition, tests were repeated on three samples. Then, the compressed samples were directly subjected to artificial isothermal aging at 185 °C, representing the T5 temper, an industrially practical procedure aimed at minimizing energy consumption and processing steps while enhancing productivity.

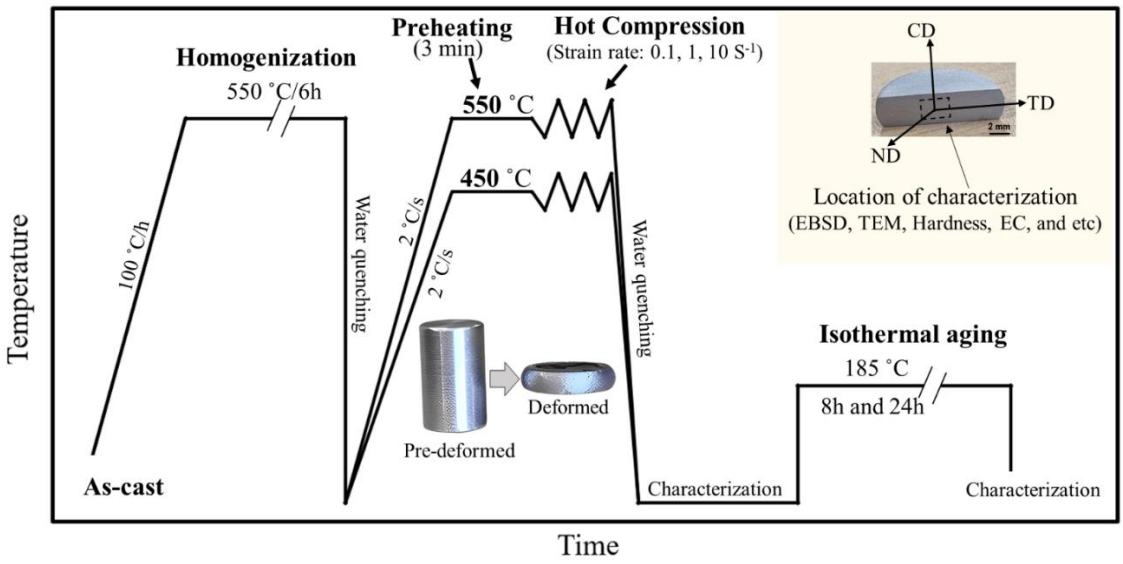

Figure 4-1.Schematic diagram illustrating the experimental process and study approach for the investigated alloys and the orientation of characterization planes (inset), including CD (Compression Direction), ND (Normal Direction), and TD (Transverse Direction).

For the characterization of hot-deformed samples, including microstructural analysis, electrical property evaluation, and microhardness measurements, all samples were sectioned parallel to the compression axis, and the center of each sample was analyzed, as shown in Figure 4-1.

The Vickers microhardness was measured with a 25 g load and a 20-second dwell time. The average hardness values were determined from eight indentations. The EC of the samples

was measured using the Sigmascope method at a frequency of 480 kHz at 21 ˚C, following ASTM E1004. The average EC values were calculated from ten measurements.

For the microstructural investigation, samples were prepared following a standard metallographic procedure and analyzed using optical microscopy (Nikon^{TM}-Eclipse^{TM} ME600) and scanning electron microscopy (SEM, JEOL^{TM}-6480LV). To examine the coarse equilibrium β-Mg_2Si precipitates and intermetallic phases, the samples were observed after etching with Keller's reagent for 20 seconds. The electron backscatter diffraction (EBSD) analysis was performed on a plane perpendicular to the normal direction (ND), as shown in Figure 4-1, to evaluate the grain and subgrain structures with the step sizes of 1 and 1.6 μm. During analysis, the samples were tilted 70° from the horizontal plane. Orientation maps with over 80% reliable indexed data were acquired using HKL technology, and Channel 5 Tango software applied standard noise reduction by replacing poorly indexed or unindexed points with neighboring valid data. Boundaries and sub-boundaries were categorized based on their misorientation angles as low-angle grain boundaries (LAGBs: 2–5°), medium-angle grain boundaries (MAGBs: 5–15°), and high-angle grain boundaries (HAGBs: >15°). Misorientation angles greater than 15° were excluded from the calculation of the mean misorientation angle, as they were considered to be high-angle grain boundaries.

A transmission electron microscope (TEM, JEM 2100) operating at 200 kV was used to investigate the precipitates. TEM-EDS was also employed to determine the chemical compositions of the precipitates formed during hot deformation. For TEM observation, the samples were mechanically ground into thin discs (35–60 μm thick) and subsequently electropolished using a twin-jet system at 15 V and −20 to −25 °C in a solution of 30% nitric acid and 70% methanol. Bright-field images were captured near the [001] zone axis of α-Al matrix to examine the precipitates. The statistical analysis of the length (l) and cross-sectional diameter (d) of the precipitates was performed on the TEM images using an image analysis software (Image J). The number density (ρ) and volume fraction (V_f) of precipitates were calculated by the following equations, respectively [37]:

$$\rho = \frac{3N}{A(t+\lambda)} \qquad (1)$$

$$V_f = \rho V_P = \rho A_P \lambda \quad (2)$$

Where N is the number of needle-like precipitates in the <001> zone axis perpendicular to the image plane, t is the thickness of the foil, A is the area of the matrix containing the precipitates, λ is the average length of the precipitates, V_P is volume of the precipitates and A_P is the average cross-sectional area of the precipitates. The foil thickness (t) was measured using the convergent beam electron diffraction (CBED) technique. For each TEM sample, at least four images were selected from the study area indicated in Figure *4-1*.

Differential scanning calorimetry (DSC) was also utilized to investigate the microstructural features, using a Mettler Toledo™ system in an argon atmosphere. DSC was conducted three times for each condition to verify the repeatability and accuracy of the results. The temperature range for the DSC measurements was 25°C to 600°C, with a heating rate of 10°C/min. The sample weights ranged from 15 mg to 25 mg. The DSC results were normalized by dividing the heat flow signal by the sample weight for each test.

Furthermore, Thermo-Calc™ with TCAL7 database was also employed to predict phase stability and transformation temperatures for the studied alloys, providing an understanding of phase equilibria and thermodynamic behavior essential for optimizing alloy design and heat treatment processes.

4.3. Results

4.3.1. Microstructure in the as-cast and homogenized conditions

Figure 4-2 shows the representative as-cast and homogenized microstructures of the Al-Mg-Si-Cu alloy Cu1 and Cu4. The microstructure of the as-cast sample, shown in Figure 4-2 (a-c), includes a dark, skeleton-like phase identified as primary Mg_2Si as well as a needle-like phase identified as Fe-bearing intermetallics (see supplementary Figure S1) [39, 40]. Some equilibrium β-Mg_2Si particles were also observed precipitating near the interdendritic regions, as shown in Figure 4-2 (c); however, they were present in very small amounts. Additionally, EDS mapping revealed the presence of Cu-rich phases in the microstructure of the as-cast Cu4 alloy as shown in Figure 4-2 (d). These findings are in agreement with previous studies on various Fe/Cu-bearing intermetallics in Al-Mg-Si-Cu alloys [17, 25].

The microstructures after homogenization, shown in Figure 4-2 (e)-(f), mainly consisted of an α-Al matrix, with Fe/Cu-bearing intermetallics. The segregation of Mg and Si elements has disappeared after homogenization, and the eutectic Mg_2Si phases previously located at the grain boundaries have mostly dissolved into the Al matrix. The remaining insoluble second phases were also uniformly distributed along the grain boundaries and within the grains. Furthermore, Figure 4-2 (g) illustrates the grain structure of the homogenized Cu1 alloy, characterized by coarse equiaxed grains with an average grain size of approximately 89 μm.

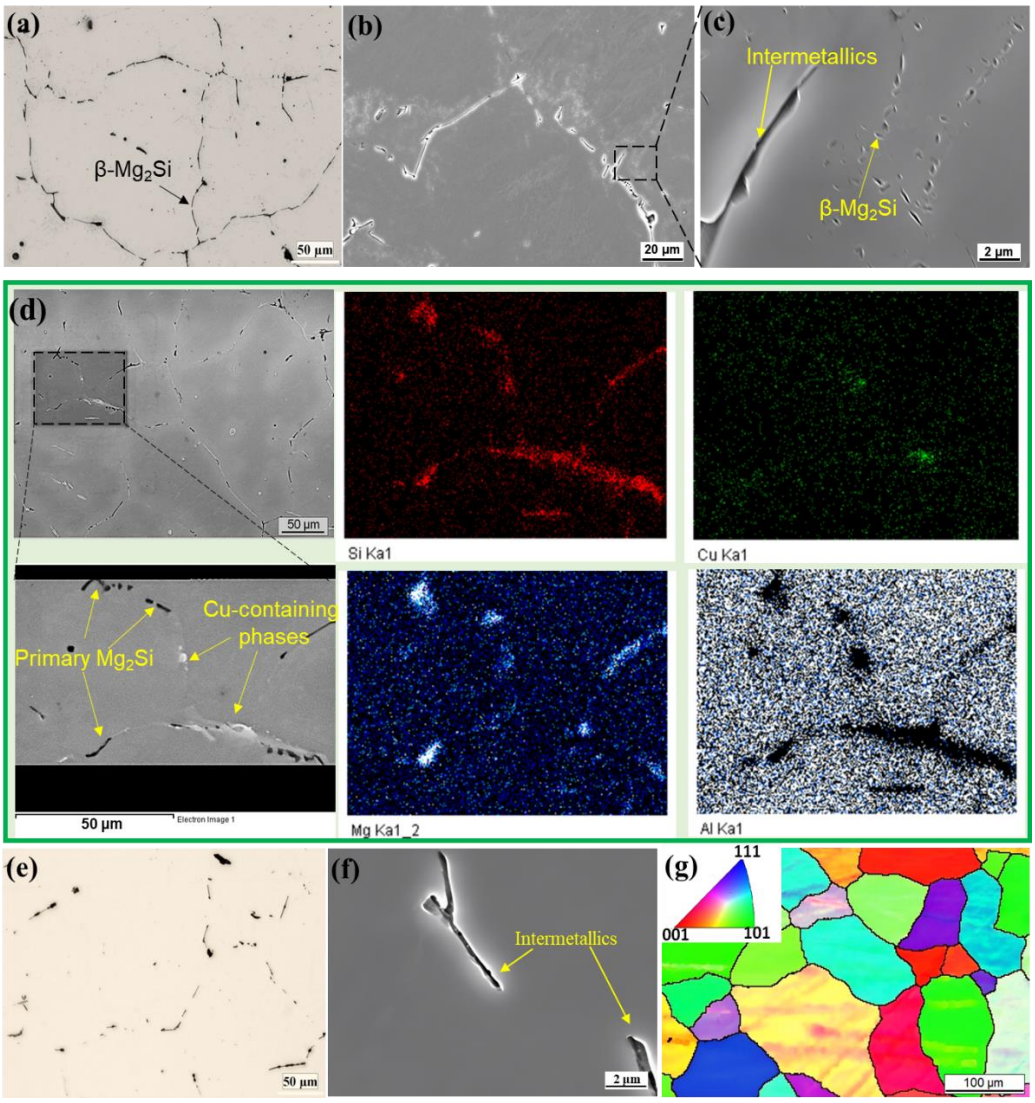

Figure 4-2. OM and SEM images of the Cu1 alloy: (a)-(c) as-cast condition, (d) microstructure of as-cast Cu4 and corresponding EDS mapping revealing regions enriched with Cu, Mg, and Si. (e)-(f) homogenized condition and (g) IPF map of the homogenized Cu1 alloy.

4.3.2. Flow stress behavior

Uniaxial hot compression tests were conducted on conductor alloys with varying Cu contents at deformation temperatures of 450 to 550°C and strain rates from 0.1, 1 and 10 s^{-1}. Figure 4-3 shows typical true stress-strain curves of the alloys. The flow stress behavior is influenced by the deformation temperature, strain rate, and Cu content. The initial deformation process showed a sharp rise in flow stress due to the predominant work hardening during the initial stages of deformation, induced by the multiplication of dislocations and a substantial increase in the dislocation number density [37, 41]. After the initial stage and a sharp increase in stress, the true stress-strain curves revealed three distinct trends corresponding to different strain rates in the subsequent step: (1) A steady-state plateau, characterized by a relatively stable plateau of flow stress, which persisted until the end of the deformation process. This phenomenon was observed under the strain rate of 0.1 s^{-1}, as shown in Figure 4-3 (a). The plateau of the flow stress represents a dynamic equilibrium between work-hardening and softening mechanism [42]. (2) A slow but steady rise in flow stress was observed with continued strain, which was often observed at a strain rate of 1 s^{-1}, as illustrated in Figure 4-3 (b). This steady increase suggests that work hardening is the main mechanism, dominating over softening processes [32]. (3) The third observed trend, which can be seen in Figure 4-3 (c), is a gradually rising stress up to a peak around a strain of 0.5, followed by a gradually declining stress trend that persists until the end of the deformation process. These results indicate that up to a strain of 0.5, hardening mechanisms were dominant over softening mechanisms. Then softening behavior appears in dynamic balance with work hardening [43]. However, beyond this point, softening mechanisms take precedence.

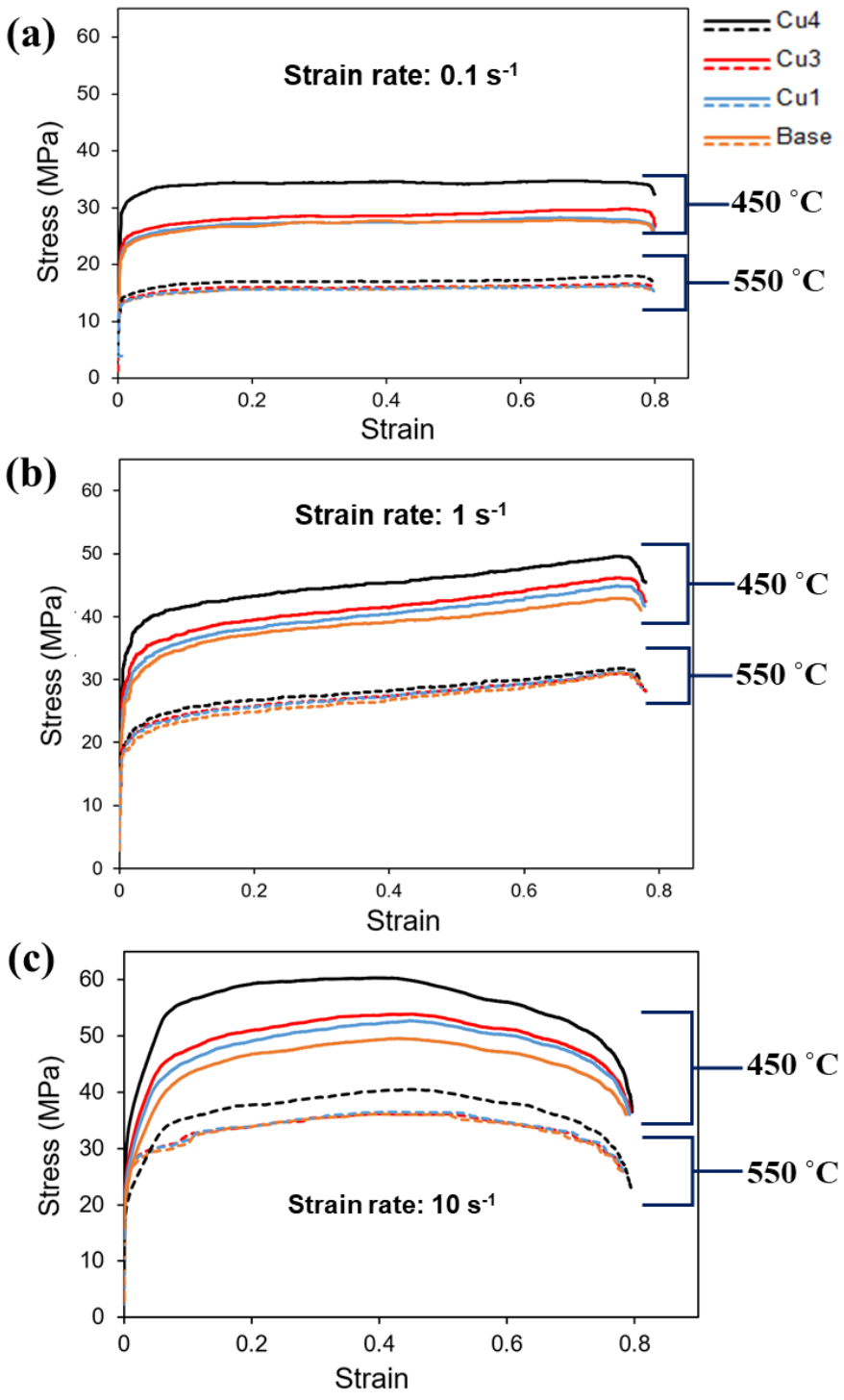

Figure 4-3. True stress-strain curves of Al-Mg-Si alloys with varying Cu contents, deformed at temperatures of 450°C and 550°C, at strain rates of (a) 0.1 s^{-1}, (b) 1 s^{-1}, and (c) 10 s^{-1}.

According to the Figure 4-3, in general, the flow stress tends to decrease with an increase in deformation temperature, whereas it tends to increase with a higher strain rate. An increase in the temperature promoted dynamic recovery and recrystallization processes [34]. For a

given temperature, an increase in the strain rate increased the flow stress due to accelerated dislocation interactions and multiplication, resulting in a higher density of dislocations [32, 34].

Figure 4-4 shows the variation in peak flow stress of the studied alloys with different Cu contents. The peak flow stress at the deformation temperature of 450°C, indicated by the solid line in Figure 4-4, exhibited a slight increase (7-8.2%) with Cu content up to 0.3% compared to the base alloy. However, beyond 0.3% Cu (Cu4), a significant increase in peak flow stress was observed (15-25.2%), demonstrating the higher effectiveness of Cu in inhibiting softening mechanisms at concentrations above 0.3%. For alloys deformed at 550°C (indicated by the dashed lines in Figure 4-4), the peak flow stress exhibited only a slight increase with Cu content, even for the Cu4 alloy. For instance, the peak flow stress at strain rates of 0.1 s^{-1} and 1 s^{-1} showed increments of 1.5 MPa and 1.1 MPa, respectively, which is less than 4%. This suggests that Cu is less effective at inhibiting softening mechanisms at elevated temperatures.

According to these results, the influence of alloying elements like Cu on the flow stress behavior depends on various factors, including concentration, temperature, and strain rate. These factors affect strengthening mechanisms such as solid solution strengthening, precipitation strengthening, and work hardening [31, 42, 44]. Additional explanations are provided in Sections 3.5 and 4.1.

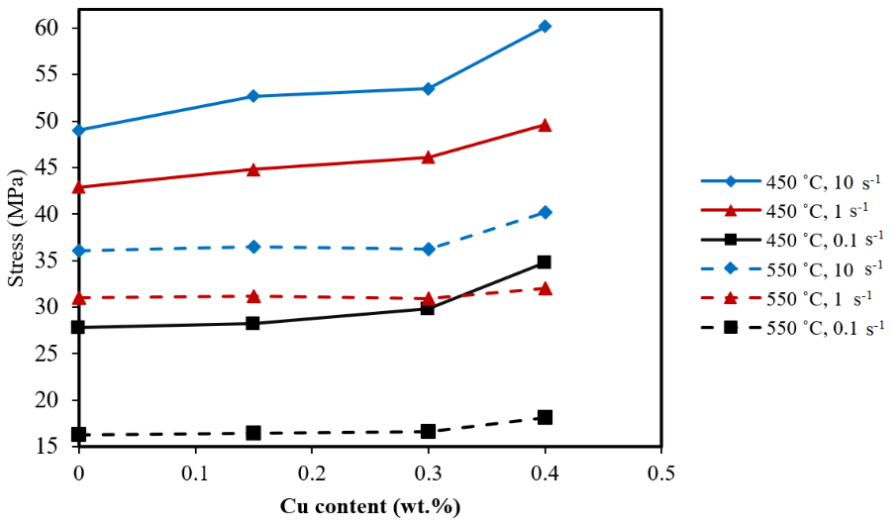

Figure 4-4. The effect of varying Cu content on the peak flow stresses of Al-Mg-Si alloys deformed at 450°C and 550°C.

4.3.3. Constitutive analyses

Constitutive equations are useful to indicate the influences of the deformation parameters on the state of the flow stress. The hyperbolic sine Arrhenius type equation proposed by Sellars and McTegart [45], known as the Zener-Hollomon parameter (Z), is commonly used to describe the relationship between strain rate, deformation temperature, and flow stress in similar 6xxx series alloys [46-48]. It captures the combined effects of temperature and strain rate over wide ranges [42, 49]. The equation is expressed as follows [45]:

$$Z = \dot{\varepsilon} \exp\left(\frac{Q}{RT}\right) = A\left[\sinh(\alpha\sigma)\right]^n \qquad (3)$$

where $\dot{\varepsilon}$ is the deformation strain rate (s^{-1}), A and n are constants, α is a stress multiplier, σ is the flow stress (MPa), Q is the activation energy for hot deformation (kJ mol^{-1}), R is the universal gas constant (8.314 J mol^{-1} K^{-1}) and T is the absolute temperature (K). Here, the peak stress σ_p is used as the σ term, commonly applied in Al alloys, and represents a dynamic equilibrium between work hardening and dynamic restoration [50].

The material constants and activation energy in Eq. (3) can be determined for all the alloys studied using experimental data from hot compression tests under various deformation conditions. The following outlines the solution procedure for determining these material constants and the activation energy, using the Al-Mg-Si base alloy as an example. In this study, the value of σ is derived from the peak flow stress. The stress multiplier α can be calculated using the equation $\alpha=\beta/n_1$, where the values of β and n_1 are obtained from the slopes of the lines in the $\ln\dot{\varepsilon} - \sigma$ and $\ln\dot{\varepsilon} - \ln\sigma$ plots, respectively. Therefore, the mean values of n_1 and β can be obtained from Figure 4-5 (a) and (b), respectively. The average values of β and n_1 at different temperatures were found to be 0.221 and 6.84, respectively. Thus, α was calculated as $\alpha = \beta/n_1 = 0.032$ MPa^{-1} for base alloy. This multiplier was recalculated for each composition based on the corresponding fitted slope.

Differentiating Eq. (3) results in the following equation:

$$Q = R\left[\frac{\partial \ln \dot{\varepsilon}}{\partial \ln[\sinh(\alpha\sigma)]}\right]_T \left[\frac{\partial \ln[\sinh(\alpha\sigma_p)}{\partial\left(\frac{1}{T}\right)}\right]_{\dot{\varepsilon}} = RnS \quad (4)$$

where R is a universal gas constant, n is the mean slope of the plots of $ln\dot{\varepsilon} - ln\left[sinh(\alpha\sigma)\right]$ at various temperatures and S is the mean slope of the plots of $ln\left[sinh(\alpha\sigma)\right] - 1000/T$ at different strain rates. The mean slope of the $ln\dot{\varepsilon} - ln\left[sinh(\alpha\sigma)\right]$ gives the n value of 5.08 (Figure 4-5 (c)). Additionally, the mean slope of the $ln\left[sinh(\alpha\sigma)\right] - 1000/T$ plot at all strain rates was calculated to obtain S = 3.23 (Figure 4-5 (d)). The activation energy can then be determined using Eq. (4).

Taking the natural logarithm of both sides of Eq. (3) yields:

$$\ln Z = \ln\ \dot{\varepsilon} + \frac{Q}{RT} = \ln A + n \ln\left[\sinh(\alpha\sigma_p)\right] \quad (5)$$

Figure 4-6 illustrates the linear correlation between $\ln Z$ and $\ln\left[\sinh(\alpha\sigma)\right]$. The value of $\ln A$ can be obtained from the intercept of the $\ln Z$ vs. $\ln\left[\sinh(\alpha\sigma)\right]$ plot.

Similarly, the material constants α, n, A, and Q (activation energy) were computed for all the alloys studied. These values are listed in Table 4-2.

The hot deformation activation energy is an important parameter in understanding the mechanisms controlling deformation processes at elevated temperatures associated with microstructural evolution, especially the dislocation movement, DRV, and DRX [31, 51]. This feature indicates the difficulty of the hot deformation process and refers to the energy required to initiate and sustain the deformation process at elevated temperatures [31, 50]. Figure 4-7 illustrates the variation in hot deformation activation energy as a function of alloy Cu content. As shown, the activation energy for the base alloy is 136.42 kJ/mol. With an increase in Cu content, the activation energy also rises. This increase is attributed to lattice distortion caused by Cu solute atoms at 550°C and Cu-bearing phases/Cu solute at 450°C, which enhance resistance to dislocation movement and raise both the flow stress and

activation energy during deformation [44, 52]. The addition of 0.15%, 0.3%, and 0.4% Cu increases the activation energy by 7.47 kJ/mol, 19.94 kJ/mol, and 36.9 kJ/mol, respectively, compared to the base alloy, resulting in activation energies of 143.9 kJ/mol, 156.4 kJ/mol, and 173.3 kJ/mol. While 0.15% Cu had a slight effect, 0.4% Cu (along with the extra Si in alloy Cu4) resulted in a significant increase in the activation energy of hot deformation. The addition of 0.3% Cu to the base alloy moderately increased the activation energy from 136.42 to 156.36 kJ/mol.

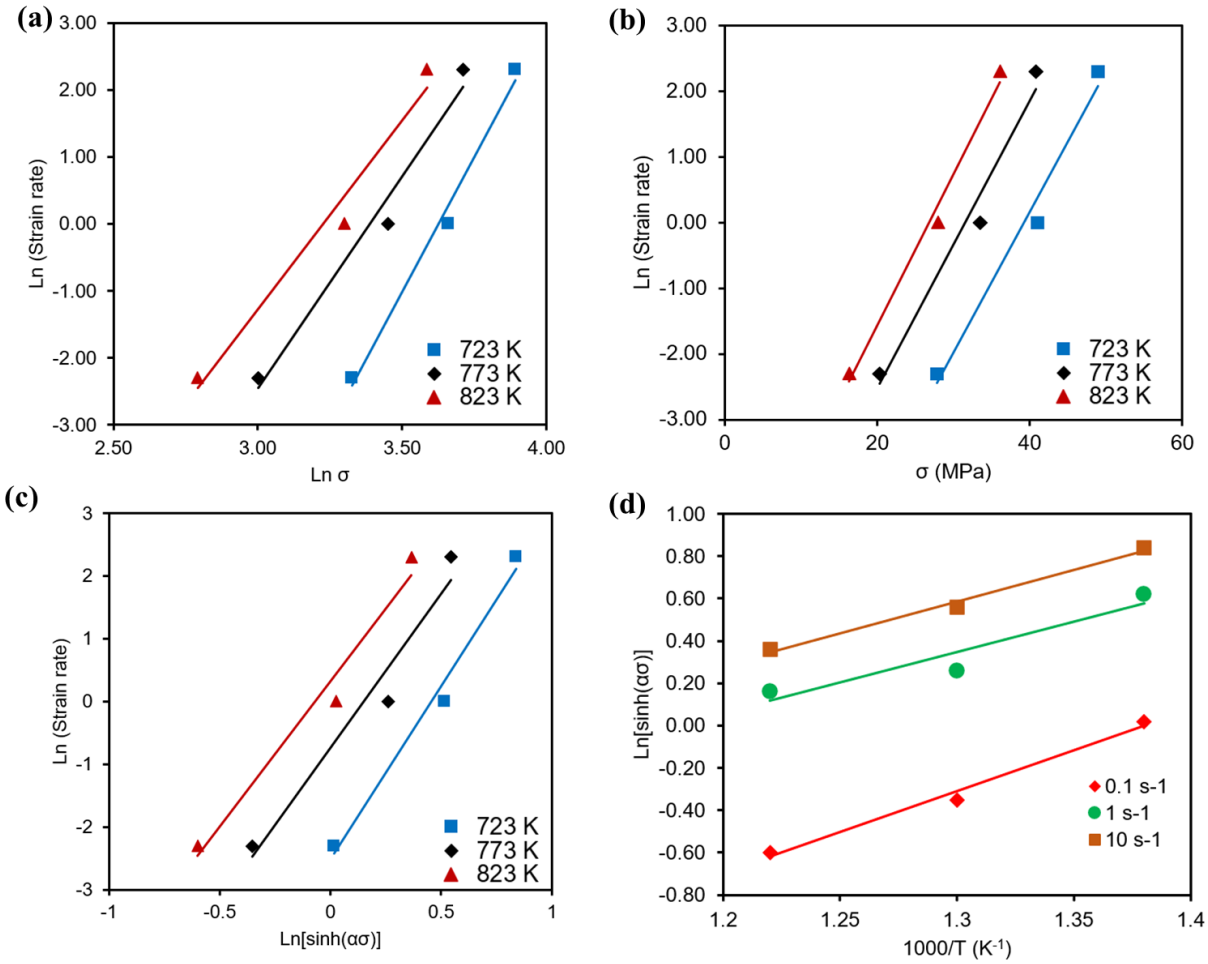

Figure 4-5. Relationships between a) $\ln \dot{\varepsilon}$ and $\ln \sigma$, b) $\ln \dot{\varepsilon}$ and σ, c) $\ln \dot{\varepsilon}$ and ln[sinh (ασ)] and d) ln[sinh (ασ)] and 1000/T.

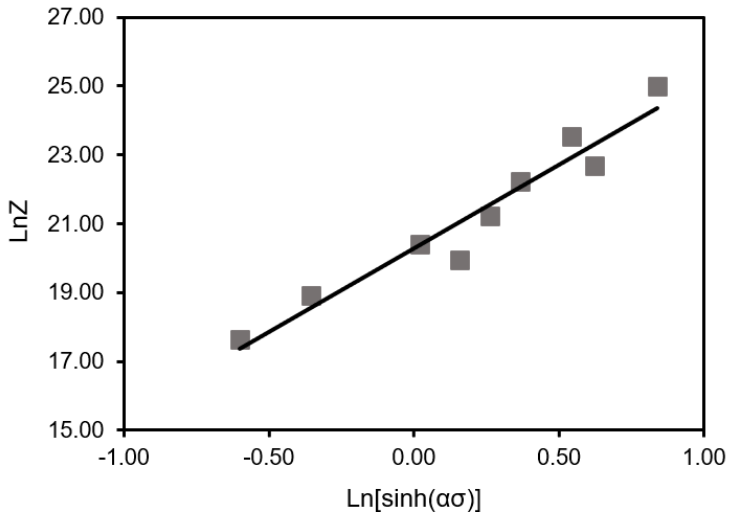

Figure 4-6. Relationship between $\ln Z$ vs. ln[sinh (ασ)].

Table 4-2. Values of material constants and the hot deformation activation energy of the four alloys studied.

Alloys	A (s^{-1})	N	α (MPa^{-1})	Q (kJ mol^{-1})
Base	5.81E+08	5.08	0.032	136.4
Cu1	1.39E+09	4.64	0.033	143.9
Cu3	8.45E+09	4.69	0.033	156.4
Cu4	1.49E+11	4.94	0.028	173.3

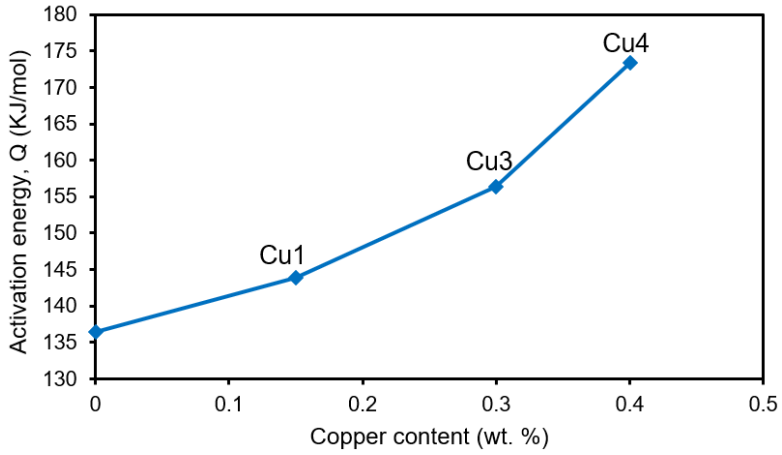

Figure 4-7. The hot deformation activation energy of Al-Mg-Si alloys as a function of Cu content

4.3.4. Hardness and EC evolution during isothermal aging of hot-deformed alloys

The microhardness and EC results for all hot-deformed alloys after 8 and 24 hours aging at 185°C are summarized in Figure 4-8. Hot-deformed alloys, after being water quenched from an elevated temperature, are directly aged without solution heat treatment. The Cu4 hot-deformed alloy shows significantly higher hardness compared to the other alloys after 8 and

24 hours of aging under various deformation conditions. However, it has the lowest EC (46.3-50.6 %IACS), which does not provide the proper EC required for typical Al-Mg-Si conductors after both aging durations. Increasing Cu in 6xxx (Al–Mg–Si) alloys strengthens via both solid solution and precipitation (Mg_2Si+Cu-modified phases). However, higher Cu levels also reduce EC due to increased electron scattering within the atomic lattice of matrix [21, 23]. The minimum EC requirements for Al-Mg-Si conductor alloys, such as 6201 and 6101, are 52.5% IACS and 55% IACS, respectively [6, 28]. Although Cu4 contains slightly more Si (~0.1%) compared to the base, Cu1, and Cu3, research by Khangholi, S.N., et al. [3] on a similar base alloy suggests that this difference has a minor effect on EC and hardness. Instead, Cu is the main factor contributing to the significant reduction in EC and the increase in hardness [53]. Given the importance of EC for the studied alloys, the Cu4 alloy was excluded from further studies. The focus is on comparing the results of the remaining three alloys (base, Cu1, and Cu3), which exhibit reasonable EC for 6xxx conductor alloys. For these three alloys, as shown in Figure 4-8 (a), after 8 hours of aging, the samples deformed at 550°C did not achieve a sufficiently high EC to be considered suitable for Al-Mg-Si conductor alloys. In contrast, the samples deformed at 450°C exceeded 52.5% IACS and approached the 55% threshold required for these conductor alloys after 8 hours of aging. When the aging time was extended to 24 hours, nearly all alloys, except Cu4, achieved the EC of 52.5% IACS, with the base alloy deformed at 450°C reaching 55% IACS, as illustrated in Figure 4-8 (b). While the base alloy demonstrates higher EC (52.3–53.8% IACS after 8 hours and 54.5–55.2% IACS after 24 hours) across various deformation parameters, its hardness remains lower than that of the Cu-containing Al-Mg-Si alloys after both 8 and 24 hours of aging. Among the base, Cu1, and Cu3 alloys, the highest hardness at deformation temperatures of 550°C and 450°C is observed in Cu3 after 8 hours of aging, with values of 84 HV at a strain rate of 0.1 s^{-1} and 77 HV at a strain rate of 10 s^{-1}, respectively. After 24 hours of aging, the highest hardness is also found for Cu3, with values of 82 HV at deformation temperatures of 550°C and 77 HV at 450°C, both at a strain rate of 0.1 s^{-1}.

Two key issues can be addressed here. First, alloys hot-deformed at 550°C exhibit greater hardness (by 6 to 12 HV) and reduced EC (by 1 to 1.8% IACS) after both 8 and 24 hours of aging, compared to those deformed at 450°C. Second, extending the aging time from 8 to 24 hours results in only a slight change in hardness (less than 4 HV), while the EC increases

significantly, by 1 to 2.7% IACS, for the studied alloys. As shown in Figure 4-8 (b), extending the aging time to 24 hours causes the EC values of the alloys deformed at 450°C and 550°C to become more similar, reducing the difference between them. Figure 4-8 (c) provides a detailed illustration of the hardness and EC ranges for the base, Cu1, and Cu3 alloys, all of which meet the acceptable EC of 52.5% IACS. Hot-deformed Cu3 alloys aged at 185°C for 24 hours after deformation at 450°C and 550°C provide the optimal balance between EC and hardness. These alloys not only exhibit sufficient EC for conductor applications but also achieve higher hardness compared to alloy Cu1 and the Cu-free base alloy. If EC is the primary concern, then the green-highlighted region in Figure 4-8 (c), representing the Cu3 alloy deformed at 450°C under strain rates of 0.1, 1, and 10 s^{-1}, is the better choice, offering higher EC with adequate hardness. Conversely, if maximum hardness with the acceptable EC is the priority, then the yellow-highlighted region, corresponding to the Cu3 alloy deformed at 550°C under strain rates of 0.1 and 10 s^{-1}, is the preferred option.

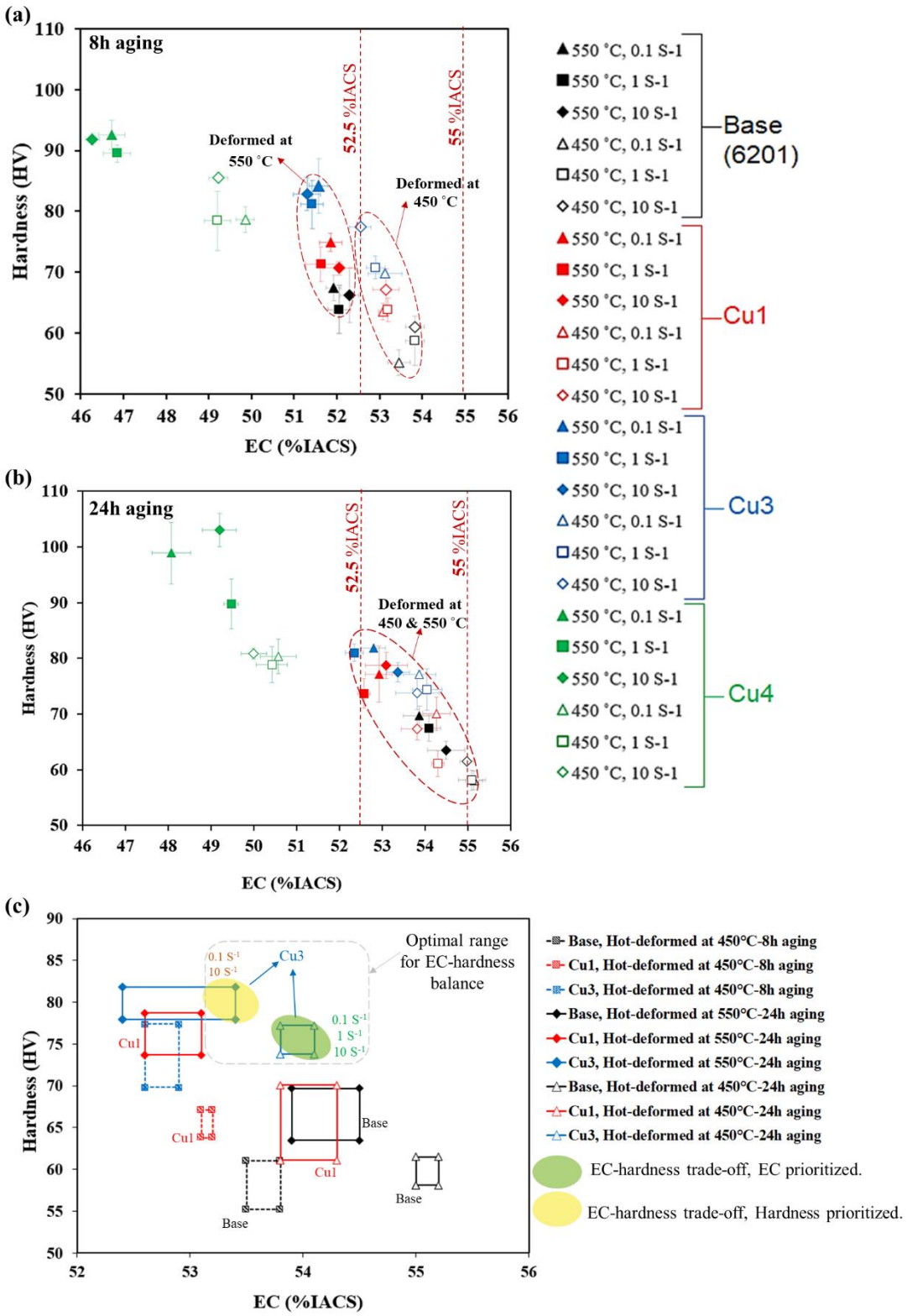

Figure 4-8. Vickers hardness (HV) as a function of EC for all hot-deformed alloys after (a) 8h and (b) 24h of direct aging at 185 ˚C. (c) the range of hardness and EC variations for the alloys shown in (a) and (b) that satisfy the EC of 52.5% IACS.

4.3.5. Microstructural evolution during hot compression test

Figure 4-9 illustrates the EBSD characterization of the hot-deformed alloys with 0, 0.15%, 0.3%, and 0.4% Cu content, deformed at temperatures of 450 ˚C and 550 ˚C with a strain rate of 1 s^{-1}. The inverse pole figure (IPF) maps reveal that the deformed microstructures of all alloys, when deformed at a given temperature, appear similar, consisting of pancake-shaped grain structures elongated perpendicular to the compression direction. The original grains experienced severe deformation, leading to a significant increase in the dislocation density, volume of sub-boundaries, and interfaces within all grain interiors. In Figure 4-9, low-angle boundaries (2º–5º), medium-angle boundaries (5º–15º), and high-angle boundaries (>15º) are represented by white, blue, and black lines, respectively. The presence of intense substructures and sub-boundaries in the elongated grains are characteristic of DRV which was the predominant softening mechanism in the alloys. This process includes the annihilation and rearrangement of dislocations into low- and medium-angle subgrain boundaries, reducing dislocation energy [31, 32]. However, DRX was observed along the grain boundaries in the studied hot-deformed alloys. To determine recrystallization behavior, grain orientation spread (GOS) maps were generated for the studied alloys deformed at 450°C and 550°C with a strain rate of 1 s^{-1}, as shown in Figure 4-10. GOS measures the average orientation deviation of all points in a grain from the average orientation of the grain. According to the literature, a GOS value of 2° or less indicates a recrystallized grain, while GOS values between 2° and 15° correspond to a substructured grain, and values above 15° is the indicative of deformed grains [41, 54].

Furthermore, Figure 4-11 shows the misorientation angle distribution, mean misorientation angle, and recrystallization fraction, which vary with Cu content and hot deformation temperature. During hot deformation at 450°C, alloys with high Cu content (Cu3 and Cu4) exhibited high fractions of LAGBs (2–5°) and low fractions of MAGBs (5–15°) and HAGBs (>15°). This misorientation angle behavior suggests that higher Cu content reduces dislocation mobility, delaying subgrain formation, dislocation annihilation, and DRV. These findings are consistent with those of Huang and Humphreys [55], who reported that lower misorientation angles are associated with reduced grain boundary mobility, requiring higher activation energy for the migration of (sub)grain boundaries. On the other hand, the fraction of MAGBs (5–15°) can be an indicator of the extent of DRV. Alloys with lower Cu content

show a higher fraction of MAGBs, indicating increased dislocation movement and climb, leading to DRV. Moreover, the red diagram in Figure 4-11 (a) shows that the mean boundary misorientation angle decreased with the addition of Cu. For Cu1, the mean misorientation angle is 4.05°, whereas for Cu4, it is 3.6°. This reduction suggests a retardation of DRV softening mechanism, which is consistent with the flow stress trends observed in Figure 4-3 and Figure 4-4. The relationship of fraction of LAGBs and the mean misorientation angle in slowing down and retarding DRV during the hot deformation of Al alloys is well-documented in the literature [4, 31, 42]. Furthermore, increasing Cu content reduced subgrain size, as provided in Table 4-3, indicating that Cu retards dynamic recovery and promotes finer subgrain structures, consistent with the trend reported by Shakiba et al. [31].

Although DRV is the predominant softening mechanism during deformation at 450 ˚C, changes in the recrystallization fraction were observed with varying Cu content in the hot deformation of the studied alloys. At 450 ˚C, as illustrated in Figure 4-10 (a), (c), (e), and (g), recrystallization occurred mainly near grain boundaries, which indicate features of discontinuous dynamic recrystallization (DDRX). DDRX results from slower dislocation movement and the accumulation of strain in localized areas under applied stress, driven by mechanisms such as grain boundary bulging, nucleation of new strain-free grains at the boundaries, and subsequent grain growth [56-58]. Additionally, due to localized strain concentration, the triple points served as favorable nucleation sites for DRX. As illustrated in the green curve of Figure 4-11 (a), as Cu content increases, the fraction of recrystallization decreases from 4.5% (Cu1) to 1.2% (Cu3) and 1.0% (Cu4). This trend indicates a reduction in overall DRX with increasing Cu content during hot deformation of studied alloy at 450 ˚C. According to Figure 4-11 (a), for alloys deformed at 450°C, it can be concluded that the addition of Cu delays the softening mechanism by increasing the fraction of LAGBs, reducing the mean misorientation angle, and decreasing the fraction of recrystallization.

As shown in Figure 4-11 (b), the microstructural evolution of alloys deformed at 550°C differs from that of those deformed at 450°C when Cu is added. In the hot-deformed alloys at 550°C, the fraction of LAGBs increases with Cu additions up to 0.15%. However, further increases in Cu content did not lead to a significant rise in the fraction of LAGBs. Moreover, the mean misorientation angle slightly decreased with higher Cu content. Accordingly, no

further retardation of DRV occurred at higher deformation temperatures with increased Cu content.

As illustrated in Figure 4-11 (b), samples deformed at 550°C exhibited greater recrystallization compared to those deformed at 450°C. This is due to the enhanced mobility of grain boundaries at higher temperatures, which promotes both rapid DRV and DRX softening mechanisms [54, 58]. As shown in Figure 4-10 (b), (d), (f), and (h), at the elevated hot deformation temperature of 550°C, recrystallized grains were observed not only along the grain boundaries but also within the grains. Recrystallization within the grains can be a characteristic feature of continuous dynamic recrystallization (CDRX). In contrast to DDRX grains, CDRX grains typically nucleate inside the grain. The high density of dislocations, along with the abundance of LAGBs and subgrains in the refined and deformed grain layers, suggests that the refined grains in this zone are a result of CDRX behavior [58, 59]. Figure 4-10 illustrates that alloys deformed at 550°C, generally exhibit a higher fraction of substructure, indicating that the material is transitioning towards subgrain formation. A significant fraction of substructure shows that the material is in the process of reducing its internal dislocation density and is in the early stages of DRX, prior to the complete formation and replacement of the deformed matrix by new grains [32, 56]. As revealed in Figure 4-11 (b), during deformation at 550°C, the Cu1 alloy exhibited a slight reduction in recrystallization compared to the base alloy. In contrast, the recrystallized fraction in the Cu3 and Cu4 alloys increased marginally, reaching 10.8% and 11.8%, respectively. This indicates that increasing the Cu content from 0.15% to 0.3% and 0.4% was less effective in inhibiting DRX during hot deformation at 550°C. These results indicate that during hot deformation at 550°C, the microstructural characteristics do not change with Cu in a way that delays the softening mechanism. This conclusion is consistent with the flow stress variation with Cu content shown in Figure 4-3 and Figure 4-4, where the flow stress behavior at a strain rate of 1 s^{-1} during the high-temperature deformation shows only slight changes with increasing Cu content.

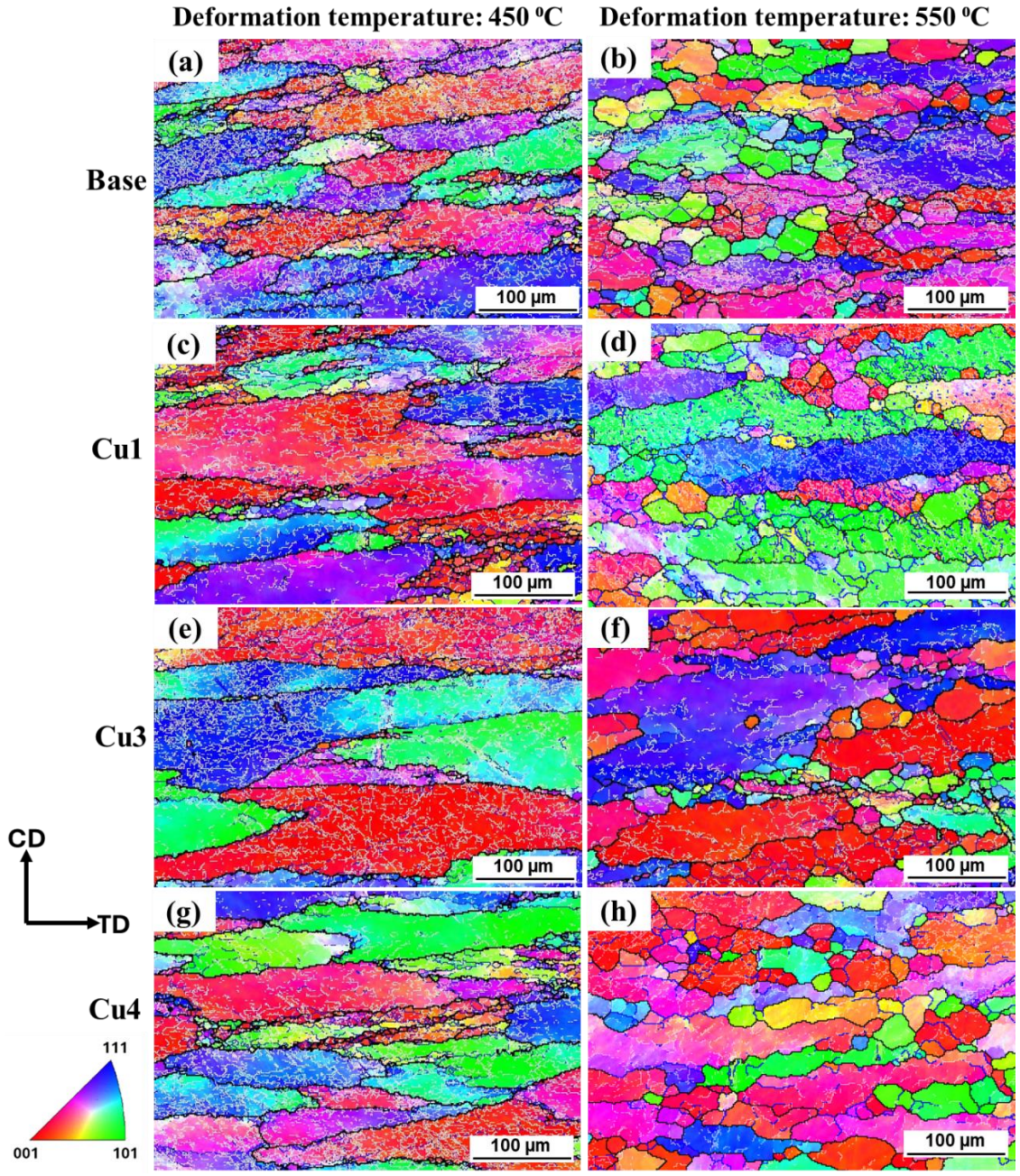

Figure 4-9. EBSD (inverse pole figure) maps of samples deformed at 450°C and 550°C for (a)-(b) Base, (c)-(d) Cu1, (e)-(f) Cu3, and (g)-(h) Cu4 alloys.

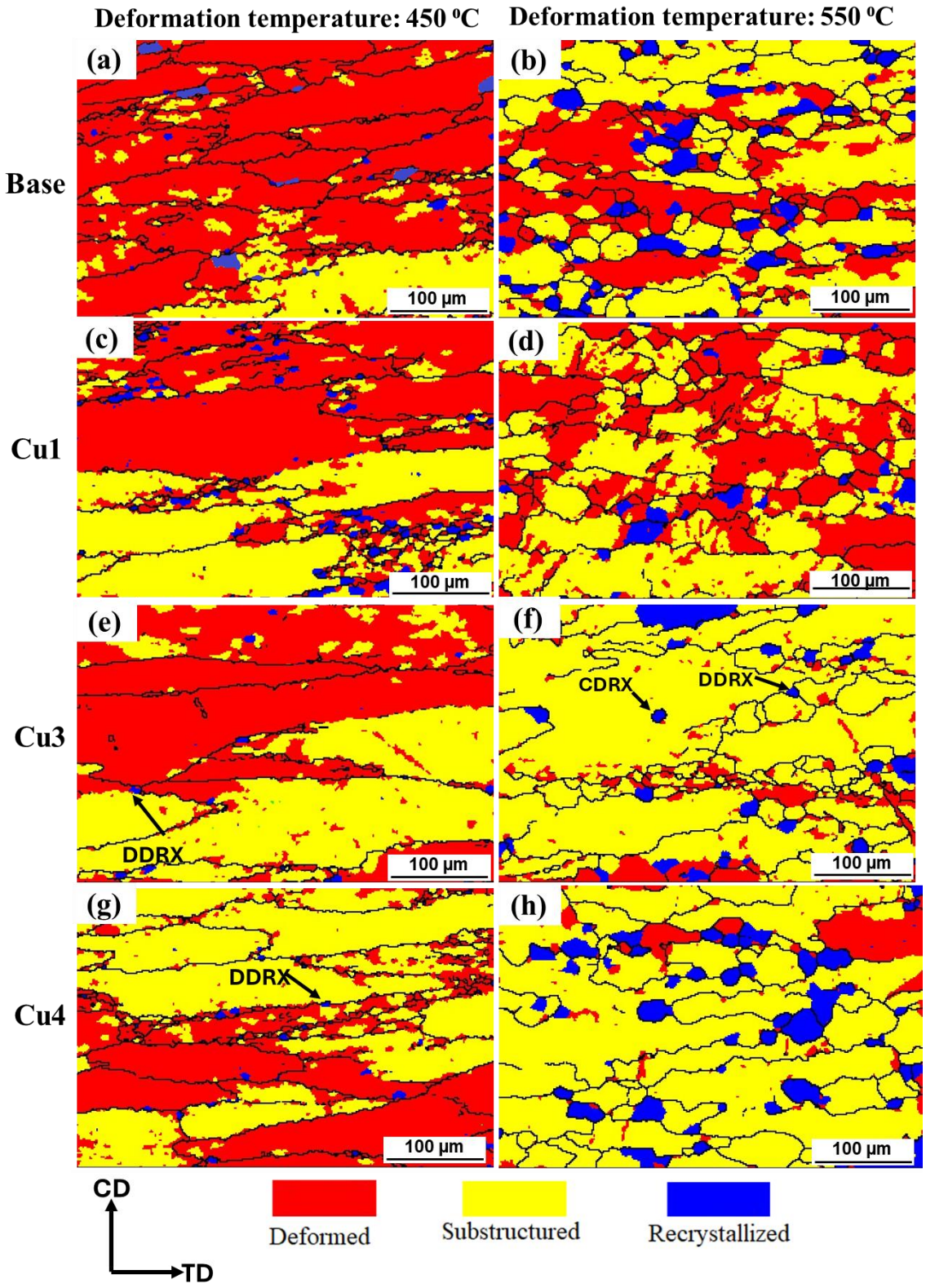

Figure 4-10. GOS maps of samples deformed at 450°C and 550°C for (a)-(b) Base, (c)-(d) Cu1, (e)-(f) Cu3, and (g)-(h) Cu4 alloys

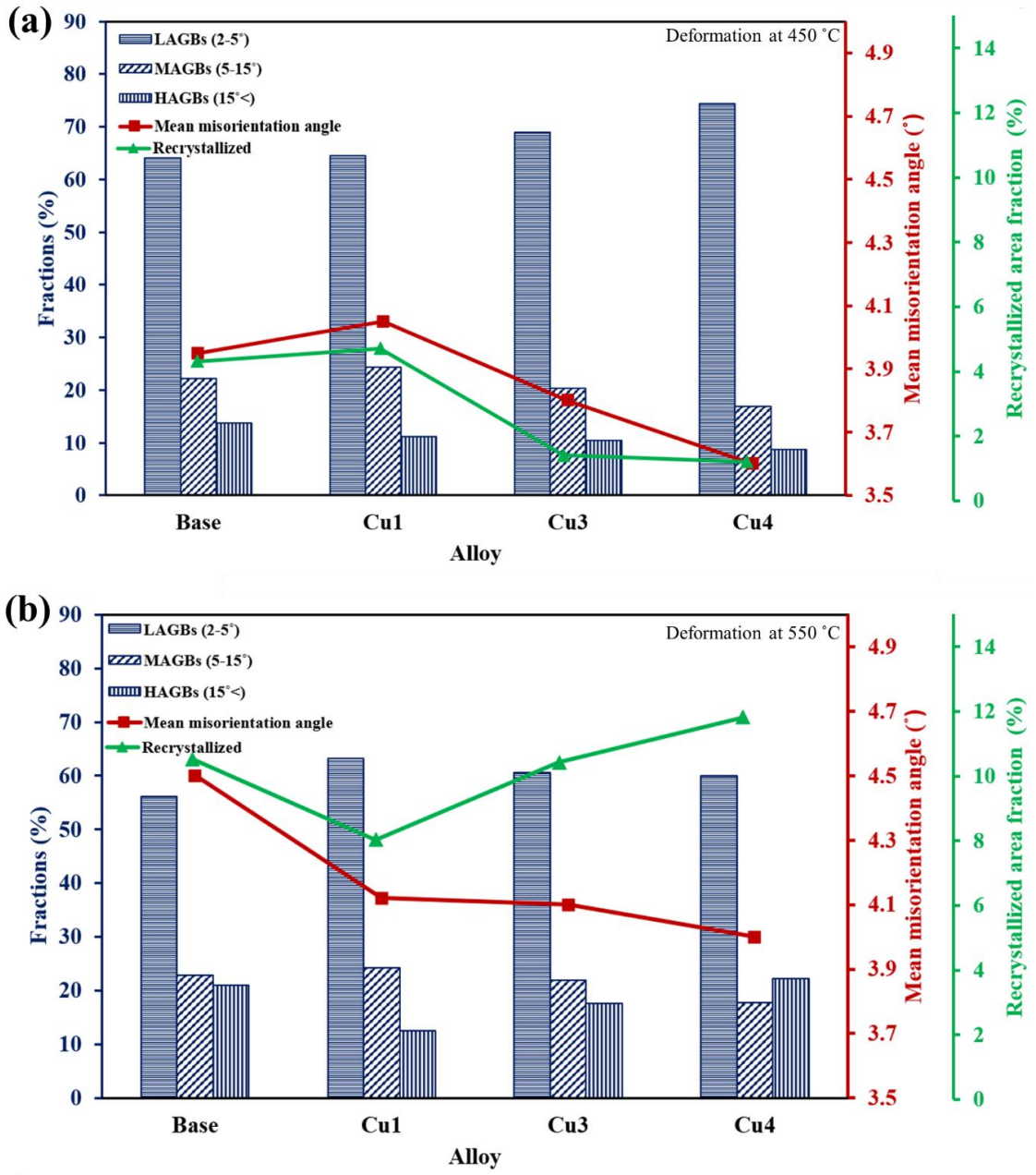

Figure 4-11. The effect of Cu content on the changed of the misorientation angle distribution and mean boundary misorientation angle, a) at 450 ˚C/1 s^{-1} and b) at 550 ˚C/1 s^{-1} conditions.

Table 4-3. Subgrain size of deformed samples at 450 °C and 550 °C.

Alloy	Subgrain Size (μm) at 450 °C	Subgrain Size (μm) at 550 °C
Base	13.7	15.8
Cu1	13.9	14.4
Cu3	13.3	14.2
Cu4	12.6	13.9

4.3.6. Precipitate changes during hot deformation

Figure 4-12 presents the optical microstructures of the base and Cu3 alloys after hot deformation at 450°C and 550°C. Based on the results presented in Section 3.4, the Cu3 alloy emerges as the best candidate, providing the optimal balance between EC and hardness. For this reason, Cu3 was chosen as the representative alloy for studying the evolution of the precipitates during hot deformation. As shown in Figure 4-12, at each deformation temperature (450°C or 550°C), the overall microstructural view, particularly in terms of particle distribution, is similar for both the base and Cu3 alloys. At 450°C, uniformly distributed particles (indicated by the red arrow) formed between the Fe/Cu-rich intermetallic compounds (indicated by the blue arrow). However, at 550°C, these particles nearly disappeared, leaving only the primary intermetallic compounds, as displayed in Figure 4-12 (b) and (d). Such an arrangement of particles in 6xxx alloys has been previously reported at temperatures of 450°C and 550°C [60].

According to the Figure 4-12 (a) and (c), two types of precipitates are observed: small, rounded ones and elongated (rod-shaped) ones. The base alloy shows a higher fraction of small, rounded precipitates, whereas the Cu3 alloy predominantly features elongated (rod-shaped) precipitates. This difference can be attributed to the presence of Cu, which accelerates precipitation in 6xxx alloys, leading to an earlier onset of coarsening compared to the base alloy [21, 23]. This phenomenon was further verified through DSC analysis in Section 3.7. The abundance of small, rounded precipitates in the base alloy microstructure indicates they are in the early stages of coarsening and may adopt a similar elongated morphology if the holding time at 450°C is slightly extended.

The distributed particles, described in Figure 4-12 (a) and (c), were analyzed using TEM-EDS. Figure 4-13 (a) and (b) provides a close-up view of the distributed particles in Cu3, mostly cylindrical in shape. Figure 4-13 (c)-(f) presents the TEM images and their corresponding TEM-EDS analysis (inset) of the various particles and matrix. Most of the particles were identified as cylindrical β-Mg_2Si phases, with a small fraction identified as Si particles. Si-network phases have been previously reported in 6xxx Al-Mg-Si alloys containing Cu with Mg/Si (wt. %) ~1.45 [17, 61]. Additionally, a few polygonal-shaped particles containing Al, Mg, Si, and Cu were detected in the TEM-EDS analysis. According

to the literature, these are likely quaternary Q-phase particles [61, 62]. Figure 4-13 (f) presents the TEM-EDS analysis of the matrix for samples hot-deformed at 450°C, indicating that a significant fraction of Mg and Si solute atoms was removed from the matrix, leaving Cu as the main alloying element. In contrast, in samples hot-deformed at 550°C, these solute atoms (Mg and Si) were dissolved in the matrix, forming a supersaturated solid solution (SSSS) after water quenching. The changes in microstructure during hot deformation at 450°C and 550°C, and how these affect the mechanical and electrical properties of the alloys, are discussed in detail in Section 4.2.

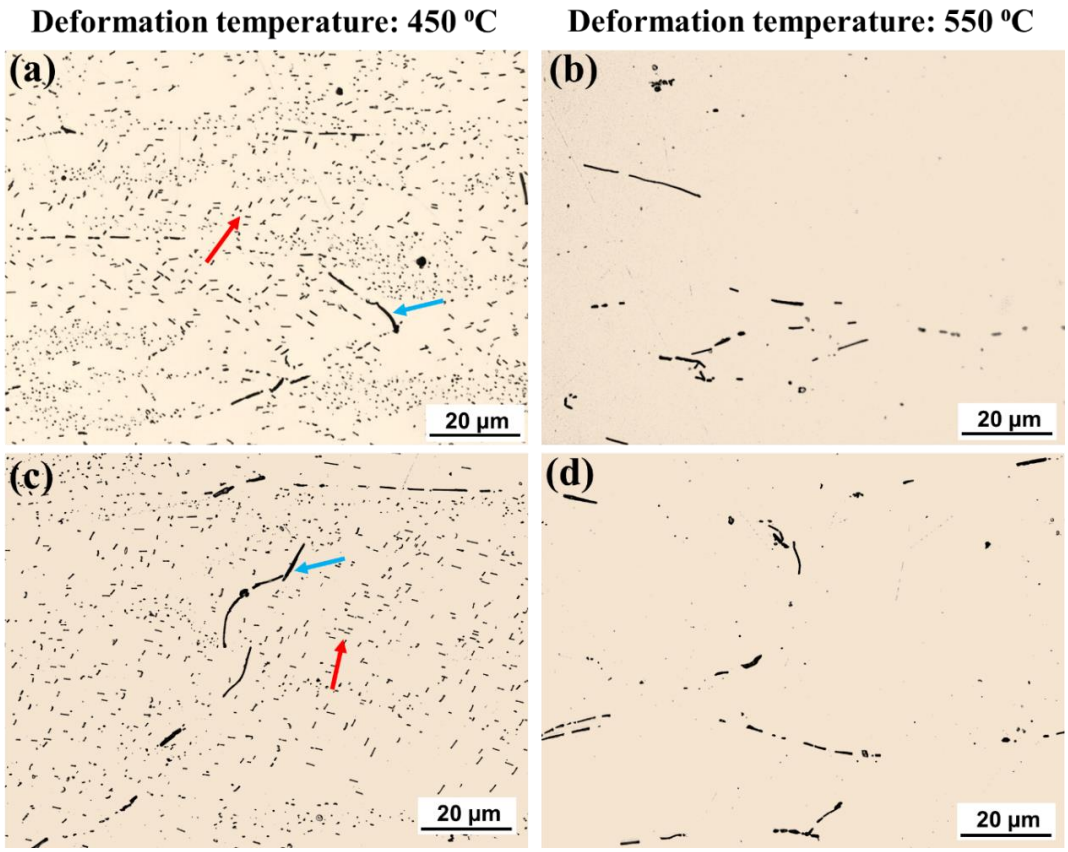

Figure 4-12. Optical micrographs of the base alloy (a-b) and Cu3 alloy (c-d) after hot deformation at 450°C and 550°C with the strain rate of 1 s^{-1}.

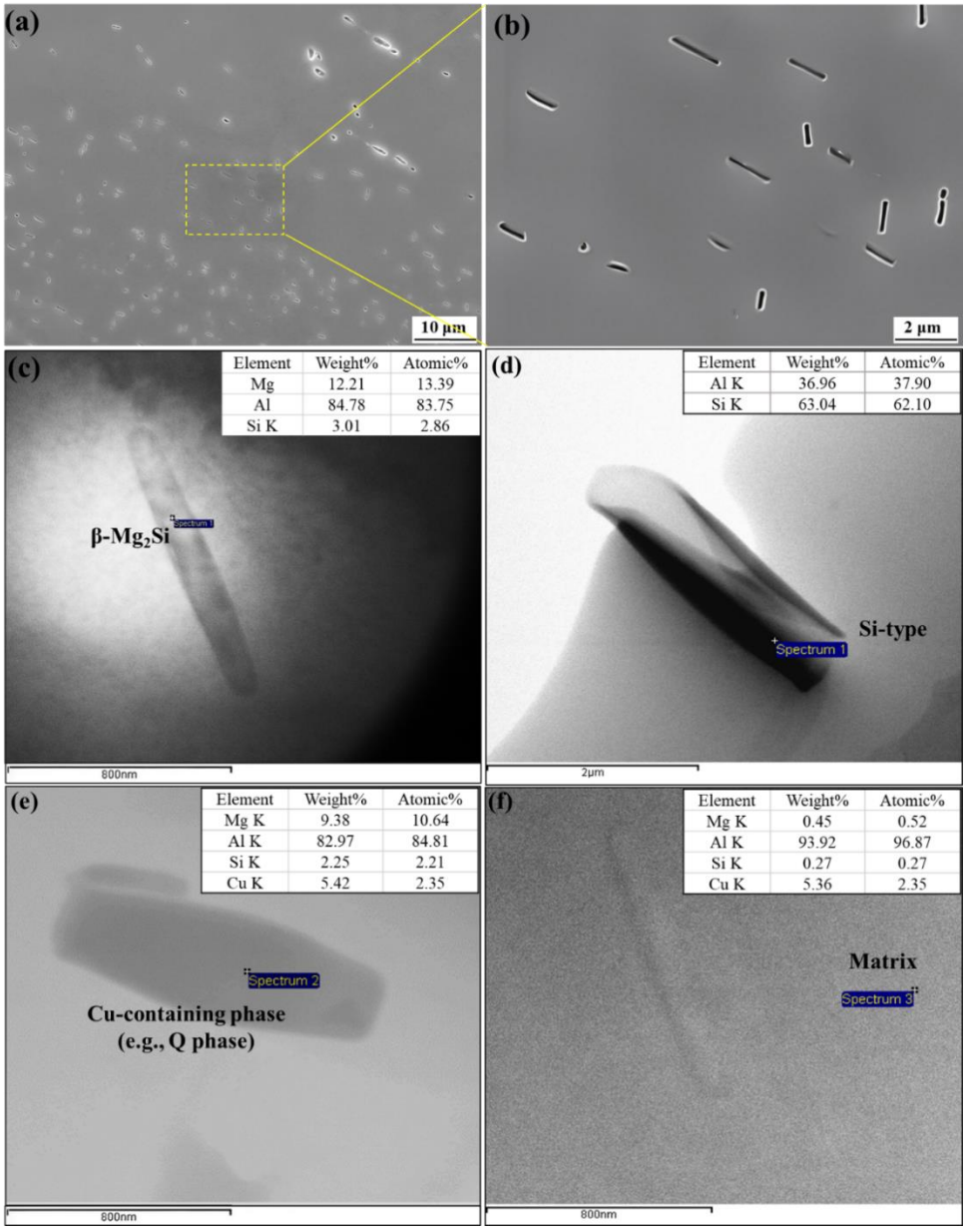

Figure 4-13. (a) and (b) SEM images of the small particles mentioned in Figure 4-12 (c) for the Cu3 alloy; (c)-(f) are TEM images and their corresponding TEM-EDS analysis results (insets) of the selected particles and matrix shown in (a) and (b).

4.3.7. DSC analysis of precipitation evolution during the hot deformation

To further validate the precipitation sequence, DSC analysis was performed to examine phase transformations during heating. The base and Cu3 samples were homogenized, quenched, and heated to 600°C at 10°C/min. Despite differing from hot compression preheating rates, DSC results reveal precipitation behavior in the as-quenched state before deformation. Figure 4-14 (a) presents DSC curves where exothermic peaks A, B, and C correspond to the

formation of β″, β′, and β precipitates, respectively, consistent with the DSC results reported in the literature [63, 64]. A closer examination of exothermic peak A shows that the peak temperatures for β″ precipitation are 277°C for the base alloy and 269°C for the Cu3 alloy. This suggests that Cu additions shifted the β″ peak to lower temperatures, indicating an increase in the precipitation kinetics, as confirmed in [23]. The Cu exhibits a strong interaction energy with Mg and vacancies, which promotes precipitation. It has been reported that Cu addition results in the formation of stable clusters with higher densities and larger sizes during the early stages of aging, which subsequently evolve into numerous precipitates [18, 23]. Peak A has a wider temperature range (from 218°C to 335°C) in Cu3 compared to the base alloy (242°C to 315°C). This may be attributed to additional precipitates associated with Cu, such as Q′, rather than just the single β″ precipitation observed in other 6xxx series alloys [65, 66].

As shown in Figure 4-14 (a), the DSC results of the base and Cu3 alloys display a significant difference at peak C. A dashed blue line was overlaid on the base DSC curve to enhance clarity and facilitate comparison. The base alloy exhibits a larger peak, while the Cu3 alloy shows a shallower and less sharp peak. To investigate this, Thermo-Calc^{TM} software was used to predict the temperature intervals of the main phases in the equilibrium state, as shown in Figure 4-14 (b). An enlarged view of the Thermo-Calc^{TM} in Figure 4-14 (b) indicates that at around 325°C, two phenomena occur simultaneously: the endothermic dissolution of the Q phase and the exothermic formation of Mg_2Si as indicated by the dashed lines. The overlap of these two processes results in a peak with a lower sharpness compared to the DSC of the base alloy at peak C. It is worth mentioning that the temperature range of this overlap differs between the DSC results and the Thermo-Calc^{TM} predictions due to the higher heating rate of the DSC compared to the equilibrium states. In DSC analysis, the transformation occurs at higher temperatures compared to the equilibrium state [25, 66].

The Thermo-Calc^{TM} results presented in Figure 4-14 (b) and (c) reveal the onset of the dissolution of equilibrium precipitates and specify the stable temperature range for the precipitates (θ, Q, and β) in as-homogenized Cu3 alloys. As shown, in the equilibrium state, increasing the temperature leads to the dissolution of two Cu-containing precipitates, θ and Q, above 260°C and 325°C, respectively. However, under actual hot deformation conditions, the dissolution temperatures may be higher than those predicted at equilibrium. Therefore,

alloys deformed at 450°C have the potential to completely dissolve the θ and Q precipitates. Under equilibrium conditions, as predicted by Thermo-Calc™ software, the β phase starts dissolving in the matrix at 330°C but remains stable up to 500°C. Accordingly, at 450°C, some β phase is expected to be present in hot-deformed alloys. However, at 550°C, the β phase also completely dissolved in the matrix. These results are consistent with the microstructure shown in Figure *4-12*.

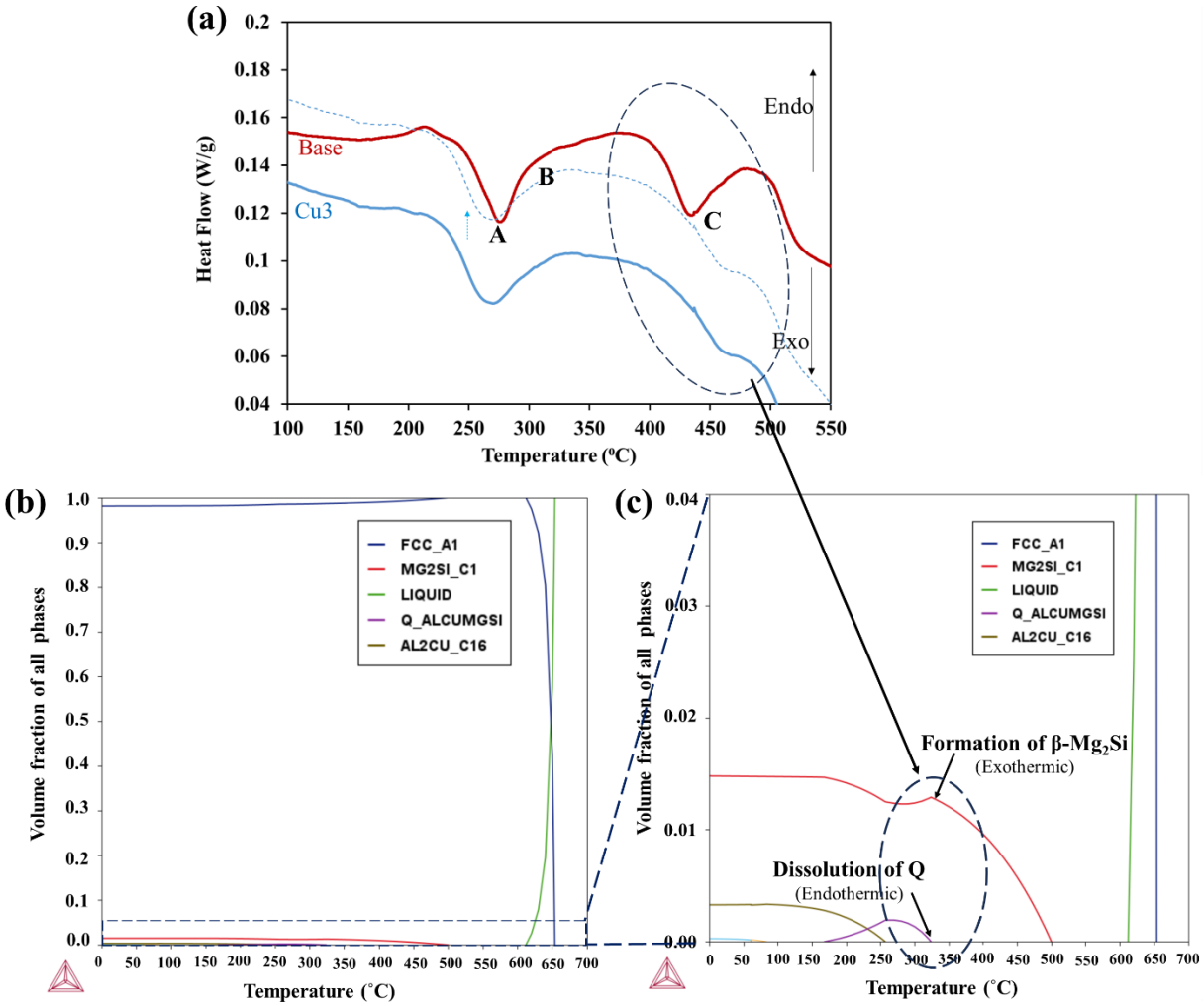

Figure 4-14. (a) DSC analysis of as-homogenized base and Cu3 alloys. (b) Thermo-Calc™ software predictions of temperature interval for the main phases during the heating of the base and Cu3 alloys. (c) An enlarged view of the Thermo-Calc™ results (b) for phases with a volume fraction lower than 0.04.

4.3.8. Precipitation characteristics of aged alloys

Figure 4-15 shows the TEM bright-field images of the Cu3 alloy, which was hot-deformed at 550°C with a strain rate of 1 s^{-1} and subsequently aged at 185°C for 8 and 24 hours. As

discussed in the previous section, the samples hot-deformed at 550°C contain solute atoms (Mg, Si, and Cu) in the matrix, resulting in a supersaturated solid solution after water quenching. The predominant microstructural feature of the alloy after 8 hours of aging (Figure 4-15 (a)) is the gray, needle-like precipitates, which are commonly identified in the literature as the β′ or β″ structure [63, 66, 67]. In the Cu3 alloy, a small number of Q′ phases are predicted, based on previous studies with similar chemistry [23, 24]. After 24 hours of aging, the needle-like precipitates lengthened, and lath-shaped precipitates appeared more frequently in the microstructure. This coarsening of the precipitates indicates a slight degree of overaging. The characteristics of these precipitates, including density, volume fraction, length, and cross-sectional area, have been calculated under these conditions and are summarized in Table 4-4. By prolonging the aging time from 8 to 24 hours, two main phenomena occurred in the microstructure. First, the coarsening of the strengthening phases, characterized by a reduction in number density and an increase in the length and average cross-sectional area of the precipitates. As a result, no further hardening is anticipated, and a slight decrease in hardness expected. Second, the volume fraction of precipitates increased from 0.97% to 1.28%, indicating greater removal of solute atoms from solution, which is beneficial for enhancing EC. These observations are consistent with the hardness and EC trends shown in Figure 4-8.

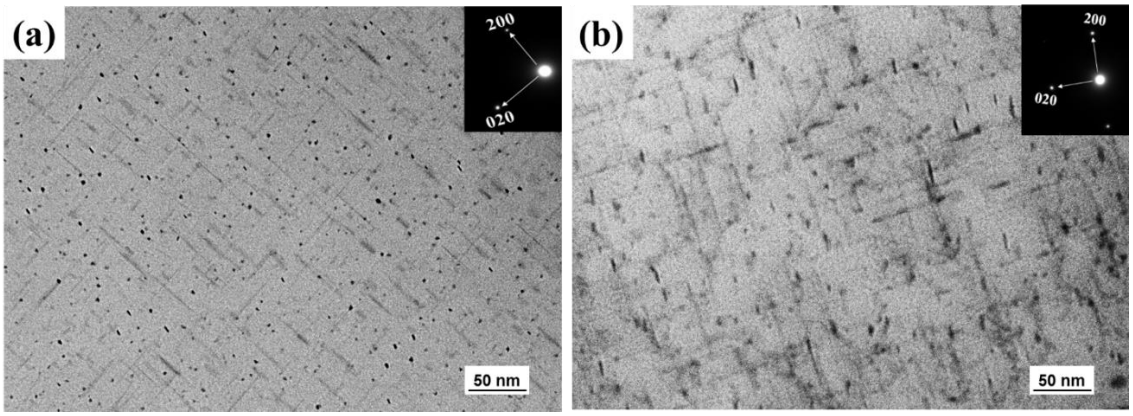

Figure 4-15. Bright-field TEM micrographs of Cu3 alloy, hot-deformed at 550ºC with strain rate of 1 s^{-1}, after (a) 8 h (b) 24 h aging at 185 ºC.

Table 4-4. Characteristics of the precipitates in the Cu3 alloy, hot-deformed at 550ºC with strain rate of $1s^{-1}$, after 8h and 24h aging at 185 ºC

Aging time	Number density of precipitates ($\times 10^{23}$ m^{-3})	Volume fraction of precipitates (%)	Average cross section of precipitates (nm^2)	Length of precipitates (nm)
8h	1.04±0.21	0.97±0.15	4.2±2.4	19.8±9.7
24h	0.42±0.08	1.28±0.12	9.6±7.9	29.7±13.6

According to Figure 4-12 (a) and (c), hot deformation at 450°C resulted in coarse equilibrium precipitates, mostly β-Mg_2Si, and Cu solute atoms, with possible small amounts of Mg and Si in the α-Al matrix. After hot deformation and quenching, the Cu in the matrix remained in a supersaturated solid solution (SSSS) state, which could precipitate during subsequent aging. As shown in the TEM images in Figure 4-16, the equilibrium precipitate-free regions revealed a low number density of nanoscale strengthening precipitates. Therefore, the observed nanoscale precipitates are likely to be Cu-containing needle-like and lath-shaped θ′ and Q′ phases, as reported in the literature [26, 27].

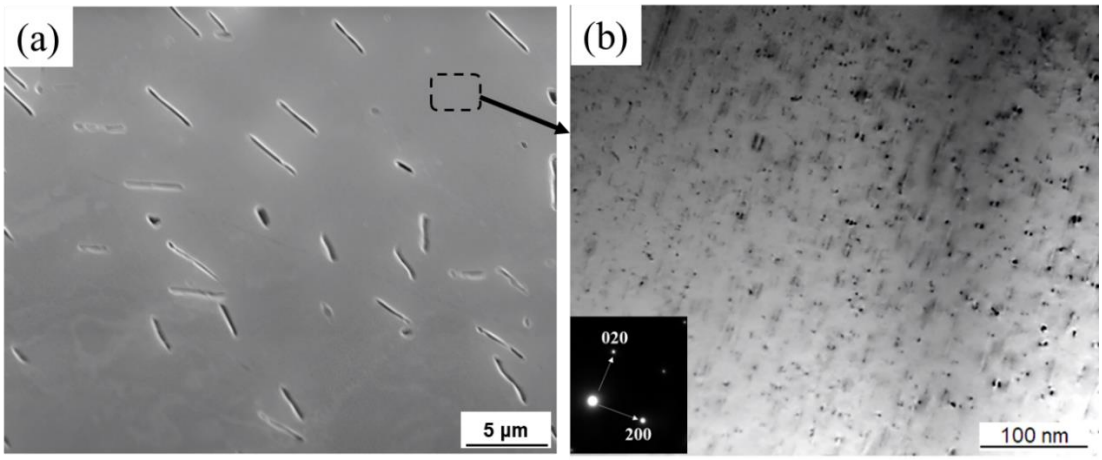

Figure 4-16. (a) SEM image of the microstructure of the Cu3 alloy highlighting the presence of equilibrium precipitates described in Figure 4-13 (b) Bright-field TEM image of the equilibrium precipitate-free region of the Cu3 alloy, hot-deformed at 450ºC with a strain rate of 1 s^{-1}, following 8 hours of aging at 185ºC.

4.4. Discussion

4.4.1. Correlation between Cu content, processing temperature and hot deformation behavior

During hot deformation, the effect of Cu content on the flow stress of Al-Mg-Si alloys varies considerably with temperature, as shown in Figure 4-3 and Figure 4-4. At 450°C, the addition of 0.15 and 0.3 wt.% Cu caused a slight increase in flow stress, whereas 0.4 wt.% Cu along

with some extra Si resulted in a significant increase. Due to the higher diffusivity of Si compared to Cu (7×10^{-14} m^2/s vs. 9×10^{-15} m^2/s) [68], it is assumed that this extra Si in Cu4 reacts with excessive Mg during deformation at 450°C to form equilibrium Mg_2Si. Therefore, Cu also plays a key role in influencing the flow stress in Cu4. In contrast, increasing the hot deformation temperature to 550°C reduced the influence of Cu on flow stress across all concentrations (0.15%, 0.3%, and 0.4%), particularly at lower strain rates of 0.1 and 1 s^{-1}.

Deformation at 450°C resulted in a considerable amount of Cu being incorporated into the matrix as solute atoms. The microstructure is mainly characterized by coarse precipitation of equilibrium Mg_2Si (β) phases at this temperature, which does not contribute significantly to hardness. At 550°C, these Mg_2Si (β) phases also dissolved into the matrix during deformation. Therefore, the flow stress behavior cannot be attributed to precipitation hardening. The strengthening of the studied alloys during hot deformation could mainly be attributed to the solid solution at both 450°C and 550°C. In the research conducted by Odoh et al. [44] and Shakiba et al. [31] on 6xxx and 1xxx alloys, the solute atoms were similarly found to play the primary role in flow stress behavior during hot deformation. Strengthening originates from solute-dislocation interactions and the ability of foreign atoms within the Al crystal lattice to obstruct dislocation motion [44].

The microstructural changes and variations in the composition of the α-Al matrix during hot deformation are schematically presented in Figure 4-17, providing deeper insights into their effects on flow stress. As shown in Figure 4-13 (f) for Cu3, during deformation at 450°C, Cu acts as the main solute atom in the matrix for the studied alloys. A similar TEM-EDS analysis (see Supplementary Figure S2) for Cu4 yielded comparable results, confirming that Cu remains the primary alloying element in the matrix during deformation at 450°C. The presence of Cu introduces lattice distortions due to the atomic size difference between Cu and Al. These distortions create localized stress fields around the Cu solute atoms, which impede dislocation movement. Furthermore, Cu solute atoms can segregate at (sub)grain boundaries during the early stages of hot deformation, reducing the boundary energy and enhancing structural stability [32, 69]. The accumulation of Cu atoms at (sub)grain boundaries hinder the movement of dislocation pile-ups, promoting their multiplication and

acting as a barrier to further movement. Therefore, this leads to an increased work hardening rate and restrained dynamic recovery [70, 71]. Moreover, Cu solute in the Al matrix slows down dislocation motion due to the solute drag effect, which influences the boundary velocity, promoting the formation of finer subgrains during hot deformation which presented in Table 4-3. A grain boundary moves with a velocity (v) in response to the net pressure P acting on it, as described by Humphreys and Hatherly [32] in Eq. 6.

$$v = MP \quad \text{or} \quad v = M\left(P_d - P_{sol}\right) \quad (6)$$

Where M represents the grain boundary mobility, P_d is the driving pressure, and P_{sol} is the retarding pressure caused by the solute drag effect. If the mobility is independent of the driving force, Cu solute atom segregation in (sub)grain boundaries can generate a retarding pressure (P_{sol}) that counteracts the driving pressure for deformation, slowing the boundary velocity and softening [32].

During hot deformation at 450°C, as the Cu content in solution increases, the higher concentration of solute atoms enhances the obstruction of dislocation motion, resulting in a reduced rate of DRV and DRX [31]. The higher stress required to move dislocations is reflected in the increase in activation energy for deformation, as seen in Table 4-2. This study observed that the smaller increase in flow stress of Cu1 and Cu3 alloys, deformed at 450°C, can be attributed to the minimal solute drag effect, resulting from the limited segregation of Cu atoms at (sub)grain boundaries, as shown in Figure 4-17. This arises from the minor difference in Cu diffusivity compared to Al self-diffusion [72]. At low Cu concentrations (Cu1 and Cu3), as the boundaries move, Cu solute atoms diffuse and redistribute to maintain equilibrium within a grain. This redistribution prevents weighty atom segregation and solute clustering near the boundaries, as depicted schematically in Figure 4-17 (e.g. see Cu3, 450°C). Subsequently, boundary migration occurs with minimal hindrance, facilitating softening mechanisms [32, 73, 74].

It seems that, at higher Cu content (0.4%), the slower diffusivity of Cu in Al becomes more pronounced during deformation at 450°C. In the Cu4 alloy, a small fraction of Cu atoms likely diffuses and redistributes within the lattice structure during boundary migration, leading to a non-uniform redistribution of Cu solute atoms and the formation of cluster-like concentration fluctuations near the boundaries, as displayed in Figure 4-17 (see Cu4, 450°C).

These solute clusters act as localized obstacles, akin to the Zener pinning effect, hindering dislocation motion and increasing resistance to boundary migration [32]. This leads to a delay in recovery and recrystallization processes. In other words, for the Cu4 alloy at 450°C, dislocations exhibit reduced mobility, leading to a lower mean misorientation angle, smaller subgrain size, and a higher fraction of LAGBs compared to alloys with lower Cu content, as previously reported in Section 3.5. Consequently, the flow stress increases significantly, likely due to higher resistance of grain boundaries against deformation caused by enhanced pinning effects. Therefore, the different behaviors at lower and higher Cu contents can be attributed to the balance between solute redistribution within the matrix and clustering effects at the boundaries. The results of the present study are consistent with the qualitative predictions of the Cahn–Lücke–Stüwe (CLS) model [75], which describes the relationships between driving pressure, solute concentration, and boundary velocity. According to this model, at low solute concentrations, the boundary velocity remains close to that of the base material, showing only minor deviations. However, as the solute concentration increases, it predicts a significant discontinuous change in boundary velocity, necessitating a higher driving force for boundary migration [32, 75].

Another aspect of the greater effectiveness of higher concentrations of Cu (e.g., Cu4) in solute segregation and eventually flow stress is their impact on vacancy availability, as shown in Figure 4-17 at 450°C. Diffusion in materials predominantly occurs through vacancy-mediated or interstitial mechanisms [76]. Higher concentrations of Cu are more likely to suppress vacancy formation by locally strengthening atomic bonds, which increases the energy required to create a vacancy. This results in a reduced overall vacancy concentration within the lattice, slowing diffusion and hindering redistribution processes. Consequently, this accelerates the segregation of solute atoms at the boundaries [77].

At elevated deformation temperatures (550°C), high Cu concentrations (0.4%) have a limited effect on flow stress compared to lower deformation temperatures (450°C). This is ascribed to the formation of a much weaker segregation atmosphere, which provides less resistance to dislocation motion and grain boundary movement. With an increase of the temperature to 550˚C, the diffusion coefficient of Cu atoms in α-Al as well as the self-diffusion coefficient

of Al increase [78]. The diffusion coefficient D for substitutional solutes like Cu in Al typically follows an Arrhenius relationship (Eq. 7) [79]:

$$D = D_0 \exp(\frac{Q}{RT}) \quad (7)$$

Where D_0 (m^2/s) is the pre-exponential factor, Q (J/mol) is the activation energy for diffusion, R (8.314 J/(mol·K)) is the universal gas constant, T (K) is the absolute temperature. The corresponding pre-exponential factor (D_0) and activation energy (Q) for the diffusion of Cu in Al are 5.31×10^{-4} m^2/s and 136 kJ/mol, respectively [80, 81]. Accordingly, the diffusion coefficient of Cu in Al is 9.75×10^{-15} m^2/s at 450 °C and 1.52×10^{-13} m^2/s at 550 °C. This means Cu diffuses about 15.6 times faster at 550 °C than at 450 °C, enabling Cu atoms to redistribute more readily away from grain boundaries during deformation. As a result, their pinning effect (solute drag) on migrating boundaries and substructures is reduced, promoting easier recrystallization and/or grain growth, and consequently lowering the flow stress. Moreover, diffusion often relies on vacancies to facilitate atomic movement. At higher temperatures, the number and mobility of vacancies increase, further promoting the diffusion of solute atoms. This accelerates the rate of atomic movement in the structure and contributes to a uniform redistribution of solute atoms and the prevention of atomic segregation near grain boundaries [82]. Therefore, the effect of a higher content of Cu solute is less at higher temperatures of deformation. This behavior is demonstrated schematically in Figure 4-17 for Cu4 at 550°C.

The CLS theory [75] describes the solute concentration near the grain boundary (c) according to Eq. 8 [33]:

$$c = c_0 \exp\left(-\frac{U(x)}{kT}\right) \quad (8)$$

Here, x shows the distance between the solute atom and the grain boundary, while U(x) represents the interaction free energy. Additionally, c_0 shows the equilibrium solute concentration (far from the grain boundary), T is the temperature, and k is Boltzmann's constant. This relationship indicates that increasing the hot deformation temperature reduces the difference between c and c_0 (e.g. when x=0), leading to a decreased solute concentration

near the grain boundary. As a result, solute atom segregation at the boundaries is minimized, effectively depleting the surrounding atmosphere of solute atoms. Consequently, the solute drag effect diminishes, reducing the retarding force on the boundary and increasing its velocity [33, 70].

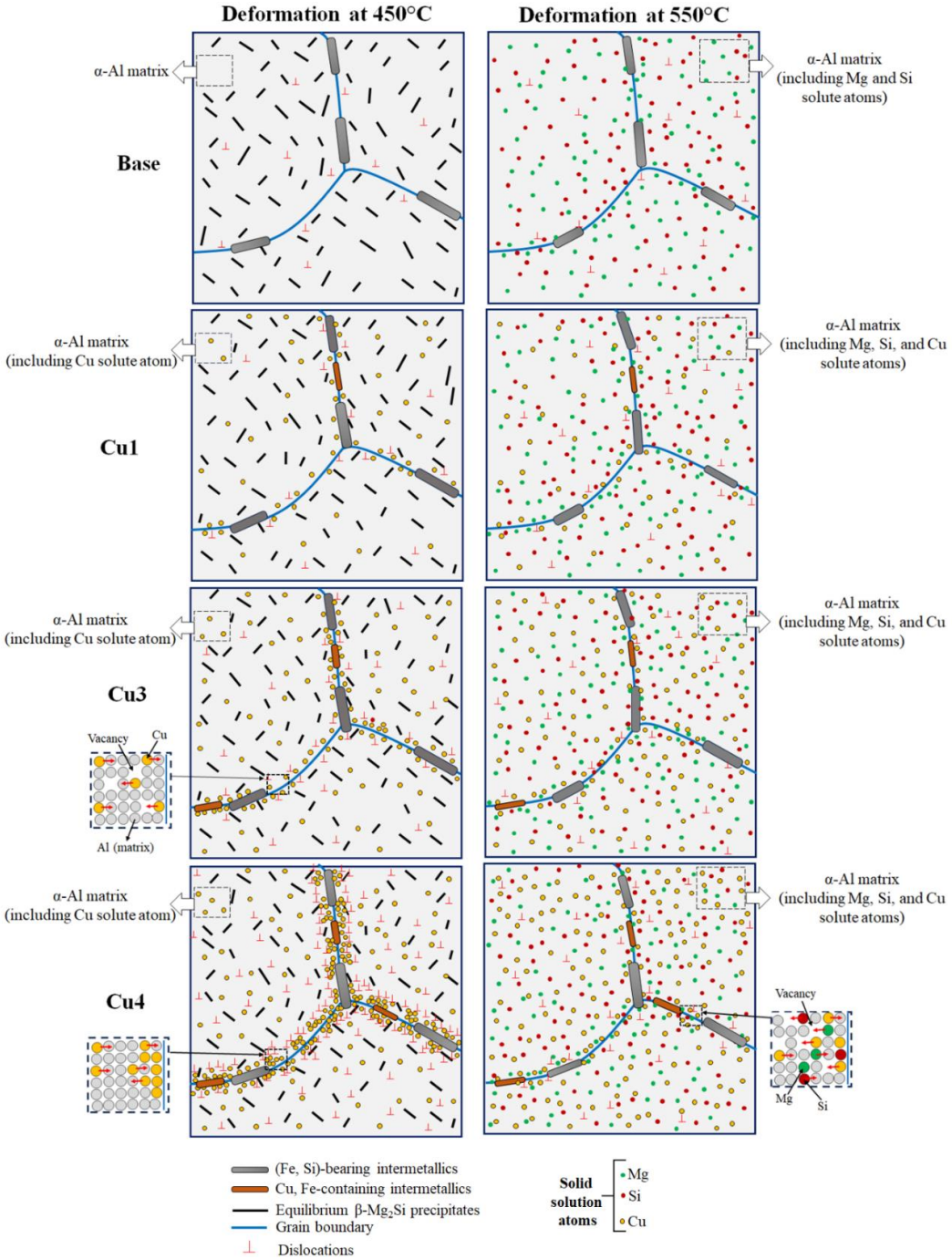

Figure 4-17. Schematic illustration of the microstructure and α-Al matrix composition variation during hot deformation at 450°C and 550°C for various alloys.

The fraction of DRX in alloys deformed at 450°C ranges from 1% to 4.5%, while at 550°C, it increases significantly to 8%–11.8%. As discussed above, this difference can be attributed to less Cu segregation, enhanced dislocation movement, and faster grain boundary motion at 550°C, which might decrease the critical strain required for nucleation and contribute to an increased DRX fraction [58, 83]. Additionally, different trends in the fraction of DRX with varying Cu content were observed at 450°C and 550°C. As shown in Figure 4-11 (a), at 450°C, the DRX fractions for the base alloy and Cu1 are nearly identical (~1%); however, higher Cu contents results in a reduced DRX fraction due to the formation of barriers to dislocation motion, which retards the orientation of grains to form new grains. In contrast, at 550°C, the DRX fraction slightly decreases from the base alloy to Cu1, but a further increase in Cu content (e.g., 0.4%) leads to a higher DRX fraction, as indicated in Figure 4-11 (b). It is speculated that the slight decrease in DRX at 550°C for the Cu1 alloy may be caused due to the reduced thermodynamic driving force for the nucleation of new grains [84]. The addition of 0.15% Cu is insufficient to significantly accelerate the dislocation rearrangement and accumulation required for the nucleation of new grains. This could explain the lowest proportion of HAGBs observed for Cu1, compared to the base, Cu3, and Cu4 alloys, as shown in Figure 4-11 (b). In contract, during high-temperature deformation (550°C), a higher Cu content increases the driving force for dislocation activity and (sub)grain boundary migration, promoting the formation of HAGBs and enhancing the nucleation of new grains [58]. It can be concluded that at 550°C, alloys with lower Cu content exhibit a higher degree of DRV compared to those with higher Cu content.

4.4.2. Relationship between microstructural changes during hot deformation and their impact on mechanical and electrical properties

The precipitation evolution during the hot deformation of the alloys were analyzed by comparing the equilibrium phase diagram, calculated using Thermo-Calc^{TM} software, with the observed microstructure, as shown in Figure 4-18. Although the phase diagram represents an equilibrium state and may differ slightly from actual heating conditions, it still provides a good basis for predicting microstructural changes during the heating and hot deformation process of Al-Mg-Si-Cu alloys. Figure 4-18 shows three points, labeled A, B and C, for the hot-deformed samples. A represents the as-homogenized sample, while B and C represent

samples deformed at 450°C and 550°C, respectively. For 6xxx Al alloys containing Cu, the theoretical precipitation sequence can be summarized as follows [25, 67]:

$$SSSS \rightarrow \text{Solute clusters} \rightarrow \text{GP zones} \rightarrow \beta'', \beta', Q', \theta' \rightarrow \beta, Q, \theta \text{ (Over aging)}$$

The positions of these transformations in the equilibrium phase diagram are shown in Figure 4-18. With increasing temperature in as-homogenized Al-0.7Mg-0.5Si-0.3Cu alloys, precipitation begins with the formation of GP zones, followed by the development of coherent β″ precipitates. As the temperature rises, the alloy enters a region characterized by the presence of β′, Q′, and θ′ precipitates. Exceeding this region leads to an overaged condition, where these precipitates transform into coarser particles of β, Q, and θ phases [25, 85]. Based on the equilibrium phase diagram in Figure 4-18, for the Cu3 alloy, the stable θ (Al_2Cu) phase dissolves in the α-Al matrix at 260°C, and the Q phase (a quaternary Al-Mg-Si-Cu phase) dissolves into the matrix at 320°C. When the temperature reaches 450°C, β should supposedly be the only stable phase that exists as coarse precipitates outside the matrix in an equilibrium state. Meanwhile, Cu-containing precipitates dissolve into the α-Al matrix. However, the EDS analysis in Figure 4-13 (c) revealed that during heating and holding at 450°C prior to deformation, the limited time available in the process allows a small fraction of Cu to remain as Q precipitates, which do not fully dissolve by the time the material reaches position B in Figure 20.

Furthermore, in the alloy studied, the Mg/Si atomic ratio is 2, which typically suggests that no Si-type precipitates are expected in 6xxx series Al alloys. However, a few Si-type precipitates were observed under the actual hot deformation conditions at 450 °C, as indicated by TEM-EDS in Figure 4-13. This unexpected formation of Si precipitates can be attributed to two main factors. First, the formation of the Q phase consumes additional Mg, leading to an excess of Si [61]. Second, the short duration of the hot deformation process (approximately 6 minutes) limited the diffusion time for alloying elements to reach equilibrium, resulting in a minimal presence of Si-type precipitates. When hot deformation is performed at 550°C, the alloy exceeds the Mg_2Si (β) solvus line at 500°C, indicating that the β phase dissolves above this temperature. At 550°C, all Mg_2Si should be dissolved into the matrix (labeled with C).

In Al conductor alloys, the solid solution is the most detrimental factor affecting EC [15, 35]. During hot deformation at 450°C, much of the Mg and Si has precipitated out of the α-Al matrix as Mg_2Si precipitates. This results in minimal distortion of the atomic structure and reduced electron scattering, leading to increased EC in the deformed samples at this temperature. Additionally, the equilibrium β-Mg_2Si precipitates, as shown in Figure 4-12 (a) and (c), remain during hot deformation at 450°C and do not contribute to strengthening due to their large size. In contrast, at 550°C, Mg and Si dissolve nearly completely in the matrix, causing significant distortion of the lattice and increased electron scattering. This reduces the EC while enhancing strength through solid solution strengthening. Furthermore, due to the supersaturation of alloying elements, samples deformed at 550°C are more amenable to precipitation hardening during subsequent aging. Therefore, hot deformation at a temperature close to the solution temperature (i.e. 550°C) results in a higher hardness and lower EC compared to deformation at 450°C, as reported in Section 3.4.

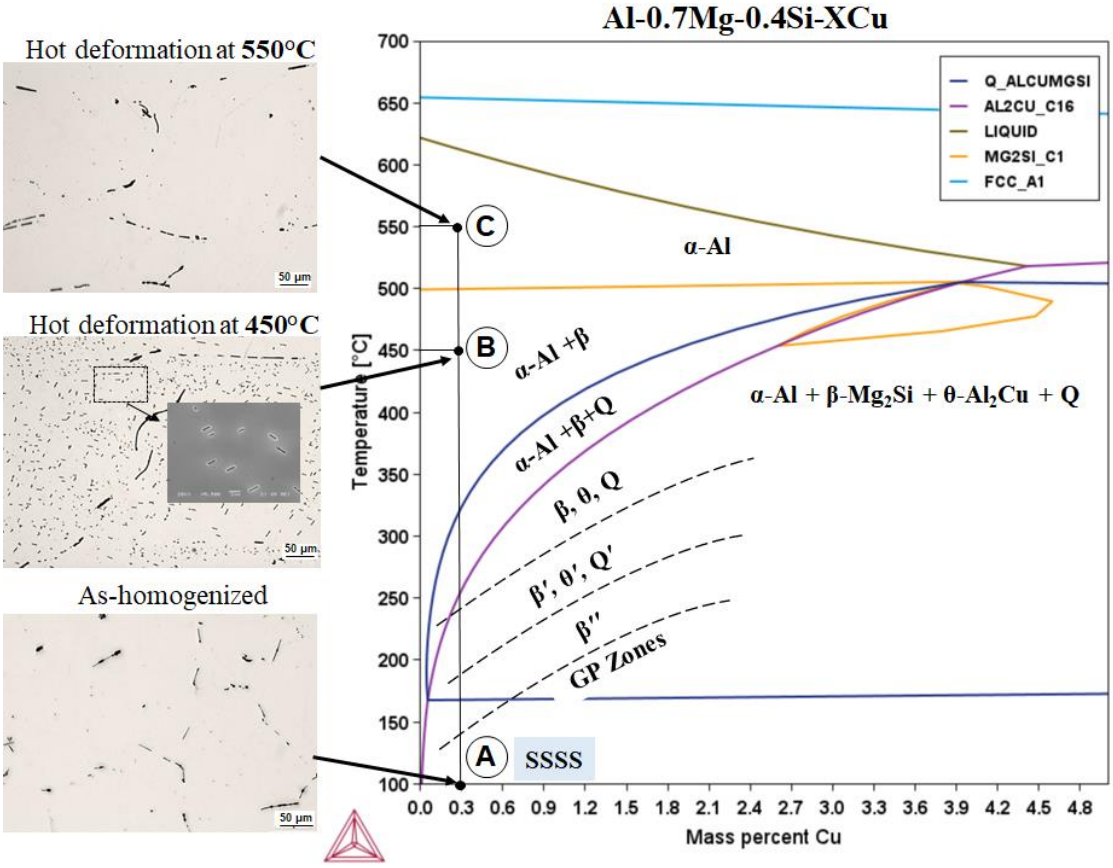

Figure 4-18. Microstructure evolution for the Cu3 alloy during hot deformation at 450°C and 550°C, as predicted by Thermo-Calc™ software and observed in optical microscope micrographs.

4.5. Future work

To further advance Cu-modified Al-Mg-Si conductors, future investigations should explore the T6 temper's influence on electrical and mechanical properties. Long-term studies on thermal stability and corrosion resistance are essential to ensure performance reliability in service environments. It is also worth mentioning that thermally stable Al conductor alloys are generally achieved with Zr and/or Sc additions. Additionally, evaluating fatigue and creep behavior under elevated temperatures will provide critical insight into the alloy's suitability for high-temperature applications. These efforts will help optimize microstructural stability, durability, and the strength-conductivity balance in the next-generation conductor alloys.

4.6. Conclusion

This study explored the impact of Cu additions and hot deformation parameters on the performance and thermomechanical behavior of Al-Mg-Si conductors. The findings are summarized below.

1. The addition of 0.3 wt% Cu to an Al-Mg-Si alloy slightly increased flow stress by 7-8.2% during hot deformation at 450°C. Higher Cu concentrations (0.4 wt.%) significantly increased flow stress by 15–25.2%. This increase is attributed to a higher fraction of low-angle grain boundaries, reduced mean misorientation angle, finer subgrain size, and suppressed dynamic recrystallization — all of which contributed to retarding the dynamic recovery process. However, during hot deformation at 550°C, the influence of Cu on flow stress diminished, with 0.4 wt.% Cu causing less than a 4% increase compared to the base alloy at 1 and 10 s^{-1} strain rates. This suggests higher Cu content is less effective at retarding softening mechanisms at elevated temperatures.
2. Hot deformation at 450°C produced 6–12 HV lower hardness but 1.0–2.5 %IACS higher electrical conductivity compared to deformation at 550°C, after 8 and 24 hours of direct aging at 185°C. This is attributed to the precipitation of equilibrium Mg_2Si (β) phases at 450°C, which do not contribute to the hardness significantly. In contrast, at 550°C, precipitate dissolution enhanced solid solution and precipitation strengthening after aging, increased electron scattering, and consequently reduced electrical conductivity.
3. Aging for 24 hours of as-deformed alloys led to a 1-2.7 %IACS increase in EC while reducing the hardness by less than 4 HV compared to aging for 8 hours. The coarsening

of precipitates during prolonged aging caused a slight decrease in hardness. However, the increased volume fraction of precipitates and the subsequent removal of more solute atoms from the matrix led to an improvement in EC after 24 hours aging.

4. The alloy with 0.3 wt.% Cu emerged as the most promising candidate for conductor applications. It showed low deformation resistance, with less than a 7% increase in flow stress versus the base alloy, while achieving a 20–30% microhardness improvement and maintaining 52.4-54.1 %IACS acceptable electrical conductivity for Al-Mg-Si conductor applications.

Acknowledgments

The authors gratefully acknowledge the industrial partners of the project: Rio Tinto Aluminum, MindCore Technologies, and CANMEC Group Inc. Furthermore, the authors extend their appreciation to the technical teams of Rio Tinto Aluminum, Center de M´etallurgie du Quebec (CMQ), Center Universitaire de Recherche sur l'Aluminium (CURAL), the Aluminium Research Centre–REGAL, and Chaire de recherche Institutionnelle en M´etallurgie de la Transformation de l'Aluminium (CIMTAL) for their invaluable support in preparing and characterizing samples

Authors contribution

Behrouz Abnar: Investigation, Methodology, Formal analysis, Writing – original draft. *Siamak Nikzad Khangholi:* Conceptualization, Methodology, Writing – review & editing. *Paul Rometsch:* Conceptualization, Validation, Writing – review & editing. *Mousa Javidani:* Conceptualization, Validation, Writing – review & editing, Project administration.

4.7. References

[1] M. Khoshghadam-Pireyousefan, M. Javidani, A. Maltais, J. Lévesque, and X.-G. Chen, "Strength-conductivity synergy in hypoeutectic Al-Si conductors via ultrafine-grained embedded Si nanoprecipitates," *Materials Science and Engineering: A,* vol. 929, p. 148124, 2025.

[2] S. N. Khangholi, M. Javidani, A. Maltais, and X. G. Chen, "Review on recent progress in Al–Mg–Si 6xxx conductor alloys," *Journal of Materials Research,* vol. 37, no. 3, pp. 670–691, 2022.

[3] S. N. Khangholi, M. Javidani, A. Maltais, and X.-G. Chen, "Optimization of mechanical properties and electrical conductivity in Al–Mg–Si 6201 alloys with different Mg/Si ratios," *Journal of Materials Research,* vol. 35, no. 20, pp. 2765–2776, 2020.

[4] M. Khoshghadam-Pireyousefan, M. Javidani, A. Maltais, J. Lévesque, and X.-G. Chen, "Breaking the strength-conductivity paradigm in hypoeutectic Al–Si alloy via annealing-induced Si nanoprecipitation," *Materials Science and Engineering: A,* vol. 911, p. 146924, 2024.

[5] Y. Wang, L. Zhu, G. Niu, and J. Mao, "Conductive Al alloys: the contradiction between strength and electrical conductivity," *Advanced Engineering Materials,* vol. 23, no. 5, p. 2001249, 2021.

[6] *ASTM B317/B317M: Standard Specification for Aluminum-Alloy Extruded Bar, Rod, Tube, Pipe, and Structural Profiles for Electrical Purposes (Bus Conductor)*, A. International, 2017.
[7] D. Ólafsson, P. Vilaça, and J. Vesanko, "Multiphysical characterization of FSW of aluminum electrical busbars with copper ends," *Welding in the World,* vol. 64, no. 1, pp. 59–71, 2020.
[8] A. D. Callegaro *et al.*, "Bus bar design for high-power inverters," *IEEE Transactions on Power Electronics,* vol. 33, no. 3, pp. 2354–2367, 2017.
[9] T. Yoshida, N. Inoue, and T. Otsubo, "Bus bar connection device and switchgear including the same," ed: Google Patents, 2018.
[10] S. Braun, G. Micard, and G. Hahn, "Solar cell improvement by using a multi busbar design as front electrode," *Energy Procedia,* vol. 27, pp. 227–233, 2012.
[11] Z. Yi-Feng and G. Qiong-Xuan, "Study on busbar-structure for prototype of the high-speed railway traction converter," in *2011 International Conference on Electrical and Control Engineering*, 2011: IEEE, pp. 3177–3180.
[12] P. G. Ross and N. Mcgee, "Modular uninterruptible power supply," ed: Google Patents, 2018.
[13] H. Van Nguyen, K. M. Wildstone, P. A. Churnock, and M. D. Striffler, "Reserve power bus ring for data center," ed: Google Patents, 2016.
[14] *ASTM B236: Standard Specification for Aluminum Bars for Electrical Purposes (Bus Bars)*, A. International, 2015.
[15] J. Zhang and J. Peng, "A review on aluminum alloy conductors influenced by alloying elements and thermomechanical treatments: Microstructure and properties," *Journal of Materials Research,* pp. 1–22, 2023.
[16] X. Li *et al.*, "Influence of Mg and Si content and heat treatment on electrical conductivity and hardness of AA6101 Al alloy," *Journal of Materials Science,* vol. 58, no. 20, pp. 8478–8488, 2023.
[17] D. Chakrabarti and D. E. Laughlin, "Phase relations and precipitation in Al–Mg–Si alloys with Cu additions," *Progress in Materials Science,* vol. 49, no. 3-4, pp. 389–410, 2004.
[18] J. Kim, C. D. Marioara, R. Holmestad, E. Kobayashi, and T. Sato, "Effects of Cu and Ag additions on age-hardening behavior during multi-step aging in Al□ Mg□ Si alloys," *Materials Science and Engineering: A,* vol. 560, pp. 154–162, 2013.
[19] S. Duan, K. Matsuda, Y. Zou, and T. Wang, "Influence of two-stage ageing process and Cu additions on conductive Al alloys based on AA 6063," *Materials Research Express,* vol. 6, no. 10, p. 106509, 2019.
[20] S. Gashtiazar, E. Elgallad, B. Abnar, M. Javidani, A. Maltais, and X.-G. Chen, "Effect of solution heat treatment on the microstructure of hot-rolled Al-Mg-Si 6xxx alloy microalloyed with Sc and Zr," *Materials Letters,* p. 138784, 2025.
[21] E. Elgallad, S. Khangholi, M. Javidani, A. Maltais, and X.-G. Chen, "Development of ultra-high-strength Al-Mg-Si conductor alloys with copper addition via scalable thermomechanical processes," *Scripta Materialia,* vol. 257, p. 116462, 2025.
[22] Y. Weng, Z. Jia, L. Ding, S. Muraishi, and Q. Liu, "Clustering behavior during natural aging and artificial aging in Al-Mg-Si alloys with different Ag and Cu addition," *Materials Science and Engineering: A,* vol. 732, pp. 273–283, 2018.
[23] S. N. Khangholi, M. Javidani, A. Maltais, and X.-G. Chen, "Effect of Ag and Cu addition on the strength and electrical conductivity of Al-Mg-Si alloys using conventional and modified thermomechanical treatments," *Journal of Alloys and Compounds,* vol. 914, p. 165242, 2022.
[24] S. N. Khangholi, M. Javidani, A. Maltais, and X.-G. Chen, "Novel approach to high-strength, highly conductive Al-Mg-Si conductor alloys with Ag/Cu additions," *Materials Today Communications,* vol. 39, p. 108921, 2024.
[25] T. Zheng *et al.*, "Study on nano-treating of Al-Mg-Si-Cu alloys with TiC nanoparticles," *Journal of Alloys and Compounds,* vol. 947, p. 169405, 2023.

[26] Q. Xiao *et al.*, "Effect of Cu content on precipitation and age-hardening behavior in Al-Mg-Si-xCu alloys," *Journal of Alloys and Compounds,* vol. 695, pp. 1005–1013, 2017.
[27] H. Jin, D. Tie, and R. Guan, "Precipitation behavior during re-aging of Al-Mg-Si-Cu alloy," *Materials & Design,* vol. 220, p. 110883, 2022.
[28] *ASTM B398/B398M: Standard Specification for Aluminum-Alloy 6201-T81 and 6201-T83 Wire for Electrical Purposes*, A. International, 2022.
[29] N. K. Rawat, N. Jain, A. K. Mishra, and A. Verma, "Atomistic-scale simulations on grain boundary migration mechanisms involved in metals and alloys: a critical review," *Archives of Computational Methods in Engineering,* pp. 1–38, 2024.
[30] C. K. Iii, H. Ehrhardt, and R. Birringer, "Thermodynamic stabilization of nanocrystallinity," *International Journal of Materials Research,* vol. 96, no. 10, pp. 1134–1141, 2022.
[31] M. Shakiba, N. Parson, and X.-G. Chen, "Hot deformation behavior and rate-controlling mechanism in dilute Al–Fe–Si alloys with minor additions of Mn and Cu," *Materials Science and Engineering: A,* vol. 636, pp. 572–581, 2015.
[32] F. J. Humphreys and M. Hatherly, *Recrystallization and related annealing phenomena*. Elsevier, 2012.
[33] E. Hersent, K. Marthinsen, and E. Nes, "The effect of solute atoms on grain boundary migration: A solute pinning approach," *Metallurgical and Materials Transactions A,* vol. 44, pp. 3364–3375, 2013.
[34] H. J. McQueen, S. Spigarelli, M. E. Kassner, and E. Evangelista, *Hot deformation and processing of aluminum alloys*. CRC press, 2011.
[35] J. R. Davis, *Aluminum and aluminum alloys*. ASM international, 1993.
[36] Z. Chen *et al.*, "Microstructural characteristics and deformation behaviors of an Al–Mg–Si alloy with improved strength and conductivity processed by continuous casting and expansion extrusion," *Journal of Materials Research and Technology,* vol. 22, pp. 445–460, 2023.
[37] D. Jin, H. Li, Z. Zhu, C. Yang, B. Chen, and Y. Miao, "Effects of cooling rate in homogenization on microstructure, hot deformation resistance and subsequent age-hardening behavior of an Al–Mg–Si alloy," *Journal of Materials Research and Technology,* vol. 27, pp. 3283–3300, 2023.
[38] J. Zhang, Z. Fan, Y. Wang, and B. Zhou, "Equilibrium pseudobinary Al–Mg2Si phase diagram," *Materials science and technology,* vol. 17, no. 5, pp. 494–496, 2001.
[39] A. Elasheri, E. M. Elgallad, N. Parson, and X. G. Chen, "Effect of Si level on the evolution of Zr-bearing dispersoids and the related hot deformation and recrystallization behaviors in Al–Si–Mg 6xxx alloys," *Advanced Engineering Materials,* vol. 24, no. 8, p. 2101606, 2022.
[40] A. Elasheri, N. Parson, and X.-G. Chen, "Microstructure, tensile and bending properties of extruded Al–Mg–Si 6xxx alloys with individual and combined additions of Zr and Mn," *Materials Science and Engineering: A,* vol. 894, p. 146156, 2024.
[41] A. Ghosh, A. Elasheri, N. Parson, and X.-G. Chen, "Microstructure and texture evolution during high-temperature compression of Al-Mg-Si-Zr-Mn alloy," *Materials Characterization,* vol. 205, p. 113312, 2023.
[42] M. Mofarrehi, M. Javidani, and X.-G. Chen, "Effect of Mn content on the hot deformation behavior and microstructure evolution of Al–Mg–Mn 5xxx alloys," *Materials Science and Engineering: A,* vol. 845, p. 143217, 2022.
[43] B. Verlinden, J. Driver, I. Samajdar, and R. D. Doherty, *Thermo-mechanical processing of metallic materials*. Elsevier, 2007.
[44] D. Odoh, Y. Mahmoodkhani, and M. Wells, "Effect of alloy composition on hot deformation behavior of some Al-Mg-Si alloys," *Vacuum,* vol. 149, pp. 248–255, 2018.
[45] W. J. M. C.M. Sellars, "On the mechanism of hot deformation," *Acta Metallurgica,* vol. 14, no. 9, pp. 1136–1138, 1966.

[46] H. Yi *et al.*, "Hot compression deformation behavior and processing maps of Al–0.5 Mg–0.4 Si–0.1 Cu alloy," *Journal of Materials Research and Technology,* vol. 19, pp. 4890–4904, 2022.
[47] E. A. El-Danaf, M. S. Soliman, and A. A. Almajid, "Effect of solution heat treatment on the hot workability of Al–Mg–Si alloy," *Materials and Manufacturing Processes,* vol. 24, no. 6, pp. 637–643, 2009.
[48] Y. Xu, H. Nagaumi, Y. Han, G. Zhang, and T. Zhai, "The deformation behavior and microstructure evolution of a Mn-and Cr-containing Al-Mg-Si-Cu alloy during hot compression and subsequent heat treatment," *Metallurgical and Materials Transactions A,* vol. 48, pp. 1355–1365, 2017.
[49] S. Babaniaris, M. Ramajayam, L. Jiang, R. Varma, T. Langan, and T. Dorin, "Effect of Al3 (Sc, Zr) dispersoids on the hot deformation behaviour of 6xxx-series alloys: A physically based constitutive model," *Materials Science and Engineering: A,* vol. 793, p. 139873, 2020.
[50] C. Shi, W. Mao, and X.-G. Chen, "Evolution of activation energy during hot deformation of AA7150 aluminum alloy," *Materials Science and Engineering: A,* vol. 571, pp. 83–91, 2013.
[51] T. Sakai, A. Belyakov, R. Kaibyshev, H. Miura, and J. J. Jonas, "Dynamic and post-dynamic recrystallization under hot, cold and severe plastic deformation conditions," *Progress in materials science,* vol. 60, pp. 130–207, 2014.
[52] K. Ling, W. Mo, P. Deng, J. Chen, B. Luo, and Z. Bai, "Hot deformation behavior and dynamic softening mechanisms of hot-extruded Al-Cu-Mg-Ag-Mn-Zr-Ti alloy," *Materials Today Communications,* vol. 34, p. 105300, 2023.
[53] B. Abnar, S. N. Khangholi, P. Rometsch, and M. Javidani, "Effects of Cu Addition and Temperature on Hot Deformation Behavior of Al–Mg–Si 6201 Conductor Alloys," in *Conference of Metallurgists*, 2024: Springer, pp. 1649–1651.
[54] A. Elasheri, E. M. Elgallad, N. Parson, and X.-G. Chen, "Improving the dispersoid distribution and recrystallization resistance of a Zr-containing 6xxx alloy using two-step homogenization," *Philosophical Magazine,* vol. 102, no. 23, pp. 2345–2361, 2022.
[55] Y. Huang and F. Humphreys, "Subgrain growth and low angle boundary mobility in aluminium crystals of orientation {110}< 001," *Acta materialia,* vol. 48, no. 8, pp. 2017–2030, 2000.
[56] K. K. Alaneme and E. A. Okotete, "Recrystallization mechanisms and microstructure development in emerging metallic materials: A review," *Journal of science: Advanced materials and devices,* vol. 4, no. 1, pp. 19–33, 2019.
[57] J. Lv, J.-H. Zheng, V. A. Yardley, Z. Shi, and J. Lin, "A review of microstructural evolution and modelling of aluminium alloys under hot forming conditions," *Metals,* vol. 10, no. 11, p. 1516, 2020.
[58] K. Huang and R. E. Logé, "A review of dynamic recrystallization phenomena in metallic materials," *Materials & Design,* vol. 111, pp. 548–574, 2016.
[59] M. Long, F. Jiang, Y. Su, and Z. Xiao, "Dynamic recrystallization mechanisms and microstructure evolution of a novel Al-Zn-Mg-Cu-Zr alloy by isothermal compression," *Journal of Materials Research and Technology,* vol. 33, pp. 1740–1755, 2024.
[60] A. Elasheri, E. Elgallad, N. Parson, and X.-G. Chen, "Evolution of Zr-bearing dispersoids during homogenization and their effects on hot deformation and recrystallization resistance in Al-0.8% Mg-1.0% Si alloy," *Journal of Materials Engineering and Performance,* vol. 30, pp. 7851–7862, 2021.
[61] M. Gazizov, C. D. Marioara, J. Friis, S. Wenner, R. Holmestad, and R. Kaibyshev, "Precipitation behavior in an Al–Cu–Mg–Si alloy during ageing," *Materials Science and Engineering: A,* vol. 767, p. 138369, 2019.
[62] J. Buha, R. Lumley, A. Crosky, and K. Hono, "Secondary precipitation in an Al–Mg–Si–Cu alloy," *Acta Materialia,* vol. 55, no. 9, pp. 3015–3024, 2007.

[63] S. N. Khangholi, M. Javidani, A. Maltais, and X.-G. Chen, "Effects of natural aging and pre-aging on the strength and electrical conductivity in Al-Mg-Si AA6201 conductor alloys," *Materials Science and Engineering: A,* vol. 820, p. 141538, 2021.
[64] G. Edwards, K. Stiller, G. Dunlop, and M. Couper, "The precipitation sequence in Al–Mg–Si alloys," *Acta materialia,* vol. 46, no. 11, pp. 3893–3904, 1998.
[65] E. Kobayashi, M. Ohnuma, S. Kuramoto, J. Kobayashi, and G. Itoh, "Nanoscale Analysis of Solute Distribution in Ultrahigh-Strength Aluminum Alloys," *Materials Transactions,* vol. 64, no. 7, pp. 1441–1448, 2023.
[66] M. Liu *et al.*, "DSC analyses of static and dynamic precipitation of an Al–Mg–Si–Cu aluminum alloy," *Progress in Natural Science: Materials International,* vol. 25, no. 2, pp. 153–158, 2015.
[67] H.-W. Son, J.-Y. Lee, Y.-H. Cho, J.-i. Jang, S.-B. Kim, and J.-M. Lee, "Enhanced mechanical properties and homogeneous T5 age-hardening behavior of Al-Si-Cu-Mg casting alloys," *Journal of Alloys and Compounds,* vol. 960, p. 170982, 2023.
[68] Y. Qi *et al.*, "Achieving superior high-temperature mechanical properties in Al-Cu-Li-Sc-Zr alloy with nano-scale microstructure via laser additive manufacturing," *Materials Research Letters,* vol. 12, no. 1, pp. 17–25, 2024.
[69] X. Zhang, L. Zhang, Z. Zhang, and X. Huang, "Effect of solute atoms segregation on Al grain boundary energy and mechanical properties by first-principles study," *Mechanics of Materials,* vol. 185, p. 104775, 2023.
[70] H. Sun and C. Deng, "Adapted solute drag model for impurity-controlled grain boundary motion," *Journal of Materials Research,* vol. 29, no. 12, pp. 1369–1375, 2014.
[71] D. Chen, T. Ghoneim, and Y. Kulkarni, "Effect of pinning particles on grain boundary motion from interface random walk," *Applied Physics Letters,* vol. 111, no. 16, 2017.
[72] G. Neumann and C. Tuijn, *Self-diffusion and impurity diffusion in pure metals: handbook of experimental data*. Elsevier, 2011.
[73] Y. Huang and F. Humphreys, "The effect of solutes on grain boundary mobility during recrystallization and grain growth in some single-phase aluminium alloys," *Materials Chemistry and Physics,* vol. 132, no. 1, pp. 166–174, 2012.
[74] G. Dak, K. Guguloth, S. Sirohi, M. Ş. Adin, and C. Pandey, "Creep and high-temperature tensile deformation behavior of the TIG welded P92/304L dissimilar steel weld joints," *Journal of Materials Engineering and Performance,* pp. 1–26, 2024.
[75] K. Lücke and H. Stüwe, "Recovery and Recystallization of Metals, L. Himmel, ed," ed: Wiley, New York, 1963.
[76] Y. Yang, K. G. Field, T. R. Allen, and J. T. Busby, "Roles of vacancy/interstitial diffusion and segregation in the microchemistry at grain boundaries of irradiated Fe–Cr–Ni alloys," *Journal of nuclear materials,* vol. 473, pp. 35–53, 2016.
[77] C. Chun, Z. Wenjie, W. Zhenmin, L. Runxia, and W. Biao, "Effect of additional solutes on the vacancy-mediated diffusion of Mg in biodegradable Zn-based alloys: A first-principles study," *Journal of Materials Research and Technology,* 2024, doi: https://doi.org/10.1016/j.jmrt.2024.11.229.
[78] A. Mao *et al.*, "The diffusion behaviors at the Cu-Al solid-liquid interface: A molecular dynamics study," *Results in Physics,* vol. 16, p. 102998, 2020.
[79] M. Bishop and K. Fletcher, "Diffusion in aluminium," *International Metallurgical Reviews,* vol. 17, no. 1, pp. 203–225, 1972.
[80] E. A. Brandes and G. Brook, *Smithells metals reference book*. Elsevier, 2013.
[81] W. D. Callister and D. G. Rethwisch, *Fundamentals of materials science and engineering*. John Wiley & Sons, 2022.
[82] B. Dong, Y. Fu, H. Zhan, and C. Lü, "Thermal and stress impacts on vacancy diffusion through atomistic simulations," *International Journal of Mechanical Sciences,* vol. 240, p. 107944, 2023.

[83] H. Zhang, H. Xiao, X. Fang, Q. Zhang, R. Logé, and K. Huang, "A critical assessment of experimental investigation of dynamic recrystallization of metallic materials," *Materials & Design,* vol. 193, p. 108873, 2020.
[84] R. Fu, Y. Liu, Z. Xiao, Y. Huang, and H. Li, "Dynamic precipitation and its effect on microstructure of 2195 Al–Li alloy during medium/high temperature deformation," *Journal of Materials Research and Technology,* vol. 27, pp. 3259–3273, 2023.
[85] X. Zhang *et al.*, "Effects of Cu Addition on Age Hardening Behavior and Mechanical Properties of High-Strength Al-1.2 Mg-1.2 Si Alloy," *Materials,* vol. 16, no. 8, p. 3126, 2023.

Chapitre 5. Influence de la température de préchauffage avant extrusion et de la stratégie de vieillissement sur la précipitation et les performances d'un alliage conducteur Al–Sc–Zr

Cet article a été publié dans:
Materials Today Communications, Volume 51, février 2026, 114911

Résumé

Cette étude examine comment la température de préchauffage de l'extrusion à chaud (420 °C contre 480 °C) et la stratégie de vieillissement subséquente (vieillissement en une étape et en deux étapes) gouvernent le comportement de précipitation, l'évolution de la microstructure et les performances mécaniques et électriques d'un alliage conducteur extrudé Al–0,1Sc–0,1Zr (wt.%). Les résultats indiquent qu'une extrusion à plus basse température de préchauffage (420 °C) limite le grossissement précoce et conduit à une densité plus élevée de fines particules cohérentes $Al_3Sc/Al_3(Sc,Zr)$ de structure L12 après vieillissement, ce qui améliore la résistance mécanique. Les conditions de vieillissement comprennent un traitement en une étape à 300, 350 et 400 °C, ainsi qu'un schéma en deux étapes (300 °C/24 h + 400 °C/8 h). Le vieillissement en deux étapes appliqué à l'alliage extrudé à 420 °C génère la distribution de précipités la plus fine ($4{,}41 \times 10^{21}$ m^{-3}) en favorisant la formation d'un cœur enrichi en Sc à 300 °C, suivie d'une diffusion contrôlée du Zr à 400 °C, produisant une structure cœur–coquille offrant une résistance supérieure au grossissement. Cet état de précipitation optimisé apporte la contribution de renforcement la plus élevée via le contournement d'Orowan, ainsi qu'une croissance contrôlée des sous-grains due à une pression accrue de traînage de Zener. Ainsi, la combinaison d'une faible température de préchauffage d'extrusion (420 °C) avec un traitement de vieillissement en deux étapes permet d'obtenir le meilleur compromis de propriétés, avec une résistance ultime à la traction (UTS) de 172 MPa et une conductivité électrique de 57,5 % IACS, constituant une voie efficace pour produire des alliages d'aluminium conducteurs à haute résistance et haute conductivité. En revanche, les alliages extrudés à 480 °C présentent un grossissement important des précipités pour tous les traitements de vieillissement, entraînant une diminution du renforcement et une stabilité thermique réduite.

Mots-clés: alliages conducteurs d'aluminium, précipités $Al_3(Sc,Zr)$, traitement thermomécanique, conductivité électrique, extrusion à chaud

Influence of extrusion preheating temperature and aging strategy on precipitation and performance of Al–Sc–Zr conductor alloy

Behrouz Abnar [a], Paul Rometsch[b], Mousa Javidani [a]

[a] University Research Centre on Aluminium (CURAL) and Aluminium Research Centre–REGAL, Department of Applied Science, University of Québec at Chicoutimi, Saguenay, QC, G7H 2B1, Canada
[b] Arvida Research and Development Center, Rio Tinto Aluminum, Saguenay, QC, G7S 4K8, Canada

This article has been published in:
Materials Today Communications, Volume 51, February 2026, 114911

Abstract

This study investigates how the preheating temperature of hot extrusion (420 °C vs. 480 °C) and subsequent aging strategy (one-step and two-step aging) govern precipitation behavior, microstructure evolution, and the resulting mechanical and electrical performance of an extruded Al–0.1Sc–0.1Zr (wt.%) conductor alloy. Results indicate that lower preheat extrusion at 420 °C suppresses early coarsening and produces a higher density of fine, coherent $Al_3Sc/Al_3(Sc,Zr)$ particles with the $L1_2$ structure after aging, leading to enhanced strength. Aging conditions included one-step aging at 300, 350, and 400 °C, as well as a two-step schedule (300 °C/24 h + 400 °C/8 h). Two-step aging applied to the 420 °C-extruded alloy generated the finest precipitate distribution (4.41×10^{21} m^{-3}) by promoting Sc-rich core formation at 300 °C followed by controlled Zr diffusion at 400 °C, yielding a core–shell structure with superior coarsening resistance. This optimized precipitation state delivered the highest strengthening contribution through Orowan bypass, along with controlled subgrain growth resulting from increased Zener drag pressure. Consequently, coupling a low extrusion preheat temperature (420 °C) with a tailored two-step aging treatment achieved the best property balance, delivering a UTS of 172 MPa and an electrical conductivity of 57.5% IACS—an effective pathway to producing high-strength, high-conductivity aluminum conductor alloys. In contrast, alloys extruded at 480 °C experienced significant precipitate coarsening across all aging treatments, resulting in lower strengthening and reduced thermal stability.

Key words: Aluminum conductor alloys, $Al_3(Sc,Zr)$ precipitates, thermomechanical processing, electrical conductivity, hot extrusion

5.1. Introduction

The growing demand for lightweight, high-strength, and cost-effective materials in the electrical industry has positioned aluminum (Al) alloys as viable alternatives to copper conductors [1, 2]. Al alloy conductors are widely utilized across various electrical applications including power transmission and distribution systems, such as electrical cables and bus bars [3, 4].

Aluminum bus bars efficiently transmit electricity in power distribution systems, ensuring reliable high-current flow over short distances [5, 6]. These products are widely used in various industries, including Electric Vehicles, switchgear, renewable energy systems, railway, aerospace, power electronics, UPS, and data centers [7-12]. Electrical bars are typically manufactured in strip form using a hot extrusion process [13, 14]. Unlike wire conductors, Al electrical bus bars are not subjected to cold drawing during manufacturing [13-15]. As a result, dislocation strengthening plays a minor role, highlighting the need to optimize thermomechanical processing to enhance alternative mechanisms, especially precipitation hardening. The two main Al alloys used for electrical bus bars are AA1350 and AA6101. AA1350 is a high-purity Al alloy that offers excellent electrical conductivity (EC), with a minimum of 61 %IACS. However, it has a relatively low tensile strength, with a minimum of 85 MPa in the H12 temper [14, 16]. In contrast, AA6101, an Al-Mg-Si alloy, provides significantly higher tensile strength (e.g., minimum 200 MPa in the T6 temper) while maintaining an acceptable EC of at least 55% IACS [13].

With increasing energy demands, the need for high-current-carrying conductors has grown, leading to elevated conductor temperatures. These temperatures significantly degrade the mechanical properties of Al conductors, reducing the reliability of power networks. Traditional 6xxx Al alloys have limited thermal resistance, restricting service performance and current-carrying capacity [17-20]. The addition of Sc and Zr enables the development of thermally stable Al conductors with improved strength and high EC [15, 21]. Sc forms coherent Al_3Sc precipitates with an $L1_2$ structure, which offer strong precipitation strengthening through a fine, uniform distribution. Although Sc offers excellent strengthening effects, its high cost limits widespread use; therefore, Zr is often added as a more economical alternative to reduce overall alloying costs [21]. Zr addition promotes the

formation of nanoscale $Al_3(Sc,Zr)$ precipitates during aging, where Zr segregates to the precipitate/matrix interface, forming a shell that retards coarsening and enhances thermal stability [22, 23]. This special core-shell structure forms as Sc-rich Al_3Sc precipitates nucleate first due to the higher diffusivity of Sc, followed by a gradual Zr incorporation into the outer shell [17, 24]. These precipitates strengthen the alloy by impeding dislocation motion and significantly improve recrystallization resistance through the Zener pinning effect [15, 25].

Research on Al–Sc–Zr conductor wires shows that tailored aging promotes fine, coherent $Al_3(Sc,Zr)$ precipitates, enhancing strengthening and thermal stability while suppressing coarsening without degrading EC. Table *5-1* summarizes various Al-Sc-Zr alloy conductor wires, highlighting the applied thermomechanical treatments and their corresponding property results. Compared to pure Al wires (UTS 87–114 MPa, ≥61% IACS), Al–Sc–Zr conductors processed via optimized thermomechanical routes achieve ~170–200 MPa UTS while maintaining acceptable EC (~58–61% IACS) [3, 26-29]. In this context, a two-step aging process— consisting of an initial aging at 250–300 °C for at least 24 hours, followed by a second stage at around 400 °C— has been identified as a promising approach for optimizing the strength–conductivity balance in Al–Sc–Zr conductor wires [15, 29, 30]. Liu et al. [15] reported that, after solutionizing and quenching an extruded Al–0.06Sc–0.23Zr (wt.%) alloy, two-stage ageing (300 °C/25 h + 400 °C/5 h) following wire drawing produces higher strength (191 MPa) and EC (59.7 % IACS). This improvement results from the synergistic effects of cold deformation, precipitation, recrystallization, and defect recovery. Furthermore, Siyue Fan et al. [29] demonstrated that in Al–0.2Zr–0.06Sc (wt.%) alloy wires, a processing route consisting of a two-step aging treatment (250 °C/4 h + 400 °C/8 h) followed by hot extrusion and cold drawing yields the highest strength (192 MPa) while maintaining a high EC of 58.8 % IACS.

Table 5-1. Tensile strength and electrical conductivity of various Al-Zr-Sc conductors processed through different thermomechanical treatments.

Composition (wt.%)	Thermomechanical process	UTS (MPa)	Electrical conductivity (%IACS)	Ref.
Al-0.06Sc-0.23 Zr	Hot extrusion, Cold drawing, Two-stage ageing	194.3	61.4	[15]
Al-0.06Sc-0.23 Zr	Extrusion, Two-stage ageing, Cold drawing	199.4	57.6	[15]
Al-0.2Zr-0.06Sc	Continue casting direct rolling, Ageing, Cold drawing	195	61.2	[28]
Al-0.2Zr-0.06Sc	Homogenization, Ageing treatment, Hot extrusion, Cold drawing	190	57.7	[29]
Al-0.2Zr-0.06Sc	Homogenization, Hot extrusion, Ageing treatment, Cold drawing	168	59.6	[29]
Al-0.4Sc-0.2Zr	Semisolid extrusion, Solutionizing, Cold drawing, Ageing treatment	182	58.6	[17]
Al-0.10Zr-0.10Sc	Rolling, Solution treatment, Aging treatment, Cold drawing, Annealing	196.3	58.5	[19]
Al-0.10Zr-0.10Sc	Rolling, Solution treatment, Cold drawing, Aging treatment	192.5	59.8	[19]

Despite these studies on two-step aging in Al–Sc–Zr alloys, several critical research gaps remain. First, existing works do not clearly establish whether two-step aging is universally effective across different hot extrusion conditions. Hot extrusion parameters—including billet preheating temperature, deformation temperature, strain, and exit temperature—strongly influence solute distribution and precipitation behavior [31]; however, their individual and combined impacts on the subsequent effectiveness of two-step aging have not been investigated. In particular, the role of extrusion-induced thermal exposure in promoting unwanted or premature precipitate formation during preheating, deformation, and exit stages remains largely unexplored. The extent to which deformation temperature can compromise or alter the response to post-extrusion aging is also not well understood. Second, the underlying mechanisms governing core–shell $Al_3(Sc,Zr)$ precipitates during two-step aging remain insufficiently clarified. Specifically, it is not well understood why a single-step aging treatment at 400 °C fails to reproduce the precipitate architecture achieved by a two-step sequence (e.g., 300 °C + 400 °C). The thermodynamic and kinetic reasons governing this divergence—particularly in terms of nucleation, solute partitioning, and shell formation—have not been unambiguously addressed in prior studies.

The present study systematically addresses these gaps by optimizing the thermomechanical processing and aging strategy of Al–0.1Sc–0.1Zr (wt.%) alloys for electrical bus bar applications, a product form that has been rarely investigated. Hot-extruded 1xxx Al strips containing Sc and Zr are processed using different billet preheating temperatures and one-step and two-step aging schedules. Mechanical strength, electrical conductivity, and precipitation evolution are evaluated to identify optimal processing paths. Predictive modeling is employed to elucidate precipitate behavior and explain the success or failure of specific aging routes.

5.2. Experimental procedure

The investigated Al–0.1Sc–0.1Zr (wt.%) alloy was prepared from commercially pure Al (99.7 wt.%), along with Al–2 wt.% Sc and Al–10 wt.% Zr master alloys. The melt was direct-chill (DC) cast into 4-inch-diameter billets, which were cut to a length of 203 mm for extrusion. The chemical composition of the alloy, measured by optical emission spectrometry (OES), is given in Table 5-2.

Table 5-2. Chemical composition (wt.%) of the studied alloy.

Sc*	Zr	Si	Fe	Ti	Al
0.10	0.10	0.12	0.19	0.02	Bal

*ICP analysis showed a Sc concentration of 0.09 wt%.

Figure 5-1 displays a schematic diagram of the experimental process in the present research. The Al–0.1Sc–0.1Zr alloy samples (all compositions in this study are in wt.%) were homogenized at 600°C for 4 hours followed by immediate fast cooling (>600 °C/h) to room temperature. Homogenized alloy billets were rapidly preheated using induction heating—either to 420 °C or to 480 °C—designated as E420 and E480, respectively, in this study. They were then extruded into 41.7 mm × 3 mm flat strips using the 780-tonne experimental press with an extrusion ratio of 70, followed by a standing wave water quench at the press exit to ensure controlled rapid cooling. Table 5-3 presents the extrusion process parameters for the Al–0.1Sc–0.1Zr alloy under two different conditions. The key differences between these conditions stem from the billet temperature, which influences the extrusion parameters, particularly the exit temperature and maximum ram pressure. In this work, the total hot extrusion processing time—including preheating, transfer to container, and extrusion—was approximately 1.5 to 2 minutes.

After extrusion, the samples were directly subjected to one-step isothermal aging at 300°C, 350°C, and 400°C for 1, 12, and 24 hours, or two-step aging at 300°C for 24 hours, followed by aging at 400°C for 8 hours, as shown in Figure 5-1 (b) and (c), respectively.

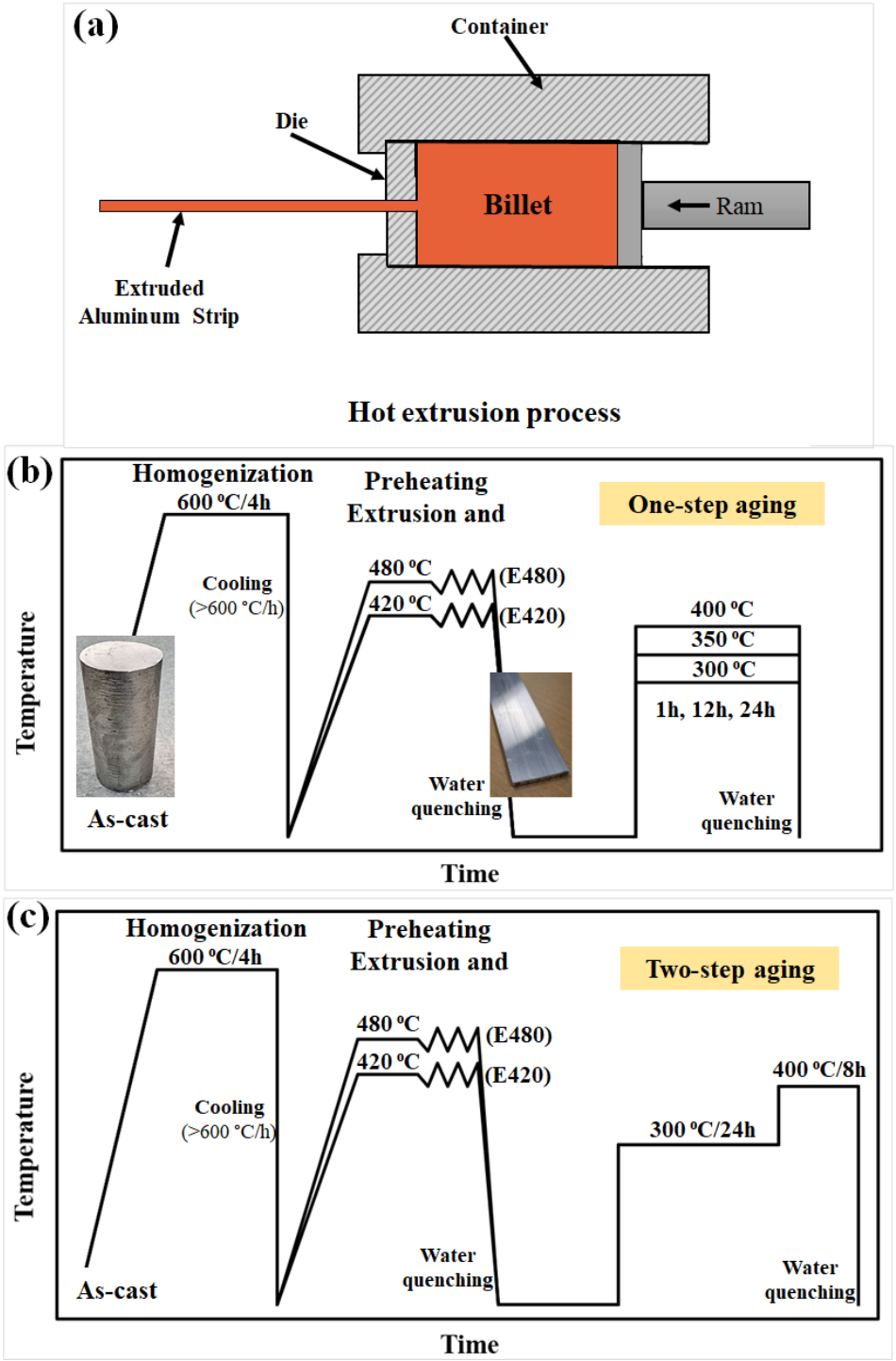

Figure 5-1. Schematic diagram of the experimental process for the studied alloy, (a) Schematic of hot extrusion process, (b) one-step aging and (c) two-step aging.

Table 5-3. Extrusion process parameters for Al–0.1Sc–0.1Zr alloy under two different conditions.

Condition designation	Nominal Billet Temperature (°C)	Actual Billet Temperature (°C)	Exit Temperature (°C)	Maximum Die Bearing Temperature (°C)	Maximum Ram Pressure (psi)	Ram Speed (mm/s)	Exit Speed (m/min)
E420	420	426-430	480-483	548	1775	12	51
E480	480	480-483	507-512	580	1419	12	51

The materials were characterized using standard metallographic and mechanical testing methods. To analyze the grain structure and measure the microhardness, all samples were sectioned in the longitudinal orientation, and examinations were conducted at the strip center. Grain structure analysis was performed using optical microscopy with Barker's etching and polarized light. Vickers microhardness awas measured using a 25 g load and a 20-second dwell time, with average hardness values determined from twelve indentations. EC was measured using the Sigmascope method at a frequency of 480 kHz and a temperature of 21°C, following ASTM E1004. Tensile testing was performed in accordance with ASTM B557M using full-size sheet-type specimens with an overall length of 200 mm and a gauge length of 50 mm. The tests were conducted at ambient temperature using a strain rate of 0.2 mm/mm/min, corresponding to 3.3×10^{-3} s^{-1}.

The microstructure of the homogenized alloy and the intermetallic phases were examined using scanning electron microscopy (SEM, JEOL^{TM}-6480LV) equipped with energy-dispersive spectroscopy (EDS). Additionally, electron backscatter diffraction (EBSD) analysis was conducted to evaluate the grain and subgrain structures with a step size of 0.4 μm. Boundaries and sub-boundaries were categorized based on their misorientation angles as low-angle grain boundaries (LAGBs: 2–5°), medium-angle grain boundaries (MAGBs: 5–15°), and high-angle grain boundaries (HAGBs: >15°), represented by white, blue, and black lines, respectively.

A transmission electron microscope (TEM, JEM 2100) operating at 200 kV was used to investigate the Sc- and Zr-containing precipitate evolution. Elemental analysis by TEM-EDS was also employed to determine the chemical compositions of the precipitates formed during hot extrusion and aging. TEM samples were prepared using a twin-jet electropolishing system at 15 V and a temperature of -20 to -25 °C, with a solution of 30% nitric acid and 70% methanol. TEM images were captured near the [001] zone axis of the α-Al matrix to

examine the precipitates. A statistical analysis of precipitates was conducted using at least eight TEM images per sample and processed with ImageJ image analysis software. The number density (N_d) and volume fraction (F_V) of precipitates were calculated by the following equations, respectively [32, 33]:

$$N_d = \frac{N}{A\left(D_{avg} + t\right)} \quad (1)$$

$$F_V = N_d V_P \quad (2)$$

Where N is the number of precipitates, D_{avg} represents the average diameter of the precipitates, t thickness of the foil, A is the area of the matrix containing the precipitates, and V_P is the average volume of the precipitates. The foil thickness (t) was measured using the convergent beam electron diffraction (CBED) technique.

5.3. Results

5.3.1. Microstructure of homogenized alloy

Figure 5-2 (a)-(b) shows the homogenized microstructures of the Al–0.1Sc–0.1Zr alloy, which mainly consists of an α-Al matrix along with the Fe-bearing intermetallic, including a feather-like Al_mFe phase [19]. The SEM-EDS mapping in Figure 5-2 (c) reveals regions enriched with Fe, while no segregation of Sc and Zr elements was observed after homogenization.

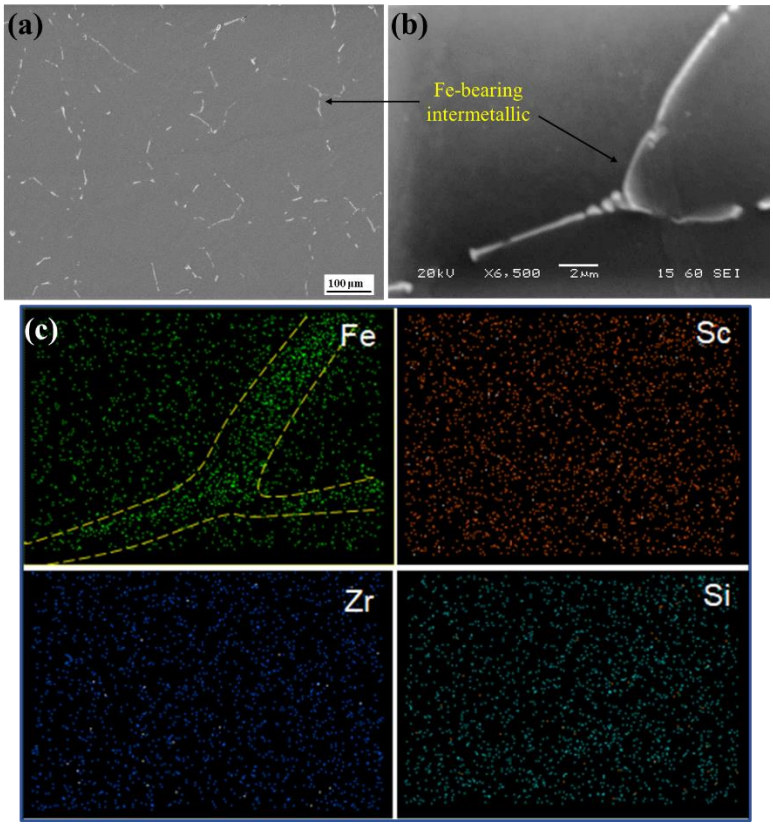

Figure 5-2. (a) SEM image of the as-homogenized Al–0.1Sc–0.1Zr alloy, (b) magnified SEM image displaying Fe-bearing intermetallics, and (c) EDS mapping revealing regions enriched with Fe.

5.3.2. Microstructure of as-extruded alloys

As shown in Figure 5-3 (a) and (d), the Al–0.1Sc–0.1Zr alloy extruded at billet temperatures of 420°C and 480°C exhibits a fully fibrous grain structure. Additionally, Figure 5-3 (b) and (e) present the corresponding inverse pole figure (IPF) maps for E420 and E480. The GOS (grain orientation spread) map, inserted in Figure 5-3 (b) and (e), represents the average misorientation angles within individual grains. A GOS value of 2° or less indicates recrystallized grains, while values between 2° and 15° correspond to substructured grains, and values above 15° are indicative of deformed grains. The geometrically necessary dislocation (GND) results, presented in Figure 5-3 (c) and (f), show that E480 experienced greater dislocation annihilation and recovery, as evidenced by a lower ρ_{GND} of 1.5×10^{14} m^{-2} compared to E420, which exhibited a higher ρ_{GND} of 1.8×10^{14} m^{-2}. This reduction suggests a more pronounced softening mechanism in E480.

Figure 5-3 (g) displays the distribution of misorientation angles and the recrystallization fraction. During hot extrusion, the E480 material exhibited lower fractions of LAGBs and

higher fractions of MAGBs compared to E420. This suggests increased dislocation movement and climb, leading to dynamic recovery (DRV) for E480 [34]. Additionally, HAGBs in E480 were slightly higher than in E420, indicating a greater tendency toward recrystallization. Figure 5-3 (g) shows that E480 resulted in a higher dynamic recrystallization (DRX) fraction compared to E420, with values of 17.8% and 11.2%, respectively. These findings indicate that softening mechanisms (DRV and DRX), were more pronounced in E480, which explain the lower flow stress and correspondingly reduced ram pressure provided in Table *5-3*, being lower for E480 (1419 Psi) compared to E420 (1775 Psi).

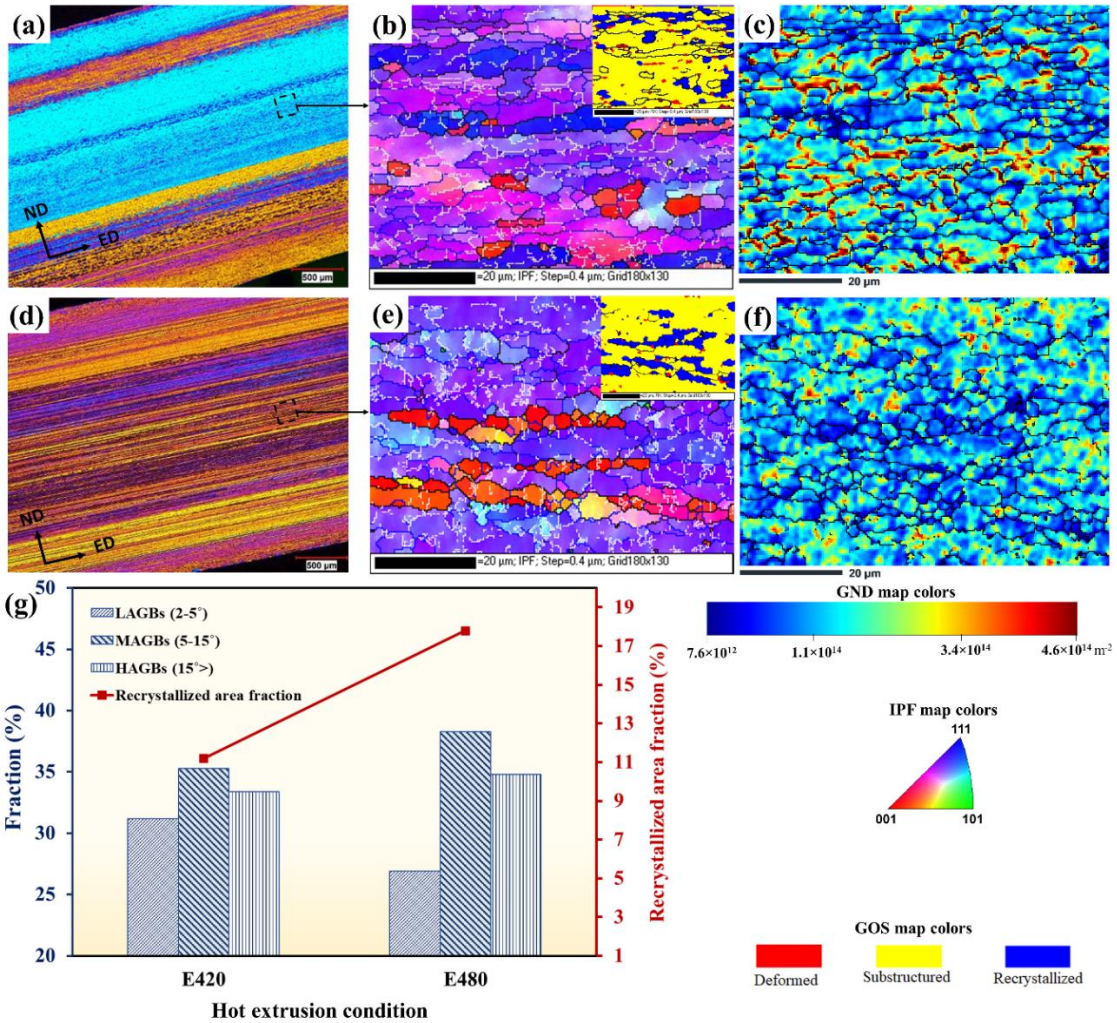

Figure 5-3. As-extruded longitudinal sections of the strip, showing grain structures along with corresponding EBSD IPF maps, GOS (inset), and GND with a step size of 0.4 µm for (a)-(c) E420 and (d)-(f) E480; (g) the misorientation angle distribution and recrystallized fraction for both E420 and E480 conditions.

Dark-field TEM images in Figure 5-4 (a) and (d) show spherical precipitates formed during hot extrusion. Figure 5-4 (b)–(c) and (e)–(f) present TEM-EDS analyses of representative precipitates (>17 nm) from the E420 and E480 conditions. In E420, the precipitates are mainly Sc-rich. In contrast, E480 shows two types: Sc-rich precipitates with negligible Zr, and precipitates containing both Sc and Zr elements, with Sc as the dominant component. This compositional difference is attributed to the varying diffusion coefficients of Sc and Zr, a topic further discussed in Section 4.1.

The selected area electron diffraction (SAED) pattern for E420 is inserted in Figure 5-4 (a), while that for E480 is shown in Figure 5-4 (g). Two systems of periodic spots can be seen in the SAED patterns. One set of spots, labeled in white, corresponds to the α-Al matrix (face-centered cubic, FCC) and is indexed along the [001] zone axis. Another set of spots, marked in yellow, is indexed as the FCC, $L1_2$-structure with the $Al_3Sc/Al_3(Sc,Zr)$ phase along the [001] zone axis [17, 19]. The indexed patterns indicate that the spherical $Al_3(Sc,Zr)$ precipitates and the α-Al matrix have coherent boundaries, with a misorientation relationship of $[001]_{Al_3(Sc,Zr)}//[001]_{Al}$ [35, 36]. Therefore, it can be concluded that the as-extruded E420 alloy mainly contains coherent Al_3Sc precipitates, while the E480 alloy contains both Al_3Sc and $Al_3(Sc,Zr)$ phases in its microstructure.

According to the size distribution of Sc- and Zr-containing precipitates shown in Figure 5-4 (h), the E420 condition exhibits a higher proportion of precipitates in the 3–7 nm range, with a peak at 5–7 nm (~37%), and fewer precipitates larger than 15 nm compared to E480. In contrast, E480 shows a higher percentage of precipitates in the 7–15 nm and >15 nm (~32%) ranges. The presence of more and larger precipitates in E480 indicates increased coarsening during the hot extrusion process, which reduces their contribution to strengthening. Table 5-4 presents a quantitative analysis of the precipitate characteristics in the Al–0.1Sc–0.1Zr alloy. Hot extrusion in E480 led to a slightly increased number density of precipitates in the as-extruded alloy, along with a larger average precipitate size compared to E420. This can be attributed to enhanced diffusion kinetics at elevated temperatures, which promote both the nucleation and growth of $Al_3(Sc,Zr)$ precipitates [30, 37]. However, despite the higher number of precipitates in E480, the susceptibility to coarsening limited its ability to inhibit

softening mechanisms during extrusion compared to E420. As a result, E480 exhibited higher DRV and DRX compared to E420, as mentioned above based on Figure 5-3 (g).

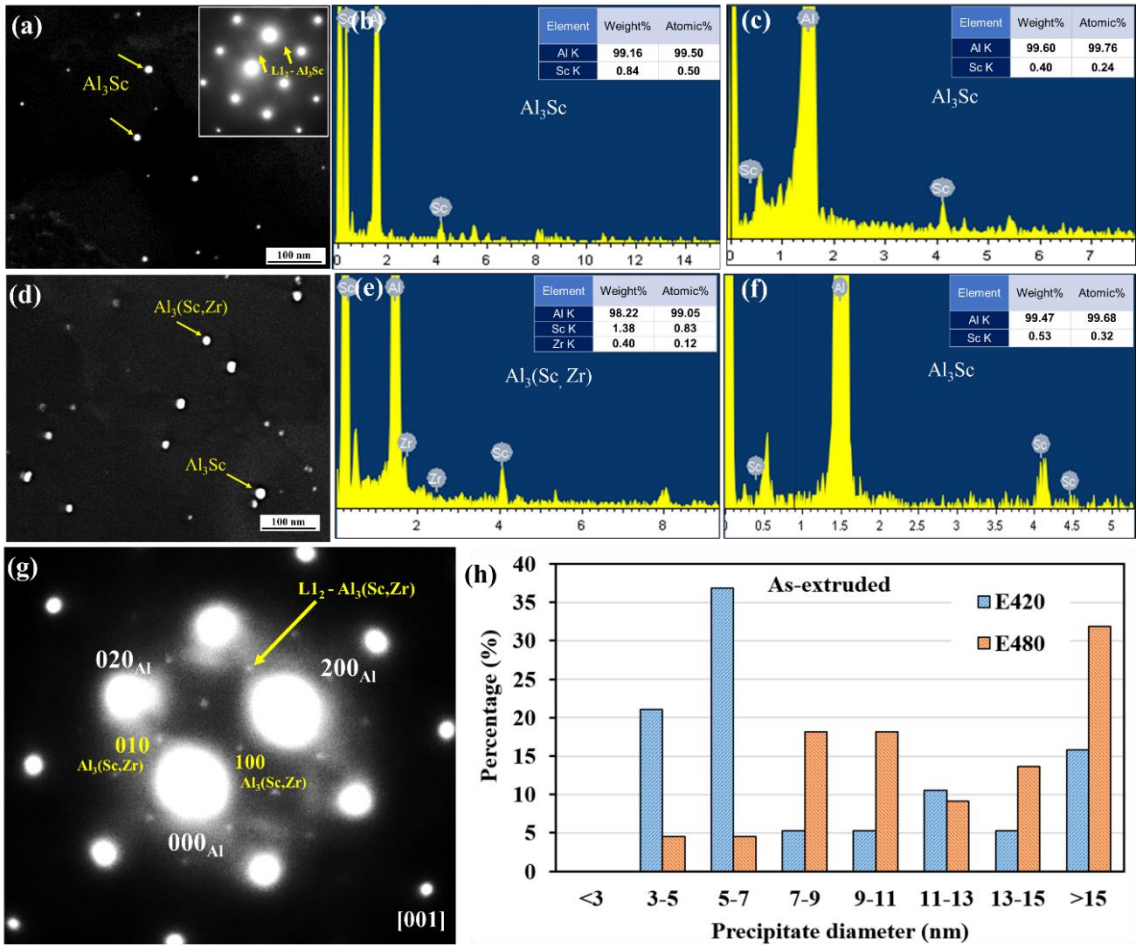

Figure 5-4. Dark-field TEM images showing the distribution of Sc- and Zr-containing precipitates in the as-extruded Al–0.1Sc–0.1Zr alloy processed at (a) E420 and (d) E480. Typical TEM-EDS analyses of the precipitates, including their atomic and weight compositions, are shown for (b-c) E420 and (e-f) E480. (g) Selected area electron diffraction (SAED) pattern for E480. (h) Precipitate size distribution for E420 and E480.

Table 5-4. Number density (N_d) and average diameter (D_{avg}) of Sc- and Zr-containing precipitates in the as-extruded Al-Sc-Zr alloy under E420 and E480 conditions.

Extrusion condition	Number density of precipitates ($\times 10^{21} m^{-3}$)	Average diameter of precipitates (nm) (Min–Max)
E420	0.42±0.07	8.4 (3.1-18.2)
E480	0.51±0.10	12.3 (4.2-20.6)

5.3.3. Electrical and mechanical properties of hot-extruded alloys under different aging conditions

Figure 5-5 shows the relationship between microhardness (HV) and EC (%IACS) for E420 and E480 samples subjected to various aging treatments. These include one-step aging at 300°C, 350°C, and 400°C for 1, 12, and 24 hours, and a two-step aging process of 300°C for 24 hours followed by 400°C for 8 hours. For both E420 and E480, the EC values are close to each other under all conditions and exhibit a same trend with varying aging treatments. Both longer aging time and higher aging temperature enhance EC. However, the rate of increase of EC with aging time at 400 °C is more noticeable compared to aging at 300 °C and 350 °C. For instance, in the E420 condition aged at 400 °C, EC increased from 55.2% IACS to 58% IACS—a 2.8% IACS increment—when the aging time was extended from 1 to 24 hours. In contrast, the increase in EC at 300 °C and 350 °C over the same aging duration was less than 1.2% IACS. This can be attributed to the lower diffusivity of Zr compared to Sc in Al at 300 °C and 350 °C [38]. Both Sc and Zr solute atoms in the atomic lattice of the Al matrix have a detrimental effect on EC, and their removal from the matrix can enhance the EC of the Al-0.1Sc-0.1Zr alloy [30, 39]. Further discussion is provided in Section 4.3. The two-step aging treatment yielded EC values of 57.5% IACS for E420 and 57.3% IACS for E480, both slightly lower than the peak values achieved through one-step aging at 400 °C.

Notable differences in hardness trends were observed between E480 and E420 with aging temperature and time. The hardness results for E480 showed that, overall, increasing the aging temperature from 300 °C to 400 °C led to a reduction in hardness, which became more pronounced with prolonged aging time. For example, in the E480 condition, the hardness dropped from 63 HV to 51 HV as the aging temperature increased from 300 °C to 400 °C (24 h). At 400 °C, the hardness fell below the as-extruded condition, which had a hardness of 54 HV. In contrast, for E420, aging at 300 °C to 400 °C increased the hardness from 56 HV to 60 HV. In terms of aging duration, extending the time from 1 hour to 24 hours at both 300 °C and 350 °C led to an increase in hardness for the alloy extruded under the E480 condition. However, at 400 °C, prolonged aging caused a decrease in hardness below the level of the as-extruded alloy. In the E420 condition, while extended aging at 300 °C slightly reduced the hardness to below 60 HV, aging at 400 °C steadily increased it from 54 HV (1 h) to a stable value of ~60 HV after 12 and 24 hours. These results suggest that E420 has a greater potential

to form thermally resistant precipitates compared to E480. This behavior can be attributed to the chemical composition and coarsening of $Al_3Sc/Al_3(Sc,Zr)$ phases formed during hot extrusion and aging, which are discussed in the section 4.1.

For the E420 condition, the two-step aging process achieved the highest hardness (67 HV) among all aging treatments. In contrast, for E480, although two-step aging yielded a higher hardness (58 HV) than aging at 400 °C, it was still 7% lower than the peak value obtained after aging at 300 °C for 12 hours. Thus, unlike E420, the two-step aging process does not provide superior hardening for E480. However, considering the balance between EC and hardness, two-step aging offers optimal results for E420. Although its EC (57.5 %IACS) is slightly lower than that at 400 °C (58 %IACS), the significant hardness improvement makes it a more promising treatment for conductor applications.

To reliably investigate the effectiveness of the two-step aging process on mechanical properties, tensile tests were performed on E420 samples under various aging conditions, as shown in Figure 5-6. The two-stage aging of E420, which achieved an EC of 57.5% IACS, yielded an ultimate tensile strength (UTS) of 172 MPa and a yield strength of 133 MPa, outperforming other conditions. In contrast, aging at 400°C, which resulted in the highest EC (58% IACS) for E420, led to lower UTS (~147 MPa). By comparing the tensile strength of E420 under different aging conditions (Figure 5-6), it can be observed that thermal stability gradually decreases with increasing aging temperature from 300 °C/24 h to 400 °C/24 h. In contrast, the two-step aging treatment exhibits stronger resistance to strength degradation. This behavior is attributed to the reduced tendency of precipitate coarsening during two-step aging compared to one-step treatments, as discussed in detail in Section 4.1.

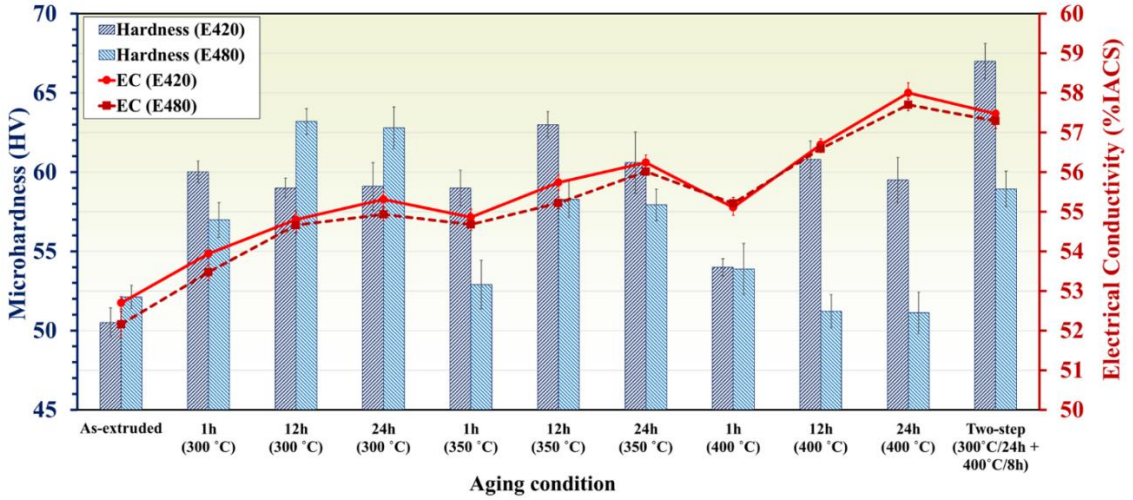

Figure 5-5. Hardness and electrical conductivity of Al–0.1Sc–0.1Zr alloy in E420 and E480 extrusion conditions with different aging temperatures and times.

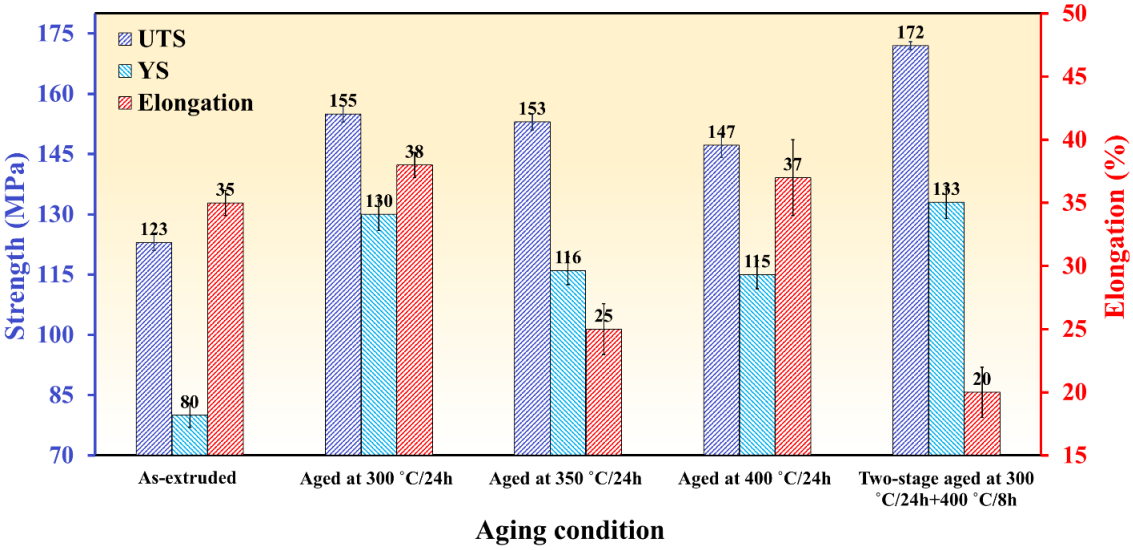

Figure 5-6. Tensile properties of E420 samples under different aging conditions.

5.3.4. Microstructure evolution during aging of extruded strips

Dark-field TEM images and selected area electron diffraction (SAED) patterns of the Al–0.1Sc–0.1Zr alloy after various aging conditions are shown in Figure *5-7*, revealing mainly spherical precipitates dispersed within the matrix. Generally, these precipitates can be classified into two types: pre-existing precipitates, formed during hot extrusion, and newly formed precipitates, which nucleated and grew during the aging treatment. SAED patterns and TEM-EDS analysis (not shown) indicate that the precipitates are primarily composed of Al, Sc, and Zr, corresponding to $Al_3(Sc,Zr)$ with an $L1_2$ crystal structure [36]. Although most

precipitates are spherical, some $Al_3(Sc,Zr)$ with of elongated, disk-shaped morphologies appear in the E480 samples aged at 350°C and especially 400°C (Figure *5-7* (d), (f)). These features likely indicate the early stages of transformation toward the equilibrium $D0_{23}$ phase, consistent with the observations reported by Knipling et al. [40, 41].

According to the Table *5-5* and Figure 5-8, for both the E420 and E480 conditions, increasing the aging temperature from 300°C to 400°C leads to a decrease in precipitate number density and an increase in average precipitate diameter. This effect is more pronounced in E480, which shows significant coarsening with temperature. In E480, the number density decreases from 2.46×10^{21} m^{-3} at 300°C to 0.58×10^{21} m^{-3} and 0.39×10^{21} m^{-3} at 350°C and 400°C, respectively. As shown in Figure 5-8, higher aging temperatures result in a greater proportion of coarse precipitates (>15 nm). Specifically, 55% and 83% of precipitates formed at 350°C and 400°C in E480 exceed 15 nm, indicating a much coarser size distribution compared to other conditions. Accordingly, the average precipitate diameter in aged E480 is larger than in E420, and the coarsest precipitates with an average diameter of 23.4 nm (min 11.2-max 30.6) are observed at 400°C in the E480 alloy.

The two-step aging for both E420 and E480 led to a higher precipitate number density than the one-step aging processes. The highest number density, 4.41×10^{21} m^{-3}, was observed in E420 after two-step aging (Table *5-5*), with an average precipitate diameter of 8.5 nm. As shown in Figure 5-8, the two-step aging process results in a broader precipitate size distribution for both E420 and E480, with most precipitates concentrated in the 3–7 nm range. Two-step aging promotes finer precipitate formation, with 50% of the precipitates in E420 and 55% in E480 being within the 3–7 nm range. However, under this aging condition, 13% of E480 and 1% of E420 precipitates exceeded 15 nm in size, likely due to pre-existing precipitates from hot extrusion. As a result, E420—which had finer initial precipitates formed during hot extrusion (Figure *5-4* (a), (h))—showed fewer precipitates larger than 15 nm after two-step aging compared to E480.

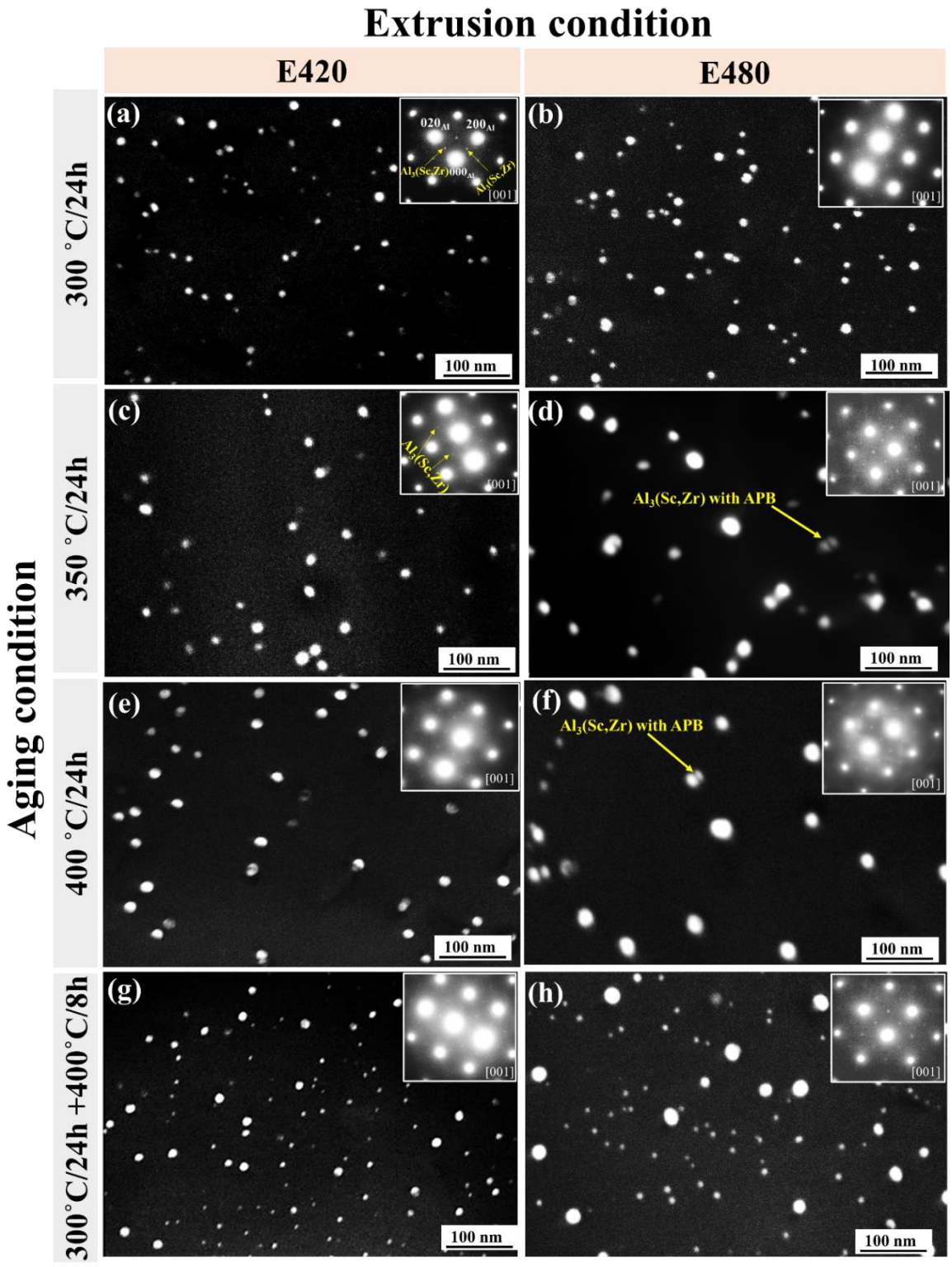

Figure 5-7. Dark-field TEM images showing the precipitate distribution in E420 and E480 alloys. (a, b) Aging at 300°C for 24h. (c, d) Aging at 350°C for 24h. (e, f) Aging at 400°C for 24h. (g, h) Two-step aging process (300°C for 24h followed by 400°C for 8h). Insets show SAED patterns corresponding to the precipitates.

Table 5-5. Precipitate characteristics of Al–0.1Sc–0.1Zr alloy under different aging conditions.

	Aging condition	Number density of precipitates (N_d) ($\times 10^{21} m^{-3}$)	Average Precipitate Diameter (D_{avg}) (nm) (Min–Max)
E420	300 ˚C/24h	2.03±0.21	8.7 (2.7-15.8)
	350 ˚C/24h	1.96±0.12	12.1 (6.6-21.1)
	400 ˚C/24h	1.52±0.17	15.5 (7.6-23.5)
	300 ˚C/24h + 400 ˚C/8h	4.41±0.44	8.5 (2.9 -19.2)
E480	300 ˚C/24h	2.46±0.23	11.8 (4.5-22.1)
	350 ˚C/24h	0.58±0.07	18.1 (8.9-28.7)
	400 ˚C/24h	0.39±0.05	23.4 (11.2-30.6)
	300 ˚C/24h + 400 ˚C/8h	2.57±0.30	12.2 (3.0-29.6)

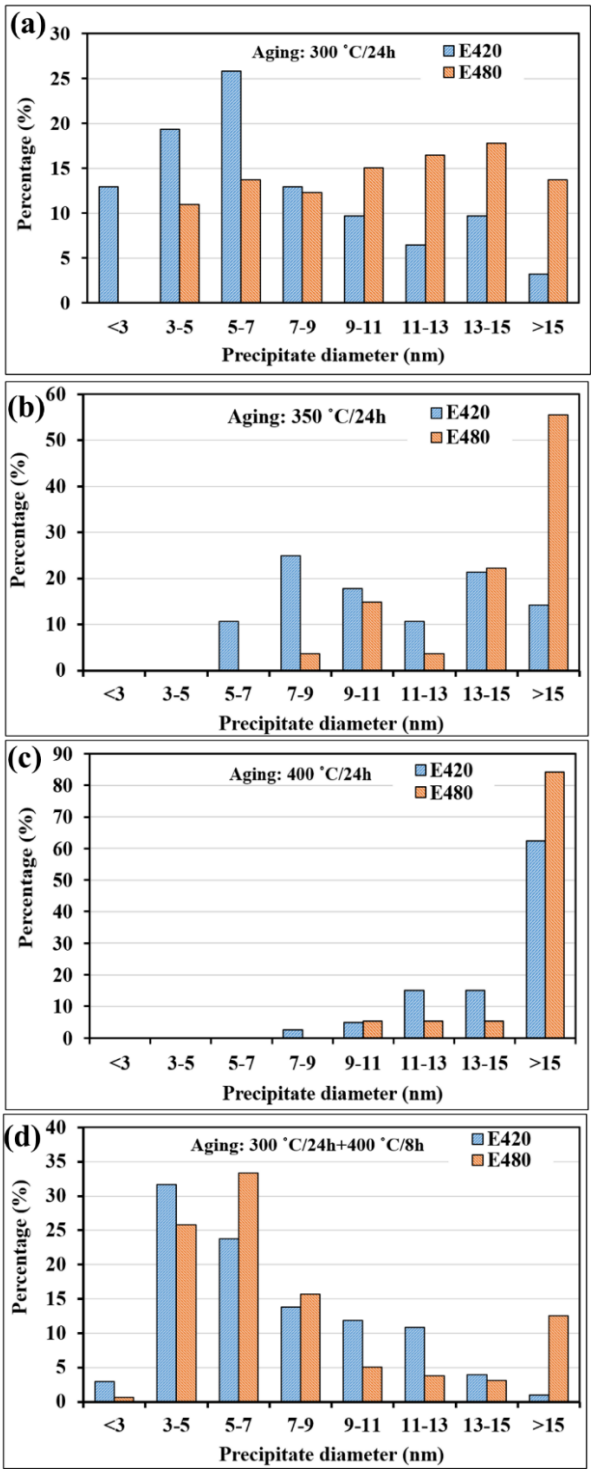

Figure 5-8. Precipitate size distribution of Al–0.1Sc–0.1Zr alloy aged under different conditions: (a) Aging at 300°C for 24 hours, (b) Aging at 350°C for 24 hours, (c) Aging at 400°C for 24 hours, and (d) Two-step aging: 300°C for 24 hours followed by 400°C for 8 hours.

Figure 5-9 (a) shows the spherical precipitates in the extruded E420 sample aged by the two-step process, observed at a lower magnification. Coarse precipitates (larger than 18 nm) were

analyzed using TEM-EDS to determine their chemical composition. Sc- and Zr-containing precipitates with a wide range of compositions were identified, as shown in Figure 5-9 (b-e). Type A precipitates are rich in Sc, and precipitation-free zones (PFZs) were observed around them. This suggests that, most likely during the second step at 400 °C, the pre-existing larger Al_3Sc precipitates grew at the expense of smaller ones. This phenomenon, known as Ostwald ripening, is driven by the reduction of total interfacial free energy [42, 43]. Type B precipitates contain more Zr than Type A, while Sc remains the predominant element. These precipitates are thought to have formed during extrusion with a relatively small size, followed by a slight coarsening during the first aging step and an incorporation of more Zr during the second step at 400 °C. Type C precipitates show the additional presence of Si in their composition. The presence of Si in Al_3(Sc,Zr) phases is expected, since Si can substitute for Al in the $L1_2$ lattice. This substitution promotes precipitate nucleation and leads to the formation of $(Al,Si)_3$(Sc,Zr) precipitates [44, 45]. Finally, Type D precipitates are Zr-rich compared to Sc, suggesting that they were formed at a higher temperature.

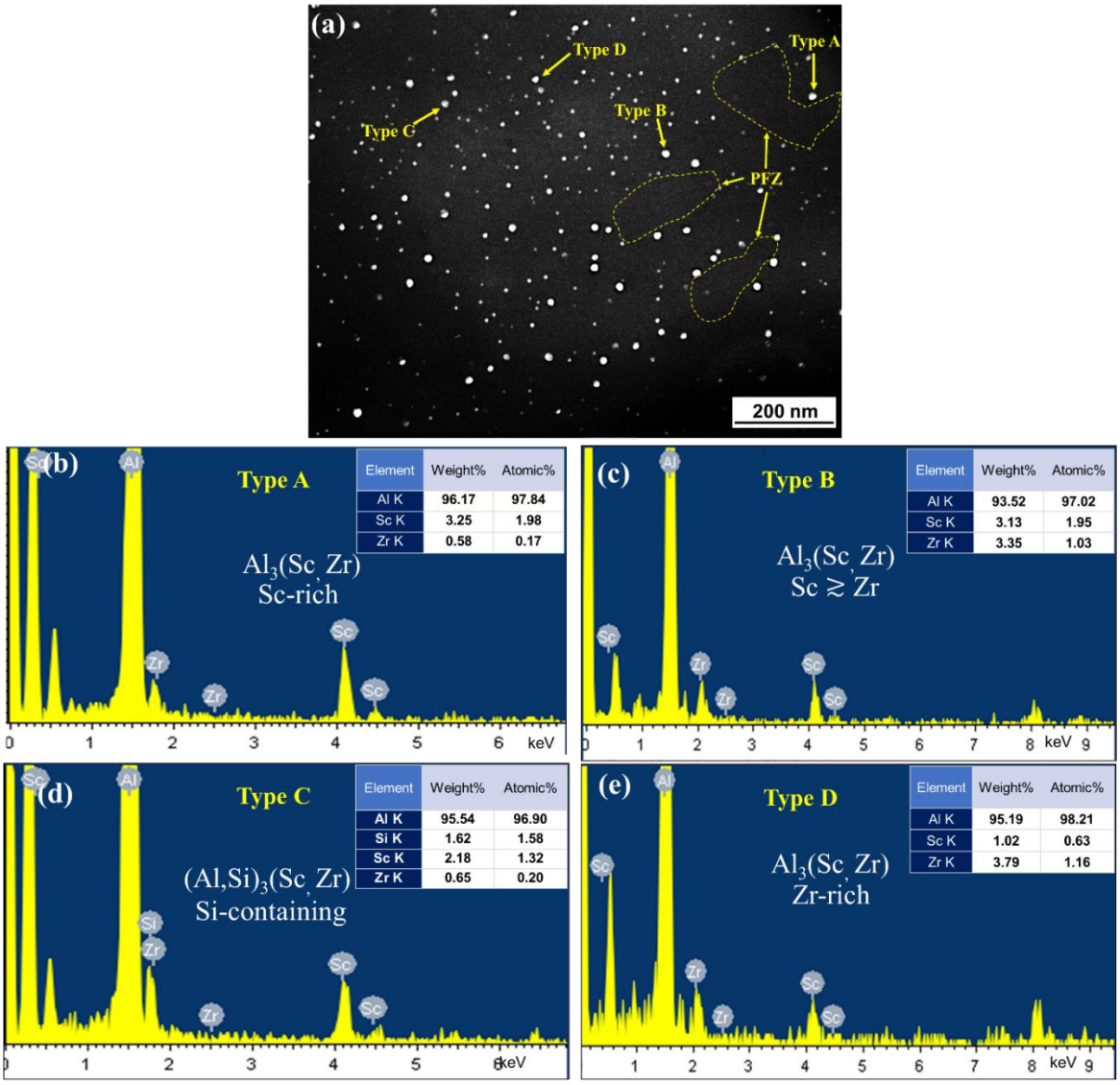

Figure 5-9. Microstructural and compositional analysis of the Al–0.1Sc–0.1Zr alloy aged using a two-step treatment under the E420 condition. (a) Dark-field TEM image highlighting precipitate-free zones (PFZ) and different $Al_3(Sc,Zr)$ precipitates. (b)–(e) TEM-EDS analyses from different precipitates, showing the elemental composition.

Furthermore, precipitate evolution and subgrain growth in Al–0.1Sc–0.1Zr alloys are closely interconnected during thermal exposure. Figure *5-10* compares subgrain structures from EBSD results for samples extruded under the E420 condition and subjected to two-step aging (300 °C + 400 °C) versus one-step aging at 400 °C for 24 h. The two-step aged condition exhibits a higher precipitate number density (4.41×10^{21} m^{-3}) and a smaller average precipitate size (8.5 nm), resulting in finer subgrains (6.2 μm). In contrast, the one-step aged sample, characterized by a lower precipitate density (1.52×10^{21} m^{-3}) and larger precipitate

size (15.5 nm), exhibits coarser subgrains measuring 14.3 μm. These results demonstrate the strong relationship between precipitate characteristics and subgrain growth, as further discussed in Section 4.4.

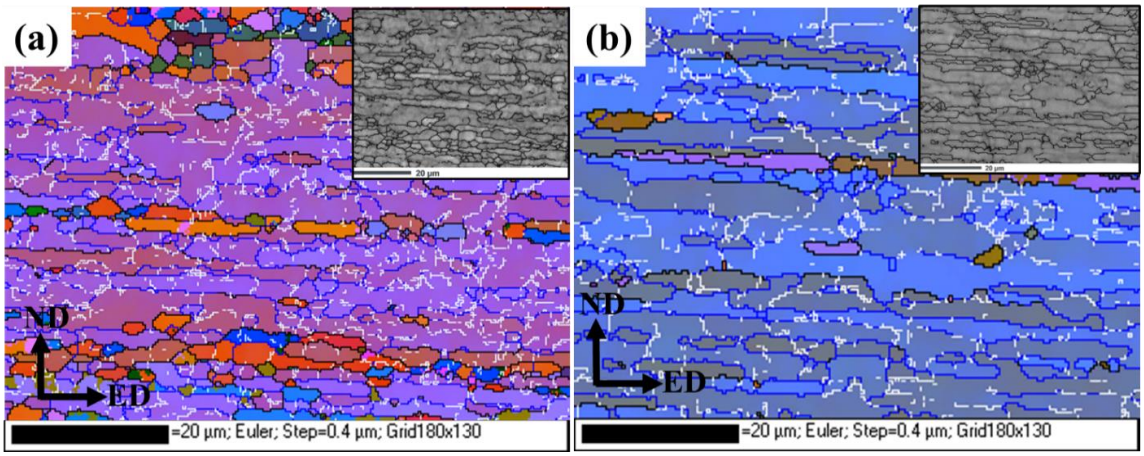

Figure 5-10. Euler orientation and quality maps (insert) of E420 samples: (a) two-step aged at 300 °C/24 h + 400 °C/8 h and (b) one-step aged at 400 °C/24 h. White, blue, and black lines indicate misorientations of 2–5°, 5–15°, and >15°, respectively.

5.4. Discussion

5.4.1. Modeling the evolution of precipitate composition and its relationship with coarsening resistance

Understanding aging condition effects on the Al–0.1Sc–0.1Zr alloy requires analyzing how diffusivity, temperature, and time affect precipitate structure and properties. The Arrhenius relationship describes how diffusion coefficients vary with temperature, and it is given by the following equation [46]:

$$D = D_0 \exp(-\frac{Q}{RT}) \quad (3)$$

Where D_0 (m^2/s) is the pre-exponential factor, Q (J/mol) is the activation energy for diffusion, R (8.314 J/(mol·K)) is the universal gas constant, T (K) is the absolute temperature. Sc has a lower activation energy (Q) for diffusion compared to Zr, with Q =173 kJ/mol for Sc, and 242 kJ/mol for Zr. The corresponding pre-exponential factors (D0) are 5.31×10−4 m2/s and 7.28×10−2 m²/s for Sc and Zr, respectively [24, 33, 47, 48]. Figure *5-11* (a) shows the diffusion coefficients of Sc and Zr in Al over a temperature range of 250 to 520°C. The diffusion rates of both elements increase with temperature, and Sc consistently diffuses faster than Zr.

To better understand the influence of temperature and time on Sc and Zr mobility in the matrix, a one-dimensional 'root-mean-square (RMS) displacement' model was employed. This statistical measure, used in diffusion studies, predicts the approximate one-dimensional displacement of atoms over time [49, 50]. Although the results of this model are hypothetical, they provide reliable insight into how temperature affects the mobility of solute atoms within the material. The RMS atomic displacement as a function of temperature can be calculated using the following general formula:

$$\left\langle x^2 \right\rangle = 2tD_{(T)}$$
$$x = \sqrt{2tD_{(T)}} \quad (2)$$

Here, x represents the RMS atomic displacement, t denotes time (sec), and $D_{(T)}$ is the temperature-dependent diffusion coefficient. Figure *5-11* (b) illustrates the RMS atomic displacement as a function of temperature for exposure durations of 2 minutes, 8 and 24 hours.

In the E420 condition, the alloy was preheated to 420°C, over a maximum process time of 2 minutes. Based on the RMS displacement model prediction shown in Figure *5-11* (b), even at the exit temperature of 480°C–483°C of E420 condition, the atomic displacement of Zr may remain ≤17 nm after 2 minutes of exposure. However, during the extrusion process, the exposure time to the exit temperature is considerably shorter (only a few seconds), and the atomic displacement of Zr is likely limited to around 1 to 5 nm. This level of displacement is insufficient for Zr atoms to significantly participate in the formation of $Al_3(Sc_{1-x},Zr_x)$ or Al_3Zr within the $L1_2$ structure. In contrast, Sc with predicted atomic displacements of ~100 nm when exposed to the exit temperature of E420, is sufficiently mobile to form clusters and precipitates. This explains why Zr-containing pre-existing precipitates were not detected in the as-extruded E420 condition, as illustrated in Figure *5-4* (a)-(c). In the E480 condition, the exit temperature reached ~512 °C, causing atomic displacements nearly five times greater and hence sufficient to induce Zr atoms to participate in $L1_2$-structure formation, though still to a limited extent relative to its full potential (Figure *5-4* (d)-(f)).

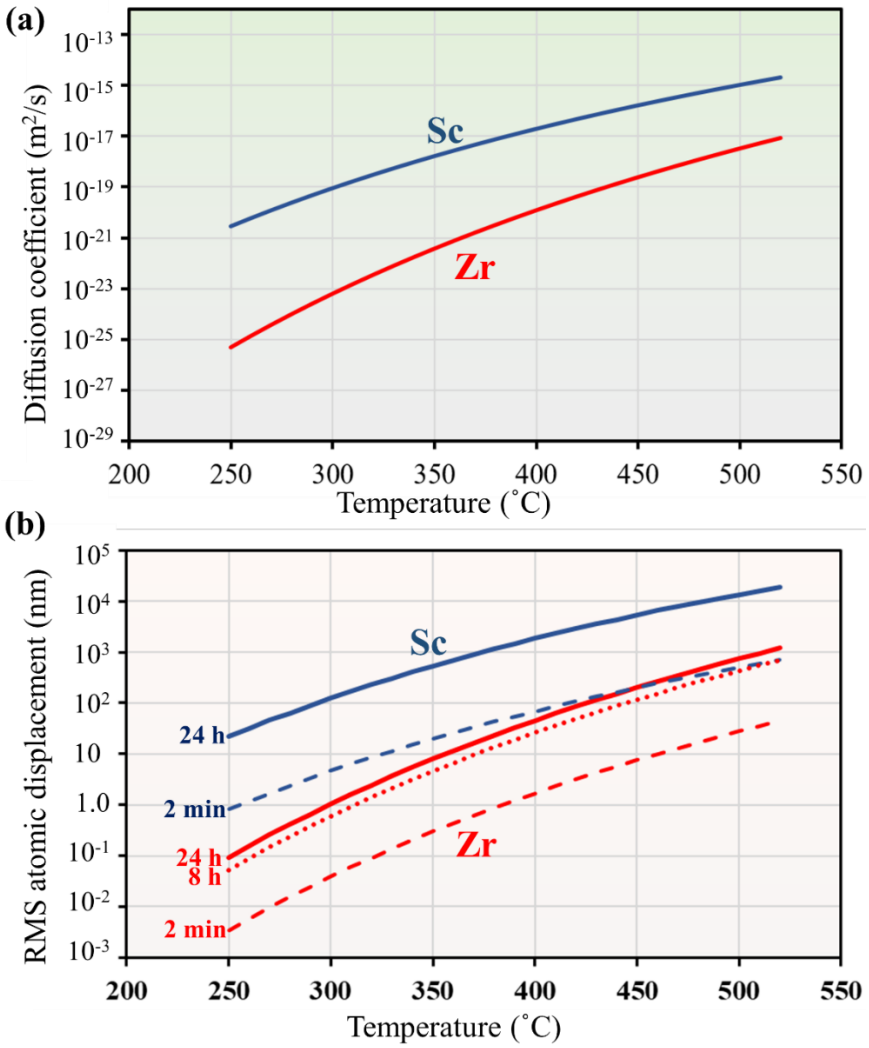

Figure 5-11. (a) Diffusion coefficients of Sc and Zr in Al at various temperatures; (b) Temperature-dependent RMS atomic displacement of Sc and Zr in Al for various exposure times.

Figure 5-12 (a) provides a schematic illustration of the general structure of $Al_3(Sc,Zr)$ precipitates in the Al-Sc-Zr system, including a Sc-rich core, a transition zone, and a Zr-rich shell [24, 51]. Under thermal exposure, due to the significantly higher diffusivity of Sc compared to Zr in Al, only Sc atoms are kinetically capable of participating in the early stages of nucleation and growth of Al_3Sc precipitates, which form the Sc-rich core (Al_3Sc) with a cubic ordered $L1_2$ crystal structure [52, 53]. Then, given the relatively high solubility of Zr in Al_3Sc (~16 wt.%), compared to its negligible solubility in the Al matrix, there is a driving force for Zr atoms to be incorporated into existing Al_3Sc precipitates with the $L1_2$ structure, rather than forming a separate Al_3Zr phase [23, 24]. This results in the formation of a transition zone, as shown in Figure 5-12 (a). The Sc and Zr concentrations within this region

vary between the Sc-rich core and the outer region, yielding a stoichiometric composition of $Al_3(Sc_{1-x}Zr_x)$ [54]. With continued thermal exposure of the Al-Sc-Zr alloy—and following the earlier depletion of Sc in the Al matrix—the precipitate becomes encapsulated by a coherent or semi-coherent Zr-rich shell (Al_3Zr) with an $L1_2$ structure, forming the outermost layer predominantly composed of Zr [51, 52, 54]. The Zr-rich shell significantly improves the coarsening resistance of $Al_3(Sc,Zr)$ precipitates by reducing the interfacial free energy, which strongly influences coarsening kinetics. The lower Al_3Zr/Al interfacial free energy as well as the slow diffusion rate of Zr enhance the precipitate stability, making Al_3Zr more resistant to coarsening than Al_3Sc in the Al matrix [47, 55].

Figure 5-12 (b) illustrates how precipitate structures evolve under one-stage aging of 300°C/24h and 400°C/24h, and two-stage aging of 300°C/24h + 400°C/8h. During isothermal aging at 300 °C, Zr remains relatively immobile since its precipitation typically begins around 375 °C [24, 47]. According to the prediction in Figure 5-11 (b), Zr diffuses only about ~1 nm over 24 h at 300 °C, confirming its extremely limited mobility under this aging condition. As a result, the precipitates newly formed during aging at 300 °C are predominantly Sc-rich Al_3Sc with an $L1_2$ crystal structure, as shown in Figure 5-12 (b) [53].

During isothermal aging at 400 °C, both Sc and Zr exhibit sufficient diffusivity to participate in precipitate formation. The higher diffusivity of Sc accelerates the initial formation of Al_3Sc cores under this aging condition by rapidly depleting Sc from the matrix, leading to coarser precipitates. Moreover, the increased mobility of Zr atoms at 400 °C allows their diffusion and incorporation, alongside Sc, into the evolving precipitates, which over time leads to the formation of a transition zone. As schematically illustrated in Figure 5-12 (b), under this aging condition, a higher fraction of precipitates is predicted to develop a transition zone with $Al_3(Sc_{1-x}Zr_x)$ stoichiometry due to increased Zr incorporation into the $L1_2$ structure. Knipling et al. [24] supported this by providing solute concentration profiles in the α-Al matrix and $Al_3(Sc,Zr)$ precipitates, showing that increasing the aging temperature from 300 °C to 400 °C in an Al–0.1Sc–0.1Zr (at.%) promotes greater Zr incorporation into the transition zone, thereby increasing its Zr content. Such a transition zone, influenced by the higher diffusivity of Sc, results in Sc being the dominant element in the $Al_3(Sc_{1-x}Zr_x)$ phase, with x typically less than 0.5 [47]. During isothermal aging at 400 °C, the coarsening kinetics

of the transition zone of $Al_3(Sc_{1-x}Zr_x)$ is similar to that of Al_3Sc, due to the similar anisotropy in their interfacial free energies [55, 56]. Therefore, due to the lower diffusivity of Zr, the outer regions of precipitates with an $Al_3(Sc_{1-x}Zr_x)$ composition cannot effectively resist coarsening during prolonged aging at 400 °C. As shown in the experimental results in Figure 5-7 (e-f), coarsening continues until Sc is depleted from the matrix. Once Sc is exhausted, the driving force for Sc incorporation weakens, a Zr-rich shell begins to form at the precipitate edge—but too late to prevent significant coarsening at 400 °C.

In the two-step aging process, the first step at 300 °C for 24 hours promotes the formation of fine, Sc-rich Al_3Sc cores without Zr involvement. This treatment depletes most Sc from the matrix without causing significant coarsening because the over-aging effect begins at ~325°C for Al_3Sc [9, 66]. In the subsequent step at 400 °C, the diffusion of Zr atoms becomes initiated, allowing Zr atoms to incorporate into the existing $L1_2$ structure. Since most Sc is consumed during the first step at 300 °C, the formation of the transition zone—exhibiting coarsening behavior similar to Al_3Sc—is limited compared to single-step aging at 400 °C. A coherent Zr-rich shell then forms, enhancing coarsening resistance due to the lower interfacial free energy of Al_3Zr/α-Al interfaces [55, 57]. In both the 400 °C/24 h and two-step (300 °C/24 h + 400 °C/8 h) aging conditions, a Zr shell forms around the precipitates. However, the Zr shell is expected to occupy a larger fraction of the precipitates in the two-step aging compared to the one-step 400 °C/24 h. This is because, at 400 °C/24 h, some Zr is consumed in developing the transition zone, whereas in the two-step aging, the transition zone is smaller, leaving more Zr available to form the outer shell of the precipitates, thereby enhancing their coarsening resistance. As a result, newly formed precipitates remain finer after two-step aging, as demonstrated experimentally in Figure 5-7 (g-h). The RMS atomic displacement of Zr after 8 h, shown in Figure 5-11 (b), exhibits behavior similar to that after 24 h. This suggests that the majority of Zr atoms have been removed from the matrix by 8 h, further confirmed by the small difference in EC between the two-step (57.5 %IACS) and one-step aging at 400 °C (58 %IACS). Briefly, the possible sequence of precipitate formation during two-step aging of the Al-0.1Sc-0.1Zr alloy can be described as follows: (i) nucleation and formation of fine Al_3Sc precipitates with a high number density, leading to Sc depletion in the matrix during aging at 300 °C; (ii) formation of a thin $Al_3(Sc_{1-x}Zr_x)$ transition layer at the onset of the second step at 400 °C; and (iii) subsequent growth of an Al_3Zr shell

surrounding the precipitates. It is noteworthy that during the second step (400 °C) of the two-step aging, individual Al_3Zr precipitates may nucleate separately within the microstructure [15].

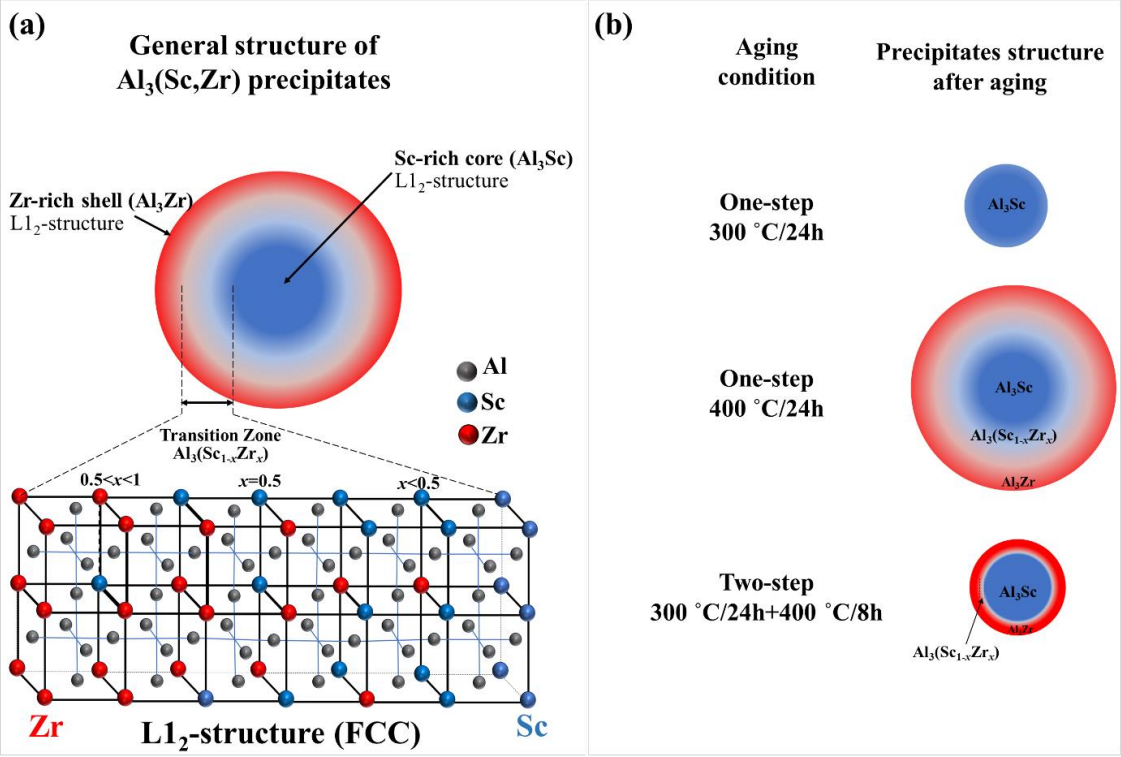

Figure 5-12. (a) Schematic representation of the general structure of $Al_3(Sc,Zr)$ precipitates, illustrating the Sc-rich core, transition zone, and Zr-rich shell. The atomic arrangement highlights the transition zone with varying Sc and Zr concentrations. (b) Schematic of precipitate structure and composition at different aging conditions.

5.4.2. The role of precipitates in strengthening of the Al–0.1Sc–0.1Zr alloy

The contributions from different strengthening mechanisms are assumed to be additive, considering they act independently. Accordingly, the total yield strength of the Al alloy is estimated as [32, 58]:

$$\sigma_{ys} = \sigma_0 + \sigma_{ss} + \sigma_{gb} + \sigma_{pre} + \sigma_{dis} \quad (3)$$

where σ_0 is the material inherent frictional resistance (Peierls–Nabarro forces), σ_{ss} is the solid solution strengthening contribution, σ_{gb} is the strength that is provided by grain-boundary

strengthening (Hall-Petch effect), σ_{pre} is the strength that is provided by precipitation, and σ_{dis} is the dislocation strengthening contribution [52, 59].

The strength of the Al–0.1Sc–0.1Zr alloy is significantly enhanced after aging, mainly due to the pinning effect of nano-sized precipitates that form within the matrix, as shown in Figure 5-7. The increase in strength due to precipitation typically occurs through one of two mechanisms, depending on the precipitate size: (i) shearing of small precipitates, which involves order strengthening, coherency strengthening, and modulus mismatch strengthening; and (ii) the Orowan bypass mechanism for larger precipitates, where dislocations loop around the precipitates rather than cutting through them [24, 33, 60].

Studies on similar alloy systems have shown that the Orowan dislocation bypass mechanism becomes the primary strengthening factor when precipitates have an average radius larger than 2 nm, whereas smaller precipitates can still be sheared [24, 30, 61, 62]. According to the average diameter of precipitates in Table 5-5, the precipitate diameters have exceeded the critical size for dislocation shearing, leading to a transition from the shearing mechanism to the Orowan looping mechanism. The increase in yield strength due to precipitates that is caused by the Orowan mechanism can be calculated from following equation [30, 63]:

$$\sigma_{Pre\ (Orowan)} = M \frac{0.4G \cdot b}{\pi\sqrt{1-\upsilon}} \frac{\ln(2r/b)}{\lambda_p} \quad (4)$$

$$\lambda_p = r\left(\frac{2\pi}{3F_V}\right)^{0.5} \quad (5)$$

M is the mean matrix orientation factor (Taylor factor) for Al with a value of 3.06 [64, 65], G is the shear modulus of Al at ambient temperature (taken as 25.4 GPa) [66], b is the magnitude of the Burgers vector with a value of 0.286 nm, υ is the Poisson's ratio of 0.34 [67], λ_p is the mean edge-to-edge inter-precipitate spacing, and r and F_V are the radius and volume fraction of $Al_3(Sc,Zr)$ precipitates, respectively.

Table 5-6 shows the Orowan strengthening contributions to the yield strength of the Al–0.1Sc–0.1Zr alloy under two extrusion conditions, E420 and E480, across various aging treatments. The two-step aged E420 condition exhibits the highest σ_{Or} (76.2 MPa). For E420,

σ_{Or} increased as the aging temperature rose from 300 °C to 350 °C, then decreased upon reaching 400 °C, while in E480, σ_{Or} decreased from 300 °C to 400 °C. The trends observed for σ_{or} are consistent with the mechanical property trends shown in Figure 5-5 and Figure 5-6, highlighting the critical role of precipitate evolution in determining the strength of the alloys under varying conditions.

According to the Orowan strengthening equation, as precipitates coarsen, their average radius r increases. However, this coarsening also leads to an increase in the interparticle spacing (λ_p) due to a decrease in the number density of precipitates. Since the Orowan stress is inversely proportional to λ_p, the greater spacing between particles reduces their effectiveness as barriers to dislocation motion, resulting in decreased strengthening [22, 25]. According to Table 5-6, among the aged conditions, the lowest λ_p (157 nm) is observed for the two-step aging of the E420 condition, with an average radius of 4.2 nm. In contrast, the highest average λ_p (379 nm) is observed for the E480 condition aged at 400°C for 24 hours, with an average radius of 11.7 nm resulting in the lowest Orowan stress, respectively.

Table 5-6. Effect of aging condition on precipitate volume fraction (F_V), average precipitate radius (r), inter-precipitate spacing (λ_p), and calculated Orowan stress (σ_{Or}) of Al–0.1Sc–0.1Zr alloy.

Extrusion condition	Aging condition	F_V %	r (nm)	F_V/r (nm^{-1})	λ_p (nm)	σ_{Or} (MPa)
E420	As-extruded	0.015	4.4	0.34×10^{-4}	520	23.3
	300 ˚C/24h	0.09	4.3	2.1×10^{-4}	207	58.1
	350 ˚C/24h	0.18	6.1	2.9×10^{-4}	214	62.1
	400 ˚C/24h	0.21	7.8	2.7×10^{-4}	246	57.5
	300/24h+400 ˚C/8h	0.15	4.2	3.6×10^{-4}	157	76.2
E480	As-extruded	0.05	6.5	0.77×10^{-4}	419	32.1
	300 ˚C/24h	0.19	5.9	3.2×10^{-4}	196	67.2
	350 ˚C/24h	0.17	9.1	1.9×10^{-4}	319	46.0
	400 ˚C/24h	0.20	11.7	1.7×10^{-4}	379	41.2
	300/24h+400 ˚C/8h	0.18	6.1	2.9×10^{-4}	208	63.8

5.4.3. Relationship between precipitation and electrical conductivity

Electrical conductivity is affected by electron scattering, which is primarily caused by lattice distortions resulting from defects, impurities, and solute atoms [68]. According to Matthiessen's rule, the total electrical resistivity can be expressed as:

$$\rho_{total} = \rho_0 + \rho_{gb} + \rho_{ss} + \rho_{pre} + \rho_{dis} + \rho_{vac} \quad (6)$$

$$EC(\%\text{IACS}) = \frac{172.4}{\rho_{total}(\mu\Omega\text{cm})} \quad (7)$$

where ρ_0 represents the lattice resistivity of the Al matrix, ρ_{gb} is the resistivity resulting from the grain boundaries, ρ_{ss} is the resistivity caused by solute atoms dissolved in the matrix, and ρ_{pre} is the resistivity associated with precipitates [15, 68]. It is well-documented that ρ_{ss} (solid solution resistivity) arises from solute atoms acting as effective lattice defects, scattering electrons more significantly than mechanisms such as grain boundary or precipitation strengthening [63, 69]. Therefore, the change in EC in the aging process is strongly related to the removal of Sc and Zr atoms from the atomic lattice.

Al_3Sc and $Al_3(Sc,Zr)$ precipitates, which form during aging, are coherent with the aluminum matrix and have a lower negative impact on EC compared to Sc and Zr in solid solution. However, in the as-homogenized condition, the EC remains relatively low (50.9% IACS), primarily due to significant lattice distortion caused by the supersaturated solid solution of Sc and Zr atoms in the α-Al matrix. Following hot extrusion, the EC increases to 52.2–52.8% IACS, mainly due to the partial precipitation of Sc and/or Zr during both the E420 and E480 extrusion processes. Despite this improvement, the EC remains noticeably lower than that of the base 1xxx alloy without Sc and Zr (58.2% IACS), indicating that a significant number of solute atoms remain in the solid solution. Subsequent aging treatments further reduce the solute concentration in α-Al through ongoing precipitation. During aging at 300 °C and 350 °C, the EC increases slowly because Zr remains in solution due to its low diffusivity, while only Sc precipitates [15, 29, 63]. In contrast, since Zr precipitation typically accelerates noticeably around 375 °C, aging at 400 °C facilitates the co-precipitation of both Sc and Zr, leading to a higher rate of EC increase over time [9, 66]. At this temperature, the EC reaches 58.0% IACS—very close to that of the base 1xxx alloy—indicating effective removal of both

Sc and Zr from solid solution. In a two-step aging process, the initial step at 300 °C/24h results in an EC of 55.2% IACS for the E420 condition. Subsequent aging at 400 °C promotes further precipitation, especially of Zr, increasing the EC to 57.5% IACS, slightly lower than the single-step aging at 400 °C. This slight difference is attributed to the small amount of Zr that may remain in the matrix.

Figure *5-13* illustrates the trade-off between tensile strength and EC for Al electrical bus bars, based on ASTM standards for 6xxx and 1xxx series alloys [13, 14]. The 6xxx series (ASTM B187) clusters at higher strength but lower EC, whereas the 1xxx series (ASTM B236) shows higher EC but lower strength. The Al–Sc–Zr alloy studied here (two-step aging of E420) lies above this trend line, demonstrating an enhanced combination of strength and conductivity and highlighting its potential as a next-generation electrical bus bar material.

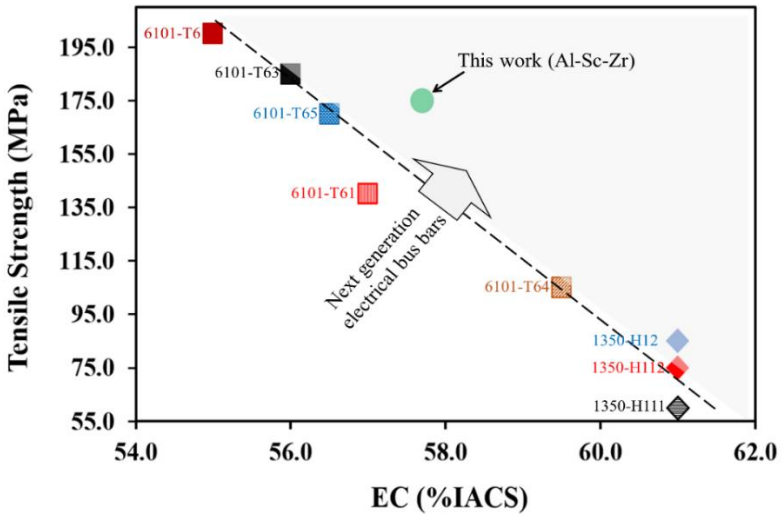

Figure 5-13. Comparison of tensile strength and EC values of the studied Al-Sc-Zr alloy subjected to two-step aging of E420 sample with ASTM standards for Al electrical bus bars.

5.4.4. Influence of precipitate coarsening on subgrain growth

Subgrain growth during aging is strongly influenced by the size and number density of second-phase particles in the Al matrix [25, 70]. They apply a Zener drag pressure, P_z, on the boundaries, effectively pinning them in place [71]. Figure 5-14 shows the interaction between precipitates and subgrains in the E420-extruded alloy following two-step aging. The fine $Al_3(Sc,Zr)$ precipitates exert a pinning effect on subgrain boundaries, restricting their movement, and effectively inhibiting subgrain growth [62]. The pinning pressure per unit

area of the subgrain boundary is quantified by the Zener drag pressure, expressed as follows [72, 73]:

$$P_z = \frac{3\gamma F_V}{2r} \quad (8)$$

Here, F_V and r represent the volume fraction and average radius of the precipitates, respectively, while γ denotes the specific grain boundary energy. According to the relationship introduced by Humphreys and Hatherly [25], this driving pressure, P, for subgrain growth is determined by balancing the stored energy in the subgrain boundaries driving growth (P_D) and the opposing Zener drag pressure (P_Z), as follows:

$$P = P_D - P_z = \frac{\alpha\gamma}{R} - \frac{3\gamma F_V}{2r} \quad (9)$$

where R is the average subgrain radius, and α is the shape factor, typically taken as 1.5. Accordingly, both the Zener drag pressure and the driving pressure for subgrain growth are directly related to the F_V/r ratio. A smaller and higher number density of precipitates (high F_V, low r) results in stronger pinning and better control of subgrain growth [74]. Based on Table 5-6, the two-step aging at E420 yields the highest F_V/r ratio (3.6×10^{-4} nm^{-1}), enhancing Zener drag pressure and reducing the driving pressure (P) of subgrain growth. In contrast, the one-step aged E420 sample (400 °C for 24 h) exhibits a lower F_V/r ratio (2.7×10^{-4}), weaker Zener drag pressure, and increased driving pressure for subgrain growth. Thus, the lower driving pressure in two-step aging leads to smaller subgrains compared to 400 °C aging, explaining the larger subgrain size at 400 °C shown in Figure 5-10.

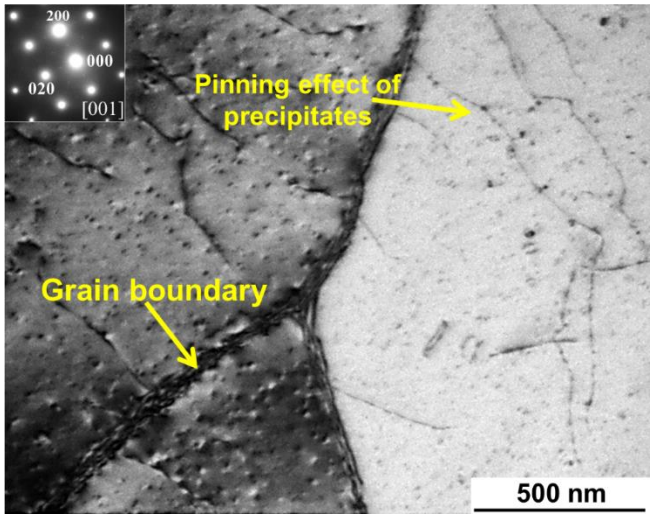

Figure 5-14. Bright-field TEM image showing subgrain boundary pinning by $Al_3(Sc,Zr)$ precipitates in the E420 alloy after two-step aging.

5.5. Conclusion

This study thoroughly explored the effects of thermomechanical processing—specifically billet preheating temperature and aging treatments—on the microstructure, mechanical properties, and electrical conductivity of an Al–0.1Sc–0.1Zr conductor alloy. The following conclusions are derived from the results obtained.

1. The results clearly demonstrate that extrusion at 420 °C (E420) suppresses early precipitate coarsening, promoting a higher number density of fine $Al_3(Sc,Zr)$ precipitates. In contrast, extrusion at 480 °C (E480) forms coarse initial precipitates, leading to further pronounced coarsening during aging and degraded mechanical properties.

2. Among the various post-extrusion aging treatments evaluated for E420, two-step aging (300 °C/24 h, followed by 400 °C/8 h) was most effective, yielding an excellent tensile strength (172 MPa) and EC (57.5% IACS), attributed to the formation of a distinct core–shell structure in $Al_3(Sc,Zr)$ precipitates. For E480, two-step aging could not lead to a higher strength than one-step aging at 400C.

3. The electrical conductivity (EC) increased as Sc and Zr atoms were removed from the Al matrix to form precipitates. The EC rise was slower during aging at 300°C and 350°C than at 400°C, where the highest EC (58% IACS) was achieved. This is due to Sc removal dominating at lower temperatures, while both Sc and Zr are removed at 400°C.

4. Based on a combination of diffusion modeling, experimental results and relevant literature, it was inferred that controlled two-step aging promotes effective Zr incorporation into the outer shell of the $Al_3(Sc_{1-x}Zr_x)$ precipitates, thereby inhibiting precipitate coarsening.

5. Two-step aging of E420 at 300°C/24h followed by 400°C/8h resulted in a higher number density of small precipitates, increasing the Zener drag pressure (P_Z) due to a higher F_V/r ratio, thereby inhibiting subgrain growth. In contrast, one-step aging at 400°C produced coarser precipitates (lower F_V/r), allowing more subgrain growth and hence reducing the grain boundary strengthening effect.

Acknowledgments

The authors express their sincere gratitude to the industrial partner, Rio Tinto Aluminium, for their support in this project. Special thanks are also extended to the technical teams at Rio Tinto Aluminium, the University Research Centre on Aluminium (CURAL), and the Chaire de recherche Institutionnelle en Métallurgie de la Transformation de l'Aluminium (CIMTAL) for their valuable collaboration and technical contributions.

Authors contribution

Behrouz Abnar: Investigation, Methodology, Formal analysis, Writing – original draft. *Paul Rometsch:* Conceptualization, Validation, Writing – review & editing. *Mousa Javidani:* Conceptualization, Validation, Writing – review & editing, Project administration.

5.6. References

[1] L. Pengfei, W. Zhigang, W. Yunli, G. Xizhu, W. Zaiyun, and L. Zhiqiang, "Effect of cerium on mechanical performance and electrical conductivity of aluminum rod for electrical purpose," *Journal of Rare Earths,* vol. 24, no. 1, pp. 355–357, 2006.

[2] M. Khoshghadam-Pireyousefan, M. Javidani, A. Maltais, J. Lévesque, and X.-G. Chen, "Strength-conductivity synergy in hypoeutectic Al-Si conductors via ultrafine-grained embedded Si nanoprecipitates," *Materials Science and Engineering: A,* vol. 929, p. 148124, 2025.

[3] Y. Wang, L. Zhu, G. Niu, and J. Mao, "Conductive Al alloys: the contradiction between strength and electrical conductivity," *Advanced Engineering Materials,* vol. 23, no. 5, p. 2001249, 2021.

[4] F. Yavari, M. Javidani, L. R. Pan, and X.-G. Chen, "The influence of Ce addition on the aging response of AlSi3Mg0. 5 cast conductor alloy: evaluation of electrical conductivity, mechanical properties, and microstructure," *Journal of Alloys and Compounds,* p. 182412, 2025.

[5] A. D. Callegaro *et al.*, "Bus bar design for high-power inverters," *IEEE Transactions on Power Electronics,* vol. 33, no. 3, pp. 2354–2367, 2017.

[6] B. Abnar, S. N. Khangholi, P. Rometsch, and M. Javidani, "Effect of hot deformation parameters on the performance and thermomechanical behavior of Cu-modified Al–Mg–Si

conductor alloys," *Journal of Materials Science,* 2025/10/06 2025, doi: 10.1007/s10853-025-11528-8.
[7] O. Mypati, T. Anwaar, D. Mitra, S. K. Pal, and P. Srirangam, "Characterization and modelling of Al and Cu busbar during charging and discharging of Li-ion battery for electric vehicles," *Applied Thermal Engineering,* vol. 218, p. 119239, 2023.
[8] T. Yoshida, N. Inoue, and T. Otsubo, "Bus bar connection device and switchgear including the same," ed: Google Patents, 2018.
[9] S. Braun, G. Micard, and G. Hahn, "Solar cell improvement by using a multi busbar design as front electrode," *Energy Procedia,* vol. 27, pp. 227–233, 2012.
[10] Z. Yi-Feng and G. Qiong-Xuan, "Study on busbar-structure for prototype of the high-speed railway traction converter," in *2011 International Conference on Electrical and Control Engineering*, 2011: IEEE, pp. 3177–3180.
[11] P. G. Ross and N. Mcgee, "Modular uninterruptible power supply," ed: Google Patents, 2018.
[12] H. Van Nguyen, K. M. Wildstone, P. A. Churnock, and M. D. Striffler, "Reserve power bus ring for data center," ed: Google Patents, 2016.
[13] *ASTM B317/B317M: Standard Specification for Aluminum-Alloy Extruded Bar, Rod, Tube, Pipe, and Structural Profiles for Electrical Purposes (Bus Conductor)*, A. International, 2017.
[14] *ASTM B236: Standard Specification for Aluminum Bars for Electrical Purposes (Bus Bars)*, A. International, 2015.
[15] L. Liu, J.-T. Jiang, B. Zhang, W.-Z. Shao, and L. Zhen, "Enhancement of strength and electrical conductivity for a dilute Al-Sc-Zr alloy via heat treatments and cold drawing," *Journal of Materials Science & Technology,* vol. 35, no. 6, pp. 962–971, 2019.
[16] P. Rocha, S. Langlois, S. Lalonde, J. Araújo, and F. Castro, "Influence of 1350 and 6201 aluminum alloys on the fatigue life of overhead conductors—A finite element analysis," *Tribology International,* p. 108661, 2023.
[17] R. Guan, Y. Shen, Z. Zhao, and X. Wang, "A high-strength, ductile Al-0.35 Sc-0.2 Zr alloy with good electrical conductivity strengthened by coherent nanosized-precipitates," *Journal of Materials Science & Technology,* vol. 33, no. 3, pp. 215–223, 2017.
[18] E. Elgallad, S. Khangholi, M. Javidani, A. Maltais, and X.-G. Chen, "Development of ultra-high-strength Al-Mg-Si conductor alloys with copper addition via scalable thermomechanical processes," *Scripta Materialia,* vol. 257, p. 116462, 2025.
[19] Q. Shao, E. M. Elgallad, A. Maltais, and X.-G. Chen, "Development of thermal-resistant Al-Zr based conductor alloys via microalloying with Sc and manipulating thermomechanical processing," *Journal of Materials Research and Technology,* 2023.
[20] S. Gashtiazar, E. Elgallad, B. Abnar, M. Javidani, A. Maltais, and X.-G. Chen, "Effect of solution heat treatment on the microstructure of hot-rolled Al-Mg-Si 6xxx alloy microalloyed with Sc and Zr," *Materials Letters,* p. 138784, 2025.
[21] T. Dorin, S. Babaniaris, L. Jiang, A. Cassel, A. Eggeman, and J. Robson, "Precipitation sequence in Al-Sc-Zr alloys revisited," *Materialia,* vol. 26, p. 101608, 2022.
[22] C. B. Fuller, D. N. Seidman, and D. C. Dunand, "Mechanical properties of Al (Sc, Zr) alloys at ambient and elevated temperatures," *Acta materialia,* vol. 51, no. 16, pp. 4803–4814, 2003.
[23] K. E. Knipling, D. N. Seidman, and D. C. Dunand, "Ambient-and high-temperature mechanical properties of isochronally aged Al–0.06 Sc, Al–0.06 Zr and Al–0.06 Sc–0.06 Zr (at.%) alloys," *Acta Materialia,* vol. 59, no. 3, pp. 943–954, 2011.
[24] K. E. Knipling, R. A. Karnesky, C. P. Lee, D. C. Dunand, and D. N. Seidman, "Precipitation evolution in Al–0.1 Sc, Al–0.1 Zr and Al–0.1 Sc–0.1 Zr (at.%) alloys during isochronal aging," *Acta Materialia,* vol. 58, no. 15, pp. 5184–5195, 2010.
[25] F. J. Humphreys and M. Hatherly, *Recrystallization and related annealing phenomena*. Elsevier, 2012.

[26] P. Koprowski *et al.*, "The effect of low content additives on strength, resistivity and microstructural changes in wire drawing of 1xxx series aluminium alloys for electrical purposes," *Materials Today Communications,* vol. 24, p. 101039, 2020.
[27] Y. Yang, J. Nie, Q. Mao, and Y. Zhao, "Improving the combination of electrical conductivity and tensile strength of Al 1070 by rotary swaging deformation," *Results in Physics,* vol. 13, p. 102236, 2019.
[28] S. Fan *et al.*, "Achieving superior strength and conductivity for Al-Zr-Sc wires by coupling design of deformation and ageing," *Materials Research Letters,* vol. 12, no. 8, pp. 590–598, 2024.
[29] S. Fan *et al.*, "Effects of processing paths on the microstructure, mechanical properties and electrical conductivity of dilute Al-Zr-Sc alloy conductive wires," *Journal of Materials Science & Technology,* vol. 188, pp. 202–215, 2024.
[30] C. Booth-Morrison, D. C. Dunand, and D. N. Seidman, "Coarsening resistance at 400 C of precipitation-strengthened Al–Zr–Sc–Er alloys," *Acta Materialia,* vol. 59, no. 18, pp. 7029–7042, 2011.
[31] B. Abnar, S. Gashtiazar, P. Rometsch, and M. Javidani, "Advanced thermal-resistant aluminum conductor alloys: A comprehensive review," *International Journal of Minerals, Metallurgy and Materials,* vol. 33, no. 1, pp. 68–93, 2026.
[32] A. Y. Algendy, K. Liu, P. Rometsch, N. Parson, and X.-G. Chen, "Effects of AlMn dispersoids and Al3 (Sc, Zr) precipitates on the microstructure and ambient/elevated-temperature mechanical properties of hot-rolled AA5083 alloys," *Materials Science and Engineering: A,* vol. 855, p. 143950, 2022.
[33] O. Senkov, M. Shagiev, S. Senkova, and D. Miracle, "Precipitation of Al3 (Sc, Zr) particles in an Al–Zn–Mg–Cu–Sc–Zr alloy during conventional solution heat treatment and its effect on tensile properties," *Acta materialia,* vol. 56, no. 15, pp. 3723–3738, 2008.
[34] Y. Huang and F. Humphreys, "Subgrain growth and low angle boundary mobility in aluminium crystals of orientation {110}< 001," *Acta materialia,* vol. 48, no. 8, pp. 2017–2030, 2000.
[35] M. Schöbel, P. Pongratz, and H. Degischer, "Coherency loss of Al3 (Sc, Zr) precipitates by deformation of an Al–Zn–Mg alloy," *Acta materialia,* vol. 60, no. 10, pp. 4247–4254, 2012.
[36] Y. Shen, R. Guan, Z. Zhao, and R. Misra, "Ultrafine-grained Al–0.2 Sc–0.1 Zr alloy: The mechanistic contribution of nano-sized precipitates on grain refinement during the novel process of accumulative continuous extrusion," *Acta Materialia,* vol. 100, pp. 247–255, 2015.
[37] S. Wu *et al.*, "Effect of Si addition on the precipitation and mechanical/electrical properties of dilute Al–Zr-Sc alloys," *Materials Science and Engineering: A,* vol. 812, p. 141150, 2021.
[38] Y. Qi *et al.*, "Achieving superior high-temperature mechanical properties in Al-Cu-Li-Sc-Zr alloy with nano-scale microstructure via laser additive manufacturing," *Materials Research Letters,* vol. 12, no. 1, pp. 17–25, 2024.
[39] L. Toropova, D. G. Eskin, M. Kharakterova, and T. Dobatkina, *Advanced aluminum alloys containing scandium: structure and properties*. Routledge, 2017.
[40] K. E. Knipling, D. C. Dunand, and D. N. Seidman, "Precipitation evolution in Al–Zr and Al–Zr–Ti alloys during isothermal aging at 375–425 C," *Acta Materialia,* vol. 56, no. 1, pp. 114–127, 2008.
[41] K. E. Knipling, D. C. Dunand, and D. N. Seidman, "Precipitation evolution in Al–Zr and Al–Zr–Ti alloys during aging at 450–600 C," *Acta Materialia,* vol. 56, no. 6, pp. 1182–1195, 2008.
[42] M. Zedalis and M. Fine, "Precipitation and ostwald ripening in dilute AI Base-Zr-V alloys," *Metallurgical Transactions A,* vol. 17, pp. 2187–2198, 1986.
[43] S. Hardy and P. Voorhees, "Ostwald ripening in a system with a high volume fraction of coarsening phase," *Metallurgical Transactions A,* vol. 19, pp. 2713–2721, 1988.

[44] C. Booth-Morrison, Z. Mao, M. Diaz, D. Dunand, C. Wolverton, and D. Seidman, "Role of silicon in accelerating the nucleation of Al3 (Sc, Zr) precipitates in dilute Al–Sc–Zr alloys," *Acta Materialia,* vol. 60, no. 12, pp. 4740–4752, 2012.
[45] S. Liang *et al.*, "The influence of Sc–Si clusters on aging hardening behavior of dilute Al-Sc-(Zr)-(Si) alloy," *Journal of Alloys and Compounds,* vol. 842, p. 155826, 2020.
[46] P. Shewmon, *Diffusion in solids*. Springer, 2016.
[47] C. B. Fuller, J. L. Murray, and D. N. Seidman, "Temporal evolution of the nanostructure of Al (Sc, Zr) alloys: Part I–Chemical compositions of Al3 (Sc1− xZrx) precipitates," *Acta materialia,* vol. 53, no. 20, pp. 5401–5413, 2005.
[48] N. Peterson and S. Rothman, "Impurity diffusion in aluminum," *Physical Review B,* vol. 1, no. 8, p. 3264, 1970.
[49] G. Ehrlich, "Atomic displacements in one-and two-dimensional diffusion," *The Journal of Chemical Physics,* vol. 44, no. 3, pp. 1050–1055, 1966.
[50] H. C. Berg, *Random walks in biology* (Diffusion: Microscopic Theory). Princeton University Press, 1993.
[51] Y. Deng, Z. Yin, Q. Pan, G. Xu, Y. Duan, and Y. Wang, "Nano-structure evolution of secondary Al3 (Sc1− xZrx) particles during superplastic deformation and their effects on deformation mechanism in Al-Zn-Mg alloys," *Journal of Alloys and Compounds,* vol. 695, pp. 142–153, 2017.
[52] S. Tian, J. Li, J. Zhang, Z. Wulabieke, and D. Lv, "Effect of Zr and Sc on microstructure and properties of 7136 aluminum alloy," *Journal of Materials Research and Technology,* vol. 8, no. 5, pp. 4130–4140, 2019.
[53] Y. Harada and D. Dunand, "Creep properties of Al3Sc and Al3 (Sc, X) intermetallics," *Acta materialia,* vol. 48, no. 13, pp. 3477–3487, 2000.
[54] K. E. Knipling, D. C. Dunand, and D. N. Seidman, "Criteria for developing castable, creep-resistant aluminum-based alloys–A review," *International Journal of Materials Research,* vol. 97, no. 3, pp. 246–265, 2022.
[55] C. B. Fuller and D. N. Seidman, "Temporal evolution of the nanostructure of Al (Sc, Zr) alloys: Part II-coarsening of Al3 (Sc1− xZrx) precipitates," *Acta Materialia,* vol. 53, no. 20, pp. 5415–5428, 2005.
[56] E. Marquis and D. N. Seidman, "Nanoscale structural evolution of Al3Sc precipitates in Al (Sc) alloys," *Acta materialia,* vol. 49, no. 11, pp. 1909–1919, 2001.
[57] R. Wagner, R. Kampmann, and P. W. Voorhees, "Homogeneous second-phase precipitation," *Phase transformations in materials,* pp. 309–407, 2001.
[58] L. Wang, B. Ye, Y. Bai, B. Zhao, and W. Ding, "Effect of Zr and Sc micro-additions on the microstructure and mechanical properties of as-cast Al-5Ce alloy," *Materials Science and Engineering: A,* vol. 822, p. 141654, 2021.
[59] Z. Li, Z. Zhang, and X.-G. Chen, "Improvement in the mechanical properties and creep resistance of Al-Mn-Mg 3004 alloy with Sc and Zr addition," *Materials Science and Engineering: A,* vol. 729, pp. 196–207, 2018.
[60] J. W. Martin, *Precipitation hardening: theory and applications*. Butterworth-Heinemann, 2012.
[61] D. N. Seidman, E. A. Marquis, and D. C. Dunand, "Precipitation strengthening at ambient and elevated temperatures of heat-treatable Al (Sc) alloys," *Acta Materialia,* vol. 50, no. 16, pp. 4021–4035, 2002.
[62] G. Li *et al.*, "Effect of Sc/Zr ratio on the microstructure and mechanical properties of new type of Al–Zn–Mg–Sc–Zr alloys," *Materials Science and Engineering: A,* vol. 617, pp. 219–227, 2014.
[63] W. Wang *et al.*, "Microstructure and properties of novel Al-Ce-Sc, Al-Ce-Y, Al-Ce-Zr and Al-Ce-Sc-Y alloy conductors processed by die casting, hot extrusion and cold drawing," *Journal of Materials Science & Technology,* vol. 58, pp. 155–170, 2020.

[64] Y. Yang, S. A. Hackney, and P. G. Sanders, "High-temperature deformation of supersaturated Al-Sc-Zr produced via melt-spinning and extrusion," *Materials Science and Engineering: A,* vol. 857, p. 144138, 2022.
[65] J. Bai, M. Gao, C. Wang, J. Pei, L. Yang, and R. Guan, "Role of Er element and two-stage heat treatment in a rheo-extruded Al–Sc–Zr alloy: Balance strength and electrical conductivity," *Materials & Design,* p. 115096, 2025.
[66] H. J. Frost and M. F. Ashby, "Deformation-mechanism maps: the plasticity and creep of metals and ceramics," *(No Title),* 1982.
[67] M. Meyers, "Mechanical metallurgy: principles and applications," *Prentice-Hall, Inc, Englewood Cliffs, N. J. 07632, U. S. A, 1984. 761,* 1984.
[68] S. N. Khangholi, M. Javidani, A. Maltais, and X. G. Chen, "Review on recent progress in Al–Mg–Si 6xxx conductor alloys," *Journal of Materials Research,* vol. 37, no. 3, pp. 670–691, 2022.
[69] S. N. Khangholi, M. Javidani, A. Maltais, and X.-G. Chen, "Optimization of mechanical properties and electrical conductivity in Al–Mg–Si 6201 alloys with different Mg/Si ratios," *Journal of Materials Research,* vol. 35, no. 20, pp. 2765–2776, 2020.
[70] J.-f. Leng, B.-h. Ren, Q.-b. Zhou, and J.-w. Zhao, "Effect of Sc and Zr on recrystallization behavior of 7075 aluminum alloy," *Transactions of Nonferrous Metals Society of China,* vol. 31, no. 9, pp. 2545–2557, 2021.
[71] D. Weygand, Y. Bréchet, and J. Lépinoux, "Zener pinning and grain growth: a two-dimensional vertex computer simulation," *Acta Materialia,* vol. 47, no. 3, pp. 961–970, 1999.
[72] A. Y. Algendy, P. Rometsch, and X.-G. Chen, "Impact of hot rolling temperature on the mechanical properties and microstructural evolution of hot/cold-rolled AA5083 with Sc and Zr microalloying," *Materials Science and Engineering: A,* vol. 896, p. 146275, 2024.
[73] E. Nes, N. Ryum, and O. Hunderi, "On the Zener drag," *Acta metallurgica,* vol. 33, no. 1, pp. 11–22, 1985.
[74] J. Zhang, H. Wang, D. Yi, B. Wang, and H. Wang, "Comparative study of Sc and Er addition on microstructure, mechanical properties, and electrical conductivity of Al-0.2 Zr-based alloy cables," *Materials Characterization,* vol. 145, pp. 126–134, 2018.

Chapitre 6. Rôle des précipités induits par le préchauffage dans l'optimisation des propriétés électriques et mécaniques des conducteurs déformés Al–0,1 % Sc

Cet article a été publié dans:
Materials Characterization, volume 240, août 2026, article 116904.

Résumé

Cette étude examine l'effet de la température de déformation à chaud sur l'évolution microstructurale et le comportement au vieillissement d'un alliage conducteur Al–0,1 % mass. Sc. À cette fin, des essais de compression uniaxiale à chaud ont été réalisés dans une plage de températures comprise entre 350 et 550 °C, suivis d'un vieillissement isotherme à 300 °C pendant 24 h. L'évolution microstructurale résultante a été caractérisée par diffraction des électrons rétrodiffusés (EBSD) et microscopie électronique en transmission (MET), tandis que des mesures de dureté et de conductivité électrique ont été effectuées afin d'évaluer la réponse au vieillissement. Le comportement contrainte–déformation indique que l'ajout de Sc augmente la contrainte d'écoulement d'environ 10 MPa à des températures de déformation inférieures à 500 °C. Cependant, à 550 °C, les contraintes d'écoulement maximales des deux alliages convergent vers des valeurs presque identiques, ce qui est cohérent avec une dissolution quasi complète du Sc au-dessus de sa température de solvus. Après vieillissement à 300 °C, l'alliage Al–Sc déformé à 350 °C et à 550 °C présente un compromis favorable entre la conductivité électrique et la dureté, atteignant respectivement environ 59 % IACS et 71 HV. En revanche, la déformation à 450 °C conduit à une conductivité électrique comparable (~59 % IACS), mais à la plus faible dureté (51 HV). L'analyse par MET révèle que la dureté significativement plus faible obtenue après déformation à 450 °C est principalement attribuée à la formation, lors du préchauffage, de précipités grossiers d'Al_3Sc présentant une morphologie en chaîne et une distribution hétérogène dans la microstructure. En revanche, la formation des précipités est limitée cinétiquement à 350 °C en raison de la courte durée de préchauffage, tandis qu'elle est thermodynamiquement absente à 550 °C, au-dessus de la température de solvus du Sc. Le Sc demeure ainsi en solution solide sursaturée, ce qui favorise, lors du vieillissement ultérieur, la précipitation uniforme de précipités nanométriques $L1_2$-Al_3Sc.

Mots-clés: alliage conducteur Al-Sc, essai de compression à chaud, conductivité électrique, dureté

The role of preheating–induced precipitates in tailoring the electrical and mechanical properties of deformed Al–0.1 wt.% Sc conductors

Behrouz Abnar [a], Paul Rometsch[b], Mousa Javidani [a]

[a] University Research Centre on Aluminium (CURAL) and Aluminium Research Centre–REGAL, Department of Applied Science, University of Québec at Chicoutimi, Saguenay, QC, G7H 2B1, Canada
[b] Arvida Research and Development Center, Rio Tinto Aluminum, Saguenay, QC, G7S 4K8, Canada

This article has been published in:
Materials Characterization, Volume 240, August 2026, 116904

Abstract

This study investigates the effect of hot deformation temperature on the microstructural evolution and aging behavior of an Al–0.1 wt.% Sc conductor alloy. For this purpose, uniaxial hot compression tests were conducted over a temperature range of 350–550 °C, followed by isothermal aging at 300 °C for 24 h. The resulting microstructural evolution was characterized by using electron backscatter diffraction (EBSD) and transmission electron microscopy (TEM), while hardness and electrical conductivity measurements were used to evaluate the aging response. The stress–strain behavior indicates that Sc addition increases the flow stress by ~10 MPa at deformation temperatures below 500 °C. However, at 550 °C, the peak flow stresses of both alloys converge to nearly identical values, consistent with near-complete Sc dissolution above the solvus temperature. The Al-Sc alloy aged at 300 °C shows that hot deformation at 350 °C and 550 °C provides a favorable balance between electrical conductivity and hardness, achieving ~59 % IACS and ~71 HV, respectively. In contrast, deformation at 450 °C results in a comparable EC (~59 % IACS) but yields the lowest hardness (51 HV). TEM analysis reveals that the significantly lower hardness at 450 °C is mainly attributed to the formation of coarse, chain-like Al_3Sc precipitates during preheating, which are heterogeneously distributed within the microstructure. In contrast, precipitate formation is kinetically limited at 350 °C by the short preheating duration and thermodynamically absent at 550 °C above the Sc solvus, retaining Sc in supersaturated solution and promoting uniform nanoscale $L1_2$-Al_3Sc precipitation during subsequent aging.

Keywords: Al-Sc conductor alloy, Hot compression test, Electrical Conductivity, Hardness

6.1. Introduction

Aluminum-based alloys have been widely used in modern power transmission systems, including electrical cables and bus bars, due to their favorable conductivity-to-weight ratio and lower cost compared with copper conductors. However, the growing demand for high-efficiency and thermally stable conductors in next-generation electrical systems has driven conventional Al conductors toward their performance limits, highlighting the need for advanced conductor materials [1-4].

Scandium in Al alloys forms nanoscale Al_3Sc precipitates during heat treatment, which significantly strengthen the alloy and enhance thermal stability [5]. Al_3Sc has an $L1_2$-ordered FCC crystal structure with a lattice parameter of 4.103 Å, which is very close to that of α-Al (FCC, 4.059 Å), resulting in a lattice mismatch of only about 1.25% [6, 7]. This minimal lattice mismatch enables the Al/Al_3Sc interface to remain fully coherent [8]. The fine $L1_2$-ordered Al_3Sc precipitates function as potent pinning centers for dislocations and subgrain boundaries, leading to a marked increase in strength and effectively inhibiting subgrain boundary migration [6, 9].

For 1xxx series Al conductors, alloying with 0.05–0.3 wt.% Sc, has emerged as one of the most effective strategies for enhancing the mechanical strength and thermal stability without compromising the electrical conductivity (EC) [10, 11]. Because Sc exhibits an extremely low solid solubility in Al at room temperature (<0.0001 wt.%), most of the supersaturated Sc precipitates as Al_3Sc particles during controlled heat treatment rather than remaining in solid solution [6, 12]. Regarding the detrimental effect of a solid solution on EC, precipitation reduces electron scattering in the Al lattice, thereby improving EC by lowering electrical resistivity [13, 14].

In the production of Al conductors for electrical bus bars, a hot deformation step such as extrusion followed by direct post-deformation aging (T5 temper) is widely favored in the conductor industry due to its efficiency and high productivity [15]. Considering that the retention of supersaturated Sc in solid solution in as-deformed Al-Sc conductor alloys is critical for subsequent aging effectiveness, careful control of Sc decomposition during deformation preheating is required. This can be achieved through optimization of deformation parameters, particularly temperature [16]. Zakharov et al. [17-19] reported that

at higher temperatures, even brief thermal exposures, such as 2 minutes at 400 °C or 50 seconds at 450 °C, cause a significant reduction in hardness after the peak, indicating an accelerated overaging process [20, 21].

Despite significant advances in Al–Sc alloys, a critical research gap remains in understanding how hot deformation temperature, particularly the short preheating stage before deformation, influences the competition between precipitates formed during preheating and those developed during direct aging (T5 temper treatment), and how this interaction ultimately governs the final mechanical and electrical properties. A comprehensive investigation of this aspect could also provide valuable guidance for optimizing the deformation temperature in Al-Sc-Zr conductor alloys. Owing to the significantly higher diffusivity of Sc compared to Zr, Sc predominantly dictates the nucleation and early growth of precipitates during thermomechanical processing [22, 23].

To address this gap, the present study systematically investigates the effect of preheating temperature (350–550 °C) during hot deformation on Sc solute retention in Al–Sc conductor alloys, the formation and evolution of Sc-containing precipitates during preheating and subsequent aging, and their combined effects on hardness, electrical conductivity, and deformation behavior. These microstructural changes are further correlated with the resulting alloy performance by integrating thermodynamic and kinetic perspectives to elucidate the temperature-dependent evolution of Al_3Sc precipitation during preheating and aging. Uniaxial hot compression tests followed by isothermal aging at 300 °C for 24 h were performed to clarify how deformation temperature influences Sc solute retention, nanoscale precipitate development, and their combined influence on EC and hardness. EBSD and TEM analyses, together with hardness–conductivity correlations, are employed to elucidate the underlying thermomechanical–microstructural interactions

6.2. Experimental procedure

Table 4-1 shows the chemical compositions of the studied alloys. The alloy designation is based on the principal alloying elements, with Al denoting the Al-base and Al-Sc representing Al containing 0.1 wt.% Sc. The alloys were direct-chill (DC) cast into billets with a 4-inch diameter and cut to a length of 200 mm.

Table 6-1. Chemical compositions of studied alloys (wt.%).

Alloy	Sc	Zr	Si	Fe	Ti	Al
Al-base	Trace	Trace	0.10	0.20	0.012	Bal
Al-Sc	0.11	Trace	0.10	0.21	0.02	Bal

Figure 6-1 (a) displays the diagram of the experimental process in the present research. The as-cast alloys were homogenized at 600°C for 8 hours (step I) and machined into cylindrical samples with a diameter of 10 mm and a length of 15 mm. Compression tests were performed on cylindrical specimens using a Gleeble™ 3800 thermomechanical simulator at temperatures ranging from 350 to 550 °C (denoted as D350 to D550). The tests were conducted at a strain rate of 1 s^{-1} and continued until reaching a true strain of 0.8. The selected strain rate of 1 s^{-1} was chosen because it is close to the average strain rate commonly used in industrial hot deformation processes.

Figure 6-1 (b) presents schematic illustration of the hot compression test setup. The homogenized specimens (step I) were heated at a rate of 2 ℃/s and held for 3 min at the target temperature (step II) to establish a uniform temperature distribution before compression. After deformation (step III), the samples were rapidly cooled by water quenching to preserve the microstructure. Graphite foils were placed between the cylindrical samples and the anvils to minimize friction during deformation. For each deformation condition, tests were repeated on three samples. The compressed samples were directly subjected to post-deformation aging (step IV) at 300 °C for 24 h, as illustrated in Figure 1(a). In a side study, we found that the peak-aged condition for this alloy occurs at around 12 h. However, extending the aging time to 24 h results in only a negligible decrease in hardness (<3%) while increasing the EC by about 1% IACS. Therefore, 24 h aging was selected in the experimental design to achieve a better balance between EC and hardness.

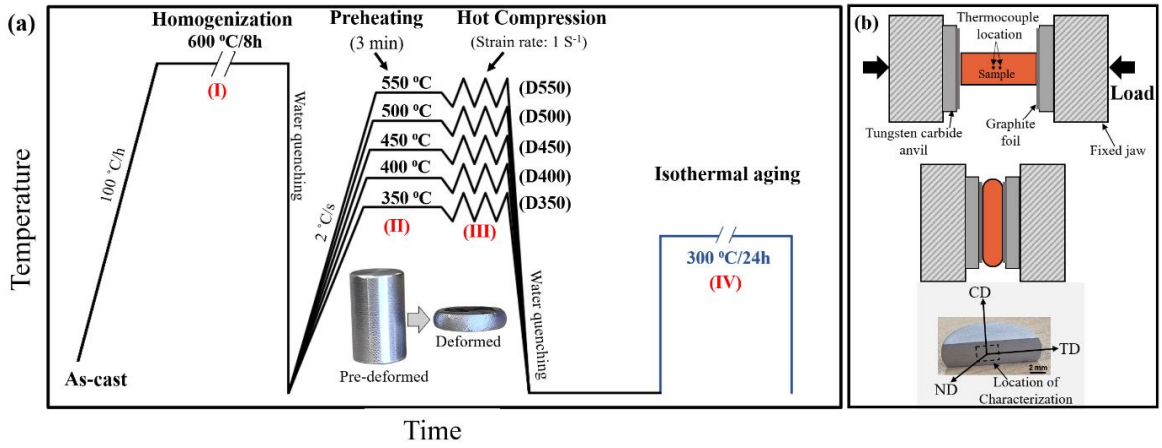

Figure 6-1. (a) Experimental procedure applied to the studied alloys, (b) schematic illustration of the hot compression test setup and characterization planes, showing the compression direction (CD), normal direction (ND), and transverse direction (TD).

For the characterization of hot-deformed samples, including microstructural analysis, electrical property evaluation, and hardness measurements, all samples were sectioned parallel to the compression axis, with analyses performed on the central region of each sample, as shown in Figure 6-1 (b). Vickers microhardness measurements were performed using a 25 g load and a dwell time of 20 s, with the reported values averaged from ten indentations. The EC of the samples was measured using the Sigmascope method at a frequency of 480 kHz and a temperature of 21 °C, in accordance with ASTM E1004.

Furthermore, electron backscatter diffraction (EBSD) analysis was conducted using scanning electron microscopy (SEM, JEOL™ 6480LV) on a plane perpendicular to the normal direction (CD-TD plane), as shown in Figure 6-1 (b), to evaluate the grain and subgrain structures with the step sizes of 1 μm. During analysis, the samples were tilted 70° from the horizontal plane. Orientation maps with over 90% reliable indexed data were acquired using HKL technology, and Channel 5 Tango software applied standard noise reduction by replacing poorly indexed or unindexed points with neighboring valid data. Boundaries and sub-boundaries were categorized based on their misorientation angles as low-angle grain boundaries (LAGBs: 2–5°), medium-angle grain boundaries (MAGBs: 5–15°), and high-angle grain boundaries (HAGBs: >15°), represented by white, blue, and black lines, respectively, in the EBSD Euler maps [24, 25]. Additionally, grain orientation spread (GOS) maps obtained from EBSD were used to assess deformation level, stored energy, and enable distinction between recrystallized, substructured, and deformed grains. GOS maps represents

the average intragranular misorientation: low values (≤2°, blue) indicate recrystallized grains; intermediate values (2–5°, yellow) correspond to partially recovered grains; and high values (≥5°, red) reflect heavily deformed grains with high dislocation density.

A transmission electron microscope (TEM, JEM 2100) operating at 200 kV was used to investigate the Sc- and Zr-containing precipitate evolution. Elemental analysis by TEM-EDS was also employed to determine the chemical compositions of the precipitates formed during hot extrusion and aging. TEM samples were prepared using a twin-jet electropolishing system at 15 V and a temperature of -20 to -25 °C, with a solution of 30% nitric acid and 70% methanol. TEM images were captured near the [001] zone axis of the α-Al matrix to examine the precipitates. The statistical analysis of precipitates was conducted using at least eight TEM images per sample and processed with ImageJ image analysis software. The number density of precipitates (N_d) and volume fraction (F_V) of precipitates were calculated by the following equations, respectively [26, 27]:

$$N_d = \frac{N}{A\left(D_{avg} + t\right)} \qquad (1)$$

$$f_V = N_d V_P \qquad (2)$$

Where N is the number of precipitates, D_{avg} represents the average diameter of the precipitates, t thickness of the foil, A is the area of the matrix containing the precipitates, and V_P is the average volume of the precipitates. The foil thickness (t) was measured using the convergent beam electron diffraction (CBED) technique. The number of counted precipitates varied depending on the condition. For the high precipitate density conditions (D350 and D550), approximately 420–560 precipitates were counted per image, corresponding to an analyzed area of 550 × 760 nm^2 and foil thicknesses ranging from 95 to 106 nm. In contrast, for the D450 condition, only 105–120 precipitates were counted per image within the same analyzed area, with foil thicknesses ranging from 101 to 115 nm.

Furthermore, Thermo-Calc™ with TCAL7 database was employed to predict phase stability and transformation temperatures in the Al–0.1 wt.% Sc alloy.

6.3. Results

6.3.1. Hot deformation behavior

6.3.1.1. Flow stress

Figure 6-2 shows true stress-strain curves of the studied alloys, along with the variation of their peak flow stress as a function of temperature. The flow stress behavior is influenced by the deformation temperature for each alloy. The process showed a sharp rise in flow stress during the initial stages of deformation due to the predominant work hardening, induced by the multiplication of dislocations and a substantial increase in the dislocation number density [28, 29]. After this initial sharp increase in stress, the true stress–true strain curves exhibited two distinct trends depending on the deformation temperature: (1) A steady-state flow stress plateau was observed, predominantly for D450, D500, and D550 in the Al-base and D500 and D550 in the Al-Sc alloy, characterized by a nearly constant stress level that persisted throughout deformation. This plateau indicates a dynamic equilibrium between work hardening and softening mechanisms [30]. (2) A gradual but continuous increase in flow stress with strain, typically at deformation temperatures of 400–450 °C for the Al-base and 350–400 °C for the Al-Sc alloy. As the temperature further decreased to 350 °C, the rate of stress increase became more pronounced, as shown in Figure 6-2 (a)–(b). This trend suggests that work hardening dominates over softening mechanisms under these lower-temperature conditions [31].

Figure 6-2 (c) illustrates the variation of peak flow stress as a function of deformation temperature for both the Al-base and Al-Sc alloys, with differences summarized in the inset table. For both alloys, the peak flow stress decreases progressively with increasing deformation temperature, as softening mechanisms become increasingly active [32]. From 350 to 450 °C, the Al-Sc alloy exhibits a peak flow stress ~10 MPa higher than that of the Al-base. This difference gradually diminishes with increasing deformation temperature, and at 550 °C, the peak flow stresses of both alloys converge to nearly identical values. The correlation between microstructural features and flow stress is discussed in Section 4.2.

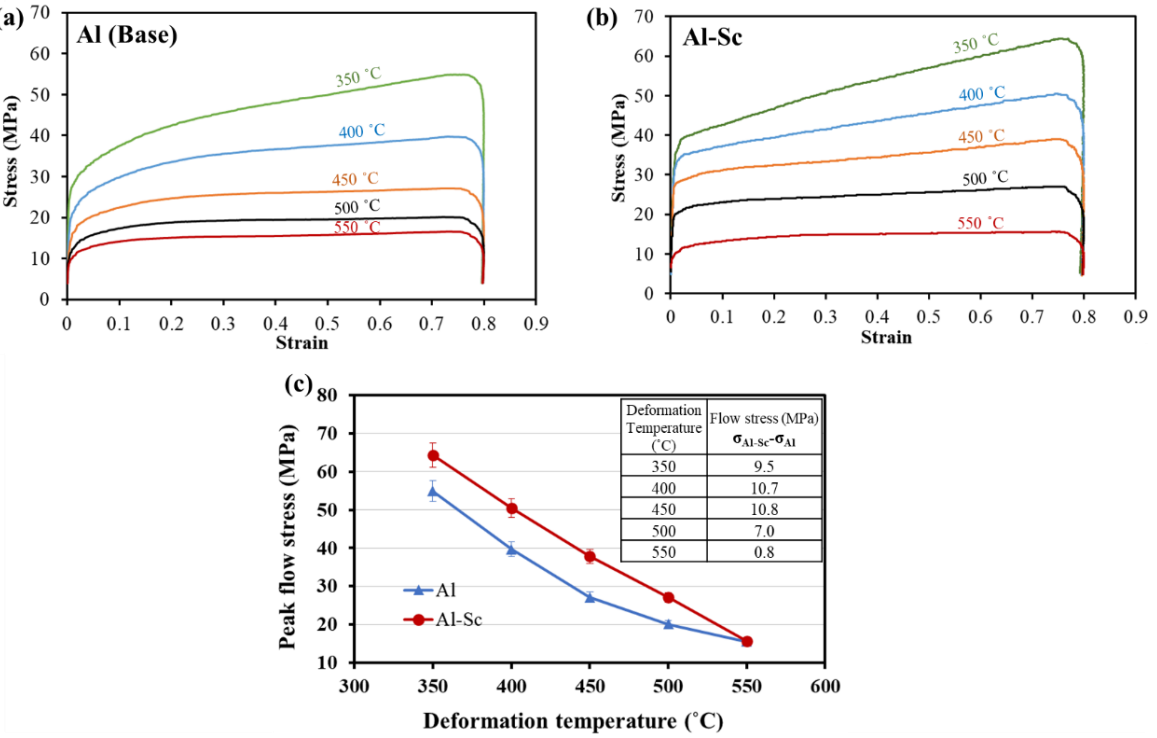

Figure 6-2. True stress–strain curves of the studied alloys at deformation temperatures from 350 to 550 °C under a constant strain rate of 1 s^{-1}: (a) Al (Al-base), (b) Al-Sc. (c) Temperature dependence of peak flow stress, including the difference between Al-base and Al-Sc (inset table).

6.3.1.2. Effect of deformation temperature on the grain and subgrain microstructure of Al-Sc alloy

Figure 6-3 shows the EBSD results, including Euler and GOS maps for the Al-base and Al-Sc alloys deformed at 350, 450, and 550 °C, with the corresponding quantitative EBSD data summarized in Table 6-2. For both alloys, increasing the deformation temperature facilitates dislocation rearrangement and annihilation, resulting in an increase in the average misorientation angle [33]. The increase in the fraction of HAGBs with temperature further supports this trend, as shown in Table 6-2. In addition, Sc addition reduces the average misorientation angle at a given temperature compared with the Al-base alloy. Consequently, the Al-Sc alloy exhibits a lower HAGB fraction and a higher proportion of LAGBs. This effect is most pronounced at 350 °C, where adding 0.1 wt.% Sc reduces the HAGB fraction from 13% to 3%. Overall, Sc suppresses misorientation development, maintaining lower misorientation levels and limiting HAGB formation, which in turn reduces recrystallization by restricting dislocation rearrangement and boundary migration [31].

As shown in Figure 6-3 (d) and (j), at D350 both the Al-base and Al-Sc alloys are predominantly in a deformed state and fall within the processing instability region. As further quantified in Figure 6-4, the microstructure at D350 is dominated by a deformed structure, accounting for approximately ~77% and ~94% in the Al-base and Al-Sc alloys, respectively. In the Al-base alloy, the presence of ~5% recrystallized grains and ~18% substructured regions at D350 indicates the onset of softening mechanisms, in contrast to the Al-Sc alloy, which remains largely in a deformed state under the same conditions. At D450, enhanced dislocation mobility facilitates their rearrangement and the formation of polygonized subgrains, leading to an increased fraction of substructured grains in both alloys, indicative of pronounced dynamic recovery. However, the fraction of recrystallized grains reaches ~16% in the Al-base alloy, compared to only ~2% in the Al-Sc alloy, highlighting the strong retardation of recrystallization in the presence of Sc. At D550, although dynamic recovery remains the dominant mechanism for both alloys, subgrain boundaries progressively migrate and transform into new strain-free recrystallized grains. This leads to recrystallized fractions of approximately ~25% and ~12% in the Al-base and Al-Sc alloys, respectively. According to Figure 6-4, at all deformation temperatures, the Al-Sc alloy exhibits lower recrystallization compared to the Al-base. This effect is most pronounced at 450 °C, where the addition of Sc results in nearly a 90% reduction in recrystallization. As presented in Table 6-2, Sc suppresses misorientation evolution, maintaining a low average misorientation angle. This reduces the formation of HAGBs and minimizes recrystallization, effectively inhibiting softening by restricting dislocation rearrangement and boundary migration [31].

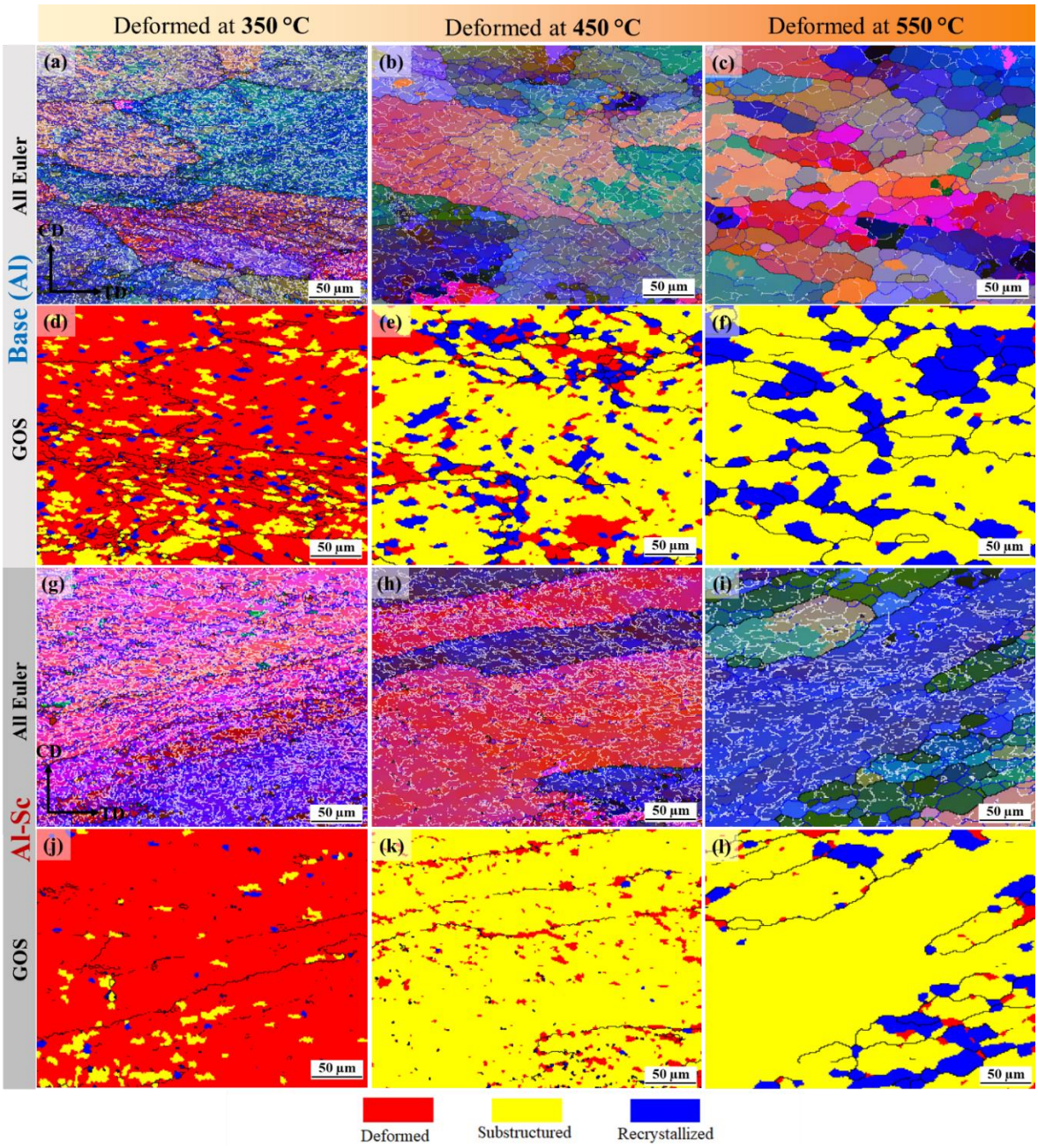

Figure 6-3. EBSD Euler maps (a–c, g–i) and GOS maps (d–f, j–l) of Al-base and Al-Sc alloys deformed at 350, 450, and 550 °C, respectively. LAGBs (2–5°), MAGBs (5–15°), and HAGBs (>15°) are represented by white, blue, and black lines, respectively.

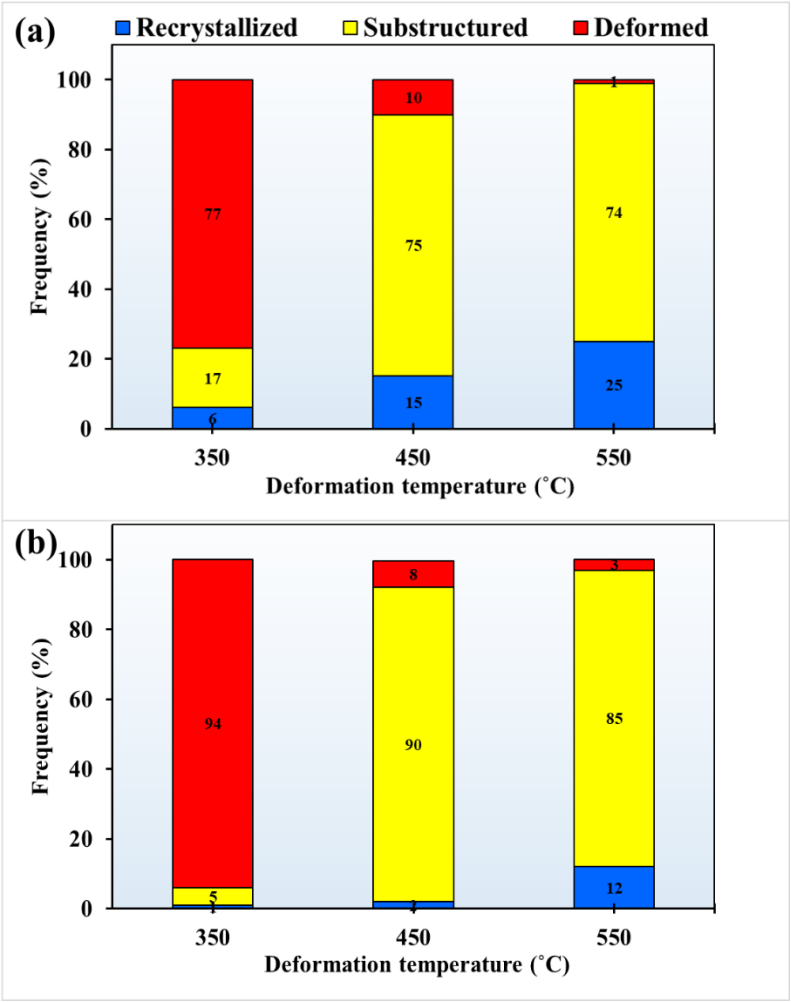

Figure 6-4. Fractional distribution of microstructural features obtained from EBSD GOS maps for (a) Al-base, and (b) Al-Sc alloys.

Table 6-2. Microstructural quantification of deformed Al-Base and Al-Sc alloys.

Alloy	Deformation Temperature (˚C)	LAGB (%)	MAGB (%)	HAGB (%)	Average misorientation angle (˚)
Al-base	350	41	46	13	8.7
	450	45	41	14	9.2
	550	33	36	31	17
Al-Sc	350	61	36	3	5.8
	450	68	24	8	6.6
	550	60	25	15	8.3

6.3.2. Hardness and electrical conductivity

Figure 6-5 presents the variation in EC and hardness for both as-deformed and aged samples. For Al-Sc alloy, before aging (red dashed curve), the EC values at D350 and D550 are

comparable (53.8 % and 53.4 % IACS, respectively), whereas the sample of D450 exhibits a higher EC of approximately 56.6 % IACS. This behavior is likely associated with the formation of Sc-containing phases during deformation at D450, which are discussed in detail in Section 4.3. After isothermal aging at 300 °C for 24 h, EC (red solid curve) increased under all deformation conditions. The Al-Sc alloy exhibited increases of 3.9% and 4.1% IACS at D350 and D550, respectively, while D450 showed the lowest rise (2.4% IACS). Nevertheless, all conditions converged to ~58.8 ± 0.4% IACS, closely matching the Al-base alloy (59.3 ± 0.2%), as presented in Figure 6-5.

Regarding hardness, the as-deformed Al-Sc samples exhibit a gradual decrease in hardness with increasing deformation temperature, which is attributed to enhanced activation of softening mechanisms, including dynamic recovery and recrystallization, as illustrated in Figure 6-3 and Figure 6-4. After aging the Al–Sc alloy at 300 °C for 24 h, hardness increases noticeably for D350 and D550, reaching 70.1 HV and 70.8 HV, respectively. Although the final hardness is similar, D550 shows a much larger relative increase (88%) from its as-deformed state compared to D350 (46%). In contrast, D450 exhibits the smallest hardness increase (17%) after isothermal aging at 300 °C for 24 h, achieving only ~50.6 HV. As shown in Figure 6-5 (b) (blue curves), the Al-base exhibits lower hardness under all conditions compared with both the as-deformed and aged Al-Sc samples. In Al-base alloy, aging mainly promotes dynamic recovery, leading to a slight reduction in hardness as a result of thermal softening [34].

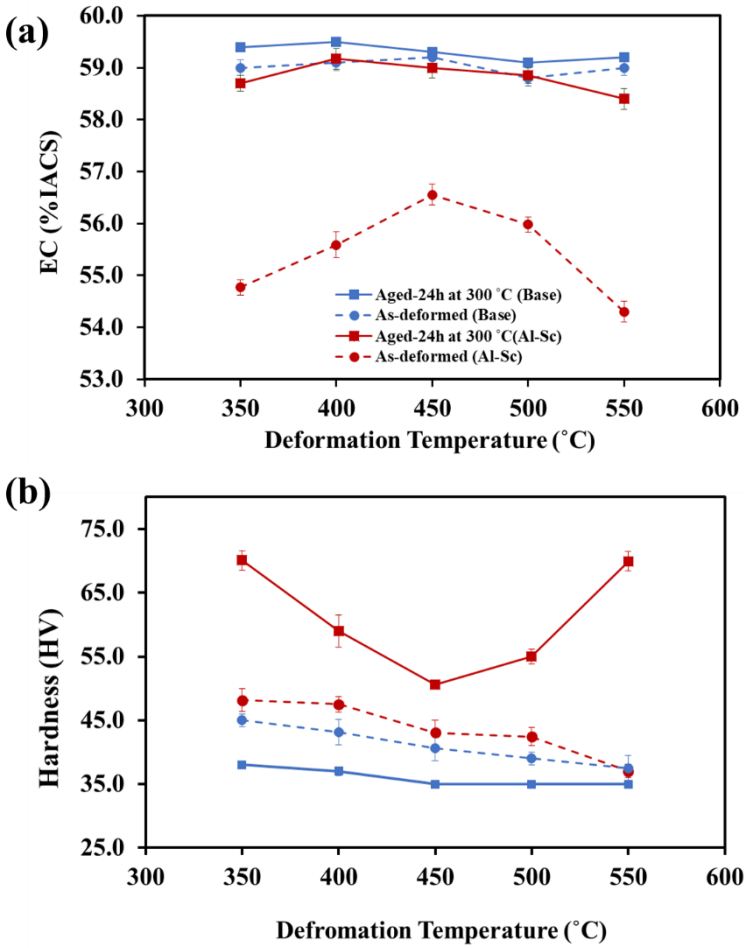

Figure 6-5. Variation of EC and hardness with deformation temperature for Al-Sc and Al-base.

6.3.3. Precipitate evolution in Al-Sc alloy

6.3.3.1. Preheating-induced precipitates (PIPs)

PIPs refer to Sc-containing spherical phases formed during the 3-minute preheating step of the Al-Sc alloy, prior to deformation and subsequent isothermal aging. As shown in Figure 6-6 (a) and (c), preheating at 350 °C and 550 °C yields a small number of precipitates with densities of 2.54×10^{20} m^{-3} and 1.87×10^{20} m^{-3}, respectively. In contrast, preheating at 450 °C exhibits a higher number density of precipitates (6.2×10^{20} m^{-3}), with a heterogeneous, chain-like distribution throughout the microstructure. For the deformed Al-Sc alloy, as indicated in Figure 6-6 (d)-(f), a similar trend in number density of precipitates from D350 to D550 is observed. The applied strain during deformation further increases the average precipitate size (Figure 6-6 (g)). For D450, the average diameter rises from 13±5 nm after 3 min preheating to 19±5 nm after deformation. This moderate coarsening is accompanied by a reduction in

number density of precipitates compared with the preheated condition, reaching 3.8×10^{20} m^{-3} after deformation. A similar trend in both the average diameter and number density of precipitates is observed for D350, although the changes are less pronounced. The high dislocation density generated by deformation creates effective pipe-diffusion paths, allowing solute atoms to migrate more rapidly along these channels and thereby accelerating the growth of precipitates initially formed during the preheating stage [35].

The selected area electron diffraction (SAED) pattern obtained from the D450 condition (Figure 6-6 (h)) reveals two distinct sets of periodic diffraction spots. The first set, highlighted in white, corresponds to the α-Al matrix with a face-centered cubic (FCC) structure and is indexed along the [001] zone axis. The second set of spots, marked in yellow, is indexed to the FCC $L1_2$-structured Al_3Sc phase, also along the [001] zone axis [36, 37].

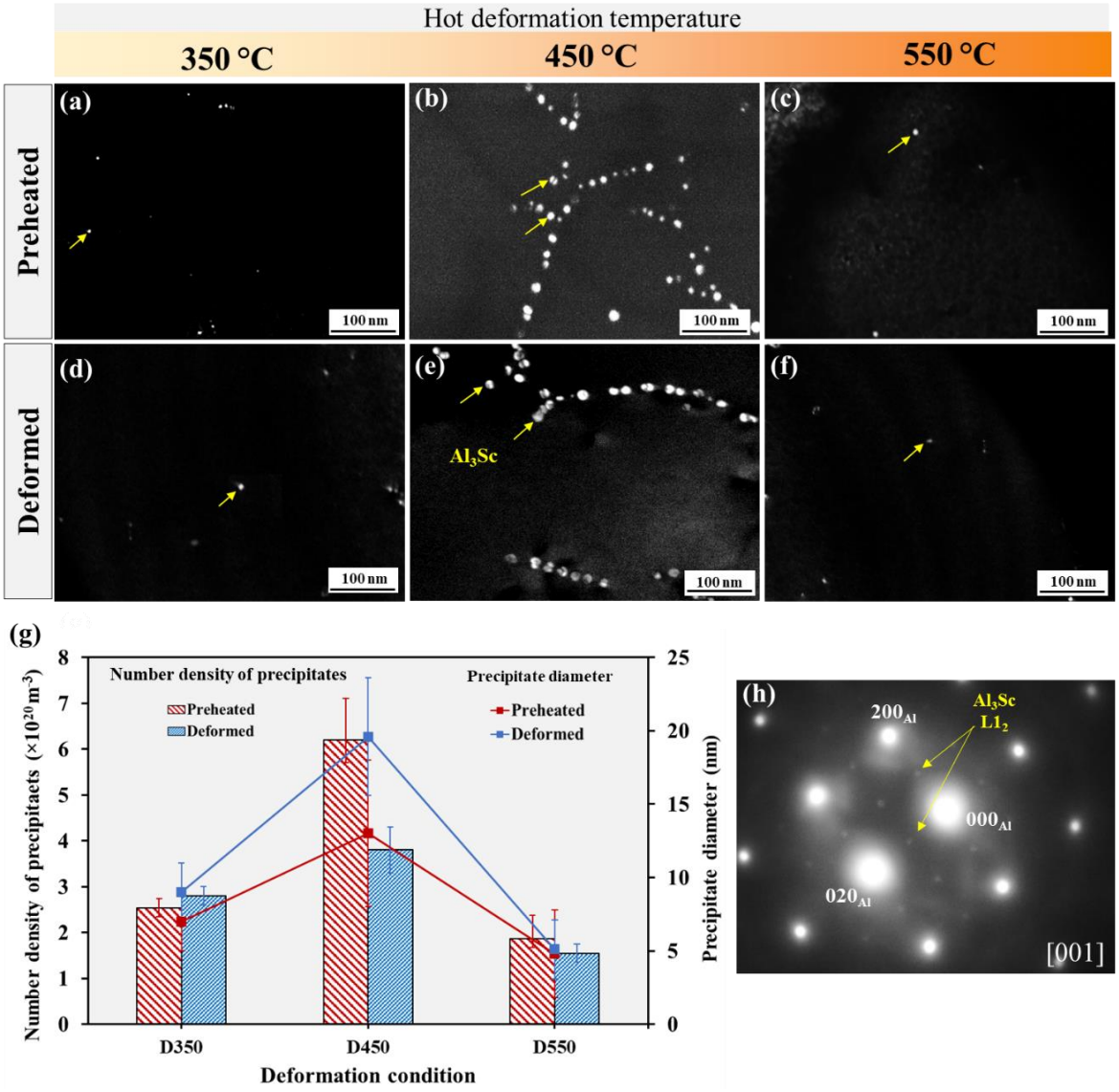

Figure 6-6. Dark-field TEM images of PIPs in (a–c) preheated and (d–f) deformed Al-Sc alloy after hot deformation at 350, 450, and 550 °C. (g) Number density and average diameter of precipitates as a function of deformation process temperature for step II (preheated) and step III (deformed), as defined in Figure 6-1. (h) SAED pattern confirming $L1_2$ Al_3Sc phase relevant to D450.

As shown in Figure 6-6 (b), during preheating at 450 °C, PIPs form as discontinuous chain-like distribution at preferential sites where the activation energy for nucleation is lower [38]. EBSD analysis of the homogenized and water-quenched Al–Sc alloy (indexing rate >97%; Figure 6-7 (a)) reveals a microstructure dominated by low-angle subgrain boundaries within coarse equiaxed grains. For improved accuracy, higher-magnification EBSD mapping Figure 6-7 (b)), performed with a reduced step size of 0.3 μm and an indexing rate exceeding 98%, further confirms the presence of LAGBs in the homogenized and quenched Al-Sc alloy. In

addition to misorientation angles of 2°–5° (white lines), boundaries with misorientation angles of 1.5°–2° are also identified. Moreover, the quality map in Figure 6-7 (c) further verifies the existence of these subgrains within the original grains after homogenization and water-quenching. Rapid cooling following homogenization at 600 °C induces localized variations in thermal contraction across the alloy, generating internal stresses that promote dislocation formation [39]. During subsequent preheating at 450 °C, these stored stresses are progressively relaxed through dislocation motion, leading to dislocation rearrangement and the formation of dislocation walls and low-angle subgrain boundaries. Consequently, the increased diffusivity of Sc atoms in the α-Al matrix at 450 °C facilitates heterogeneous nucleation and growth of precipitates along these LAGBs during preheating. A similar behavior was reported by Jones et al. [21] in Al–Sc alloys, where Al_3Sc precipitates preferentially nucleated along LAGBs (>1.5°) as well as high-angle grain boundaries (>15°).

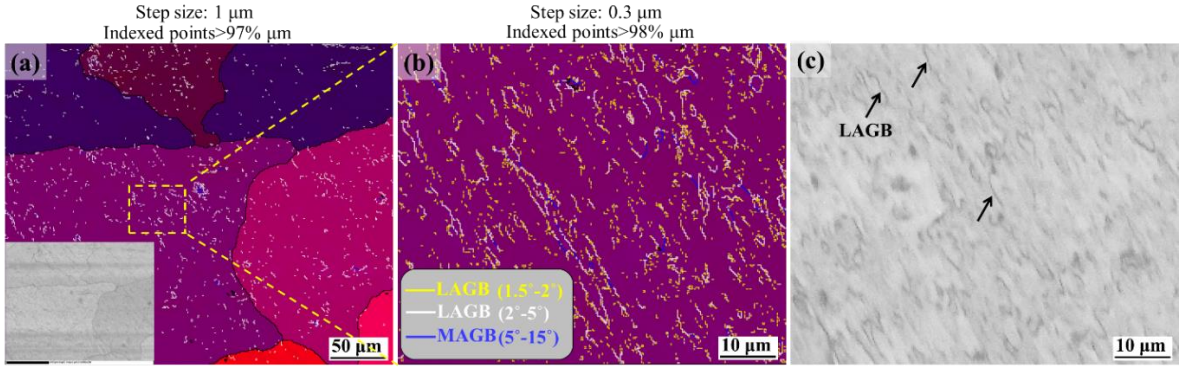

Figure 6-7. EBSD results of the Al–Sc alloy after homogenization and water quenching: (a) Euler angle orientation and grain boundary quality (inset) map with a step size of 1 μm; (b) magnified Euler angle orientation map acquired with a step size of 0.3 μm; (c) quality map corresponding to (b).

Figure 6-8 (a) shows a bright-field TEM image revealing Al_3Sc precipitates, formed during preheating at 450 ˚C, aligned along linear features. However, from this image alone, it is not possible to determine whether these preferential nucleation sites correspond to individual dislocations or subgrain boundaries. To clarify their origin, an additional sample was extracted after the 3 min preheating stage at 450 ˚C (step II in Figure 6-1), prior to deformation, and subsequently aged at 300 °C for 24 h. The dark-field TEM image in Figure 6-8 (b) shows a distinct precipitate-free zone (PFZ) adjacent to the coarse chain-like Al_3Sc precipitates formed during preheating. Since the TEM foil thickness (115 ± 15 nm) lies entirely within this PFZ, the absence of precipitates indicates complete local Sc depletion.

Such an extended depletion region is consistent with nucleation along defect walls, most likely subgrain boundaries, rather than along isolated individual dislocations.

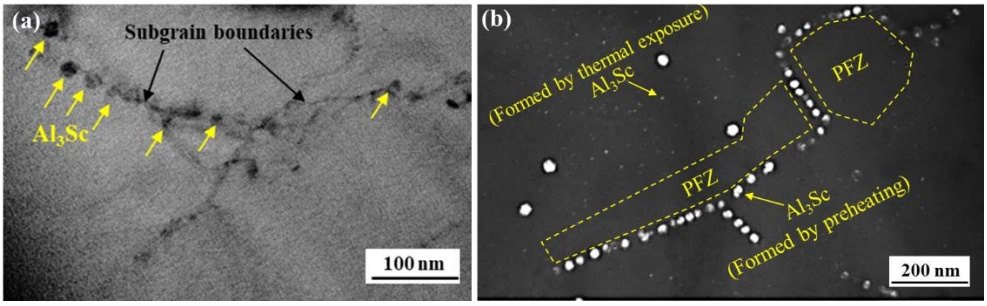

Figure 6-8. (a) Bright-field TEM image showing Al_3Sc precipitates along subgrain boundaries formed during preheating at 450 ˚C before deformation (Step II in Figure 6-1). (b) Dark-field TEM image of the sample preheated at 450 °C and subsequently thermally exposed at 300 °C for 24 h (Step II+300 °C/24 h).

6.3.3.2. Aging-induced precipitates (AIPs)

AIPs refer to Al_3Sc phases formed during isothermal aging at 300 °C for 24 h. As shown in Figure 6-9 (a) and (c), dark-field TEM images of the Al-Sc alloy under D350 and D550 conditions reveal a uniform distribution of nanoscale Al_3Sc precipitates within the Al matrix after aging. The insets display the corresponding SAED patterns, confirming the $L1_2$ crystal structure of the Al_3Sc precipitates. By comparing the number density of precipitates measured under these conditions (Figure 6-9 (d) and (f)) with those obtained prior to aging (Figure 6-6 (h)), it was determined that approximately 97.0% and 98.5% of the precipitates in the aged D350 and D550 samples, respectively, formed during aging heat treatment and can be therefore classified as AIPs. PIPs cannot be clearly distinguished in the TEM images of aged D350 and D550 samples because their sizes (8.9 ± 3 nm and 5.1 ± 2 nm, respectively) are comparable to those of certain AIPs.

At the D450 condition (Figure 6-9 (b)), the precipitates can be clearly classified into two distinct populations. The first population consists of coarse Al_3Sc precipitates with an average diameter of 19.8 ± 5 nm, while the second comprises finer precipitates with an average diameter of 6.1±4 nm. The coarse Al_3Sc precipitates can be readily attributed to PIPs, as they are distinguishable by their relatively large size, which is comparable to that observed under the D450 condition in Figure 6-6. In contrast, the finer precipitates correspond to AIPs. As shown in Figure 6-9 (b), a distinct precipitate-free zone (PFZ) is observed in the vicinity of the PIPs, indicating that most of the solute atoms in this region were consumed during the

formation of PIPs in steps II (defined in Figure 6-1). Consequently, significant local solute depletion occurred, suppressing further precipitate nucleation within this zone during isothermal aging (step IV). The number density of precipitates in the aged D550 condition was the highest (12.9×10^{21} m^{-3}), while the aged D350 condition exhibited a ~28% lower value (9.3×10^{21} m^{-3}). The D450 condition showed the lowest number density of precipitates (2.2×10^{21} m^{-3}).

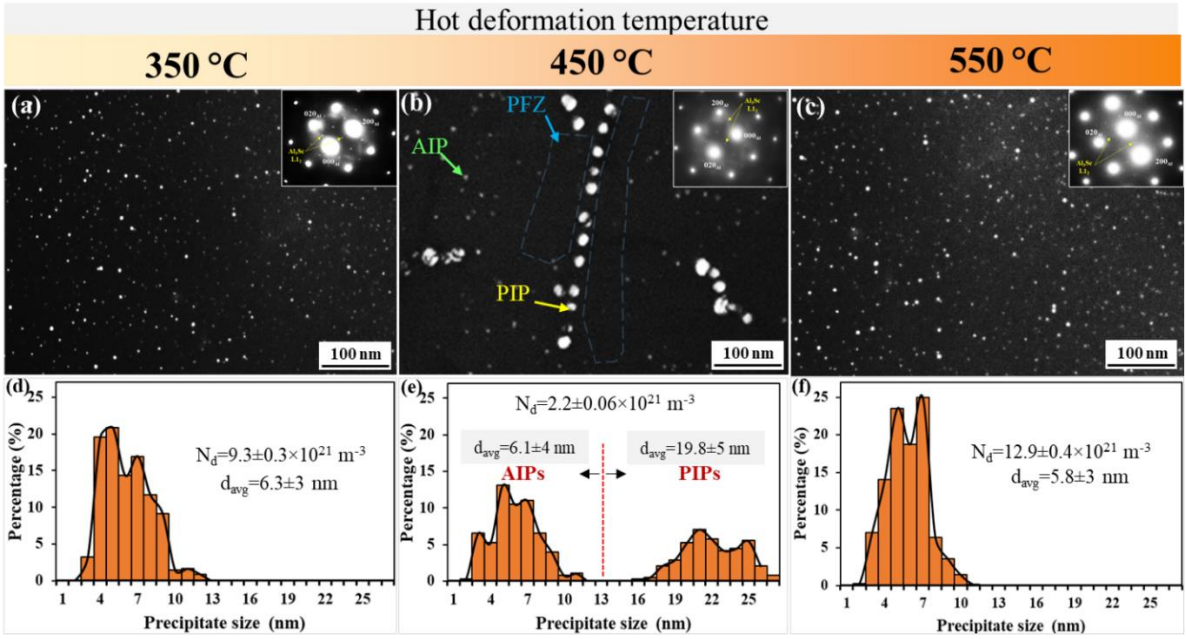

Figure 6-9. (a-c) Dark-field TEM images (with SAED insets) showing the distribution of Al_3Sc precipitates after aging at 300 °C for 24h in the Al-Sc alloy processed at various deformation temperature. (d-f) Precipitate size distribution histogram, indicating an average precipitate diameter and a number density of precipitates.

6.4. Discussion

6.4.1. Preheating temperature effects on Al3Sc PIPs and AIPs

To discuss the evolution of Al_3Sc precipitates during the thermomechanical process, both the thermodynamic driving force and kinetic limitations governing Sc precipitation must be considered, as they collectively determine the precipitation behavior and final microstructural characteristics. Figure 6-10 (a) presents the Al-Sc binary phase diagram in the low-Sc concentration regime. Below the solvus, the system lies in the two-phase field (α-Al+Al_3Sc), where Sc in excess of its equilibrium solid solubility precipitates as coherent Al_3Sc. For the Al-Sc alloy, the solvus temperature is ~516 °C; above this temperature, equilibrium conditions predict a single-phase α-Al solid solution, with complete dissolution

of Al_3Sc precipitates. During homogenization at 600 °C for 8 h (Step I in Figure 6-1), the prolonged exposure time provides sufficient opportunity for Sc diffusion, allowing a significant fraction of Sc-containing phases to dissolve into the α-Al matrix and form a supersaturated solid solution. Subsequent quenching most likely retains the majority of Sc in the form of a supersaturated solid solution (SSSS), since the equilibrium solubility of Sc in α-Al at room temperature is extremely low (<0.0001 wt.%). As a result, the as-homogenized sample provides a high driving force for Al_3Sc precipitation during thermal exposure.

During preheating (Step II), the SSSS in the Al-Sc alloy decomposes, leading to the precipitation of Al_3Sc particles. The extent and characteristics of this precipitation are governed by two primary competing factors: (i) the degree of Sc supersaturation in the α-Al matrix, which provides the thermodynamic driving force for nucleation and growth, and (ii) the temperature- and time-dependent diffusivity of Sc atoms, which determines the kinetic capability for atomic redistribution and precipitation.

During preheating (Steps II in Figure 6-1), the SSSS in the Al-Sc alloy decomposes, leading to the precipitation of Al_3Sc particles. The extent and characteristics of this precipitation are governed by two primary competing factors: (i) the level of Sc supersaturation in the α-Al matrix, which provides the thermodynamic driving force for nucleation and growth, and (ii) the temperature- and time-dependent diffusivity of Sc atoms, which governs the kinetics of precipitation.

As indicated in Figure 6-10 (a), the equilibrium solubility of Sc in α-Al increases with temperature, reducing the degree of SSSS. At lower preheating temperatures (e.g., 350 °C for 3 min), high Sc supersaturation favors a strong driving force, but sluggish Sc diffusion limits precipitate formation and growth. Conversely, higher temperatures (>450 °C) enhance Sc diffusivity, accelerating precipitation kinetics, but simultaneously reduce supersaturation (due to increasing equilibrium solubility), thereby diminishing the driving force. This interplay determines the nucleation rate, growth, and overall evolution of the PIPs, including their size, density, and distribution. For example, at 300 °C, about 0.093 wt.% Sc remains in the SSSS, whereas at 450 °C this fraction decreases to 0.053 wt.% Sc. With further temperature increase, the SSSS fraction continues to decline; at 500 °C, it is reduced to roughly 0.013 wt.% Sc. At 550 °C, which is above the solvus temperature (≈520 °C for 0.11

wt.% Sc), the phase diagram indicates that nearly all Sc is thermodynamically stable in solid solution. Although the D350 condition retains the highest amount of Sc in SSSS within the α-Al matrix, PIPs formation during preheating is strongly suppressed. In contrast, the D450 condition exhibits the highest PIPs fraction, as shown in Figure 6-6 (b).

Using the equation proposed by Senkov et al. [27], the concentration of Sc remaining in solid solution within α-Al for the deformed samples can be calculated as follows:

$$C_{Sc}(f_V) = C_{Sc}(0) - f_V[C_p(a_1/a_2)^3 - C_{Sc}(0)] \quad (3)$$

Here, $C_{Sc}(0)$ and $C_{Sc}(f_V)$ denote the Sc concentrations (at.%) in α-Al before precipitation and after the formation of an Al_3Sc volume fraction f_V during the hot deformation process, respectively. The parameters a_1 and a_2 correspond to the lattice parameters of the α-Al matrix and the Al_3Sc phase, while C_p (=25 at.%) represents the Sc concentration in the Al_3Sc phase. Using a_1=0.406 nm, a_2=0.410 nm [40, 41], the initial Sc concentration $C_{Sc}(0)$ = 0.07 at.% (0.11 wt.%), and the calculated f_V (calculated from TEM characterization), the concentration of Sc remaining in solid solution at room temperature was determined for samples deformed at different temperatures. Since the equilibrium solubility of Sc in α-Al at room temperature is negligible, the measured Sc concentration corresponds to the Sc retained in SSSS after hot deformation, as presented in Figure 6-10 (b). At the aging temperature of 300 °C, the Sc content remaining in the SSSS after hot deformation of the Al-Sc alloy is ~0.007 wt.% lower.

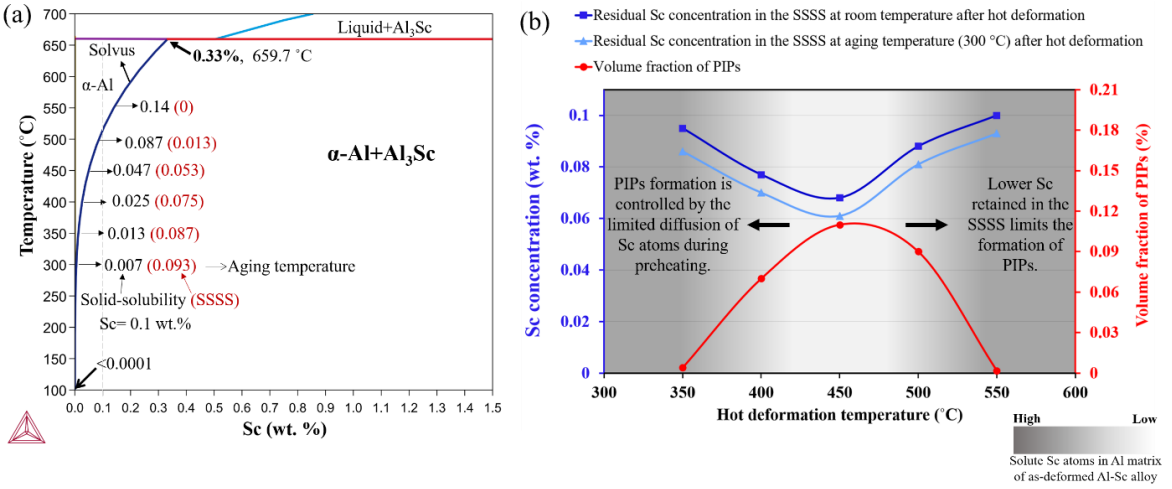

Figure 6-10. (a) Al-rich region of the Al-Sc binary phase diagram showing the solvus line and temperature-dependent solid solubility of Sc in α-Al for an Al-Sc alloy. (b) Sc concentration in different states and hot deformation temperature, along with the volume fraction of PIPs based on TEM observation at various deformation temperatures.

A detailed understanding of this behavior requires careful consideration of the strong temperature dependence of Sc diffusivity in α-Al. The Arrhenius relationship describes how diffusion coefficients vary with temperature, and it is given by the following equation [42]:

$$D = D_0 \exp(-\frac{Q}{RT}) \qquad (4)$$

Where D_0 (m^2/s) is the pre-exponential factor, Q (J/mol) is the activation energy for diffusion, R (8.314 J/(mol·K)) is the universal gas constant, T (K) is the absolute temperature. Sc has an activation energy for diffusion of Q=173 kJ/mol, with a corresponding pre-exponential factor D_0=5.31×10−4 m^2/s for Sc [14, 27, 43]. Figure 6-11 (blue curve) presents the diffusion coefficient of Sc in Al over the temperature range of 250–600 °C, showing an increase in diffusion rate with increasing temperature.

To better elucidate the combined effects of temperature and time on Sc mobility within the Al matrix, a one-dimensional root-mean-square (RMS) displacement model was employed. This statistical measure, used in diffusion studies, predicts the approximate one-dimensional displacement of atoms over time [44, 45]. The RMS atomic displacement as a function of temperature can be calculated using the following general formula:

$$\left\langle x^2 \right\rangle = 2tD_{(T)}$$
$$x = \sqrt{2tD_{(T)}} \qquad (5)$$

Here, x represents the RMS atomic displacement, t denotes time (s), and $D_{(T)}$ is the temperature-dependent diffusion coefficient. Figure 6-11 (red curve) illustrates the RMS atomic displacement as a function of temperature for exposure durations of 3 min (preheating) and 24 h (aging).

Based on a simplified one-dimensional atomic displacement model, the RMS atomic displacement during preheating at 350 °C for 3 min is estimated to be ~24 nm (without consideration of the heating ramp). Although this approach represents a 1D approximation of the actual three-dimensional diffusion process and therefore should be considered a qualitative indicator rather than a precise quantitative prediction, it provides useful insight into the relative extent of atomic mobility during the short preheating stage. The calculated

displacement (~24 nm) for 350 °C/3 min is significantly smaller than the RMS displacement of ~124 nm estimated for aging at 300 °C for 24 h, a condition known to promote the formation of uniformly distributed nanoscale precipitates (Figure 6-9 (a) and (c)). This large difference suggests that the mobility of Sc atoms during the short preheating time of 3 min at 350 °C is limited, restricting long-range diffusion and extensive precipitation.

Furthermore, according to the comprehensive study by Zakharov [17], achieving just 5% transformation in Al–0.14 wt.% Sc alloys at 350 °C requires around 55 min, indicating that substantial Al_3Sc precipitation during short preheating at 350 °C is unlikely. Consequently, under the D350 condition, the formation of Al_3Sc during preheating of Al-Sc alloy is strongly suppressed, resulting in only a small fraction of Sc (~6%) precipitating from the SSSS precipitates as Al_3Sc.

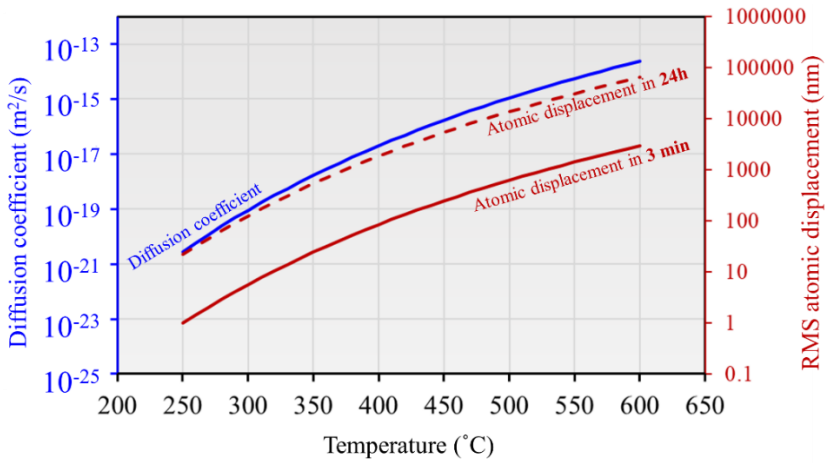

Figure 6-11. Temperature dependence of diffusion coefficient of Sc in Al (blue curve) and corresponding RMS atomic displacement over 3 min and 24 h (red curve).

At higher deformation temperatures (400–450 °C), although the level of equilibrium Sc supersaturation in the solid solution decreases, Sc diffusivity increases noticeably. Sc atoms can more readily diffuse out of the α-Al lattice during preheating, promoting rapid nucleation and growth of Al_3Sc precipitates with the $L1_2$ structure. At 450 °C, the enhanced kinetics enable the formation and growth of PIPs even within a short holding time of 3 min. At this temperature, the one-dimensional displacement of Sc atoms is around ten times greater than at 350 °C for the same preheating time, with a predicted diffusion distance of ~246 nm (Figure 6-11). This enhanced diffusivity significantly accelerates precipitate growth in

preheating step of D450, resulting in an average precipitate diameter of ~19.6 nm, as shown in Figure 6-6.

When the deformation temperature is further increased to 500–550 °C, the population of PIPs decreases. The increased equilibrium solubility of Sc in Al reduces the amount of Sc in SSSS. Therefore, at 550 °C, any small Al_3Sc precipitates that may nucleate and grow during heating are expected to dissolve back into the α-Al matrix during the holding period at 550 °C to maintain solubility equilibrium. These variations in Sc partitioning between SSSS and Al_3Sc PIPs correlate with the measured changes in EC of the as-deformed samples, which discussed in Section 4.3.

Figure 6-12 illustrates a schematic summarizing the temperature-dependent precipitation behavior of Al-Sc alloy throughout the various stages of the thermomechanical processing. During aging at 300 °C, samples D350 and D550 that had retained a higher Sc content in SSSS at aging temperature (300 ˚C) (Figure 6-10 (b)), resulting in a greater potential to form a high number density of Al_3Sc AIPs. Based on the EC results of aged Al-Sc shown in Figure 6-5 (a), it can be concluded that the Sc content in the α-Al matrix reaches a minimum under all conditions after aging. However, the stage at which Sc solute atoms are consumed, during preheating or aging, governs the resulting precipitate distribution (PIPs vs. AIPs). D350 and D550 maintain a higher number density of AIPs, whereas D450 exhibits a combination of coarse PIPs and a lower number density of AIPs.

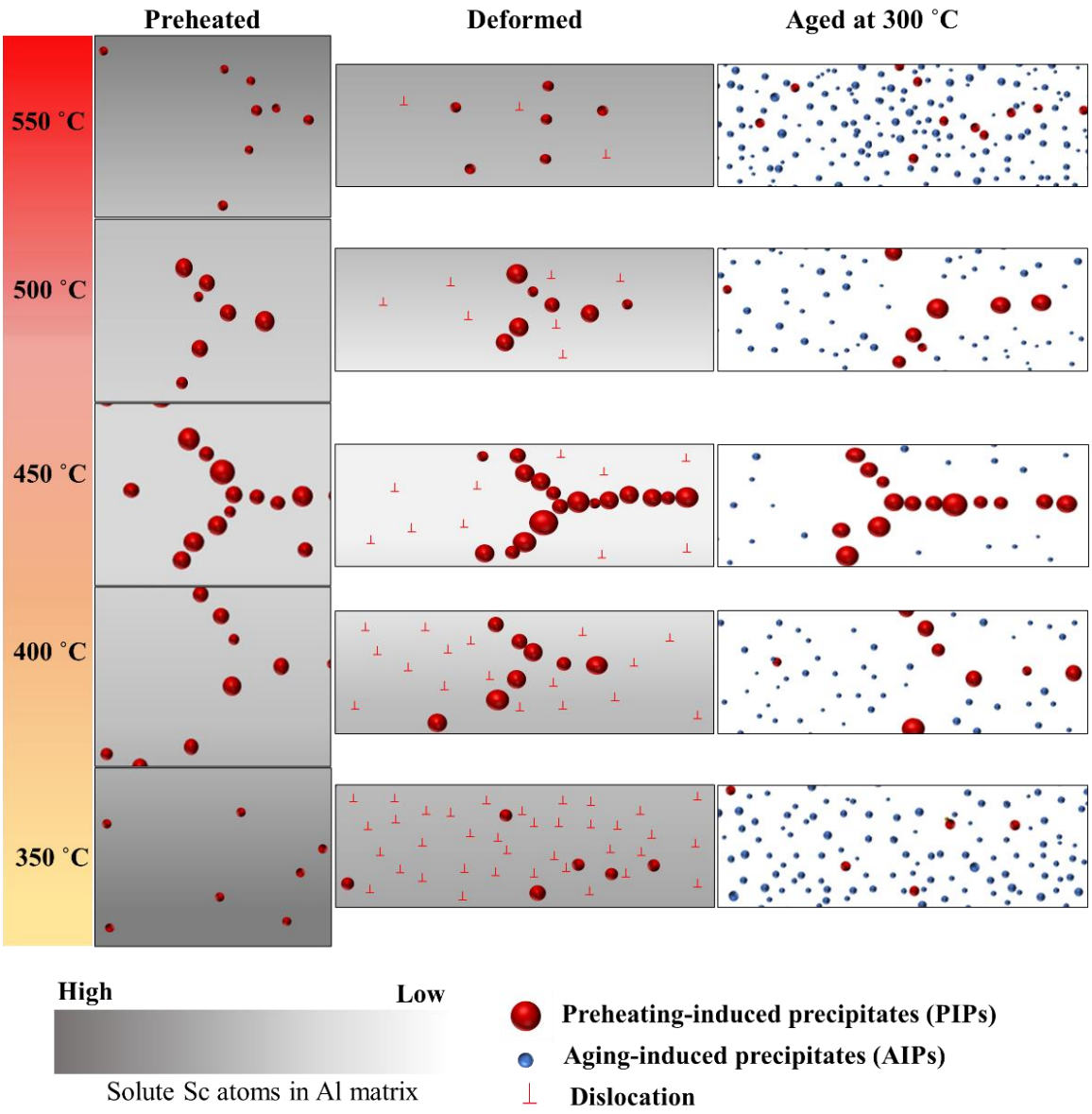

Figure 6-12. Schematic illustration of PIPs and AIPs evolution during preheating, hot deformation, and subsequent isothermal aging of an Al-Sc alloy at temperatures between 350 and 550 °C.

6.4.2. Formation mechanism of heterogeneous PIPs during preheating of 450 °C

Figure 6-13 shows the percentage increase in peak flow stress of the Al-Sc alloy compared to the Al-base across various hot deformation temperatures. Each point on this curve was calculated by dividing the difference in peak flow stress between the Al-Sc alloy and Al-base (values shown in the table inset in Figure 6-2 (c)) by the peak flow stress of the Al-base at the corresponding deformation temperature. As illustrated in Figure 6-13, the Al-Sc alloy exhibits the largest increase in flow stress at D450, showing a ~40% rise compared with the

other deformation temperatures examined. In contrast, at D550, the increase in peak flow stress relative to the Al-base is minimal, and the alloy exhibits a flow stress comparable to that of the Al-base. Specifically, the percentage increase in peak flow stress reaches ~27%, ~40%, and ~35% at D400, D450, and D500 °C, respectively, before decreasing sharply to a negligible value (~5%) at 550 °C, consistent with the reduced contribution of PIPs at this temperature. This variation in the flow stress increment can most likely be attributed to the precipitates formed during the preheating step (Step II in Figure 6-1) in the Al-Sc alloy, which provide relative strengthening at 450 °C.

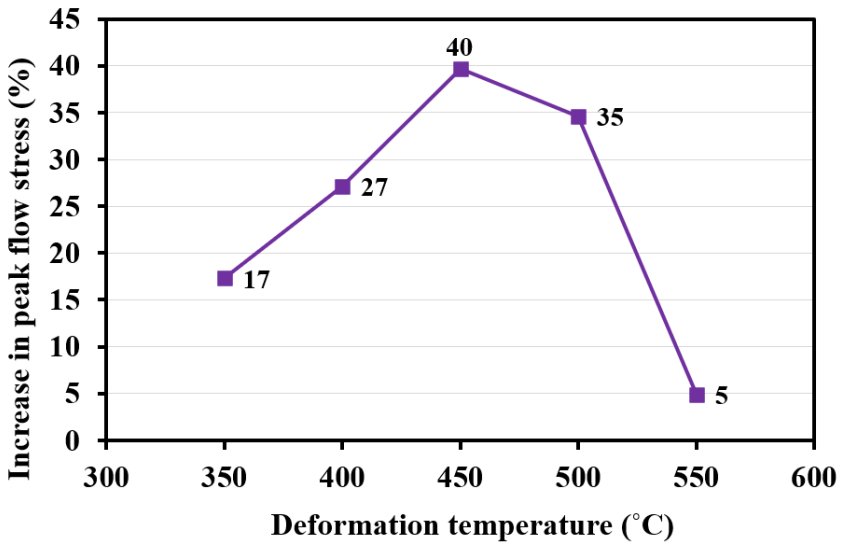

Figure 6-13. Percentage increase in peak flow stress of the Al-Sc alloy relative to the Al Al-base as a function of deformation temperature.

The chain-like precipitates that form heterogeneously during the preheating step, as shown in Figure 6-14 (a), act as strong obstacles to dislocation motion during deformation at 450 °C. As a result, multiple dislocations accumulate (pile up) behind these precipitates [46], as schematically illustrated in Figure 6-14 (b). This process increases the local stress at the head of the dislocation pile-up near the precipitates, resulting in greater resistance to deformation and a higher flow stress [47].

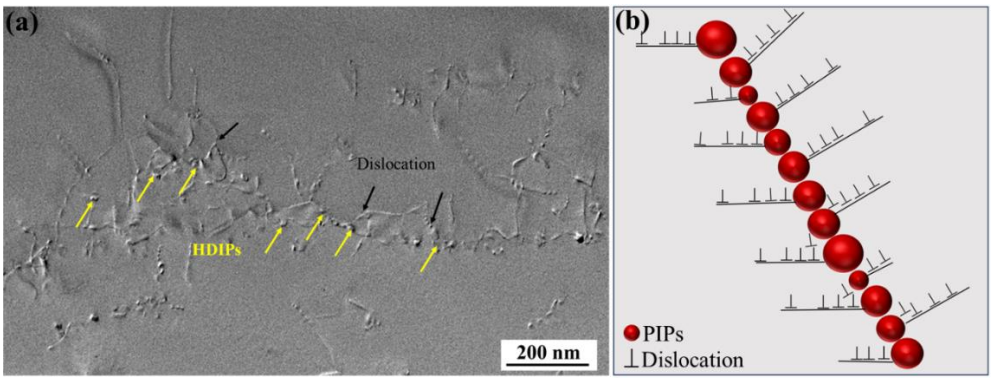

Figure 6-14. (a) Bright-field TEM image showing dislocations interacting with heterogeneously distributed PIPs at D450. (b) Schematic illustration of dislocation pile-up occurring behind the PIPs.

6.4.3. Correlation between microstructural characterization and the properties of Al-Sc conductor alloys

Electrical conductivity is affected by electron scattering, which is primarily caused by lattice distortions resulting from defects, impurities, and solute atoms [48]. It is well-documented that ρ_{ss} (solid solution resistivity) arises from solute atoms acting as effective lattice defects, scattering electrons more significantly than mechanisms such as grain boundary or precipitation strengthening [10, 49]. Therefore, the change in EC of Al-Sc alloy during the thermomechanical process is strongly associated with the depletion of Sc atoms from the Al lattice.

As shown in Figure *6-10* (b), the D350 and D550 conditions maintained a significantly higher concentration of Sc atoms in the α-Al matrix after deformation compared with D450. This is further supported by their lower EC in the deformed state, as shown in Figure *6-5* (a) (red dashed curve). Higher Sc solute concentrations in D350 and D550 cause stronger lattice distortion and electron scattering, increasing electrical resistivity and thus reducing EC in the deformed Al-Sc alloy [13]. The highest EC of D450 prior to aging is consistent with the extensive depletion of Sc from the α-Al matrix during deformation, resulting from the formation of heterogeneous Al_3Sc precipitates. During subsequent isothermal aging at 300 °C for 24 hours (step IV), the majority of the remaining Sc solute atoms finely precipitated from the α-Al matrix, leading to a further increase in EC for all deformation conditions, as shown in Figure *6-5* (a) (red solid curve). The minimal EC increment during aging for D450 (≈2.4 %IACS) is attributed to its lower SSSS level before aging and the consequently

reduced extent of Al_3Sc precipitation. In contrast, the larger EC increase (4±1 %IACS) observed in D350 and D550 during aging is associated with their higher SSSS content in deformed state and the more pronounced precipitation. After isothermal aging at 300 °C for 24 h, the EC values of all deformation conditions (D350 to D550) converged to a similar level of ~59±0.2 %IACS, which is close to that of the Al-base. It can be concluded that, after aging, the Sc concentration in the α-Al matrix becomes similarly low and limited across all deformation conditions.

Nanosized $L1_2$-structured Al_3Sc precipitates strengthen Al-Sc alloys by hindering dislocation motion, thereby enhancing hardness. For the deformed samples, PIPs may provide a slight contribution to strengthening and, consequently, to hardness. However, their direct contribution to hardness cannot be reliably quantified. A more appropriate approach is to estimate the precipitation strengthening contribution to the yield strength. Given the direct relationship between hardness and strength, the results can be interpreted qualitatively to verify the strengthening effectiveness of Al_3Sc precipitates. For this purpose, the well-known Orowan mechanism is considered, as it has been reported to be the dominant strengthening mechanism when precipitates have an average radius larger than ~2 nm [14, 50-52]. According to this mechanism, the contribution of precipitates to the yield stress can be expressed as follows [50, 53]:

$$\sigma_{Pre\ (Orowan)} = M \frac{0.4G \cdot b}{\pi\sqrt{1-\upsilon}} \frac{\ln(2r/b)}{\lambda_p} \qquad (6)$$

$$\lambda_p = r\left(\frac{2\pi}{3f_V}\right)^{0.5} \qquad (7)$$

M is the mean matrix orientation factor (Taylor factor) for Al with a value of 3.06 [54, 55], G is the shear modulus of Al at ambient temperature (taken as 25.4 GPa) [56], b is the magnitude of the Burgers vector with a value of 0.286 nm, υ is the Poisson's ratio of 0.34 [57], λ_p is the mean edge-to-edge inter-precipitate spacing, and r and f_V are the radius and volume fraction of Al_3Sc precipitates, respectively. Table 6-3 presents the Orowan strengthening contributions to the yield strength of the Al-Sc alloy in the deformed and aged conditions for D350, D450, and D550. Furthermore, in Figure 6-15, ΔH represents the experimentally measured increase in Vickers hardness due to aging, while $\Delta\sigma_{pre}$ corresponds

to the calculated increase in yield strength arising from precipitation strengthening after aging based on the Orowan bypass mechanism. The trend in ΔH is nearly consistent with that of $\Delta\sigma_{pre}$, indicating that precipitates play a primary role in strengthening of aged Al-Sc alloy, rather than other contributions such as solid-solution, grain-boundary, or dislocation strengthening.

As shown in Table 6-3, for deformed conditions, σ_{Pre} arising from PIPs contributes 34.1 MPa for D450. However, based on the results in Figure 6-5 (b), the hardness of D450 for the Al-base and Al-Sc alloy is very similar in deformed condition, showing no meaningful difference. This indicates that PIPs in D450 have little effect on hardness and strength, unlike the predicted σ_{pre}. The discrepancy arises from the heterogeneous distribution of precipitates. This may lead to measurement uncertainties, such as an overestimation of volume fraction and number density, since the TEM sampling volume is very limited. In the Orowan model, it is assumed that particles are uniformly distributed with an average inter-precipitate spacing, λ_p, of 432 nm. In practice, as shown in Figure 6-6 (b), λ_p deviates significantly from the ideal prediction of the Orowan mechanism due to the accumulation of precipitates in chain-like arrangements. This heterogeneous distribution increases the effective λ_p, thereby reducing their contribution to σ_{pre}.

According to Table 6-3, the higher Sc concentration in the SSSS of the D350 and D550 conditions promotes the formation of AIPs with a more uniform distribution in the microstructure after aging at 300 °C for 24 h, resulting in higher σ_{pre} and hardness values. Owing to the slightly higher number density of precipitates, the aged D550 condition shows a higher σ_{pre} compared to aged D350, which is consistent with the ΔH results presented in Figure 6-15. In contrast, the D450 condition exhibits the minimum σ_{pre} due to the lower Sc content in the SSSS and the reduced formation of AIPs, because a significant portion of the high-potential supersaturated Sc for precipitation was already consumed during preheating and deformation.

Table 6-3. Calculated Orowan stress (σ_{Pre}) of the Al-Sc alloy at D350, D450, and D550 under deformed and aged conditions, based on precipitate volume fraction (F_v), average precipitate radius (r), and inter-precipitate spacing (λ_p).

Aging condition		F_V %	r (nm)	λ_p (nm)	σ_{Pre} (MPa)
D350	Deformed	0.011	4.5	630	19.1

	Aged	0.105	3.2	143	75.8
D450	Deformed	0.108	9.8	432	34.1
	Aged	0.121	6.0	278	51.5
D550	Deformed	0.002	2.6	841	12.0
	Aged	0.112	2.9	125	83.7

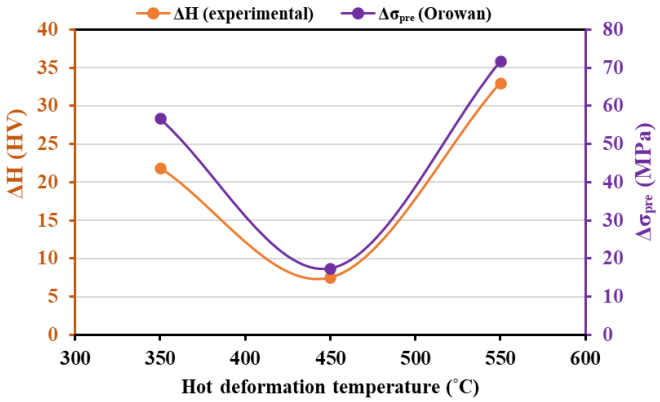

Figure 6-15. Comparison between the hardness increment after aging ($\Delta H = H_{aged} - H_{deformed}$) and the Orowan strengthening increment after aging ($\Delta\sigma_{pre} = \sigma_{pre(aged)} - \sigma_{pre(deformed)}$).

The schematic presented in Figure 6-16 summarizes how microstructural evolution during hot deformation in the temperature range of 350–550 °C critically governs the balance of properties in Al–Sc alloys. Lower (≤350 °C) and higher deformation temperatures (above the solvus temperature of ~516 °C) provide favorable processing windows for achieving higher supersaturation in the deformed state and, subsequently, more effective nanoscale Al_3Sc precipitate strengthening during aging. Although the contribution of precipitates to strengthening at 350 °C is slightly smaller than that at 550 °C, the final hardness values are comparable. This similarity arises from the additional work-hardening introduced during low-temperature deformation, which compensates for the relatively lower precipitation contribution [58]. This interpretation is supported by Figure 6-4, where the 550 °C condition exhibits a higher fraction of substructured regions, indicating dominant softening mechanisms associated with dynamic recovery and recrystallization. In contrast, deformation at 350 °C suppresses these softening mechanisms, resulting in a higher fraction of deformed regions with greater stored strain energy and limited recovery/recrystallization.

D350 and D550 exhibited superior performance compared to D450 in the Al-Sc alloy, showing comparable EC and hardness. However, between the D350 and D550 conditions, a

key question arises: which deformation temperature is more suitable for large-scale industrial processing? In hot extrusion, factors such as strain, ram speed, exit temperature, bearing length and temperature, and die geometry significantly influence the actual thermal–mechanical conditions [46]. For instance, a higher ram speed during extrusion with 350 °C preheating may increase the exit temperature and stimulate the formation of PIPs, which could be unfavorable for subsequent aging. Conversely, long deformation process near 550 °C, especially at low strain rates, may promote recrystallization and excessive grain growth. Therefore, the optimal deformation temperature must be selected in conjunction with the full set of processing parameters to ensure a desirable microstructure and performance.

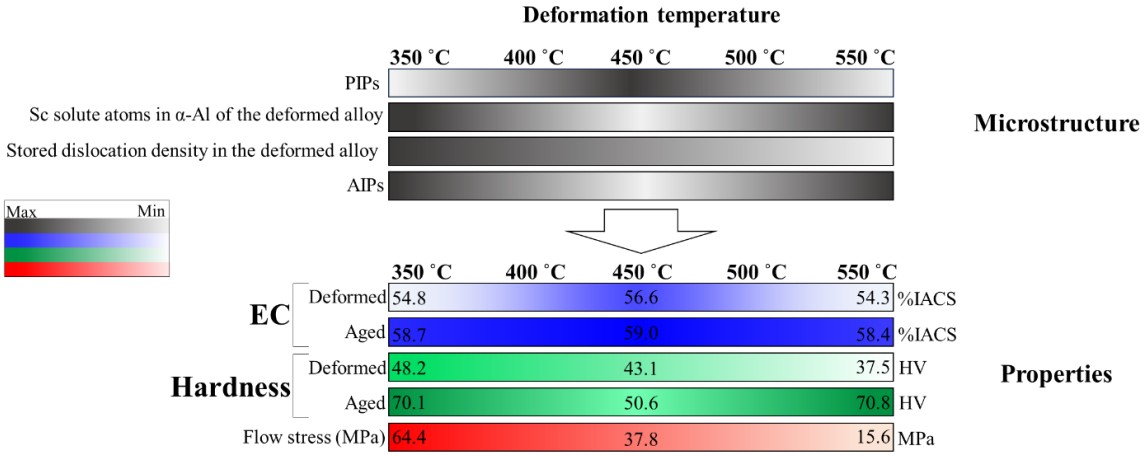

Figure 6-16. Schematic illustration showing how microstructural variations influence different properties of Al-Sc alloys during hot deformation in the temperature range of 350–550 °C.

6.5. Conclusion

This study examines how hot deformation temperature governs the interaction between preheating-induced Al_3Sc precipitates (PIPs) and aging-induced precipitates (AIPs), and their effects on mechanical and electrical properties of an Al–0.1 wt.% Sc alloy processed by uniaxial hot compression. The principal conclusions are:

1. Preheating at 450 °C promotes heterogeneous PIPs formation along LAGBs (1.5˚-2˚). This results in significant Sc depletion from the α-Al matrix during preheating, reducing the AIPs number density during final aging, and resulting in the lowest hardness (51 HV) despite relatively high EC (~59 %IACS).
2. Deformation at 350 °C and 550 °C largely retains Sc in a supersaturated solid solution, with approximately 0.095 wt.% Sc remaining in the Al matrix. Under these conditions,

PIPs formation is suppressed, enabling the development of a uniform dispersion of nanoscale coherent Al_3Sc AIPs during aging at 300 °C for 24 h.

3. A favorable combination of hardness (~70 HV) and EC (~59 % IACS) is achieved after aging for samples deformed at 350 °C and 550 °C for dilute Al-Sc conductor alloys.
4. The highest percentage increase in peak flow stress relative to the Al-base occurs at 450 °C, which is attributed to coarse chain-like Al_3Sc PIPs acting as barriers to dislocation motion.
5. These findings indicate that extrusion process parameters, particularly the billet preheating temperature, must be carefully optimized for a given Al–Sc alloy to fully realize the strengthening potential of the Sc addition.

Acknowledgments

The authors would like to express their sincere gratitude to the industrial partners, Rio Tinto Aluminium and Mindcore Technology, for their valuable support and collaboration throughout this project. The authors also wish to thank the technical teams at Rio Tinto Aluminium, the University Research Centre on Aluminium (CURAL), and the Chaire de recherche Institutionnelle en Métallurgie de la Transformation de l'Aluminium (CIMTAL) for their collaboration, technical expertise, and contributions to the successful completion of this work.

Funding

This research was funded by Rio Tinto Aluminum, Center Quebecois de Recherche et de Developpement de l'Aluminium (CQRDA), and Natural Sciences and Engineering Research Council of Canada (NSERC) under Grant Number ALLRP 576503–22.

Authors contribution

Behrouz Abnar: Investigation, Methodology, Formal analysis, Writing – original draft. *Paul Rometsch:* Conceptualization, Validation, Writing – review & editing. *Mousa Javidani:* Conceptualization, Validation, Writing – review & editing, Project administration.

6.6. References

[1] F. Czerwinski, "Aluminum alloys for electrical engineering: a review," *Journal of Materials Science,* vol. 59, no. 32, pp. 14847–14892, 2024.

[2] M. Khoshghadam-Pireyousefan, M. Javidani, A. Maltais, J. Lévesque, and X.-G. Chen, "Strength-conductivity synergy in hypoeutectic Al-Si conductors via ultrafine-grained

embedded Si nanoprecipitates," *Materials Science and Engineering: A,* vol. 929, p. 148124, 2025.
[3] F. Yavari, M. Javidani, L. R. Pan, and X.-G. Chen, "The influence of Ce addition on the aging response of AlSi3Mg0. 5 cast conductor alloy: evaluation of electrical conductivity, mechanical properties, and microstructure," *Journal of Alloys and Compounds,* p. 182412, 2025.
[4] Z. Yuan *et al.*, "Research on process regulation and deformation mechanism of Mg/Al composite plates during hot bending forming," *Journal of Materials Research and Technology,* 2026.
[5] G. M. Novotny and A. J. Ardell, "Precipitation of Al3Sc in binary Al–Sc alloys," *Materials Science and Engineering: A,* vol. 318, no. 1-2, pp. 144–154, 2001.
[6] E. Marquis and D. N. Seidman, "Nanoscale structural evolution of Al3Sc precipitates in Al (Sc) alloys," *Acta materialia,* vol. 49, no. 11, pp. 1909–1919, 2001.
[7] K. Yan, Z. Chen, W. Lu, Y. Zhao, W. Le, and S. Naseem, "Nucleation and growth of Al3Sc precipitates during isothermal aging of Al-0.55 wt% Sc alloy," *Materials Characterization,* vol. 179, p. 111331, 2021.
[8] X. Zhang, Y. Huang, Y. Liu, and X. Ren, "A systematic study of interface properties for L12-Al3Sc/Al based on the first-principles calculation," *Results in Physics,* vol. 19, p. 103378, 2020.
[9] Y. Liu *et al.*, "Effect of chemical composition and heat treatment on the microstructure and performance of Ag-based alloy wires," *Materials & Design,* p. 114728, 2025.
[10] W. Wang *et al.*, "Microstructure and properties of novel Al-Ce-Sc, Al-Ce-Y, Al-Ce-Zr and Al-Ce-Sc-Y alloy conductors processed by die casting, hot extrusion and cold drawing," *Journal of Materials Science & Technology,* vol. 58, pp. 155–170, 2020.
[11] K. E. Knipling, D. N. Seidman, and D. C. Dunand, "Ambient-and high-temperature mechanical properties of isochronally aged Al–0.06 Sc, Al–0.06 Zr and Al–0.06 Sc–0.06 Zr (at.%) alloys," *Acta Materialia,* vol. 59, no. 3, pp. 943–954, 2011.
[12] J. Røyset and N. Ryum, "Scandium in aluminium alloys," *International Materials Reviews,* vol. 50, no. 1, pp. 19–44, 2005.
[13] B. Abnar, S. Gashtiazar, P. Rometsch, and M. Javidani, "Advanced thermal-resistant aluminum conductor alloys: A comprehensive review," *International Journal of Minerals, Metallurgy and Materials,* vol. 33, no. 1, pp. 68–93, 2026.
[14] K. E. Knipling, R. A. Karnesky, C. P. Lee, D. C. Dunand, and D. N. Seidman, "Precipitation evolution in Al–0.1 Sc, Al–0.1 Zr and Al–0.1 Sc–0.1 Zr (at.%) alloys during isochronal aging," *Acta Materialia,* vol. 58, no. 15, pp. 5184–5195, 2010.
[15] B. Abnar, S. N. Khangholi, P. Rometsch, and M. Javidani, "Effect of hot deformation parameters on the performance and thermomechanical behavior of Cu-modified Al–Mg–Si conductor alloys," *Journal of Materials Science,* 2025/10/06 2025, doi: 10.1007/s10853-025-11528-8.
[16] A. Y. Algendy, K. Liu, P. Rometsch, N. Parson, and X. G. Chen, "Evolution of discontinuous/continuous Al3 (Sc, Zr) precipitation in Al-Mg-Mn 5083 alloy during thermomechanical process and its impact on tensile properties," *Materials Characterization,* vol. 192, p. 112241, 2022.
[17] V. Zakharov, "Stability of the solid solution of scandium in aluminum," *Metal Science and Heat Treatment,* vol. 39, no. 2, pp. 61–66, 1997.
[18] V. Zakharov, "Effect of scandium on the structure and properties of aluminum alloys," *Metal science and heat treatment,* vol. 45, no. 7, pp. 246–253, 2003.
[19] V. Zakharov and I. Fisenko, "Alloying aluminum alloys with scandium," *Metal Science and Heat Treatment,* vol. 59, no. 5, pp. 278–284, 2017.

[20] X. Na, L. Wenqing, Z. Liu, and T. Muthuramalingam, "Effect of scandium in Al–Sc and Al–Sc–Zr alloys under precipitation strengthening mechanism at 350° C aging," *Metals and Materials International,* vol. 27, no. 12, pp. 5145–5153, 2021.
[21] M. Jones and F. Humphreys, "Interaction of recrystallization and precipitation: The effect of Al3Sc on the recrystallization behaviour of deformed aluminium," *Acta materialia,* vol. 51, no. 8, pp. 2149–2159, 2003.
[22] S. Fan *et al.*, "Effects of processing paths on the microstructure, mechanical properties and electrical conductivity of dilute Al-Zr-Sc alloy conductive wires," *Journal of Materials Science & Technology,* vol. 188, pp. 202–215, 2024.
[23] B. Abnar, P. Rometsch, and M. Javidani, "Influence of extrusion preheating temperature and aging strategy on precipitation and performance of Al–Sc–Zr conductor alloys," *Materials Today Communications,* p. 114911, 2026.
[24] J. Wei, J. Han, Y. Jia, T. Wang, and Q. Huang, "Evolution of multiscale heterostructures and comprehensive properties improvement in the large thickness ratio Ti/Al/Mg clad plates under heterothermal rolling," *Journal of Magnesium and Alloys,* 2025.
[25] Q. Li *et al.*, "Exceptional grain refinement and the mechanism of columnar-to-equiaxed transition in arc welding of a cast AlLi alloy," *Materials Characterization,* p. 115446, 2025.
[26] A. Y. Algendy, K. Liu, P. Rometsch, N. Parson, and X.-G. Chen, "Effects of AlMn dispersoids and Al3 (Sc, Zr) precipitates on the microstructure and ambient/elevated-temperature mechanical properties of hot-rolled AA5083 alloys," *Materials Science and Engineering: A,* vol. 855, p. 143950, 2022.
[27] O. Senkov, M. Shagiev, S. Senkova, and D. Miracle, "Precipitation of Al3 (Sc, Zr) particles in an Al–Zn–Mg–Cu–Sc–Zr alloy during conventional solution heat treatment and its effect on tensile properties," *Acta materialia,* vol. 56, no. 15, pp. 3723–3738, 2008.
[28] D. Jin, H. Li, Z. Zhu, C. Yang, B. Chen, and Y. Miao, "Effects of cooling rate in homogenization on microstructure, hot deformation resistance and subsequent age-hardening behavior of an Al–Mg–Si alloy," *Journal of Materials Research and Technology,* vol. 27, pp. 3283–3300, 2023.
[29] A. Ghosh, A. Elasheri, N. Parson, and X.-G. Chen, "Microstructure and texture evolution during high-temperature compression of Al-Mg-Si-Zr-Mn alloy," *Materials Characterization,* vol. 205, p. 113312, 2023.
[30] M. Mofarrehi, M. Javidani, and X.-G. Chen, "Effect of Mn content on the hot deformation behavior and microstructure evolution of Al–Mg–Mn 5xxx alloys," *Materials Science and Engineering: A,* vol. 845, p. 143217, 2022.
[31] F. J. Humphreys and M. Hatherly, *Recrystallization and related annealing phenomena*. Elsevier, 2012.
[32] K. Huang and R. E. Logé, "A review of dynamic recrystallization phenomena in metallic materials," *Materials & Design,* vol. 111, pp. 548–574, 2016.
[33] M. Shakiba, N. Parson, and X.-G. Chen, "Hot deformation behavior and rate-controlling mechanism in dilute Al–Fe–Si alloys with minor additions of Mn and Cu," *Materials Science and Engineering: A,* vol. 636, pp. 572–581, 2015.
[34] F. Czerwinski, "Thermal stability of aluminum alloys," *Materials,* vol. 13, no. 15, p. 3441, 2020.
[35] R. W. Cahn and P. Haasen, *Physical metallurgy*. Elsevier, 1996.
[36] R. Guan, Y. Shen, Z. Zhao, and X. Wang, "A high-strength, ductile Al-0.35 Sc-0.2 Zr alloy with good electrical conductivity strengthened by coherent nanosized-precipitates," *Journal of Materials Science & Technology,* vol. 33, no. 3, pp. 215–223, 2017.
[37] Y. Shen, R. Guan, Z. Zhao, and R. Misra, "Ultrafine-grained Al–0.2 Sc–0.1 Zr alloy: The mechanistic contribution of nano-sized precipitates on grain refinement during the novel process of accumulative continuous extrusion," *Acta Materialia,* vol. 100, pp. 247–255, 2015.

[38] E. Clouet, M. Nastar, and C. Sigli, "Nucleation of Al 3 Zr and Al 3 Sc in aluminum alloys: From kinetic Monte Carlo simulations to classical theory," *Physical Review B,* vol. 69, no. 6, p. 064109, 2004.
[39] G. E. Totten, *Heat treating of nonferrous alloys*. ASM International, 2016.
[40] Y. Harada and D. Dunand, "Microstructure of Al3Sc with ternary transition-metal additions," *Materials Science and Engineering: A,* vol. 329, pp. 686–695, 2002.
[41] K. Fukunaga, T. Shouji, and Y. Miura, "Temperature dependence of dislocation structure of L12–Al3Sc," *Materials Science and Engineering: A,* vol. 239, pp. 202–205, 1997.
[42] P. Shewmon, *Diffusion in solids*. Springer, 2016.
[43] N. Peterson and S. Rothman, "Impurity diffusion in aluminum," *Physical Review B,* vol. 1, no. 8, p. 3264, 1970.
[44] G. Ehrlich, "Atomic displacements in one-and two-dimensional diffusion," *The Journal of Chemical Physics,* vol. 44, no. 3, pp. 1050–1055, 1966.
[45] H. C. Berg, *Random walks in biology* (Diffusion: Microscopic Theory). Princeton University Press, 1993.
[46] T. Sheppard, *Extrusion of aluminium alloys*. Springer Science & Business Media, 2013.
[47] S. Ha *et al.*, "Microscopic-plastic deformation behavior of grain boundary precipitates in an Al–Zn–Mg alloy," *Journal of Materials Research and Technology,* vol. 30, pp. 3420–3429, 2024.
[48] S. N. Khangholi, M. Javidani, A. Maltais, and X. G. Chen, "Review on recent progress in Al–Mg–Si 6xxx conductor alloys," *Journal of Materials Research,* vol. 37, no. 3, pp. 670–691, 2022.
[49] S. N. Khangholi, M. Javidani, A. Maltais, and X.-G. Chen, "Optimization of mechanical properties and electrical conductivity in Al–Mg–Si 6201 alloys with different Mg/Si ratios," *Journal of Materials Research,* vol. 35, no. 20, pp. 2765–2776, 2020.
[50] C. Booth-Morrison, D. C. Dunand, and D. N. Seidman, "Coarsening resistance at 400 C of precipitation-strengthened Al–Zr–Sc–Er alloys," *Acta Materialia,* vol. 59, no. 18, pp. 7029–7042, 2011.
[51] D. N. Seidman, E. A. Marquis, and D. C. Dunand, "Precipitation strengthening at ambient and elevated temperatures of heat-treatable Al (Sc) alloys," *Acta Materialia,* vol. 50, no. 16, pp. 4021–4035, 2002.
[52] G. Li *et al.*, "Effect of Sc/Zr ratio on the microstructure and mechanical properties of new type of Al–Zn–Mg–Sc–Zr alloys," *Materials Science and Engineering: A,* vol. 617, pp. 219–227, 2014.
[53] Z. Li, Z. Zhang, and X.-G. Chen, "Improvement in the mechanical properties and creep resistance of Al-Mn-Mg 3004 alloy with Sc and Zr addition," *Materials Science and Engineering: A,* vol. 729, pp. 196–207, 2018.
[54] Y. Yang, S. A. Hackney, and P. G. Sanders, "High-temperature deformation of supersaturated Al-Sc-Zr produced via melt-spinning and extrusion," *Materials Science and Engineering: A,* vol. 857, p. 144138, 2022.
[55] J. Bai, M. Gao, C. Wang, J. Pei, L. Yang, and R. Guan, "Role of Er element and two-stage heat treatment in a rheo-extruded Al–Sc–Zr alloy: Balance strength and electrical conductivity," *Materials & Design,* p. 115096, 2025.
[56] H. J. Frost and M. F. Ashby, "Deformation-mechanism maps: the plasticity and creep of metals and ceramics," *(No Title),* 1982.
[57] M. Meyers, "Mechanical metallurgy: principles and applications," *Prentice-Hall, Inc, Englewood Cliffs, N. J. 07632, U. S. A, 1984. 761,* 1984.
[58] Z. Zhang, L. Wan, Y. Yang, Z. Feng, and Y. Shi, "Improving interlayer bonding and tensile isotropy in additive friction stir deposition of Al-Zn-Mg-Cu alloys via a novel tool design strategy," *Additive Manufacturing,* p. 105250, 2026.

Chapitre 7. Conclusions et recommandations

7.1. Conclusions générales

1. Cette étude a systématiquement examiné les effets de la composition de l'alliage et du traitement thermomécanique sur la microstructure, les propriétés mécaniques et la conductivité électrique des alliages conducteurs d'Al destinés aux applications de barres omnibus électriques. Une attention particulière a été accordée aux alliages Al–Mg–Si modifiés par Cu ainsi qu'aux alliages de série 1xxx contenant Sc et Zr, en mettant en évidence le rôle des conditions de déformation, du comportement de précipitation et des stratégies de vieillissement dans l'optimisation du compromis résistance–conductivité pour les applications avancées de conducteurs. Le résumé des principales conclusions générales de toutes les parties de cette étude est présenté ci-dessous.
2. La température de déformation à chaud est un paramètre critique gouvernant le compromis résistance–CE dans les alliages conducteurs des séries 1xxx et 6xxx, par son contrôle de la distribution des éléments en solution solide et du comportement de précipitation.
3. Les ajouts de Cu augmentent la résistance à la déformation en supprimant la restauration dynamique, en affinant la structure des sous-grains et en augmentant l'énergie d'activation; toutefois, leur effet de renforcement diminue à des températures de déformation plus élevées (par exemple, 550 °C).
4. Une teneur optimale en Cu (~0,3 % en poids) procure le meilleur équilibre entre la résistance et la CE dans les alliages Al–Mg–Si, permettant une amélioration significative de la dureté tout en maintenant une conductivité acceptable pour les applications de conducteurs.
5. Une température de déformation plus basse (450 °C) améliore la CE des alliages Al–Mg–Si–Cu, mais réduit la dureté, principalement en raison de la formation de précipités β d'équilibre grossiers qui retirent les atomes de soluté de la matrice sans contribuer efficacement au renforcement.
6. La température de préchauffage avant extrusion influence fortement la précipitation dans les alliages Al–Sc–Zr, où un préchauffage plus faible (420 °C) supprime le grossissement prématuré et favorise une distribution fine et dense des précipités de renforcement.

7. Le vieillissement en deux étapes est significativement plus efficace que le vieillissement en une étape dans les alliages conducteurs Al–Sc–Zr, en produisant une structure de précipités cœur–coquille $Al_3(Sc,Zr)$ fine qui améliore la résistance et la résistance au grossissement tout en maintenant une CE élevée.
8. La formation de précipités cœur–coquille (cœur riche en Sc, coquille riche en Zr) constitue un mécanisme clé pour améliorer la stabilité thermique et le renforcement, puisqu'elle ralentit la diffusion et inhibe le grossissement des précipités.
9. Les précipités induits par le préchauffage (PIPs) jouent un rôle déterminant dans les alliages Al–Sc, puisque leur formation durant le préchauffage peut consommer les atomes de soluté et réduire l'efficacité du vieillissement subséquent.
10. La déformation à 450 °C entraîne un rôle néfaste de la formation hétérogène des PIPs dans les alliages Al–Sc, provoquant un appauvrissement en Sc et conduisant à la plus faible dureté après vieillissement malgré une CE relativement élevée.
11. Des conditions de déformation optimales (350 °C ou 550 °C) suppriment la formation des PIPs et préservent les éléments en solution solide, permettant ainsi la formation uniforme de précipités nanométriques durant le vieillissement et l'obtention de la meilleure combinaison de dureté et de CE.
12. Les paramètres d'extrusion, en particulier la température de préchauffage des billettes, doivent être soigneusement optimisés pour un alliage Al–Sc donné afin d'exploiter pleinement les bénéfices de renforcement apportés par les ajouts de Sc.

7.2. Recommandations

1. Les études futures devraient se concentrer sur l'effet du traitement T6 sur les conducteurs Al–Mg–Si modifiés par Cu, ainsi que sur la stabilité thermique à long terme, la résistance à la corrosion, le comportement en fatigue et le fluage. Les ajouts de Zr et de Sc devraient être davantage étudiés afin d'améliorer la stabilité microstructurale et d'optimiser le compromis résistance–conductivité pour les applications à haute température des conducteurs Al–Mg–Si modifiés par Cu.
2. La mise en œuvre d'un traitement de vieillissement en deux étapes sur des conducteurs en fil Al–Sc–Zr thermorésistants peut améliorer considérablement leur stabilité microstructurale et leurs performances mécaniques en optimisant la séquence de

précipitation, en améliorant la distribution des particules Al3(Sc,Zr) et en augmentant la résistance au grossissement à des températures de service élevées.

3. L'application d'un traitement au bore aux alliages d'Al contenant Sc et Zr peut améliorer la CE, la rapprochant de celle de l'aluminium pur après un traitement de vieillissement approprié. Cette amélioration est associée à une réduction de la teneur en solutés nuisibles dans la matrice. En mettant en œuvre cette stratégie tout en tenant compte des températures optimales de préchauffage et de déformation identifiées au chapitre 6, le procédé d'extrusion pourrait être réalisé avec succès. Les résultats devraient permettre d'atteindre une résistance à la traction d'environ 200 MPa, tout en maintenant une conductivité électrique supérieure d'au moins 2 % IACS (environ 61 % IACS), ce qui permettrait d'obtenir un alliage conducteur nettement plus avancé, offrant un meilleur compromis entre la résistance mécanique et la conductivité électrique.
4. Le développement approfondi des précipités cœur–coquille Al_3(Sc,Zr) et de leur évolution dans des alliages multicomposants (par exemple, avec des ajouts de Cu) est essentiel. La modélisation computationnelle avancée, combinée à des techniques de caractérisation à l'échelle atomique telles que la tomographie par sonde atomique (APT) et la microscopie électronique en transmission à haute résolution (HRTEM), sera essentielle pour comprendre et optimiser ces structures afin d'améliorer la résistance mécanique et la stabilité thermique.
5. Une optimisation précise des paramètres de traitement est nécessaire pour exploiter pleinement les alliages contenant Sc et Zr. Les travaux futurs devraient affiner les stratégies de vieillissement en deux étapes afin de contrôler la distribution des précipités et de limiter leur grossissement. De plus, des approches telles que la déformation plastique sévère (SPD) pourraient améliorer le raffinement des grains et accélérer la cinétique de précipitation.
6. Une autre orientation prometteuse est le développement de composites hybrides à base d'alliages Al–Sc–Zr renforcés par du graphène, des nanotubes de carbone ou des céramiques. Ces matériaux peuvent améliorer significativement la conductivité électrique, la résistance mécanique et la stabilité thermique, permettant ainsi la conception de conducteurs légers et haute performance pour des applications avancées en puissance et en électronique.

Liste des publications

Articles de revue scientifique

1. B. Abnar, S. N. Khangholi, P. Rometsch, and M. Javidani, "Effect of hot deformation parameters on the performance and thermomechanical behavior of Cu-modified Al–Mg–Si conductor alloys," Journal of Materials Science, vol. 60, no. 41, pp. 19912–19941, 2025.
2. B. Abnar, S. Gashtiazar, P. Rometsch, and M. Javidani, "Advanced thermal-resistant aluminum conductor alloys: A comprehensive review," International Journal of Minerals, Metallurgy and Materials, vol. 33, no. 1, pp. 68–93, 2026.
3. B. Abnar, P. Rometsch, and M. Javidani, "Influence of extrusion preheating temperature and aging strategy on precipitation and performance of Al–Sc–Zr conductor alloys," Materials Today Communications, vol. 51, p. 114911, 2026.
4. B. Abnar, P. Rometsch, and M. Javidani, " The role of preheating–induced precipitates in tailoring the electrical and mechanical properties of deformed Al–0.1 wt.% Sc conductors ", Materials Characterization, vol. 240, p. 116904, 2026.

Communications en conférence

1. B. Abnar, S. N. Khangholi, P. Rometsch, and M. Javidani, "Effects of Cu Addition and Temperature on Hot Deformation Behavior of Al–Mg–Si 6201 Conductor Alloys," in *Conference of Metallurgists*, 2024: Springer, pp. 1649–1651.

Affiches de conférence

1. Investigation the effect of heat treatment procedures on the strength and electrical conductivity of Sc- and Zr-containing 1xxx extruded Al conductors, Behrouz Abnar, Paul Rometsch, Mousa Javidani, REGAL Students' Day, Chicoutimi, Canada, October. 2024.
2. Influence of hot deformation temperature on Al-Sc and Al-Sc-Zr conductor alloys, Behrouz Abnar, Paul Rometsch, Mousa Javidani, REGAL Students' Day, Trois-Rivières, Canada, October. 2025.

Présentation

1. Recent progress in aluminum conductor alloys containing Sc and Zr, Behrouz Abnar, Samaneh Gashtiazar, Paul Rometsch, Mousa Javidani, The 37th Canadian Materials Science Conference (CMSC), Québec City, May 4-7, 2026
2. Effect of hot deformation temperature on the performance of Al-Sc and Al-Sc-Zr conductor alloys, Behrouz Abnar, Paul Rometsch, Mousa Javidani, The 63rd Annual Conference of Metallurgists, Montreal, Canada, July 7-10, 2025.
3. Effects of Cu Addition on Hot Deformation Behavior of Al-Mg-Si Conductor Alloys, Behrouz Abnar, Siamak Nikzad Khangholi, Paul Rometsch, Mousa Javidani, The 63rd Annual Conference of Metallurgists, Halifax, Nova Scotia, Canada August 19-22, 2024,COM-2024